AUTOMATED PROXIMAL SENSING FOR ESTIMATION OF THE BIDIRECTIONAL REFLECTANCE DISTRIBUTION FUNCTION IN A MEDITERRANEAN TREE-GRASS ECOSYSTEM

Tesis Doctoral presentada por

JAVIER PACHECO-LABRADOR

Bajo la dirección de

Dra. María del Pilar Martín Isabel

Programa de Doctorado en Tecnologías de la Información Geográfica.

DEPARTAMENTO DE GEOLOGÍA, GEOGRAFÍA Y MEDIO AMBIENTE

Alcalá de Henares, Septiembre de 2015

PREFACE

This Thesis has been written at the Environmental Remote Sensing and Spectroscopy Laboratory (SpecLab) from the Spanish National Research Council (CSIC) in Madrid, Spain. The works were carried out between October 2011 and August 2015 and included 3 international research stays: 6 weeks at the *Institut de Physique du Globe de Paris*, *Université Paris Diderot* (France) supervised by the Dr. Stéphane Jacquemoud; 6 months at the college of Forestry, Oregon State University (USA) supervised by Dr. Thomas Hilker; and 3 months of stay at the Remote Sensing of Environmental Dynamics Laboratory, University of Milano-Bicocca (Italy) supervised by Dr. Micol Rossini.

The PhD was funded by the JAE-Predoc Fellowship Program which is cofounded by the European Social Fund. Part of the research stays and activities were funded by the COST Action ES0903 EUROSPEC and COST Action ES1309 OPTIMISE and the projects BIOSPEC "Linking spectral information at different spatial scales with biophysical parameters of Mediterranean vegetation in the context of Global Change" (http://www.lineas.cchs.csic.es/biospec) (CGL2008- 02301/CLI, Ministry of Science and Innovation) and FLUχPEC "Monitoring changes in water and carbon fluxes from remote and proximal sensing in a Mediterranean "dehesa" ecosystem" (http://www.lineas.cchs.csic.es/fluxpec) (CGL2012- 34383, Ministry of Economy and Competitiveness).

AGRADECIMIENTOS

Mucha gente ha contribuido de diferentes formas a la elaboración de esta tesis, tanto profesional como personalmente.

Primero, quisiera agradecer a mi directora Mª del Pilar Martín por su apoyo, su confianza, su paciencia y su consejo durante todos estos años. Por darme todas las oportunidades y por hacerme ver mis errores, a pesar de mi cabezonería. Y también por enseñarme que detrás de tanto espectro, tanto *paper* y tanto píxel, al final, siempre hay personas.

También quisiera agradecer a todos mis compañeros y colegas del Laboratorio de Espectro-radiometría y Teledetección Ambiental, David Riaño, Fco Javier Martínez, Pilar Echavarría, Israel Gómez, Lara Vilar, Gorka Mendiguren, Marta Gallardo, Elia Durá, Silvia Sánchez y todos los demás que han pasado algún tiempo en el laboratorio; así como al resto de compañeros de despacho. En primer lugar gracias por todo lo que nada tenía que ver con la ciencia, por hacer que trabajar con vosotros fuese divertido. Todos los problemas siempre han pasado mejor con un café y unas risas. Y en cuanto a la ciencia, gracias por todo lo aprendido y por ayudarme con todo lo que no he podido aprender; y a David Riaño, por incitarme a programar.

Esta tesis no hubiese sido posible sin el trabajo de los miembros del CEAM y su colaboración en el desarrollo e instalación de AMSPEC-MED. Especialmente a Ramón López y Arnaud Carrara, por compartir todo su tiempo, su conocimiento y sus datos hasta conseguir que todo funcionase. Gracias también a PP Systems, por su colaboración con la instalación y caracterización del Unispec DC.

Agradezco también haber podido trabajar y coincidir con tanta gente en los proyectos BIOSPEC y FLUχPEC: colegas de las Universidades de Alcalá, Copenhague, Zaragoza, San Diego, Talca o Plasencia; CEAM, INIA, INTA o *Max Planck Institute* entre otros muchos. Hemos pasado muchas horas juntos bajo el sol, o cuando hubo peor suerte bajo las nubes, en Majadas; y también interminables reuniones, emails y video-conferencias. Ha sido un lujo poder trabajar en un ambiente tan variado y con visiones tan diferentes.

También quisiera agradecer a los supervisores de mis estancias Stèphane Jacquemoud, Thomas Hilker y Micol Rossini, por acogerme y dedicarme todo lo que habéis podido; y a todos los colegas que he conocido en el *Institut de Physique du Globe de Paris*, en el *College of Forestry* de OSU, y en el *Remote Sensing of Environmental Dynamics Laboratory*, en Milano-Bicocca. Si hay algo común a todas mis estancias es que nunca he conseguido lo que quería, pero siempre he aprendido más de lo que esperaba.

Igualmente debo dar gracias a todos los miembros de las COST Action EUROSPEC y OPTIMISE, con los que he compartido reuniones, cursos y experimentos; durante los cuales he aprendido mucho y he conocido a mucha gente. Gracias a Alasdair MacArthur, Karen Anderson, Micol Rossini y el resto de profesores que en la primera *training school* en Monte Bondone cambiaron completamente mi concepción de la espectro-radiometría. Y gracias también a Tommaso Julitta, a Karolina Sakowska, Francesco Fava, Sergio Cogliati y tantos otros con los que he compartido tanto tiempo, dentro y fuera de las aulas y los laboratorios.

Y finalmente, tengo mucho que agradecer a tantos otros que poco o nada tienen que ver con mi tesis y en gran medida nada saben de ella; pero sin los que no hubiese podido llegar hasta aquí. Los primero mis padres, por haberme apoyado incondicionalmente y por haberme dado todas las oportunidades que han estado a su alcance; y por haber soportado con paciencia mis errores y mis aciertos. El siguiente es mi hermano, el único tal vez que entendía algo de lo que hacía y que siempre me ha ayudado con todo lo que le he pedido pacientemente, empezando por Nyquist. Gracias por estar ahí como ejemplo y como guía; sin vosotros, no sería lo que soy.

También debo agradecer haber llegado aquí a mis amigos; mi ancla con todo lo mundano y lo profano; tan divertido como necesario. Gracias a Alberto, Ana, Kike, Hugo, Ana y Alberto; mis amigos de siempre a pesar de la creciente distancia geográfica. Gracias por estar ahí para hacerme olvidar todo lo relacionado con la "caza de satélites" a base de risas, cañas, fiestas de pueblos, excursiones, visitas a los expatriados, discusiones sobre cualquier tema o lo que hiciese falta. Gracias también a Raquel e Iván por estar ahí cuando lo necesitaba y cuando no también. Gracias a todos por la amistad y la confianza, por compartir los buenos y los malos momentos para que siempre quedase un buen recuerdo.

Y gracias también a Noëmie, por tu amor, tu paciencia y tu esfuerzo; gracias por obligarme a buscar lo mejor que hay en mí y por darme lo mejor que tienes. Gracias a pesar de la distancia, los aviones y los tiempos. *Je t'aime!*

TABLE OF CONTENTS

SUMMARY

Automated proximal sensing is a useful tool to acquire spectral information of earth covers and vegetation with a high temporal frequency. This information can be connected with remote observations as well as with information provided by other field sensors, such as those included in the eddy covariance systems. Though initially, simple multiband sensors were used in automated systems; in the last years the use of hyperspectral sensors is increasing. These provide overdetermined spectral information that allows the analysis of specific spectral features, the use of complex models and the spectral convolution to other sensors´ bands, improving data integration. However, field spectroscopy is subject to multiple sources of uncertainty. On one hand, the instrumentation is sensible to environmental variables such as the temperature or signal levels among others. On the other hand, radiometric quantities depend on the illumination and observation geometry. Automated systems operate continuously and, therefore, deal with large ranges of these variables, which can introduce significant biases in the measurements.

Instrumental dependencies can be characterized or prevented in several ways, e.g. controlling the instrument temperature or the signal level measured by the sensors. In other cases, the parametrization and use of sensor models to correct the data is necessary. In this PhD dissertation a complete characterization of a portable field spectroradiometer installed in an automated system is presented in chapters 1 to 3. Chapters 1 and 2 intensively analyze the sources of nonlinearity of this instrument, one of which had not been previously reported in this type of instruments. The third chapter shows the complete set of sensor models and the correction chain process.

Automated systems measurements also experience strong directional effects since measurements are acquired continuously during the daily solar cycle and under any sky condition. This maximizes the ranges of illumination angles and diffuse fraction of irradiance. Combining this variability in the illumination with simultaneous variation of the observation angles can provide the information necessary to characterize the directional responses of the observed cover. Automated multi-angular systems have been already used to accomplish this characterization by retrieving the Bidirectional Reflectance Distribution Function (BRDF) in homogeneous ecosystems. However, this has not yet achieved in heterogeneous areas such as tree-grass ecosystems or savannas. Also, previous works have not accounted for the effect of diffuse irradiance in the retrieval of BRDF. In chapter 4 we propose a methodology to simultaneously unmix and characterize the hemispherical-directional reflectance distribution function of the two vegetation covers in a tree-grass ecosystem. The effects of the different features of the approach are analyzed. Moreover, results are up-scaled and compared with satellite global products as the MODIS BRDF product.

We concluded that further efforts are necessary in the deployment and characterization of hyperspectral sensors operating in outdoors automated systems. These systems should take multi-angular configurations so that the directional responses can be characterized. To do so diffuse radiation must be accounted for, and in some cases, scene heterogeneity should be characterized.

RESUMEN

Los sistemas automáticos de *proximal sensing* son una herramienta útil para adquirir información espectral de las cubiertas terrestres con una frecuencia temporal alta. Esta información puede relacionarse con observaciones remotas o con la información suministrada por otros sensores de campo como los incluidos en los sistemas de *eddy covariance*. Si bien inicialmente los sistemas automáticos empleaban sensores multi-banda, en los últimos años ha incrementado el uso sensores hiperespectrales. Estos ofrecen información espectralmente redundante, que permite el análisis de características espectrales específicas, el uso de modelos más complejos y la convolución a bandas espectrales de otros sensores, permitiendo una mejor integración de la información. Sin embargo la espectroscopia de campo está sujeta a múltiples fuentes de incertidumbre. Por un lado, la instrumentación es sensible a variables ambientales como la temperatura o el nivel de señal. Por el otro, las magnitudes radiométricas son dependientes de la geometría de observación e iluminación.

Las dependencias instrumentales pueden ser caracterizadas o evitadas de diferentes formas, por ejemplo, controlando la temperatura del instrumento o el nivel de señal registrado por el sensor. En otros casos, es necesario parametrizar y emplear modelos para corregir los datos. En la presente tesis doctoral los capítulos 1 al 3 presentan la caracterización completa de un espectrómetro de campo instalado en un sistema automático. Los capítulos 1 y 2 analizan las fuentes de no linealidad en este instrumento, una de las cuales no había sido anteriormente descrita en este tipo de instrumentos. El tercer capítulo muestra el conjunto completo de modelos de corrección de los efectos instrumentales y la cadena de procesado correspondiente.

Por otro lado, los sistemas automáticos se enfrentan a efectos direccionales ya que adquieren mediciones continuamente durante el ciclo solar diario y bajo cualquier condición de iluminación. Esto maximiza los rangos de los ángulos de iluminación y también de la fracción difusa de la irradiancia. Esta variabilidad de condiciones de iluminación, combinada con una variación de los ángulos de observación permite obtener la información necesaria para caracterizar las respuestas direccionales de la cubierta observada. Algunos sistemas automáticos multi-angulares ya han sido empleados para realizar esta caracterización mediante la estimación de la Función de Distribución de Reflectividad Bidireccional (BRDF) en ecosistemas homogéneos. Sin embargo, esto no se ha conseguido aún en áreas heterogéneas, como es el caso de los ecosistemas *tree-grass* o de sabana. Así mismo, los trabajos previos no han considerado los efectos de la radiación difusa en el estudio del BRDF. En el capítulo 4 proponemos una metodología que permite desmezclar y caracterizar simultáneamente la función de distribución de reflectividad hemisférica-direccional de las dos cubiertas de vegetación presentes en el ecosistema, pasto y arbolado. También se analizan los efectos de las diferentes características del método. Finalmente, los resultados se escalan y se comparan con productos globales de satélite como el producto BRDF de MODIS.

La conclusión obtenida es que se requieren más esfuerzos en el desarrollo y caracterización de sensores hiperespectrales instalados en sistemas automáticos de campo. Estos sistemas deberían adoptar configuraciones multi-angulares de modo que puedan caracterizarse las respuestas direccionales. Para ello, será necesario considerar los efectos de la radiación difusa; y en algunos casos también la heterogeneidad de la escena.

1. INTRODUCTION

1. SPECTRORADIOMETRIC MEASUREMENTS OF EARTH SURFACES AND VEGETATION

1.1 Spectroradiometry and radiometric quantities

Radiometry is the science of measuring radiant energy. This term is usually limited to the optical portion of the electromagnetic spectrum which includes the Ultra-violet (100 – 400 nm), Visible (400 – 700 nm) and the Infrared (700 – 10^6 nm). Spectroradiometry refers to the radiometric measurements in narrow wavelength intervals (Grum and Becherer 1979). In the earth, radiation is reflected below 2,500 nm whereas it is emitted in the Thermal Infrared (8 μm to 14 μm) and both phenomena occur between these regions (Gerber et al. 2011).

Radiant energy (Q_e) is defined as the energy of the electromagnetic radiation, and the corresponding International System of Units (SI) is the joule (J). This quantity can be derived by time unit and is defined as the radiant flux (Φ_e) whose SI unit is the watt (W). However, in the study of the earth surface properties, the quantity primarily measured is the spectral radiance ($L_{e,\Omega,\lambda}$) which is the radiant flux per unit area, solid angle (Ω) and wavelength (λ), and it is measured in watts per steradian per square meter per nanometer ($W \cdot sr^{-1} \cdot m^{-2} \cdot nm^{-1}$). The spectral radiance emitted by surface unit in all the directions is the spectral exitance ($M_{e,\lambda}$) and, analogously, the spectral radiance reaching the surface unit is the spectral irradiance ($E_{e,\lambda}$). In both cases the SI units are W m^{-2} (Nicodemus et al. 1977). In the study of earth surface properties, relative quantities are mostly used (Schaepman-Strub et al. 2006). These are defined as reflectance factors since they are the ratio between the radiant flux reflected by a surface and the one reflected by a perfectly lossless and Lambertian surface under the same geometric

configuration and illumination (Nicodemus et al. 1977). Several of these relative quantities can be considered depending on the angular region from where down-welling and up-welling radiant fluxes are measured (directional, conical or hemispherical). Extensive definitions are provided in Nicodemus et al. (1977) and later in Schaepman-Strub et al. (2006). All these quantities can be derived from the Bidirectional Reflectance Distribution Function (BRDF) which describes the relationship between the incoming and the reflected radiance fluxes in two directions of the hemisphere. Directional stands for an infinitesimal solid angle where radiant flux is not measurable, and therefore, BRDF is, in fact, a conceptual quantity. However, the shape of this function can be estimated from directional measurements and is of great importance in the study of surface properties because it defines their radiative balance is a surface property itself (Schaepman-Strub et al. 2006).

The terminology relative to spectroradiometric sensors and quantities is sometimes loosely used, and must be clarified before continuing. The term "radiometric" stands for the quantification of energy and derived quantities in physical units. Consequently a radiometer is a sensor that measures a radiant flux within a given spectral range and expresses it as a radiometric quantity (e.g. radiance) with the corresponding physical units. To do so, a relationship between the digital signal generated by the sensor and these physical units is calibrated against a radiation source of known properties, the standard. The term "spectral" stands for the separation of radiation in different wavelengths. Therefore, a spectrometer is a sensor that digitizes radiation as a function of wavelength; but it does not express the measurement as a radiometric quantity in physical units. The combination of both is the

spectroradiometer, which is the sensor that spectrally resolves and quantifies in physical units the measured radiant flux.

1.2 Spatial approaches: proximal vs remote sensing

Spectroradiometric measurements can be acquired using different approaches depending on the distance between the sensor and the measured target. According to Teillet (2010), in situ measurements are carried out at distances smaller or equal than any linear dimension of the sensor. In spectroradiometry this usually involves the use of attachments such as probes (Foley et al. 2006) or integrating spheres (Feret et al. 2008) which are in contact with the sample surface. The term proximal sensing is encompassed by the prior definition and refers to "sensing from the close range". This, in practice, refers to measurements done from a nearby location. Therefore we could differentiate between those measurements acquired contacting the sample and those taken from a short distance (Teillet et al. 2002). Proximal sensing could refer to hand held spectroradiometry, goniometers, poles, towers or terrestrial vehicles (Balzarolo et al. 2011; Milton et al. 2009). On the contrary, remote sensing involves a distance between target and sensor much greater than any linear dimension of the sensor (Teillet et al. 2002). This can be applied to spectral measurements acquired from satellites, planes, helicopters or balloons. Some devices can operate in a range of scales between the remote and the proximal, such as the Remotely Piloted Aircrafts Systems (RPAS) whose use is now increasing.

The work carried out in this Thesis is focused on the use of a tower-based non-imager field spectrometer in an automated proximal sensing configuration. Therefore,

the following sections would be dedicated to proximal non imaging sensors, though some of them could be extended to imagers and remote sensors.

1.3 Spectral configuration of spectroradiometric sensors

Spectroradiometric sensors can be classified depending on the number of bands used to measure radiant flux. These bands are characterized by the spectral resolution, which is the minimum spectral feature that the sensor can resolve, usually expressed as the Full Width Half Maximum (FWHM); and also by the spectral sampling interval or distance between the centers of the bands. Multiband sensors discriminate usually between two and about sixteen spectral bands (Porcar-Castell et al. 2015), with FWHM about 10 nm or wider and usually not overlapping bands. On the contrary, hyperspectral sensors sample a large number of overlapped bands (more than 250) and usually present spectral resolutions lower than 10 nm. Among other advantages, hyperspectral sensors can detect narrow spectral features of the observed surfaces and the atmosphere; the spectral information provided can be convolved to the spectral features of other sensors with coarser resolutions; they allow screening the relationships between spectral variables and others (Porcar-Castell et al. 2015); and provide overdetermined systems for model inversion (Cogliati et al. 2015) and the spectral un-mixing of several classes (Schaepman et al. 2009). On the contrary, these instruments are much more expensive, more complex and less robust as well as more difficult and expensive to automate than multispectral sensors (Balzarolo et al. 2011; Porcar-Castell et al. 2015).

1.4 Down and up-welling radiation sampling

For the computation of reflectance factors, it is necessary to measure the down-welling spectral radiant flux reaching the target and the up-welling radiant flux leaving the surface (Schaepman-Strub et al. 2006). These measurements can be done simultaneously in the case of the Dual Beam/Field of View (DFOV) instruments, which usually integrate two sensors each dedicated to one of the fluxes. An alternative is the acquisition of sequential measurements of the down-welling and the up-welling spectral radiation fluxes, under the assumption of no changes of illumination occurring during the measurements. In this case Single Beam/Field of View (SFOV) instruments equipped with a single sensor are used. Up-welling flux is usually measured using a bare optical fiber and/or lens; whereas down-welling flux is measured using the same optics and a lossless-like and Lambertian-like reference panel (usually Spectralon®) or a hemispherical cosine diffuser (Porcar-Castell et al. 2015; Schaepman 2007). Maybe, the simplest method to automatize field spectral measurements is combining a DFOV sensor with a diffuse head to measure incoming irradiance. Though other options exist, these require the use additional instrumentation as multiplexers (Meroni et al. 2011), bifurcated fibers and synchronized shutters (MacArthur et al. 2014), protected reference panels (Huber et al. 2014) or moving reference panels (Sakowska et al. 2015). The disadvantage of DFOV instruments is that an accurate cross-calibration and temperature stabilization of the two sensors is needed in order to avoid instrumental dependencies in the derived quantities (Porcar-Castell et al. 2015).

The optics selected to sample each radiation flux determine the reflectance quantity measured. Hemispherical down-welling flux is measured using cosine diffusers (Gamon et al. 2006a) or derived from Lambertian-like reference panels (Huber et al.

2014; Sakowska et al. 2015). Up-welling flux is commonly measured using conical optics (Foley et al. 2006), though in some cases, has been measured using hemispherical diffusers (Meroni et al. 2011). Therefore, the Hemispherical-Conical Reflectance Factor (HCRF) is the most usually quantity measured by field spectroradiometers and optical sensors (Balzarolo et al. 2011; Porcar-Castell et al. 2015).

1.5 Optical sensors in automated systems

Multispectral optical sensors are most usually installed in micro-meteorological towers were ecosystem-atmosphere exchanged fluxes are measured using the eddy covariance technique (Balzarolo et al. 2011; Gamon et al. 2010; Gamon et al. 2006b). These are automated systems sampling reflectance factors in a continuous basis; though they can be also operated hand-held. Automated multispectral sensors typically operate in a fixed position, aiming always at the same area of the ecosystem (Balzarolo et al. 2011).

Commercial field hyperspectral instruments are not designed to be readily automated, and are mostly used hand held (Milton et al. 2009). However, in the last years the number of automated hyperspectral systems operating in a continuous basis has increased (Porcar-Castell et al. 2015). These systems usually include one or more spectrometers or spectroradiometers which are controlled by an external computer programmed to acquire measurements automatically. However the approaches, designs and applications are still quite unique (Porcar-Castell et al. 2015).

2. INSTRUMENTAL DEPENDENCIES OF THE RADIOMETRIC MEASUREMENT

2.1 Instrumental artifacts and dependencies

The measurement of spectral radiation is a process technically complex, and can suffer of large uncertainties, especially in the field (Kostkowski 1997). First, radiation coming from a desired solid angle or incoming from a radiation source must be sampled. In the case of field spectroradiometers and spectrometers different fore optics are commonly used with these purposes, usually cosine diffusers and lenses. These can be attached directly to the instrument or via an optical fiber which facilitates the handling. In other occasions, bare optical fibers are used to sample radiation within a limited solid angle. These transmit light through a single core of fiber or through a bundle of several fibers. Lambertian reference panels are used to derive the total incoming flux in SFOV instruments, (Schaepman-Strub et al. 2006) and to cross-calibrate the two sensors of DFOV instruments (Gamon et al. 2006a). Reflections and absorptions produced by the fore optics and optical fibers cause a decrease of the radiation sampled. Therefore, the radiometric calibration of each instrument is unavoidably specific of the fore optics used and its attachment to the instrument. In addition, the contribution of energy to signal is no homogeneous in the solid angle of the measurement. MacArthur et al. (2012) characterized the directional responses of the fore optics of some commercial field spectroradiometers and proved that, especially in the case of the fiber optic bundle, these can be largely heterogeneous. They also showed how deviations are not only directionally, but also spectrally dependent due to chromatic aberration of the lenses and also to magnifications or attenuations produced in the optical paths within the instrument. In the case of cosine diffusers and also

reference panels, radiation sampled should decrease as a function of the cosine of the zenith illumination; however, deviations from this response occur are and also spectrally dependent (Julitta 2015; Meywerk and Ramanathan 1999). In addition, reference panels are actually not lossless, and they must be calibrated.

When sampled radiation reaches the sensor´s spectrograph, it passes through the entrance slit and reaches the diffraction grating or the monochromator. These devices reflect the radiation with different angles as a function of its wavelength. Several artifacts can affect this process, such as second order effects of the diffraction (Lerner 2006), stray light reflected inside the spectrograph (Zong et al. 2006) or instrument changes due to thermal expansion of the components of the spectrograph (Markham et al. 1995), among others. The diffracted light reaches the sensor, usually an array of photodiodes, each of them illuminated by radiation comprehended within a different range of wavelengths. The width of these ranges can vary as a function of the illumination angle. Several types of sensors can be found in commercial field spectrometers and artifacts related with the different technologies would require an extensive analysis. However, some of these artifacts are more or less common to most of these sensors, e.g. temperature dependence, nonlinearity... In all the cases, photons received must be converted to an electrical signal that is accumulated until readout. This signal can be amplified and, eventually, an analogical-to-digital converter transforms it into digital values. Several factors can bias the linearity of the relationships between the three types of signals, light, electrical and digital. These can operate at photodiode level (Ferrero et al. 2006; Ferrero et al. 2005; Stevens 1991) or in the succeeding electronics (Smith 1998). Moreover, the sensitivity of the sensors to radiation also varies as a function of temperature and wavelength (Saber et al. 2011; Starks et al. 1995),

Electronics also add an electrical random noise, the dark current, which varies with the temperature and the integration time (Kuusk 2011). Another characteristic of sensors is the quantum efficiency, which is the fraction of photons converted to charge carriers, electrons in this case. This feature together with the radiation flux impinging each pixel, primarily determine the total signal measured at each waveband.

2.2 Sensor models and corrections

Instrumental artifacts can be characterized as long as variables responsible of the artifacts can be measured. This way sensor models can be parametrized to allow the correction of operational measurements. In example, directional responses of cosine diffusers or white reference panels can be estimated by acquiring measurements under different illumination angles (Bais et al. 2005). Directional responses of other optics can also be characterized (MacArthur et al. 2012), thought understanding their effects requires knowing the contents of the observed surface. Temperature readings of the instrument can be, in some cases, obtained simultaneously to radiometric measurements. In those cases, temperature dependences of the sensor and dark current can be characterized and derived for correction by acquiring radiation and dark current measurements under different temperatures (Kuusk 2011; Saber et al. 2011). In other cases, dark current can be measured by closing the optical path with a shutter and directly removed from the radiation measurements.

The center wavelength corresponding to each spectral band can be inferred using emission lines from lamps filled with noble gases (Natalia 2009). However, determining the band width requires measuring radiation contained in bands thinner than those of the spectral resolution of the pixel, which can be achieved using monochromators

(Hopkinson et al. 2004; Zhang et al. 2011). Though sensor models can be parametrized in the laboratory under controlled conditions, these might lose accuracy in the field (Anderson et al. 2006) under different temperature, moisture and radiation conditions.

3. DIRECTIONAL DEPENDENCIES OF THE RADIOMETRIC MEASUREMENT. INTRODUCTION TO BRDF MODELS

When a given surface is observed, the illumination and observation angles determine the fractions of the different components of the scene that are viewed and that are illuminated (Roujean et al. 1992). Thus the illumination-observation geometry determine the amount of radiance sampled by a sensor, and therefore the value of the radiometric quantity measured. This represents a challenge for the study of earth surfaces since in order to determine the properties of the observed pixel, it is necessary disentangling the variance in the signal that is explained by the directional effects (Lucht and Roujean 2000). On the contrary, this represents also an opportunity since in addition to the spectral signatures; the BRDF provides information about the intrinsic pixel properties (Lucht and Roujean 2000).

The BRDF can be estimated from measurements acquired with different illumination-view geometries over the same surface using empirical (Walthall et al. 1985) semi-empirical (Wanner et al. 1995) or physical (Gastellu-Etchegorry et al. 2004; Verhoef 1984) models. The acquisition of multi-angular measurements in the field is complex and resource consuming; and therefore the nadir view configuration is preferred in order to minimize directional effects (Milton et al. 2009). However, illumination geometry does not only depend on the solar angle, but also on the diffuse component of the incoming radiation flux and its distribution over the hemisphere

(Lyapustin and Privette 1999). In the field no control of the illumination is possible, and consequently, though observation geometry can be standardized directional effects are always included in the measurements.

Goniometers (Sandmeier and Itten 1999), RPAS (Burkart et al. 2015) and tower-based automated systems (Hilker et al. 2010) have been used in the field to measure and model the BRDF of vegetation and other surfaces. However, further research is needed to overcome the uncertainties related with the sampling of the up and down-welling fluxes, and with the modeling of the BRDF.

4. AUTOMATED HYPERSPECTRAL PROXIMAL SENSING. REVIEW OF CASES AND APPLICATIONS

Automated proximal sensing is closely related to the analysis of atmosphere-ecosystem gas exchanges. In this context, the number of spectrometers and spectroradiometers that have been installed in automatic systems has increased (Porcar-Castell et al. 2015). One of the pioneer systems developed was set up on a robotic tram carrying a DFOV spectrometer (Gamon et al. 2006a). This system was used to acquire HCRF at temporal and spatial scales similar to those where gas exchanges were measured by an eddy covariance tower. Data acquired by the system allowed the analysis of the relationships between optical signals and vegetation physiology (Claudio et al. 2006; Gamon et al. 2013; Sims et al. 2006) and the upscaling of water and carbon fluxes (Cheng et al. 2006; Fuentes et al. 2006; Stow et al. 2004). However, most of current systems are not moving instruments but are fixed on towers at different heights. Some of them have been dedicated to the study of vegetation sun induced fluorescence emission related to the photosynthetic activity. Thought sometimes a single

spectroradiometer has been used (Drolet et al. 2014), in most cases, two or more spectroradiometers were combined: one dedicated to the measurement of reflectance factors in the Visible and Near Infrared regions (VNIR) and the other, with a higher spectral resolution, dedicated to the measurement of the fluorescence emission into atmospheric absorption lines (Cogliati et al. 2015; Middleton et al. 2013; Daumard et al. 2010; Meroni et al. 2011; Rascher et al. 2009). These systems have provided vegetation indices and estimates of sun induced fluorescence; and their covariance with vegetation gas exchange and light use efficiency have been analyzed. However, due to their mono-angular configuration, directional effects were always mixed in the signals measured. Nonetheless, variations of fluorescence estimates related with photosynthetic activity have still been noticeable (Cogliati et al. 2015; Daumard et al. 2010; Meroni et al. 2011).

Other automated systems were focused on the analysis of the directional effects. In this case they included a pan-tilt system or rotatory mirrors allowing the acquisition of multi-angular measurements (Hilker et al. 2007; Hilker et al. 2010; Huber et al. 2014; Leuning et al. 2006). Multi-angular observations provide much richer information about the observed scene allowing the estimation of the BRDF and disentangling directional and physiological changes in optical signals (Hilker et al. 2008), the analysis of the anisotropy factor (Huber et al. 2014) or the comparison with radiative transfer models (Leuning et al. 2006). These systems have mainly operated in homogeneous ecosystems or in scenes where the different covers could be observed separately (Hilker et al. 2009) or some of them not observed (Huber et al. 2014).

Thought most of these systems are limited to the VNIR region, lately two systems have included spectroradiometers that also measure radiation in the Short Wave Infrared (SWIR) (Huber et al. 2014; Sakowska et al. 2015).

2. OBJECTIVES

The research aim of this PhD dissertation is the characterization of the Bidirectional Reflectance Function Factor of the different vegetation covers within a Mediterranean tree-grass ecosystem through the implementation, characterization and operation of an automated multi-angular spectrometric system (the AMSPEC-MED). This system is based on the AMSPEC-II (Hilker et al. 2010), but new features and modeling approaches have been developed.

To achieve this objective, it is necessary to overcome limitations related with 1) the hyperspectral instrumentation and 2) with the BRDF models commonly used in remote sensing applications. This has been done by addressing the following specific objectives:

1. To identify and characterize the main sources of nonlinearity in the field spectrometer and analyze their effects.
2. To characterize the thermal dependencies of the sensors sensitivity and the dark signal.
3. To calibrate the sensors wavelength functions and analyze the impacts of temperature.
4. To characterize the directional response functions of the sensor optics, and correct the down-welling radiation flux measurements.
5. To understand the effects of instrumental and environmental dependencies on the HCRF.
6. To analyze and design the field deployment of an AMSPEC system in Las Majadas del Tiétar site (Cáceres, Spain), considering the resources available and the modeling needs.

7. To define a BRDF model capable to represent the tree-grass ecosystem scene at proximal observation scale.
8. To define a BRDF model capable to account for the effects of diffuse radiation.
9. To determine a methodology suitable for the robust retrieval of the BRDF of the different vegetation covers (trees and grass) observed under different illumination conditions.
10. Validate BRDF retrievals by up-scaling and comparing with remote sensing BRDF products.

The first group of objectives (1 to 5) is related with the characterization of the spectroradiometer and the parametrization of sensor models that allow the computation of HCRF independent of environmental and instrumental artifacts. The lack of temperature control and shutters jeopardize, among other reasons, the quality of the quantities derived, which led to the establishment of these objectives. These are addressed in the three first chapters of the thesis. The second group of objectives (6 to 10) is related with the modeling of BRDF in a Mediterranean tree-grass ecosystem and the inclusion of diffuse component of the down-welling flux in the BRDF model. Spatial heterogeneity is specific of the observed scene and, therefore, is modeled ad-hoc. Diffuse radiation effects are a common issue that more severely affects automated proximal sensing than remote sensing measurements, where cloudy situations are usually discarded. The outcomes of the new model are finally compared with satellite-based BRDF estimates. These objectives are tackled in the fourth chapter of the Thesis.

3. INTRODUCTION TO THESIS CHAPTERS AND STRUCTURE

This Thesis is divided in four chapters; the first three have been already published in international indexed journals and address the instrumental characterization necessary to provide corrected spectral reflectance factors in response to objectives 1 to 5. The fourth chapter presents an extensive analysis and modeling of the BRDF related with objectives 6 to 10. A fourth paper will be derived from this chapter.

Chapter 1 focuses on the detection and characterization of a nonlinear response related with the gray level measured by Unispec DC spectrometer used in this study. This artifact was first noticed during an inter-comparison experiment where different commercial spectrometers acquired simultaneous measurements of different targets (Anderson et al. 2013). The Unispec DC instrument was characterized using a methodology frequently used with other commercial field spectroradiometers. Monte Carlo simulation was applied to predict the uncertainties related with the characterization. Moreover, the impact of this artifact on the Photochemical Reflectance Index (PRI) (Gamon et al. 1992) commonly used as an estimator of light use efficiency was discussed. One of the bands of this index happened to be largely affected by nonlinearity since under sun irradiance achieved the largest digital values. This resulted in false responses of vegetation to radiation. To the best of our knowledge, this artifact had not been previously reported in this instrument, which has been extensively used for the study of vegetation.

Chapter 2 goes deeper than the first in the characterization of nonlinearity. Inconsistencies found in nonlinearity models parametrized for the same Unispec DC instrument led to the discovery of a second source of nonlinearity that had not been reported in commercial field spectroradiometers. This second nonlinearity was related

with the integration time set in the sensor. The two sources of nonlinearity identified could be characterized thanks to the specific readout technology of the sensors used. Therefore the methodology propose might not be directly applicable to other sensors, but the issue has been reported so that it can be considered and avoided. The effect of this second source of nonlinearity might not be large under field conditions, but it proved to significantly bias the characterization of the gray-level-related nonlinearity in the laboratory. The results also stressed the need of using laboratory radiance sources powers that could be comparable to outdoors levels.

Chapter 3 summarizes the complete characterization of the spectrometer and the parametrization of the different sensor models used to correct HCRF. In this work, the temperature sensitivity and the directional response function of the cosine diffuse models were parametrized. Spectral calibration of sensors wavelength was performed under different temperatures to discard the detection of spectral shifts. Moreover, the nonlinearity and dark current models presented in previous chapters were included. Also, the spectral diffuse-to-global radiation ratio was estimated using data from a broadband pyranometer. The operational chain process of the spectral data used to compute HCRF was defined and applied to real data acquired from the AMSPEC-MED system in the field. These data were used to assess the impact of each correction and of all the corrections together. No large changes in HCRF were found, both due to the instrument configuration and to the cancellation of the different effects during the computation of the reflectance factors.

In chapter 4 we propose a methodology to unmix the directional responses of the two vegetation covers present in the Mediterranean savanna where AMSPEC-MED operates. On one hand, diffuse radiation was accounted for modeling the

Hemispherical-Directional Reflectance Distribution Function (HDRDF) rather than BRDF. On the other hand, spatial heterogeneity of the ecosystem was tackled by the development of a 3D model of the scene and a ray casting model. These allowed the estimation of the contributions of each vegetation type (trees and grass) and their respective shadow fractions within the FOV. The HDRDF model was based on a linear combination of kernel functions, but in this case, the geometric-optical kernels were substituted by estimates provided by the 3D model. Moreover, diffuse radiation was included in the model adding irradiance to shaded areas and via hemispherical integration of kernel functions. Changes introduced in the models were assessed including the use of time windows to select data and the use of regularization for model inversion. HDRDF estimates were up-scaled using a 3D reconstruction of the scene and a simulation of remote observations and these were compared with operational remote sensing products such as the MODIS MCD43A1 BRDF product.

4. REFERENCES

Anderson, K., Milton, E.J., & Rollin, E.M. (2006). Calibration of dual-beam spectroradiometric data. *International Journal of Remote Sensing, 27*, 975-986

Anderson, K., Rossini, M., Pacheco-Labrador, J., Balzarolo, M., Mac Arthur, A., Fava, F., Julitta, T., & Vescovo, L. (2013). Inter-comparison of hemispherical conical reflectance factors (HCRF) measured with four fibre-based spectrometers. *Optics Express, 21*, 13

Bais, A.F., Kazadzis, S., Garane, K., Kouremeti, N., Gröbner, J., Blumthaler, M., Seckmeyer, G., Webb, A.R., Koskela, T., Görts, P., & Schreder, J. (2005). Portable device for characterizing the angular response of UV spectroradiometers. *Applied Optics, 44*, 7136-7143

Balzarolo, M., Anderson, K., Nichol, C., Rossini, M., Vescovo, L., Arriga, N., Wohlfahrt, G., Calvet, J.-C., Carrara, A., Cerasoli, S., Cogliati, S., Daumard, F., Eklundh, L., Elbers, J.A., Evrendilek, F., Handcock, R.N., Kaduk, J., Klumpp, K., Longdoz, B., Matteucci, G., Meroni, M., Montagnani, L., Ourcival, J.-M., Sánchez-Cañete, E.P., Pontailler, J.-Y., Juszczak, R., Scholes, B., & Martín, M.P. (2011). Ground-Based Optical Measurements at European Flux Sites: A Review of Methods, Instruments and Current Controversies. *Sensors, 11*, 7954-7981

Burkart, A., Aasen, H., Alonso, L., Menz, G., Bareth, G., & Rascher, U. (2015). Angular Dependency of Hyperspectral Measurements over Wheat Characterized by a Novel UAV Based Goniometer. *Remote Sensing, 7*, 725

Claudio, H.C., Cheng, Y., Fuentes, D.A., Gamon, J.A., Luo, H., Oechel, W., Qiu, H.-L., Rahman, A.F., & Sims, D.A. (2006). Monitoring drought effects on vegetation

water content and fluxes in chaparral with the 970 nm water band index. *Remote Sensing of Environment, 103*, 304-311

Cogliati, S., Rossini, M., Julitta, T., Meroni, M., Schickling, A., Burkart, A., Pinto, F., Rascher, U., & Colombo, R. (2015). Continuous and long-term measurements of reflectance and sun-induced chlorophyll fluorescence by using novel automated field spectroscopy systems. *Remote Sensing of Environment, 164*, 270-281

Cheng, Y., Gamon, J.A., Fuentes, D.A., Mao, Z., Sims, D.A., Qiu, H.-l., Claudio, H., Huete, A., & Rahman, A.F. (2006). A multi-scale analysis of dynamic optical signals in a Southern California chaparral ecosystem: A comparison of field, AVIRIS and MODIS data. *Remote Sensing of Environment, 103*, 369-378

Daumard, F., Champagne, S., Fournier, A., Goulas, Y., Ounis, A., Hanocq, J.F., & Moya, I. (2010). A Field Platform for Continuous Measurement of Canopy Fluorescence. *Geoscience and Remote Sensing, IEEE Transactions on, 48*, 3358-3368

Drolet, G., Wade, T., Nichol, C.J., MacLellan, C., Levula, J., Porcar-Castell, A., Nikinmaa, E., & Vesala, T. (2014). A temperature-controlled spectrometer system for continuous and unattended measurements of canopy spectral radiance and reflectance. *International Journal of Remote Sensing, 35*, 1769-1785

Feret, J.-B., François, C., Asner, G.P., Gitelson, A.A., Martin, R.E., Bidel, L.P.R., Ustin, S.L., le Maire, G., & Jacquemoud, S. (2008). PROSPECT-4 and 5: Advances in the leaf optical properties model separating photosynthetic pigments. *Remote Sensing of Environment, 112*, 3030-3043

Ferrero, A., Campos, J., & Pons, A. (2006). Apparent violation of the radiant exposure reciprocity law in interline CCDs. *Applied Optics, 45*, 3991-3997

Ferrero, A., Campos, J., Pons, A., & Corrons, A. (2005). New model for the internal quantum efficiency of photodiodes based on photocurrent analysis. *Applied Optics, 44*, 208-216

Foley, S., Rivard, B., Sanchez-Azofeifa, G.A., & Calvo, J. (2006). Foliar spectral properties following leaf clipping and implications for handling techniques. *Remote Sensing of Environment, 103*, 265-275

Fuentes, D.A., Gamon, J.A., Cheng, Y., Claudio, H.C., Qiu, H.-l., Mao, Z., Sims, D.A., Rahman, A.F., Oechel, W., & Luo, H. (2006). Mapping carbon and water vapor fluxes in a chaparral ecosystem using vegetation indices derived from AVIRIS. *Remote Sensing of Environment, 103*, 312-323

Gamon, J.A., Coburn, C., Flanagan, L.B., Huemmrich, K.F., Kiddle, C., Sanchez-Azofeifa, G.A., Thayer, D.R., Vescovo, L., Gianelle, D., Sims, D.A., Rahman, A.F., & Pastorello, G.Z. (2010). SpecNet revisited: bridging flux and remote sensing communities. *Canadian Journal of Remote Sensing, 36*, S376-S390

Gamon, J.A., Cheng, Y., Claudio, H., MacKinney, L., & Sims, D.A. (2006a). A mobile tram system for systematic sampling of ecosystem optical properties. *Remote Sensing of Environment, 103*, 246-254

Gamon, J.A., Huemmrich, K.F., Stone, R.S., & Tweedie, C.E. (2013). Spatial and temporal variation in primary productivity (NDVI) of coastal Alaskan tundra: Decreased vegetation growth following earlier snowmelt. *Remote Sensing of Environment, 129*, 144-153

Gamon, J.A., Peñuelas, J., & Field, C.B. (1992). A narrow-waveband spectral index that tracks diurnal changes in photosynthetic efficiency. *Remote Sensing of Environment, 41*, 35-44

Gamon, J.A., Rahman, A.F., Dungan, J.L., Schildhauer, M., & Huemmrich, K.F. (2006b). Spectral Network (SpecNet)—What is it and why do we need it? *Remote Sensing of Environment, 103*, 227-235

Gastellu-Etchegorry, J.P., Martin, E., & Gascon, F. (2004). DART: a 3D model for simulating satellite images and studying surface radiation budget. *International Journal of Remote Sensing, 25*, 73-96

Gerber, F., Marion, R., Olioso, A., Jacquemoud, S., Ribeiro da Luz, B., & Fabre, S. (2011). Modeling directional–hemispherical reflectance and transmittance of fresh and dry leaves from 0.4 μm to 5.7 μm with the PROSPECT-VISIR model. *Remote Sensing of Environment, 115*, 404-414

Grum, F.C., & Becherer, R. (1979). *Optical Radiation Measurements: Radiometry*: Academic Press

Hilker, T., Coops, N.C., Coggins, S.B., Wulder, M.A., Brownc, M., Black, T.A., Nesic, Z., & Lessard, D. (2009). Detection of foliage conditions and disturbance from multi-angular high spectral resolution remote sensing. *Remote Sensing of Environment, 113*, 421-434

Hilker, T., Coops, N.C., Hall, F.G., Black, T.A., Wulder, M.A., Nesic, Z., & Krishnan, P. (2008). Separating physiologically and directionally induced changes in PRI using BRDF models. *Remote Sensing of Environment, 112*, 2777-2788

Hilker, T., Coops, N.C., Nesic, Z., Wulder, M.A., & Black, A.T. (2007). Instrumentation and approach for unattended year round tower based measurements of spectral reflectance. *Computers and Electronics in Agriculture, 56*, 72-84

Hilker, T., Nesic, Z., Coops, N.C., & Lessard, D. (2010). A new, automated, multiangular radiometer instrument for tower-based observations of canopy reflectance (AMSPEC II). *Instrumentation Science & Technology, 38*, 319-340

Hopkinson, G.R., Goodman, T.M., & Prince, S.R. (2004). *A guide to the use and calibration of detector array equipment.*: SPIE Press

Huber, S., Tagesson, T., & Fensholt, R. (2014). An automated field spectrometer system for studying VIS, NIR and SWIR anisotropy for semi-arid savanna. *Remote Sensing of Environment, 152*, 547-556

Julitta, T. (2015). Optical proximal sensing for vegetation monitoring. In, *Department of Earth and Environmental Sciences*. Milano, Italy: University of Milano-Bicocca

Kostkowski, H.J. (1997). *Reliable Spectroradiometry*. La Plata, Md: Spectroradiometry Consulting

Kuusk, J. (2011). Dark Signal Temperature Dependence Correction Method for Miniature Spectrometer Modules. *Journal of Sensors, 2011*

Lerner, J.M. (2006). Imaging spectrometer fundamentals for researchers in the biosciences—A tutorial. *Cytometry Part A, 69A*, 712-734

Leuning, R., Hughes, D., Daniel, P., Coops, N.C., & Newnham, G. (2006). A multi-angle spectrometer for automatic measurement of plant canopy reflectance spectra. *Remote Sensing of Environment, 103*, 236-245

Lucht, W., & Roujean, J.L. (2000). Considerations in the parametric modeling of BRDF and albedo from multiangular satellite sensor observations. *Remote Sensing Reviews, 18*, 343-379

Lyapustin, A.I., & Privette, J.L. (1999). A new method of retrieving surface bidirectional reflectance from ground measurements: Atmospheric sensitivity study. *Journal of Geophysical Research: Atmospheres, 104*, 6257-6268

MacArthur, A., MacLellan, C.J., & Malthus, T. (2012). The Fields of View and Directional Response Functions of Two Field Spectroradiometers. *Geoscience and Remote Sensing, IEEE Transactions on, 50*, 3892-3907

MacArthur, A., Robinson, I., Rossini, M., Davis, N., MacDonald, K., MacArthur, A., Robinson, I., Rossini, M., Davis, N., & MacDonald, K. (2014). A dual-field-of-view spectrometer system for reflectance and fluorescence measurements (Piccolo Doppio) and correction of etaloning. *Proceedings of the Fifth International Workshop on Remote Sensing of Vegetation Fluorescence*: European Space Agency.

Markham, B.L., Williams, D.L., Schafer, J.R., Wood, F., & Kim, M.S. (1995). Radiometric characterization of diode-array field spectroradiometers. *Remote Sensing of Environment, 51*, 317-330

Meroni, M., Barducci, A., Cogliati, S., Castagnoli, F., Rossini, M., Busetto, L., Migliavacca, M., Cremonese, E., Galvagno, M., Colombo, R., & Di Cella, U.M. (2011). The hyperspectral irradiometer, a new instrument for long-term and unattended field spectroscopy measurements. *Review of Scientific Instruments, 82*

Meywerk, J., & Ramanathan, V. (1999). Observations of the spectral clear-sky aerosol forcing over the tropical Indian Ocean. *Journal of Geophysical Research: Atmospheres, 104*, 24359-24370

Middleton, E., Corp, L.A., & Cook, B.D. (2013). FUSION: Canopy Tower System for Remote Sensing Observations of Terrestrial Ecosystems. In, *White paper*

Milton, E.J., Schaepman, M.E., Anderson, K., Kneubühler, M., & Fox, N. (2009). Progress in field spectroscopy. *Remote Sensing of Environment, 113, Supplement 1*, S92-S109

Natalia, D. (2009). Light Sources. *Handbook of Optical Metrology*: CRC Press

Nicodemus, F.E., Richmond, J.C., Hsia, J.J., Ginsberg, I.W., & Limperis, T. (1977). Geometrical Consideration and Nomenclature for Reflectance. In U.D.o.C. National Bureau of Standards (Ed.) (p. 52). Washington, DC

Porcar-Castell, A., Mac Arthur, A., Rossini, M., Eklundh, L., Pacheco-Labrador, J., Anderson, K., Balzarolo, M., Martín, M.P., Jin, H., Tomelleri, E., Cerasoli, S., Sakowska, K., Hueni, A., Julitta, T., Nichol, C.J., & Vescovo, L. (2015). EUROSPEC: at the interface between remote sensing and ecosystem CO2 flux measurements in Europe. *Biogeosciences Discuss*., 12, 13069-13121

Rascher, U., Agati, G., Alonso, L., Cecchi, G., Champagne, S., Colombo, R., Damm, A., Daumard, F., de Miguel, E., Fernandez, G., Franch, B., Franke, J., Gerbig, C., Gioli, B., Gómez, J.A., Goulas, Y., Guanter, L., Gutiérrez-de-la-Cámara, Ó., Hamdi, K., Hostert, P., Jiménez, M., Kosvancova, M., Lognoli, D., Meroni, M., Miglietta, F., Moersch, A., Moreno, J., Moya, I., Neininger, B., Okujeni, A., Ounis, A., Palombi, L., Raimondi, V., Schickling, A., Sobrino, J.A., Stellmes, M., Toci, G., Toscano, P., Udelhoven, T., van der Linden, S., & Zaldei, A. (2009). CEFLES2: the remote sensing component to quantify photosynthetic efficiency from the leaf to the region by measuring sun-induced fluorescence in the oxygen absorption bands. *Biogeosciences, 6*, 1181-1198

Roujean, J.-L., Leroy, M., & Deschamps, P.-Y. (1992). A Bidirectional Reflectance Model of the Earth's Surface for the Correction of Remote Sensing Data. *J. Geophys. Res., 97*, 20455-20468

Saber, G.R.S., Fox, N.P., Theocharous, E., Sun, T., & Grattan, K.T.V. (2011). Temperature and nonlinearity corrections for a photodiode array spectrometer used in the field. *Appl. Opt., 50*, 866-875

Sakowska, K., Gianelle, D., Zaldei, A., MacArthur, A., Carotenuto, F., Miglietta, F., Zampedri, R., Cavagna, M., & Vescovo, L. (2015). WhiteRef: A New Tower-Based Hyperspectral System for Continuous Reflectance Measurements. *Sensors, 15*, 1088

Sandmeier, S.R., & Itten, K.I. (1999). A field goniometer system (FIGOS) for acquisition of hyperspectral BRDF data. *Geoscience and Remote Sensing, IEEE Transactions on, 37*, 978-986

Schaepman-Strub, G., Schaepman, M.E., Painter, T.H., Dangel, S., & Martonchik, J.V. (2006). Reflectance quantities in optical remote sensing—definitions and case studies. *Remote Sensing of Environment, 103*, 27-42

Schaepman, M.E. (2007). Spectrodirectional remote sensing: From pixels to processes. *International Journal of Applied Earth Observation and Geoinformation, 9*, 204-223

Schaepman, M.E., Ustin, S.L., Plaza, A.J., Painter, T.H., Verrelst, J., & Liang, S. (2009). Earth system science related imaging spectroscopy—An assessment. *Remote Sensing of Environment, 113, Supplement 1*, S123-S137

Sims, D.A., Luo, H., Hastings, S., Oechel, W.C., Rahman, A.F., & Gamon, J.A. (2006). Parallel adjustments in vegetation greenness and ecosystem CO2 exchange in

response to drought in a Southern California chaparral ecosystem. *Remote Sensing of Environment, 103*, 289-303

Smith, R.M. (1998). How Linear Are Typical CCDs? *Experimental Astronomy, 8*, 59-72

Starks, P.J., Walter-Shea, E.A., Schiebe, F.R., & Markham, B.L. (1995). Temperature Sensitivity Characterization of a Silicon Diode Array Spectrometer. *Remote Sensing of Environment, 51*, 385-389

Stevens, E.G. (1991). Photoresponse nonlinearity of solid-state image sensors with antiblooming protection. *Electron Devices, IEEE Transactions on, 38*, 299-302

Stow, D.A., Hope, A., McGuire, D., Verbyla, D., Gamon, J., Huemmrich, F., Houston, S., Racine, C., Sturm, M., Tape, K., Hinzman, L., Yoshikawa, K., Tweedie, C., Noyle, B., Silapaswan, C., Douglas, D., Griffith, B., Jia, G., Epstein, H., Walker, D., Daeschner, S., Petersen, A., Zhou, L., & Myneni, R. (2004). Remote sensing of vegetation and land-cover change in Arctic Tundra Ecosystems. *Remote Sensing of Environment, 89*, 281-308

Teillet, P.M. (2010). Sensor Webs: A Geostrategic Technology for Integrated Earth Sensing. *Selected Topics in Applied Earth Observations and Remote Sensing, IEEE Journal of, 3*, 473-480

Teillet, P.M., Gauthier, R.P., Chichagov, A., & Fedosejevs, G. (2002). Towards integrated Earth sensing: Advanced technologies for in situ sensing in the context of Earth observation. *Canadian Journal of Remote Sensing, 28*, 713-718

Verhoef, W. (1984). Light scattering by leaf layers with application to canopy reflectance modeling: The SAIL model. *Remote Sensing of Environment, 16*, 125-141

Walthall, C.L., Norman, J.M., Welles, J.M., Campbell, G., & Blad, B.L. (1985). Simple equation to approximate the bidirectional reflectance from vegetative canopies and bare soil surfaces. *Applied Optics, 24*, 383-387

Wanner, W., Li, X., & Strahler, A.H. (1995). On the derivation of kernels for kernel-driven models of bidirectional reflectance. *J. Geophys. Res., 100*, 21077-21089

Zhang, L., Huang, C., Wu, T., Zhang, F., & Tong, Q. (2011). Laboratory Calibration of a Field Imaging Spectrometer System. *Sensors, 11*, 2408

Zong, Y., Brown, S.W., Johnson, B.C., Lykke, K.R., & Ohno, Y. (2006). Simple spectral stray light correction method for array spectroradiometers. *Applied Optics, 45*, 1111-1119

CHAPTER 1

Nonlinear Response in a Field Portable Spectroradiometer: Characterization and Effects on Output Reflectance

---

Published paper: Pacheco-Labrador, J., & Martin, M.P. (2014). Nonlinear Response in a Field Portable Spectroradiometer: Characterization and Effects on Output Reflectance. *Geoscience and Remote Sensing, IEEE Transactions on*, 52, 920-928.

Javier Pacheco-Labrador[1], and M. Pilar Martín[1]
[1] Environmental Remote Sensing and Spectroscopy Laboratory (SpecLab)
Instituto de Economía, Geografía y Demografía; Consejo Superior de Investigaciones Científica (CSIC)
C/ Albasanz 26-28, 28037 Madrid, Spain

Manuscript Received: 15 June 2012. Revised: 28 January 2012. Accepted: 2 February 2013. Date of publication: 17 April 2013. Issued: February 2014.

ABSTRACT

We report the characterization and correction of nonlinear responses of a commercial field portable spectroradiometer intended to be used to monitor vegetation physiology. Calibration of photoresponse allowed the successful correction of spectral data and the modeling of biases in reflectance at different levels of the dynamic range. Finally, the impact of nonlinearities on a spectral estimator of photosynthetic status, the Photochemical Reflectance Index (PRI) is discussed. Significance of the biases proved that, although nonlinearity can potentially affect reflectance along most of the dynamic range of the instrument, experimental uncertainties can limit its impact. Nonlinearity biased PRI by affecting the reference band of the index and suggested unreal changes on plant physiology. Results show that nonlinearity could be a significant problem in field spectroscopy, especially in the case of spectroradiometers integrated in unattended systems to monitor vegetation responses to radiation. An automatic adjustment of integration time to reach only a certain level of the dynamic range may reduce nonlinearity effects, though may not always avoid them. We conclude that linearity characterization is necessary to understand impacts and correct potential biases.

Keywords: Nonlinearities, spectroscopy.

1. INTRODUCTION

Laboratory and field spectroscopy have a key role in Earth monitoring to characterize surface optical properties and to calibrate and downscale airborne and satellite sensor observations (Gamon et al. 2006b; Milton et al. 2009). In the context of carbon cycle monitoring, spectroscopy is being widely used by the scientific community

to track plant physiology in Eddy Covariance (EC) sites and connect this information with remote observations. The most current advances in the monitoring of carbon uptake are related to the recent development of unattended continuous hyperspectral systems, which among other advantages provide optical information at the same temporal scale than the EC systems (Balzarolo et al. 2011; Gamon et al. 2006b; Hilker et al. 2007; Hilker et al. 2010; Meroni et al. 2011; Sims et al. 2006). International networks such as SpecNet (www.specnet.info) (Gamon et al. 2006b) and Cost Action ES0903 - EUROSPEC (www.cost-es0903.fem-environment.eu) have emerged to focus efforts done in this field and try to improve the comparability of optical data, which would allow for the compilation of global estimates of carbon uptake (Balzarolo et al. 2011; Gamon et al. 2006b; Milton et al. 2009). However, despite advances achieved in field spectroscopy over the last decades, it is still described as one of the least reliable of all physical measurements (Kostkowski 1997). Comparability and reproducibility of spectral data can be compromised by different factors (Anderson et al. 2011; Jung et al. 2012; Milton et al. 2009), including the instrumentation. Spectroradiometers can introduce biases and uncertainties in the resulting signal due to stray light, dark current (DC) drift, diffraction orders, sensor linearity, or harmonic interferences, among others (ASD 1999; James 2007; Kostkowski 1997; MacArthur et al. 2006; Salisbury 1998; Schaepman and Dangel 2000).

In this paper, we focus specifically on sensor linearity and its potential impact on reflectance in the visible and Near Infrared regions. Linearity is the proportional relationship between the amount of light that a sensor receives and the resulting photocurrent; a high linear photoresponse is desirable so that the instrument's output is directly proportional to the magnitude of energy measured. However, this linear

relationship can be affected by factors related to both the electronics and/or the detector elements themselves (Hamamatsu 2011a, b, c; James 2007; PP Systems 2005). Normally, when the sensor is close to saturation, the anti-blooming structures (designed to drain the overflow off the saturated photodiodes before this reaches the adjacent ones) start draining part of the charge before saturation, reducing the sensor's response to incident light at high levels of energy (Hamamatsu 2011a; Stevens 1991).

Two different strategies are usually adopted by the manufacturers to overcome the problems caused by photoresponse nonlinearity. The first one is avoiding the region where linearity is low through automatic adjustment of integration time, so that the maximum output signal is fixed at a given percentage of the dynamic range (e.g., Analytical Spectral Devices Inc., Boulder, CO, USA; Spectra Vista Corporation, Poughkeepsie, NY, USA; PP Systems, Amesbury, MA, USA). The second strategy consists in characterizing each sensor's photoresponse and correcting the data in a post-processing stage (e.g., Ocean Optics Inc., Dunedin, FL, USA; Avantes, Apeldoorn, The Netherlands). Though instruments usually adjust integration time automatically, in some cases, it can be also manually set (ASD 1999; Spectra Vista Corporation 2008), which would require a full understanding of the sensor photoresponse. Unattended hyperspectral systems typically use double beam (dual detector) spectroradiometers, such as the Unispec DC (PP Systems), due to their capacity to simultaneously measure up-welling and down-welling radiation (Gamon et al. 2006a; Hilker et al. 2007; Hilker et al. 2010). In these systems, integration time can be fixed looking for an equilibrium, which allows avoiding saturation and obtaining an adequate signal-to-noise ratio (SNR) under different illumination conditions (Hilker et al. 2010).

We present here the results obtained with a Unispec DC spectroradiometer affected by a nonlinear photoresponse, which had not been previously reported for this instrument. The instrument photoresponse was characterized to correct the data in a post-processing stage. Then differences between the original and the corrected spectral reflectance and derived spectral indexes were assessed. Moreover, biases due to nonlinearity were compared with those uncertainties introduced by the correction model, as well as with experimental uncertainties of field measurements.

2. METHODOLOGY

2.1 Instrumentation

All experiments described in this paper were undertaken using a Unispec DC (SN 2038), a double beam field portable spectroradiometer (PP Systems) with two synchronized spectrometers, which simultaneously sample radiance and irradiance using an optical fiber (channel B) and a cosine receptor (channel A). Radiometric resolution is 16 bits [65535 Digital Numbers (DN)], nominal bin size, spectral resolution (full width at half maximum), and spectral range are 3.3 nm, < 10 nm, and 300–1100 nm, respectively.

The two spectrometers inside the Unispec DC are monolitical miniature spectrometer 1, manufactured by Carl Zeiss, Inc., (Thornwood, NY, USA) equipped with a silicon diode array S3904-256Q sensor each (Hamamatsu Photonics K.K., Tokyo, Japan). This is a Negative-channel Metal-Oxide Semiconductor (NMOS) sensor, which uses a charge integration method to read out the charges accumulated in the photodiode array, thus the output signal is proportional to the incident light intensity and the integration time. An anti-blooming switch is provided for each photodiode,

allowing the drainage of overflow. Photosensitivity is reported to be linear (absolute error < 1 %) up to 95 % of the saturation charge. Above this threshold, part of the output flows into the anti-blooming switch (Hamamatsu 2011a, c).

Linearity calibration was carried out using an ASD RTS-3ZC integrating sphere (Analytical Spectral Devices Inc.,) with a stable illumination source. A 10 W quartz-tungsten-halogen bulb powered by a battery provides a collimated beam of light, which was reflected by a 99 % Zenith Polytetrafluoroethylene (PTFE) standard (Sphereoptics Hoffman LLC, Contoocook, NH, USA) located at the opposite port of the sphere. The sphere, internally coated with highly reflective (> 95 %) Zenith PTFE, scatters the radiation in all directions, offering a homogeneous source of light through an open port.

2.2 Field experiment

An inter-comparison experiment took place in Monte Bondone (Italy) on July 2011 in the framework of the COST Action ES0903-EUROSPEC: Spectral Sampling Tools for Vegetation Biophysical Parameters and Flux Measurements in Europe. The aim of the experiment was comparing the reflectance values obtained with four different commercial spectroradiometers under controlled field conditions. Further details of this experiment can be found in Anderson et al. (2013).

For the Unispec DC, a downward looking fiber optic (channel B) was placed together with the fibers of the other spectroradiometers on a tripod with a rotating arm; whereas a cosine receptor (channel A) was placed over its axis. A white reference panel (99 % Spectralon® (hereafter called "reference") (Labsphere Inc., North Sutton, NH, USA), and three targets (a bright grey 75 % Spectralon® panel ("grey75"), a dark grey 20 % Spectralon® panel ("grey20"), and a grass plot ("grass")) were measured 50 times,

always in the same order. First, DC (DC in equations) was measured by completely covering the optical fibers. Then, a reference spectrum was taken from the 99 % Spectralon® panel, and a spectrum of each one of the targets ("grey75," "grey20," and finally "grass") was collected immediately after that. The Unispec DC integration time (common to both channels A and B) was manually adjusted in order to compensate increases in irradiance as the solar zenith angle decreased along the experiment. We tried to maximize the SNR in the channel A simultaneously avoiding saturation in the channel B.

Reflectance was calculated using two different approaches: 1) single-beam mode (SBM) where absolute reflectance was computed using the measurements of the "reference" panel in digital numbers (DN in equations) to normalize the radiance measured from the targets using only data acquired from channel B (Eq. 1), and 2) double-beam mode (DBM) where absolute reflectance was computed using the "reference" spectra to cross-calibrate both channels as described in Gamon et al. (2006a) (Eq. 2). SBM was calculated to compare the measurements of different instruments in the inter-comparison experiment, whereas DBM is the usual operation mode of this dual-channel instrument, especially in the case of unattended systems.

$$\rho_{SBM} = \frac{(DN_{ChB} - DC_{ChB})_{Target}}{(DN_{ChB} - DC_{ChB})_{Reference}} \cdot \rho_{Reference} \tag{1}$$

$$\rho_{DBM} = \frac{(DN_{ChB} - DC_{ChB})_{Target}}{(DN_{ChA} - DC_{ChA})_{Target}} \cdot \frac{(DN_{ChA} - DC_{ChA})_{Reference}}{(DN_{ChB} - DC_{ChB})_{Reference}} \cdot \rho_{Reference} \tag{2}$$

2.3 Linearity characterization under stable illumination

Different methods described to measure and model the nonlinear photoresponse of photodiode sensors require quantification of energy in absolute units (Anderson et al. 2011; Hopkinson et al. 2004; Janesick 2001; López-Álvarez et al. 2009; Markham et al. 1995; Schaepman and Dangel 2000; Smith 1998). Since no calibrated radiance sources were available for this paper, we applied another method used by Ocean Optics Inc., to correct nonlinearity of their instruments (OceanOptics 2012). However, in this experiment, we used a larger number of bins to estimate the sensors' photoresponse, and we also characterized the uncertainties of the correction.

The Unispec DC optical fibers (one of each channel) were aimed at inside of an ASD RTS-3ZC integrating sphere through an open port. A collimated light source was placed in a different port, and the light was reflected by a 99 % PTFE panel in the opposite one and then scattered within the sphere before reaching the fibers. Integration times were randomly changed from 50 to 1350 ms during the experiment in order to acquire data all along the dynamic range of both channels. Moreover, light stability was monitored by acquiring control spectra with the same integration time (500 ms) once every five measurements. In total, 31 spectra were acquired for both control and calibration. For each spectrum, DC was previously recorded by covering the sphere port with a black and opaque plate. After DC (DC in equations) subtraction, the response of each channel was computed normalizing each spectrum (in DN) by its integration time (IT in equations), and then by the highest normalized value of each spectrum (Eq. 3).

$$Response = \frac{(DN - DC)/_{IT}}{max\left((DN - DC)/_{IT}\right)} \tag{3}$$

Responses of the least noisy spectral region between 400 and 1,000 nm (181 bins), were used altogether to fit a single seventh degree polynomial for the entire sensor of each channel (Eq. 4), the fitted response. This method assumes photoresponse uniformity along the sensor array (OceanOptics 2012). The independent variable (DN) was first transformed to avoid bad conditioning (Matlab Help 2012).

$$Fitted\ Response = \sum_{i=0}^{7} a_i \cdot \left(\frac{(DN - DC) - \overline{(DN - DC)}}{\sigma_{DN}}\right)^i \tag{4}$$

2.4 Linearity correction model and error propagation

As proposed in (OceanOptics 2012), we corrected the nonlinearity of the inter-comparison experiment spectra using the fitted responses polynomial (Eq. 4) to calculate the photoresponse of each bin as a function of the measured DN, and dividing these measured DN by their responses afterward as follows:

$$DN_{Corrected} = \frac{DN_{Original} - DC}{Fitted\ Response} \tag{5}$$

Residuals of the polynomial fits would eventually lead to uncertainties in the calculation of reflectance. Thus, we quantified these uncertainties through error propagation and later compared them with the biases introduced by nonlinearity. Error propagation was not carried out using the law of propagation of uncertainty (Bureau

International des Poids et Mesures 2008), since the Probability Distribution Functions (PDF) of corrected DN errors were unknown or could not be assumed to be normal. Monte Carlo simulation was used instead, since it has proved to be a general tool for evaluating uncertainty through the propagation of PDF, avoiding assumptions about the shape of these distributions (Anderson 1976; Bureau International des Poids et Mesures 2008; Cox et al. 2003; Herrador et al. 2005).

Monte Carlo was applied to a model which included the correction of nonlinearity and to the computation of SBM (Eq. 1) and DBM (Eq. 2) reflectances. Least squares polynomial fitting produced residuals assumed to be normally distributed with mean 0. At each DN level, standard deviation was used to randomly generate 200 samples of these residuals with normal distribution. These errors were added to the fitted responses predicted by the calibrated models, generating then a set of responses associated to each original DN. These responses were used to correct the original DN and compute SBM and DBM reflectances and their 95 % confidence intervals, which represented the propagated uncertainties in reflectance. The reflectance values selected for this analysis and its simulation are described in the following section.

2.5 Modeling nonlinearity effects on reflectance

Different SBM and DBM reflectances were simulated in order to compare the biases introduced by nonlinearities with those uncertainties propagated from the nonlinearity correction and then, to assess the significance of the correction when uncertainties found under field conditions were considered. Since we used the uncertainties found in the inter-comparison experiment, reflectance values similar to those measured in the “grey75” and “grey20” panels (80 % and 20 %, respectively), and

the reflectance of the grass plot at 566.9 nm (7.52 %) -the waveband most affected by nonlinearity- were selected for the simulation. A flowchart of the simulation is shown in Figure 1. For each one of these values, a dataset of DN corresponding to measurements of the white reference (ChB WR in Figure 1) and the target (ChB T) were generated simulating perfectly linear sensors along the different levels of the dynamic range. The average signal loss introduced by the cosine receptor during the inter-comparison was used to simulate channel A values (ChA WR). Moreover, since reflectances calculated in SBM and DBM would lead to the same values due to mutual cancelation of Channel A terms in (Eq. 2) under the same ideal conditions; we decided to change the conditions after the measurement of the reference to compute DBM reflectance, a situation that an unattended system may experience. For that, the simulated linear DN values of both channels corresponding to the target measurements were halved (ChA T0, ChB T0). A second dataset was then generated by biasing the DN of the linear dataset with the calibrated fitted responses of each channel (Eq. 4). The model was inverted to estimate the biased values from the linear (or corrected) ones using the simplex method (Lagarias et al. 1998). Then, we used these datasets to calculate linear (or corrected) and nonlinear reflectances at different levels of the dynamic range.

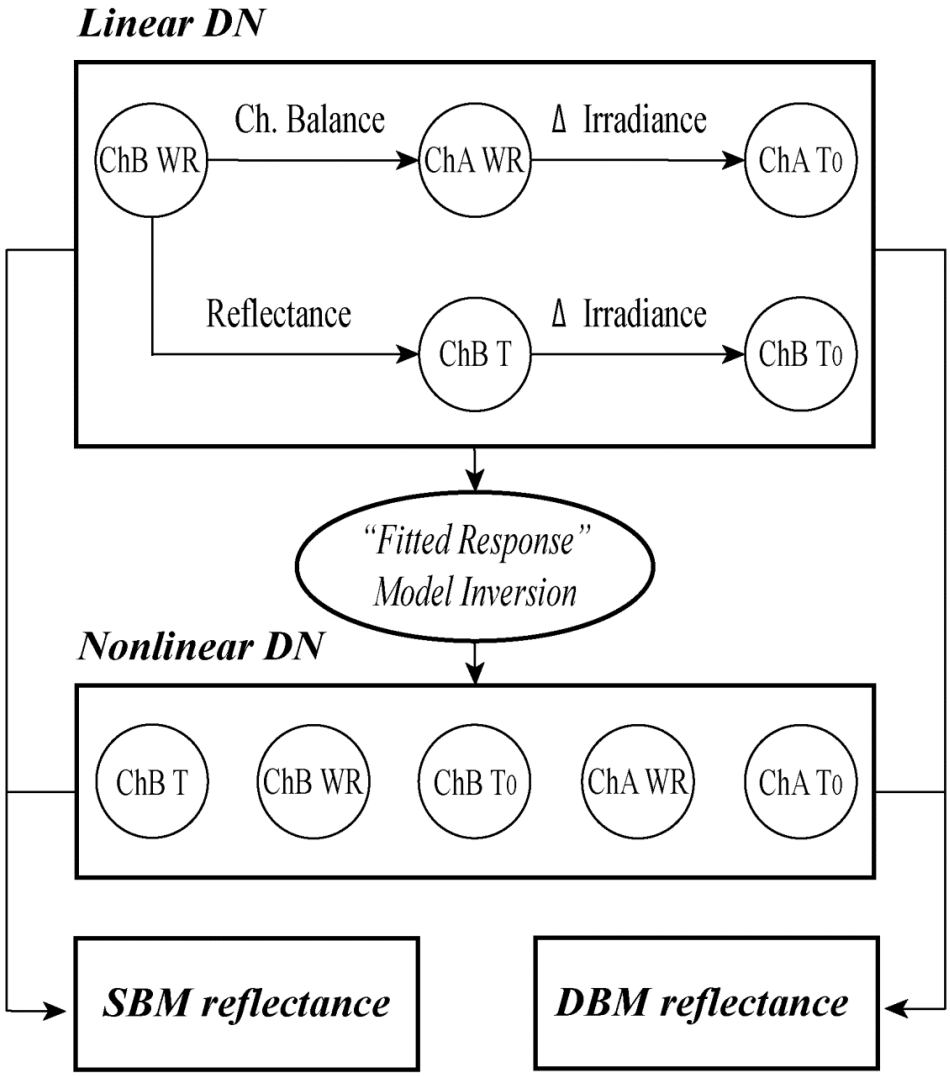

Figure 1. Spectral data simulation flowchart

2.6 Nonlinearity effects on photochemical reflectance index

The Photochemical Reflectance Index (PRI) (Gamon et al. 1992) was selected to assess the effects of nonlinearity for two reasons: the first one is that one of the narrow bands (570 nm) used in the index was greatly affected by nonlinearity in our instrument under solar irradiance. The second reason is that PRI has been widely used in the study of photosynthetic efficiency and vegetation productivity, where the first is largely

related to the level of radiation and the capability of vegetation to convert this into chemical energy through photosynthesis. Under excess radiation, the xanthophyll cycle is triggered, so that the excess of energy is liberated as heat, and a relative decrease of reflectance in a 50 nm width band centered on 531 nm is produced. The process reverses when stress is reduced (Gamon et al. 1992; Garbulsky et al. 2011; Hilker et al. 2008; Peñuelas et al. 1995).

PRI (Eq. 6) was computed from SBM and DBM reflectances using the "grass" spectra measured in the inter-comparison experiment. Reflectances at 531 and 570 nm were linearly interpolated from the adjacent wavebands.

$$PRI = \frac{\rho_{531nm} - \rho_{570nm}}{\rho_{531nm} + \rho_{570nm}} \tag{6}$$

3. RESULTS

3.1 Field experiment

Clear differences were found in the spectra acquired by the Unispec DC and the other spectrometers involved in the inter-comparison experiment. Only the first 8 spectra were close to the nominal reflectance of calibrated panels (Figure 2a), whereas 42 showed mountain-shaped reflectance increases of different magnitude centered on 453.1 and 566.9 nm, being more prominent for the "grey20" and "grey75" panels (Figure 2b). These increases were not noticeable in the vegetation spectra, for which reflectance was not known a priori.

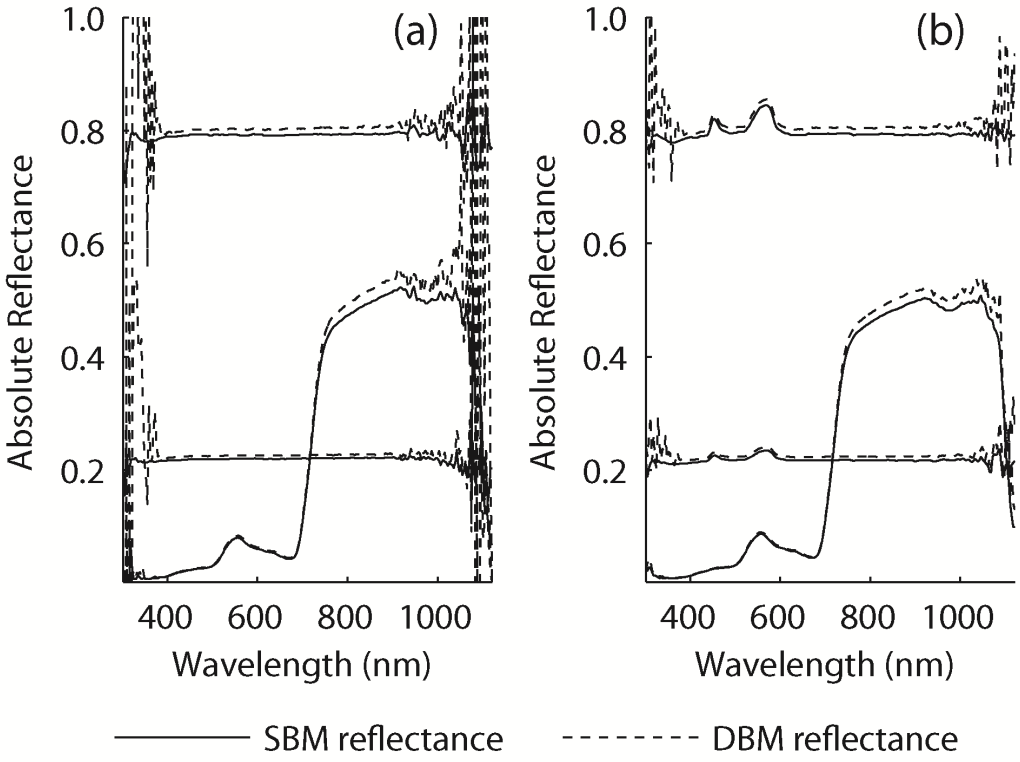

Figure 2. Absolute reflectance spectra acquired during the inter-comparison experiment corresponding to (a) first and (b) ninth rounds for both SBM and DBM reflectances.

Aberrant reflectance increases were coincident with the regions where the maximum DN values were reached, occurring only above a certain DN value (Figure 3). White reference spectra values were high (> 50,000 DN) in channel B, whereas in channel A values were on average 2.7 times lower.

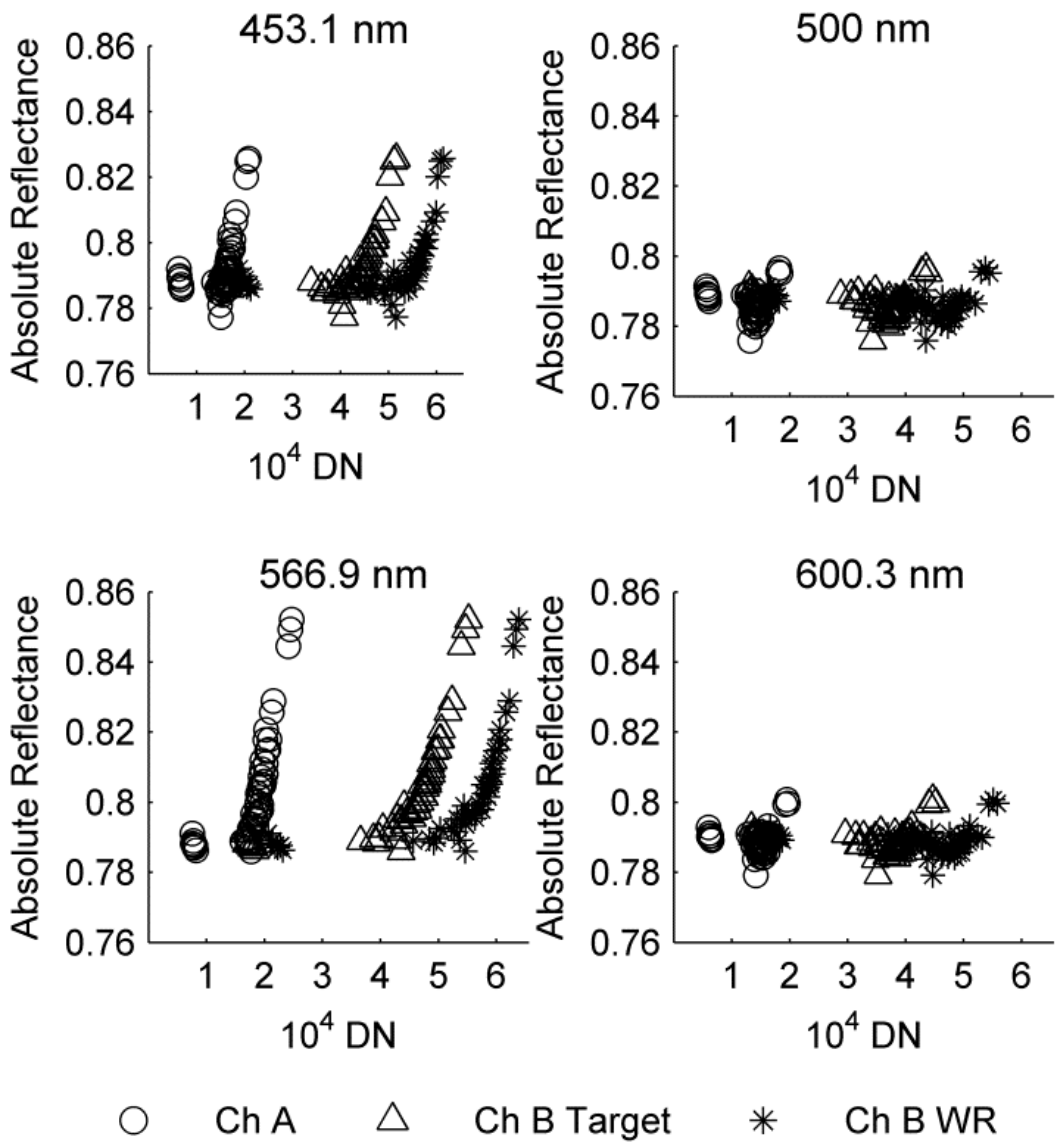

Figure 3. "Grey75" panel SBM reflectance versus channels A and B raw DN spectra at different wavebands.

3.2 Characterization of linearity under controlled conditions

The photoresponse of both spectrometers of the Unispec DC was carefully characterized under controlled illumination conditions covering the entire instrument's dynamic range. In this case, the nature of the illumination source, a quartz-tungsten-halogen bulb, was different from the solar irradiance received during the outdoors

experiment. Consequently, maximum values found in the raw DN spectra were centered at different wavelengths, around 577.0 and 726.7 nm (Figure 4). At these wavebands, coefficients of determination (R^2) between integration time and output DN were high (above 0.9986 in all the cases). Sensor photoresponses (Eq. 3) were fit to a seventh degree polynomial model (Eq. 4), (R^2=0.9743 for channel A, R^2=0.9581 for channel B).

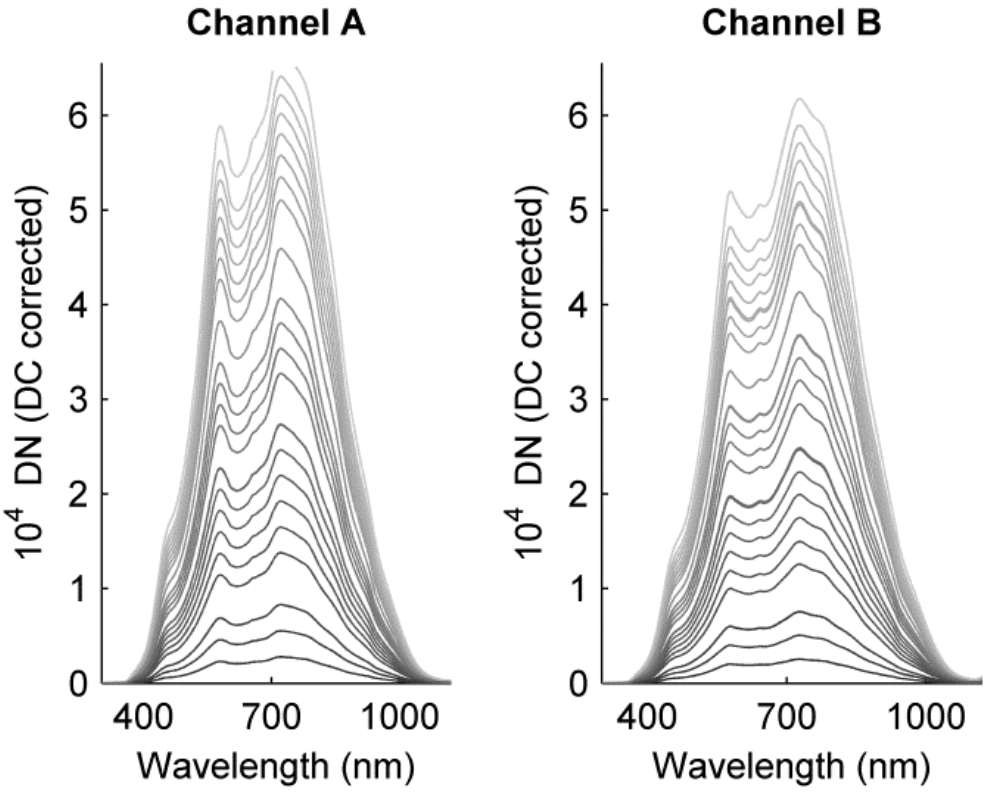

Figure 4. Raw spectra acquired for linearity characterization under controlled illumination condition.

In both cases, the photoresponse of the Unispec DC spectrometers decreased gradually along most of the dynamic range, and dropped abruptly at the top, above 50,000 DN. As can be seen in Figure 5, nonlinearity was more acute in the case of the channel B sensor.

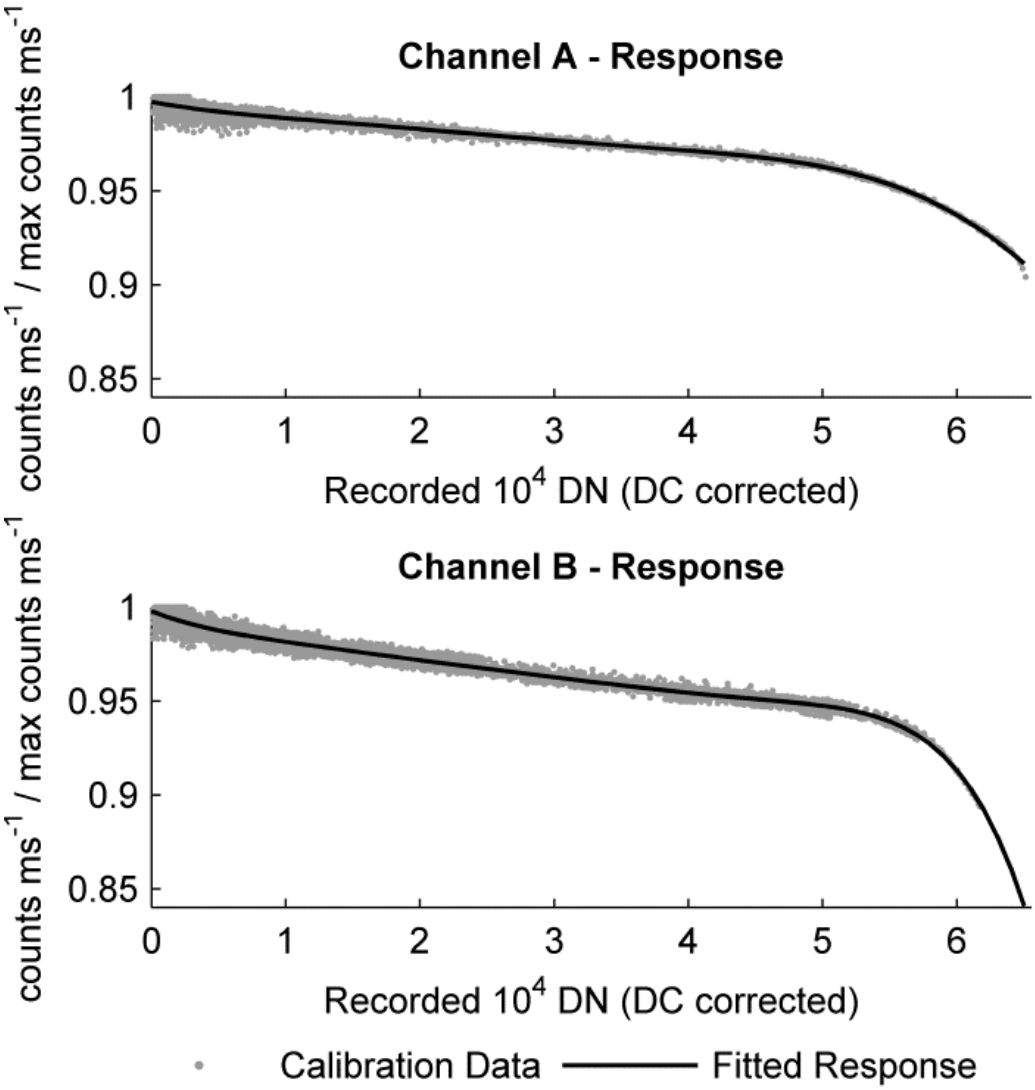

Figure 5. Response of the Unispec DC spectrometers and fitted response seventh degree polynomial.

3.3 Nonlinearity correction

The fitted responses of the instrument, allowed the correction of the field data (Eq. 5). This resulted in an overall increase of the corrected DN values, which grew larger as the measured values were closer to saturation. Figure 6a shows the corrected

and uncorrected raw spectra in DN for all the measurements taken during the ninth round of the inter-comparison experiment (Figure. 2b). When reflectance was calculated using the corrected DN, mountain-shaped reflectance increases disappeared (Figure. 6b); moreover, slight changes of reflectance occurred in all the spectra and in those regions least affected by nonlinearity.

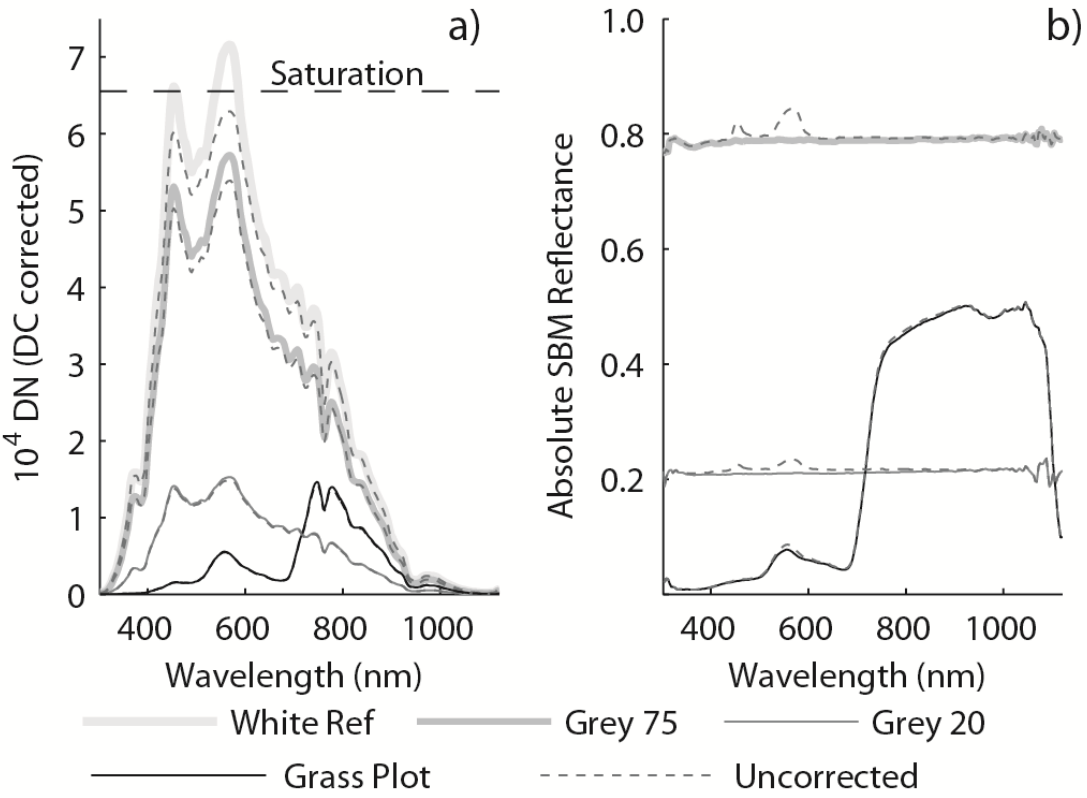

Figure 6. (a) Corrected and original channel B DN spectra. (b) SBM reflectance spectra corresponding to the ninth round of the inter-comparison experiment. The dashed line immediately next to each spectrum shows its respective uncorrected values.

3.4 Correction error propagation and experimental uncertainties

Residuals of the fitted response were propagated through Monte Carlo simulation of reflectance values. Table 1 shows the averaged values of SBM and DBM

simulated reflectances and their propagated uncertainties. Error propagation casted larger dispersions the larger the reflectance of the target, but these were similar when were normalized by the reflectance (Kruskal-Wallis test, p value > 0.05). Dispersions were larger for DBM than for SBM reflectances in all the cases (Kruskal-Wallis test, p value < 0.05).

Table 1. Average reflectance uncertainties propagated from non-linearity correction errors.

Ideal Reflectance	Absolute 95 % C.I.	Normalized 95 % C.I.	Absolute 95 % C.I. Range
SBM Reflectance			
0.8000	[0.7925, 0.8073]	[0.9906, 1.0091]	0.0148
0.2000	[0.1982, 0.2018]	[0.9910, 1.0089]	0.0036
0.0752	[0.0745, 0.0758]	[0.9911, 1.0091]	0.0014
DBM Reflectance			
0.8000	[0.7914, 0.8085]	[0.9893, 1.0107]	0.0171
0.2000	[0.1979, 0.2021]	[0.9896, 1.0106]	0.0042
0.0752	[0.0744, 0.0760]	[0.9896, 1.0106]	0.0016

The experimental uncertainties corresponding to the inter-comparison experiment (the residuals of the mean reflectance) are shown in Table 2. The largest dispersions were found in “grey20” reflectance, both for absolute and normalized values. The narrowest confidence intervals normalized by reflectance corresponded to “grey75.”

Table 2. Experimental residuals. 95 % condifence intervals.

Reflectance Mode	Grey 75	Grey 20	Grass plot
Absolute Intervals			
SBM	[-0.0066, 0.0066]	[-0.0109, 0.0146]	[-0.0025, 0.0027]
DBM	[-0.0069, 0.0086]	[-0.0121, 0.0158]	[-0.0024, 0.0026]
Normalized Intervals			
SBM	[-0.0083, 0.0083]	[-0.0543, 0.0730]	[-0.0328, 0.0357]
DBM	[-0.0087, 0.0108]	[-0.0606, 0.0788]	[-0.0322, 0.0346]

3.5 Nonlinearity effects on reflectance

The computation of SBM and DBM reflectances from modeled linear and nonlinear DN representing different levels of energy in the sensors led to similar results.

Figure 7 shows DBM reflectances and the 95 % confidence intervals corresponding to the correction errors and the experimental uncertainties; these are plotted against the uncorrected DN value of the white reference, which is used as an indicator of the signal level along the dynamic range.

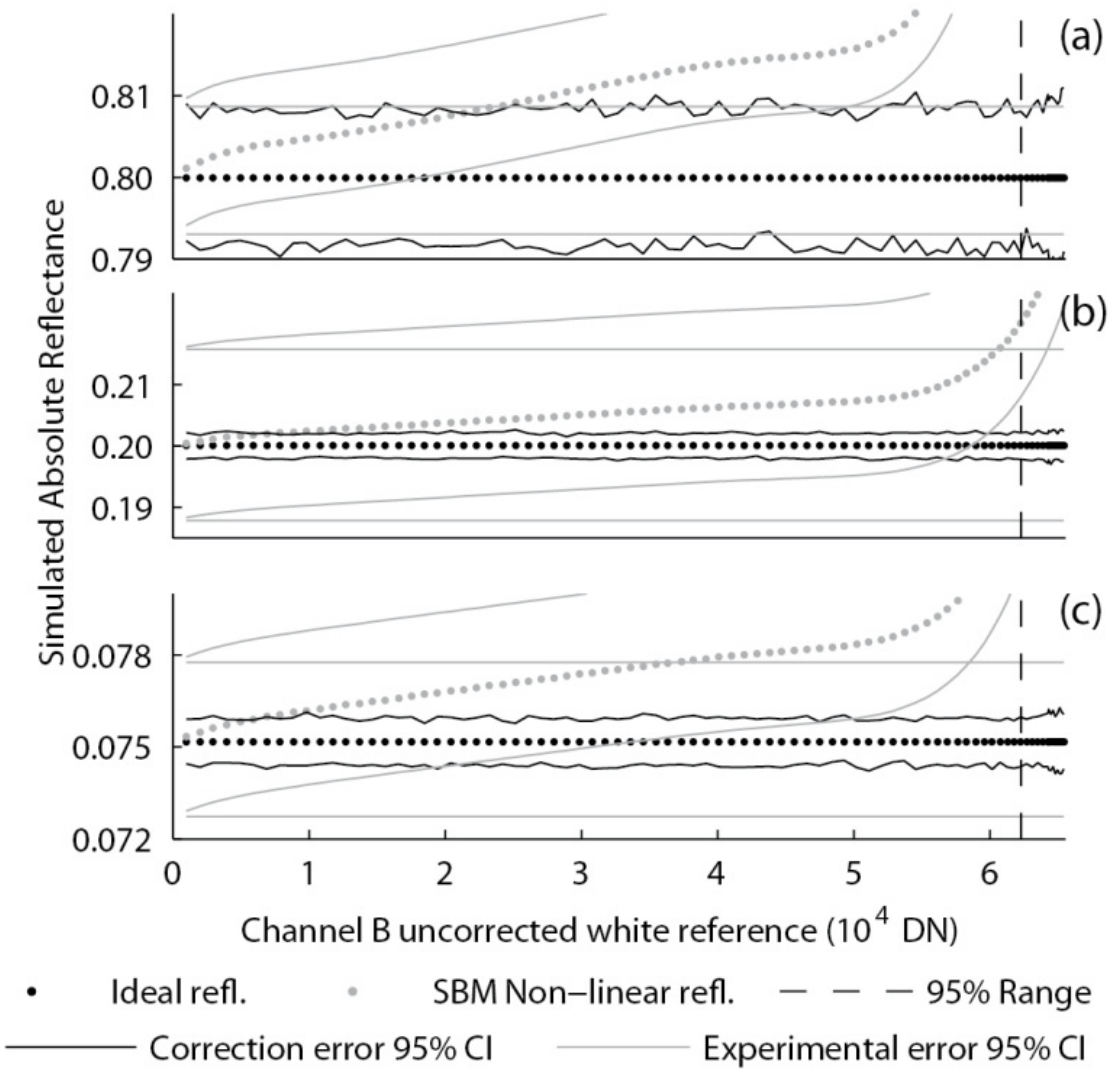

Figure 7. Corrected and original DBM simulated reflectance spectra and 95 % confidence intervals. (a) “Grey75”. (b) “Grey20”. (c) “Grass”.

As can be seen, differences between linear and nonlinear reflectances were significant at the top of the dynamic range, above a different signal level in each case (Table 3), depending on the experimental uncertainty. However, when no experimental uncertainties were considered, nonlinear reflectances were out of the confidence intervals from much lower levels of the dynamic range, especially in the case of the dark targets.

Table 3. Dynamic range limits for equality of linear and nonlinear reflectances

Reflectance Mode	Grey 75	Grey 20	Grass plot
Considering correction and experimental uncertainties			
SBM	86.23 %	97.19 %	89.46 %
DBM	75.93 %	97.76 %	89.46 %
Considering correction uncertainties only			
SBM	80.00 %	9.78 %	6.79 %
DBM	31.86 %	11.27 %	8.28 %

3.6 Nonlinearity effects on photochemical reflectance index

The PRI computed from SBM and DBM reflectances corresponding to the grass plot in the inter-comparison were very similar (maximum difference 0.0012). PRI became greatly dependent on the energy level that reached channel B during the white reference measurement, especially when it was above 50,000 DN (Figure 8a). The PRI calculated from corrected SBM and DBM reflectance ranged between -0.0759 and -0.0642, whereas variation was larger when nonlinearity effects were not corrected (from -0.0974 to -0.0650). In order to assess the importance of the biases introduced by nonlinearity, the range of variation of PRI values found in different canopies (−0.12, 0.03) (Garbulsky et al. 2011) was taken as a reference. Figure 8b shows the variation of the index along the experiment within this range. As can be seen, uncorrected PRI changed its value whenever integration time was readjusted, but decreased again while irradiance increased along the experiment. Linear PRI changes represented 7.60 % of the range in (Garbulsky et al. 2011), but when computed from nonlinear reflectances, variation increased almost three fold (21.38 %).

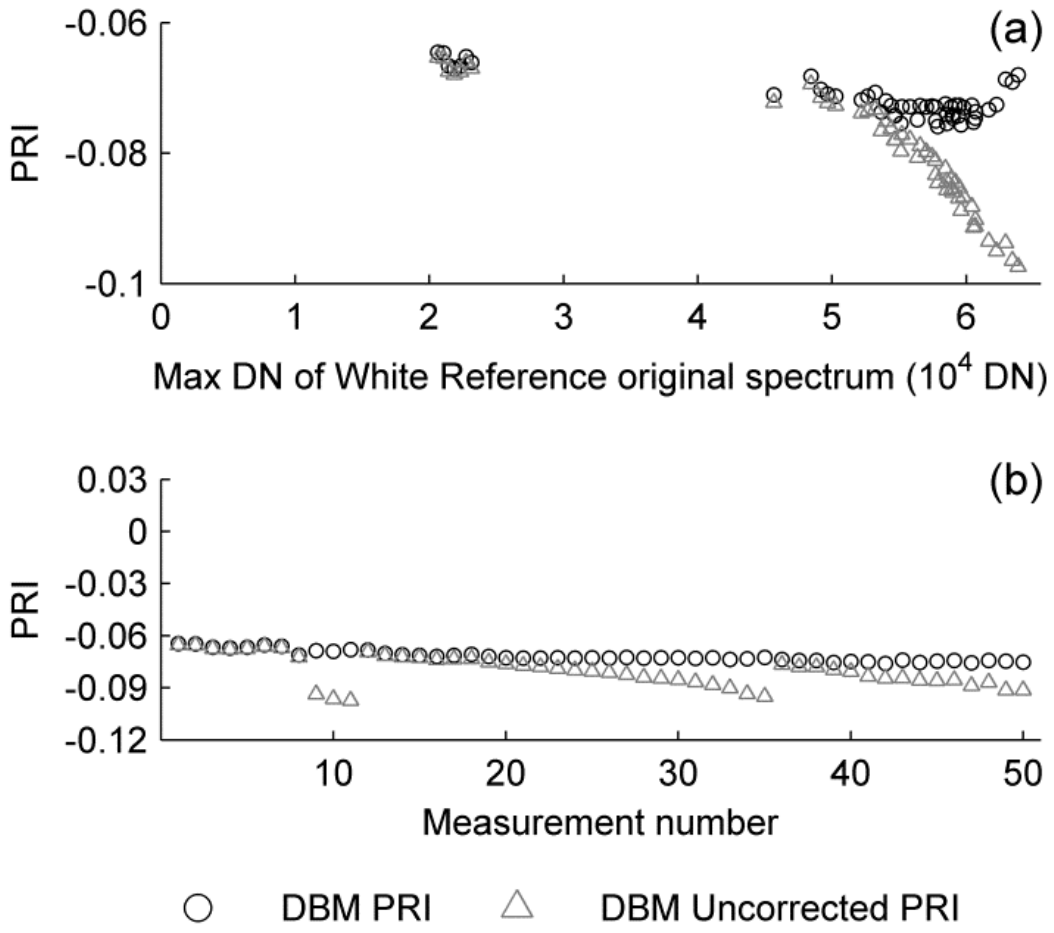

Figure 8. (a) PRI calculated from linear and nonlinear DBM reflectances of the grass plot in the inter-comparison experiment. (b) PRI range from (Garbulsky et al. 2011).

4. DISCUSSION

4.1 Detection, characterization and correction of nonlinearity

The use of calibrated panels during the inter-comparison experiment and the manual setting of integration time allowed the detection of nonlinearity of the Unispec DC unit. Nonlinearity caused DN values lower than expected from a perfectly linear sensor, which mainly affected the white reference measurements in channel B (Figure 6). This eventually produced aberrant increases in reflectance when the ratio target/reference was computed. The photoresponse characterization revealed the

existence of nonlinearity in both channels, where sensor and electronics were likely contributors. The method used here to characterize nonlinearity is empirical and relative, and it does assume photoresponse uniformity along the sensor array; this is usually close to ± 1 % (± 3 % at maximum for Hamamatsu NMOS sensors) (Hamamatsu 2011a). Thus, uncertainties introduced by this nonlinearity correction should be characterized; especially when the radiance source used for the characterization is spectrally different from the irradiance found during the measurements (compare Figures 4 and 6). The coefficients of determination between integration time and instrument output (commonly used to assess deviations from linearity) (Anderson et al. 2011; OceanOptics 2011) were high despite of nonlinearities, which may suggest that this analysis is not always capable to determine the existence of nonlinearity. Spectral differences between the illumination used for the photoresponse characterization and the solar irradiance of the outdoors measurements still allowed data correction, since photoresponse nonuniformity along the sensor array was less relevant than nonlinearity.

The manufacturer of the Unispec DC spectroradiometer used in this paper, PP Systems (www.ppsystems.com), conducted a similar experiment with a different Unispec unit (SC instead of DC), but with the same models of spectrometer and sensor, confirming that the nonlinear photoresponses we found were not exclusively shown by our unit, though they were different for each instrument. The correction method here applied was also successfully tested by PP systems, which released an application note on this matter (PP Systems 2012). Nonlinearity would most likely be different for each detector and eventually for each instrument, so the particular results stated here are perhaps unique to our unit. However, nonlinearity is a common problem in

spectroscopy, which may be found in each single spectroradiometer to some degree, significant or not. Thus, it would be recommendable to characterize nonlinearity of each instrument, among other sources of error. This is especially important for automated applications where irradiance conditions may exceed an optimal range.

4.2 Nonlinearity effects on reflectance

The Monte Carlo method permitted establishing confidence intervals for the corrected reflectances, which allowed us to determine at which levels of the dynamic range nonlinear reflectances would be significantly different from the corrected ones (and thus, correction would be worthy). In an ideal situation where no uncertainty was associated with reflectance, differences would be significant for most of the dynamic range, especially in the case of dark targets ("grey20," "grass"), since absolute uncertainty of the correction increases with the reflectance value. In this case, the threshold of the dynamic range from where nonlinearity is significant only depends on the magnitude of nonlinearity affecting both sample and target measurements (in one or two channels), and thus on the energy reaching the sensors in each measurement. This is eventually controlled by the irradiance, the instrument configuration and the reflectance of the target.

However, experimental uncertainties must be considered. In our simulation, these were larger or equal than the errors propagated from nonlinearity correction, masking the nonlinearity biases. This way differences were not significant along most of the dynamic range, though effects would still be noticeable in some cases below the 95 % of the range. Since the magnitude of experimental uncertainties would be different in each experiment, so would be the significance of nonlinearity; thus, it is not possible

establishing an absolute limit for all the cases, as it happens for the different targets compared. Simply avoiding the top of dynamic range may not always prevent instrumental uncertainties from becoming prevalent over environmental or methodological ones. Adjusting the integration time of the sensor to always reach the same percentage of the dynamic range (not strongly affected by nonlinearity) for each measurement would increase precision, providing data more intercomparable, especially if targets' reflectance is similar. However, depending on the accuracy required by the application, data still may not be intercomparable between different sensors or between different instrument configurations. Though correcting nonlinearities may reduce precision, increasing overall uncertainty (when the correction uncertainties were larger than the experimental), it would provide results more accurate and intercomparable. Nevertheless, it would always be advisable to avoid the least linear levels of the dynamic range, where the number of data available to calibrate the fitted responses (Eq. 4) would also be lower and less representative of the whole sensor response.

The effects of nonlinearity on reflectance would depend on each instrument's response, irradiance, target reflectance, and modes of operation and protocols, and their significance will depend on the experimental uncertainties and the correction errors; whereas the eventual utility of data would be limited by the requirements of each application. Thus, characterizing the linearity and the uncertainties associated with its correction would be recommended (among other tests) before using any instrument. Automatically adjusting integration time for each measurement rather than using fixed values or manual configurations would contribute to the intra-comparability of data; whereas nonlinearity correction may improve comparison of data from different sources when uncertainties analysis recommended it.

4.3 Nonlinearity effects on PRI

Nonlinearity differently affects each sensor bin, depending on the quantum efficiency and the radiation sampled, and thus, differently affects each one of the bands combined in a spectral index. Moreover, nonlinearity may become critical when retrieving weak signals such as vegetation responses to radiation using optical information (e.g., fluorescence, PRI (Hilker et al. 2008; Meroni et al. 2009)), since part of the detected response may not be physiological but instrumental. PRI, a spectral reflectance index used for the estimation of Light Use Efficiency (LUE), responds to changes of reflectance at 531 nm, which are compared with reflectance at 570 nm, a reference band mainly insensible to LUE control. PRI (and reflectance at 531 nm) decreases when LUE does. However, in our case nonlinearity photoresponse led to PRI decreases when high levels of energy were measured due to instrument-induced increases of reflectance at 570 nm. How the PRI bands are affected by nonlinearity will depend on each sensor and the illumination conditions, but effects will most likely be different for each band of the index. Therefore, nonlinearity could modify estimations of vegetation responses to radiation, since both bias and LUE may be a function of the same variable. Additionally, biases may happen to other narrowband spectral indexes not analyzed in this paper, though the meaning of these biases may also be different. Thus, those automated systems designed to track plant physiology and vegetation responses to radiation should follow the recommendations here, since the provided optical information may potentially be affected by nonlinearity, misleading responses of vegetation to environmental radiation.

5. CONCLUSIONS

This paper emphasizes the importance of performing an exhaustive characterization of field portable spectroradiometers before they are used and the need for applying calibration and maintenance procedures. Linearity of NMOS type sensors can be characterized and data can be corrected in post-process. Uncertainties associated with the correction can be quantified and propagated by nonparametric methods.

Nonlinearity may be a significant problem for spectroradiometers, especially if integration time is manually set or fixed, as well as for those automated systems tracking vegetation responses to environmental radiation. In these cases, we recommend characterizing linearity and correcting data when necessary, and avoid the least linear regions of the dynamic range if possible, adjusting integration time for each measurement to operate always at the same levels of the dynamic range.

ACKNOWLEDGMENTS

The authors would like to thank Dr. M. Rossini from the University of Milano-Bicocca, Milan, Italy, Dr. A. MacArthur from the University of Edinburgh, Edinburgh, U.K., and Dr. K. Anderson from the University of Exeter, Devon, U.K., for their valuable comments relative to the results found. The authors are also very grateful to PP Systems technical staff and Dr. J. Gamon from the University of Alberta, Edmonton, Canada, for their support and feedback provided. They would also like to thank those SpecLab, Cost Action ES0903 EUROSPEC and FSF-NERC colleagues who contributed to the field and laboratory works.

This research has been funded by the BIOSPEC project "Linking spectral information at different spatial scales with biophysical parameters of Mediterranean

vegetation in the context of Global Change" (http://www.lineas.cchs.csic.es/biospec) (CGL2008-02301/CLI, Ministry of Science and Innovation) and the FLUχPEC project "Monitoring changes in water and carbon fluxes from remote and proximal sensing in a Mediterranean "dehesa" ecosystem" (http://www.lineas.cchs.csic.es/fluxpec) (CGL2012-34383, Ministry of Economy and Competitiveness); with the collaboration of the Cost Action ES0903-EUROSPEC. Pacheco-Labrador, J. was sponsored by the JAE-Predoc Fellowship Program (CSIC).

REFERENCES

Anderson, G.M. (1976). Error propagation by the Monte Carlo method in geochemical calculations. *Geochimica et Cosmochimica Acta, 40*, 1533-1538

Anderson, K., Dungan, J.L., & MacArthur, A. (2011). On the reproducibility of field-measured reflectance factors in the context of vegetation studies. *Remote Sensing of Environment, 115*, 1893-1905

Anderson, K., Rossini, M., Pacheco-Labrador, J., Balzarolo, M., Mac Arthur, A., Fava, F., Julitta, T., & Vescovo, L. (2013). Inter-comparison of hemispherical conical reflectance factors (HCRF) measured with four fibre-based spectrometers. *Optics Express, 21*, 13

ASD (1999). *ASD Technical Guide*. Boulder, CO, USA: Analytical Spectral Devices, Inc. (ASD)

Balzarolo, M., Anderson, K., Nichol, C., Rossini, M., Vescovo, L., Arriga, N., Wohlfahrt, G., Calvet, J.-C., Carrara, A., Cerasoli, S., Cogliati, S., Daumard, F., Eklundh, L., Elbers, J.A., Evrendilek, F., Handcock, R.N., Kaduk, J., Klumpp, K., Longdoz, B., Matteucci, G., Meroni, M., Montagnani, L., Ourcival, J.-M., Sánchez-

Cañete, E.P., Pontailler, J.-Y., Juszczak, R., Scholes, B., & Martín, M.P. (2011). Ground-Based Optical Measurements at European Flux Sites: A Review of Methods, Instruments and Current Controversies. *Sensors, 11*, 7954-7981

Bureau International des Poids et Mesures, J.C.f.G.i.M.J. (2008). Evaluation of measurement data - Supplement 1 to the "Guide to the expression of uncertainty in measurement" - Propagation of distributions using a Monte Carlo method. In. Sèvres, France

Cox, M., Harris, P., & Siebert, B.R.L. (2003). Evaluation of Measurement Uncertainty Based on the Propagation of Distributions Using Monte Carlo Simulation. *Measurement Techniques, 46*, 824-833

Gamon, J.A., Cheng, Y., Claudio, H., MacKinney, L., & Sims, D.A. (2006a). A mobile tram system for systematic sampling of ecosystem optical properties. *Remote Sensing of Environment, 103*, 246-254

Gamon, J.A., Peñuelas, J., & Field, C.B. (1992). A narrow-waveband spectral index that tracks diurnal changes in photosynthetic efficiency. *Remote Sensing of Environment, 41*, 35-44

Gamon, J.A., Rahman, A.F., Dungan, J.L., Schildhauer, M., & Huemmrich, K.F. (2006b). Spectral Network (SpecNet)—What is it and why do we need it? *Remote Sensing of Environment, 103*, 227-235

Garbulsky, M.F., Peñuelas, J., Gamon, J., Inoue, Y., & Filella, I. (2011). The photochemical reflectance index (PRI) and the remote sensing of leaf, canopy and ecosystem radiation use efficiencies: A review and meta-analysis. *Remote Sensing of Environment, 115*, 281-297

Hamamatsu (2011a). Characteristic and use of NMOS linear image sensors. Technical Information SD-26. (p. 56): Hamamatsu Photonics, K. K.

Hamamatsu (2011b). Opto-semiconductor handbook. Chapter 02 Si Photodiodes. In, *Opto-semiconductor handbook* (pp. 22-36): Hamamatsu Photonics, K. K.

Hamamatsu (2011c). Opto-semiconductor handbook. Chapter 04 Image Sensors. In, *Opto-semiconductor handbook* (pp. 119-122): Hamamatsu Photonics, K. K.

Herrador, M.Á., Asuero, A.G., & González, A.G. (2005). Estimation of the uncertainty of indirect measurements from the propagation of distributions by using the Monte-Carlo method: An overview. *Chemometrics and Intelligent Laboratory Systems, 79*, 115-122

Hilker, T., Coops, N.C., Nesic, Z., Wulder, M.A., & Black, A.T. (2007). Instrumentation and approach for unattended year round tower based measurements of spectral reflectance. *Computers and Electronics in Agriculture, 56*, 72-84

Hilker, T., Coops, N.C., Wulder, M.A., Black, T.A., & Guy, R.D. (2008). The use of remote sensing in light use efficiency based models of gross primary production: A review of current status and future requirements. *Science of The Total Environment, 404*, 411-423

Hilker, T., Nesic, Z., Coops, N.C., & Lessard, D. (2010). A New, Automated, Multiangular Radiometer Instrument for Tower-Based Observations of Canopy Reflectance (AMSPEC II). *Instrumentation Science & Technology, 38*, 319-340

Hopkinson, G.R., Goodman, T.M., & Prince, S.R. (2004). *A Guide to the Use and Calibration of Detector Array Equipment*: Society of Photo Optical

James, J.F. (2007). *Spectrograph Design Fundamentals*. New York, USA: Cambridge University Press

Janesick, J.R. (2001). *Scientific charge-coupled devices*. Bellingham, USA: Society of Photo-optical Instrumentation Engineers

Jung, A., Götze, C., & Glässer, C. (2012). Overview of Experimental Setups in Spectroscopic Laboratory Measurements - the SpecTour Project. *PFG Photogrammetrie, Fernerkundung, Geoinformation, 2012*, 433-442

Kostkowski, H.J. (1997). *Reliable Spectroradiometry*. La Plata, Md: Spectroradiometry Consulting

Lagarias, J.C., Reeds, J.A., Wright, M.H., & Wright, P.E. (1998). Convergence Properties of the Nelder--Mead Simplex Method in Low Dimensions. *SIAM J. on Optimization, 9*, 112-147

López-Álvarez, M.A., Hernández-Andrés, J., Romero, J., Campos, J., & Pons, A. (2009). Calibrating the elements of a multispectral imaging system. *Journal of Imaging Science and Technology (JIST), 53*

MacArthur, A., MacLellan, C., & Malthus, T.J. (2006). What does a spectroradiometer see? In R.S.a.P. Society (Ed.), *Proceedings of the Remote Sensing and Photogrammetry Society Annual Conference*. University of Cambridge, UK

Markham, B.L., Williams, D.L., Schafer, J.R., Wood, F., & Kim, M.S. (1995). Radiometric characterization of diode-array field spectroradiometers. *Remote Sensing of Environment, 51*, 317-330

Matlab Help (2012). The MathWorks Inc., Natick, MA. Available at: www.mathworks.es/help/techdoc/ref/polyfit.html, last accesed 2012, 27th April.

Meroni, M., Barducci, A., Cogliati, S., Castagnoli, F., Rossini, M., Busetto, L., Migliavacca, M., Cremonese, E., Galvagno, M., Colombo, R., & Di Cella, U.M.

(2011). The hyperspectral irradiometer, a new instrument for long-term and unattended field spectroscopy measurements. *Review of Scientific Instruments, 82*

Meroni, M., Rossini, M., Guanter, L., Alonso, L., Rascher, U., Colombo, R., & Moreno, J. (2009). Remote sensing of solar-induced chlorophyll fluorescence: Review of methods and applications. *Remote Sensing of Environment, 113*, 2037-2051

Milton, E.J., Schaepman, M.E., Anderson, K., Kneubühler, M., & Fox, N. (2009). Progress in field spectroscopy. *Remote Sensing of Environment, 113, Supplement 1*, S92-S109

OceanOptics (2011). SpectraSuite® Spectrometer Operating Software. Installation and Operation Manual. In: Ocean Optics, Dunedin, FL. Available at www.oceanoptics.com/technical/SpectraSuite.pdf, last accesed 2012, 27th April.

OceanOptics (2012). OOINLCorrect Loading Non-Linearity Correction Coefficients Instructions. In: Ocean Optics, Dunedin, FL. Available at www.oceanoptics.com/technical/OOINLCorrect %20Linearity %20Coeff %20Proc.pdf, last accesed 2012, 27th April.

Peñuelas, J., Filella, I., & Gamon, J.A. (1995). Assessment of photosynthetic radiation-use efficiency with spectral reflectance. *New Phytologist, 131*, 291-296

PP Systems (2005). UniSpec-DC Spectral Analysis System. Operator's Manual. Version 2.03.

PP Systems (2012). UniSpec Correction for Non-linearity of Saturated Spectra. Application Note.

Salisbury, J.W. (1998). *Spectral measurements field guide*: Earth Satellite Corporation

Schaepman, M.E., & Dangel, S. (2000). Solid laboratory calibration of a nonimaging spectroradiometer. *Applied Optics, 39*, 3754-3764

Sims, D.A., Luo, H., Hastings, S., Oechel, W.C., Rahman, A.F., & Gamon, J.A. (2006). Parallel adjustments in vegetation greenness and ecosystem CO2 exchange in response to drought in a Southern California chaparral ecosystem. *Remote Sensing of Environment, 103*, 289-303

Smith, R.M. (1998). How Linear Are Typical CCDs? *Experimental Astronomy, 8*, 59-72

Spectra Vista Corporation (2008). GER 1500 User Manual. Revision 3.7. In: Spectra Vista Corporation

Stevens, E.G. (1991). Photoresponse nonlinearity of solid-state image sensors with antiblooming protection. *Electron Devices, IEEE Transactions on, 38*, 299-302

CHAPTER 2

Characterizing Integration Time and Gray-Level-Related Nonlinearities in a NMOS Sensor

---

Published paper: Pacheco-Labrador, J., Ferrero, A., & Martín, M.P. (2014). Characterizing integration time and gray-level-related nonlinearities in a NMOS sensor. *Applied Optics*, 53, 7778-7786.

Javier Pacheco-Labrador[1], and M. Pilar Martín[1]
[1] Environmental Remote Sensing and Spectroscopy Laboratory (SpecLab)
Instituto de Economía, Geografía y Demografía; Consejo Superior de Investigaciones Científica (CSIC)
C/ Albasanz 26-28, 28037 Madrid, Spain
[2] Instituto de Óptica "Daza de Valdés", Consejo Superior de Investigaciones Científicas (CSIC)
C/ Serrano 121, 28006

Received 24 July 2014; revised 17 October 2014; accepted 19 October 2014;posted 21 October 2014
(Doc. ID 217517); published 7 November 2014

ABSTRACT

We report a nonlinearity effect related to the integration time in a double-beam spectroradiometer equipped with two Negative-module Metal–Oxide Semiconductor (NMOS) sensors. This effect can be explained by the addition of photoelectrons produced by the radiant flux on the sensors during the readout phase to the photoelectrons produced during the measurement phase. A new method is proposed to characterize and correct both gray-level and integration-time-related nonlinearities in NMOS sensors. This method is experimentally simple and outperforms other commonly used correction procedures.

Keywords: Radiometry; remote sensing and sensors; photodetectors.

1. INTRODUCTION

Spectroradiometers are used in the field and in the laboratory to measure land surface reflectance factors from spectral radiance measurements, and to collect information about their properties. However, the acquisition of accurate and comparable data is challenging due to both environmental and instrumental issues (Gamon et al. 2010; Milton et al. 2009). Among the latter, nonlinearity features of detectors need to be properly assessed. A radiometric detector is said to be linear if its response -once the dark signal has been subtracted- is proportional to the number of collected photons. Linearity is usually affected by various factors, such as charge leakage during the readout phase (Ferrero et al. 2006), supraresponsivity (Stock 1986), saturation and anti-blooming switches (Stevens 1991) or the electronic transformations required to convert photoelectrons to digital numbers (DN) (Janesick 2001). During the nonlinearity

characterization and correction, the signal generated by the sensor in the absence of light (dark signal) must be subtracted. It must be considered that this dark signal is not constant, but is a function of the temperature (T) and the integration time (t_{int}); this is the time interval during which light reaching the sensor is accumulated and collected to generate the analogic signal (Kuusk 2011).

In the case of the sensors installed in field spectroradiometers, nonlinearity is usually corrected as a function of the gray level measured (OceanOptics 2012; Saber et al. 2011; Schaepman and Dangel 2000), this is the discrete brightness value produced by the analogic-to-digital conversion of the photocurrent generated in a pixel. The photoresponse of these sensors is usually almost linear during most of their dynamic range. However, Pacheco-Labrador and Martin (2014) reported a nonlinear photoresponse larger than that specified by the spectrometer manufacturer in a double-beam field spectroradiometer (Unispec DC, PP Systems, Amesbury, Massachusetts, USA). This response was modeled as a function of the gray level, as is usually done for this type of instrument. Nonetheless subsequent and more extensive repetitions of the calibration experiment revealed the existence of inconsistencies between the modeled photoresponses for the same instrument. Therefore, the existence of other sources of nonlinearity than the gray level was analyzed.

As a result, we propose in this work a methodology to characterize and correct nonlinearities that depend on both the gray level and the integration time referred to hereafter as Gray-Level and Integration Time-related Nonlinearity correction (GLIT-NL). The technique requires the same experimental setup that is needed to implement other usual methods that characterize gray-level dependencies of photoresponse (OceanOptics 2012). Specifically, the GLIT-NL method requires measuring a constant

radiance source with different integration times. Therefore, it could be easily implemented in most spectroscopy laboratories.

2. METHODOLOGY

2.1 Experimental setup

In this work we characterize and correct the nonlinearity of two spectrometers integrated in a Unispec DC double-beam field spectroradiometer. The core of the instrument consists of two MMS-1 modules (Carl Zeiss, Inc., Thornwood, NY, USA), named from now on as "module 1" and "module 2". Each one is equipped with a silicon diode array S8381-256Q NIR-enhanced sensor (Hamamatsu Photonics K.K., Tokyo, Japan). This is a Negative-module Metal-Oxide Semiconductor (NMOS) linear image sensor, with 256 pixels of 25 μm pitch each. The spectral sampling interval is 3.3 nm, the spectral resolution -Full Width at Half Maximum (FWHM)- is less than 10 nm, and it covers a spectral range from 300 to 1,100 nm. The Analog-to-Digital Converter (ADC) has 16 bits of dynamic range. Measured noise floor (at 25 ± 2.5 ºC) and saturation values are 26.7 DN and 65,534.0 DN in module 1, and 28.2 DN and 64,999.0 DN in module 2. Like most of the NMOS sensors, it uses a charge integration method to read out the signal. In this method, the generated charge is temporarily stored in the junction capacitance and each photodiode is sequentially read through an output line. Therefore, unlike Charge Coupled Devices (CCD) sensors, there is no pixel-to-pixel charge transfer, and each pixel is independently read (Hamamatsu 2010, 2011). In the Unispec DC, the fixed readout frequency is about 250 Hz. This instrument does not have shutters to enable the automatic recording of a dark signal; however, it provides temperature readings through a sensor located inside the spectroradiometer.

The nonlinearity characterization experiment was carried out at the Environmental Remote Sensing and Spectroscopy Laboratory (SpecLab), belonging to the Spanish National Research Council (CSIC). The experimental setup was similar to the one described in Pacheco-Labrador and Martin (2014). A 10 W power-stabilized radiance source irradiated an ASD RTS-3ZC integrating sphere (Analytical Spectral Devices Inc., Boulder, Colorado), coated with highly reflective (> 95 %) Zenith Polytetrafluoroethylene (Sphereoptics Hoffman LLC, Contoocook, NH, USA). Two optical fibers, each connected to one of the MMS-1 modules of the Unispec DC were placed so that their fields of view were included within an open port of the integrating sphere. In order to investigate the linearity of each sensor, forty different integration times ranging between 4 and 714 ms were randomly set. Ten spectra were simultaneously acquired with each module for each integration time.

Prior to nonlinearity characterization, the dark signal was measured and modeled as a function of the temperature and the integration time. The ends of the optical fiber cables connected to each module were covered to avoid sampling any radiation. 3,134 dark spectra were acquired at different integration times that ranged between 4 and 1,000 ms. Meanwhile the instrument's temperature was modified between 9.5 and 45.4 ºC using a Raypa DOD-90 drying oven (R. Espinar, Terrasa, Spain).

2.2 Dark signal characterization

A negative relationship of the dark spectra (N_{dark}) with the temperature at low integration times was detected; which could be explained by the presence of an electronic bias (N_{bias}) that decreased linearly with the temperature. This bias was added to the dark signal resulting exclusively from the thermally-generated signal (N_0), which

is proportional to the integration time and also varies with temperature. Consequently, we assumed that the dark signal measured in each pixel (i) is the sum of two contributions, as shown in Eq. (1). The abovementioned N_{dark} measurements were used to estimate the coefficients (a and b) in Eq. (1) by means of a least-square fitting. This way, for each measurement, the expected value of N_{dark} could be predicted as a function of the instrument's integration time and temperature as:

$$N_{\mathrm{dark},i} = N_{\mathrm{bias},i}(T) + N_{0,i}(t_{\mathrm{int}}, T) = \left(b_{0,i} + b_{1,i}T\right) + t_{\mathrm{int}}\left(a_{0,i} + a_{1,i}T + a_{2,i}T^2\right) \quad (1)$$

2.3 Nonlinearity characterization

We define the gray level recorded in each pixel and exclusively linked to the amount of collected electrons as:

$$N_{\mathrm{meas},i} = N_{\mathrm{phot},i} + N_{\mathrm{dark},i} - N_{\mathrm{bias},i} = N_{\mathrm{phot},i} + N_{0,i} \quad (2)$$

where $N_{\mathrm{phot},i}$ is the gray level produced only by the incoming photons falling directly on the pixel, expressed in Digital Numbers (DN). Therefore, the $N_{\mathrm{phot},i}$-to-t_{int} ratio (in DN/ms) must be proportional to the radiance (L), that would be estimated through a radiance calibration factor for each pixel. This factor is not required for the characterization of the nonlinearity, hence we will hereafter refer to the above-mentioned ratio as "instrumental radiance", using the notation $L^*_{\mathrm{phot}} = N_{\mathrm{phot}} / t_{\mathrm{int}}$. Therefore, based on Eq. (2) we obtain:

$$L^{*}_{\mathrm{meas},i} = L^{*}_{\mathrm{phot},i} + L^{*}_{0,i} \tag{3}$$

where $L^{*}_{\mathrm{phot},i}$ is proportional to the radiance over the pixel and L^{*}_{0} (N_0/t_{int}) is proportional to the thermally-generated signal and does not represent radiance. See Table 1 for a complete definitions of the variables used.

As described in 2.1, in order to characterize the nonlinearity we varied the integration time of the measurements keeping constant the power of the radiance source; this way a perfectly linear sensor would produce a constant $L^{*}_{\mathrm{phot},i}$ in each pixel. Nonlinearity in the sensors used in field spectroradiometers is usually related with the gray level measured (Hamamatsu 2011; OceanOptics 2012). To analyze this relationship, we computed a value L^{*}_{norm} for each pixel as the ratio of L^{*}_{meas} to a reference L^{*}_{meas} spectrum acquired with an intermediate integration time of 431 ms. Notice that in OceanOptics (2012) this responsivity is calculated dividing $L^{*}_{\mathrm{meas},i}$ by the maximum value of $L^{*}_{\mathrm{meas},i}$ instead.

Table 1. Variables and functions definition

Variables and functions definition	Symbol	Units
Pixel	i	-
Temperature	T	ºC
Integration time	t_{int}	ms
Dark signal	N_{dark}	DN
Electronic bias signal	N_0	DN
Thermally-generated signal	N_{bias}	DN
Measured signal	N_{meas}	DN
Photo-generated signal	N_{phot}	DN
Radiance	L	W m^{-2} sr^{-1}
Measured "instrumental radiance"	L^*_{meas}	DN/ms
Photo-generated "instrumental radiance"	L^*_{phot}	DN/ms or DN/(cd m^{-2})
Thermally-generated "instrumental radiance" (does not represent radiance)	L^*_0	DN/ms
Normalized "instrumental radiance"	L^*_{norm}	-
Nonlinearity correction function related to the integration time	$\mathfrak{R}_{\mathrm{IT}}(t_{\mathrm{int}})$	-
Nonlinearity correction function related to the gray level	$\mathfrak{R}_{\mathrm{GL}}(N_{\mathrm{meas}})$	-
Residuals from the $\mathfrak{R}_{\mathrm{IT}}$ fitting	ε	DN/ms
Leakage factor	B	ms
Gray level corrected measured "instrumental radiance"	$L^*_{\mathrm{measGLcor}}$	DN/ms
Corrected photo-generated "instrumental radiance"	L^*_{cor}	DN/ms

Figure 1 shows L^*_{norm} vs. N_{meas} for all the pixels of module 2 located between positions 32 and 202, where noise is low. For each particular pixel, the trail of related points represents the different acquisitions, where the integration time ranges between 4 ms and 741 ms. As expected, the responsivity decreases at the highest gray levels

(Hamamatsu 2011; OceanOptics 2012). However in those pixels irradiated by a high radiant flux, such as pixel 128, its behavior is completely different than in those pixels irradiated by a low radiant flux, such as pixel 32. On one hand, in pixel 128 L^*_{norm} seems to be hyperbolically related with the integration time. On the other hand, in pixel 32 any fitting that took into account the different error bars would led to an almost constant L^*_{norm} curve within the whole integration time range.

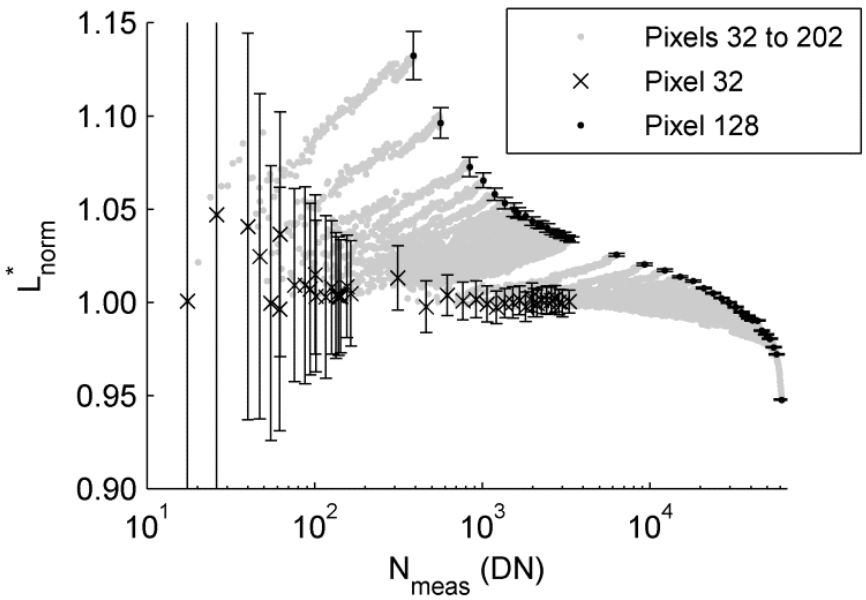

Figure 1. Normalized L^*_{norm} vs. N_{meas} in pixels 32 to 202 of MMS-1 module 2. Data corresponding to pixels 32 and 128 have been highlighted. The error bars represent the 95 % confidence interval.

A relationship between responsivity and the integration time had been previously reported (Ferrero et al. 2006) in CCD detectors. Since light is not blocked during the readout phase, the phenomenon could be explained by the leakage of a significant amount of electrons during this phase due to pixel irradiation. In that case,

the effects on responsivity would be larger the more similar the readout and the integration times are.

Since all the measurements were affected to some degree by both types of nonlinearity, the residuals (ε) from fitting of $\mathfrak{R}_{\mathrm{IT}}$ were assumed to be related with $\mathfrak{R}_{\mathrm{GL}}$. This way, both functions could be fit. To characterize $\mathfrak{R}_{\mathrm{IT}}$ two parameters were fit for each pixel: A, which represents the L^*_{meas} that the measurements should ideally yield; and B, which is related to the readout time and the leakage effect and encompasses the dependence of $\mathfrak{R}_{\mathrm{IT}}$ on the integration time:

$$L^*_{\mathrm{meas},i} = A_i \mathfrak{R}_{IT}(t_{\mathrm{int}}) + \varepsilon_i(N_{\mathrm{meas},i}) = A_i\left(1 + \frac{B_i}{t_{\mathrm{int}}}\right) + \varepsilon_i(N_{\mathrm{meas},i}) \tag{4}$$

where

$$\mathfrak{R}_{IT} = 1 + \frac{B_i}{t_{\mathrm{int}}} \tag{5}$$

After a first estimation of A and B, the residuals $\varepsilon_i(N_{\mathrm{meas},i})$ were obtained. By considering that they carry all the information about the nonlinearity respect to $N_{\mathrm{meas},i}$, they allow $\mathfrak{R}_{\mathrm{GL}}$ function to be expressed as the ratio between a nonlinear function ($L^*_{\mathrm{meas},i}$) and a linear function ($L^*_{\mathrm{meas},i}$ - $\varepsilon_{,i}$) respect to $N_{\mathrm{meas},i}$:

$$\mathfrak{R}_{GL}(N_{\mathrm{meas}}) = \frac{L^*_{\mathrm{meas},i}}{L^*_{\mathrm{meas},i} - \varepsilon_i(N_{\mathrm{meas},i})} = \frac{N_{\mathrm{meas},i}}{N_{\mathrm{meas},i} - \varepsilon_i(N_{\mathrm{meas},i})t_{\mathrm{int}}} \tag{6}$$

and a polynomial function was fit to it.

Then, $N_{\text{meas},i}$ was corrected using the function $\mathfrak{R}_{\text{GL}}$:

$$L^{*}{}_{\text{measGLcor},i} = \frac{N_{\text{meas},i}}{\mathfrak{R}_{GL}(N_{\text{meas}})t_{\text{int}}} \tag{7}$$

and both functions were fit again using the gray-level-corrected "instrumental radiance" $L^{*}{}_{\text{measGLcor},i}$ in the place of $L^{*}{}_{\text{meas},i}$ in Eq. (4). The errors from the second fit were added to the ones previously got and used both to calculate $\mathfrak{R}_{\text{GL}}$ by Eq. (6).

Figure 2 shows the fit of $\mathfrak{R}_{\text{IT}}$ in the pixel 128 of the module 2; the "instrumental radiance" is plotted against the integration time. As can be seen, data initially cannot fit the hyperbolic model, especially those corresponding to the largest gray levels. However, the accuracy of the fit improved when the $\mathfrak{R}_{\text{GL}}$ correction function is applied.

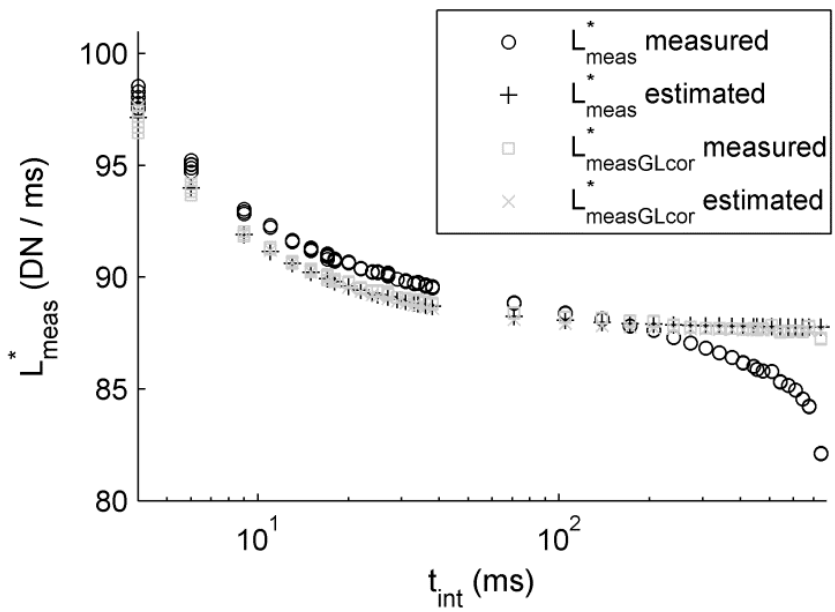

Figure 2. L^{*}_{meas} vs. integration time (t_{int}) during the simultaneous fit of parameters A and B in the pixel 128 of module 2 before and after $\mathfrak{R}_{\text{GL}}$ correction is applied.

Once fit the two nonlinearity correction functions it was observed that the magnitude of the leakage charge, represented by B, was not independent of the pixel position. That is because every pixel is irradiated at different level and it was obtained that B was tightly linked to the gray-level-corrected "instrumental radiance" calculated from Eq. (7), which suggests that the observed leakage depends on the irradiance striking the pixel. Therefore, B was not used as a constant coefficient associated to each pixel, but modeled as a function of the measured $L^*_{\mathrm{measGLcor},i}$. A single model was adjusted for each module using data from all the pixels to estimate coefficients C and D:

$$B = C - \frac{D}{L^*_{\mathrm{measGLcor}}} \log\left(1 + \frac{L^*_{\mathrm{measGLcor}}}{D}\right) \tag{8}$$

Prior to the fitting, those data that showed the highest noise levels were discarded. After characterizing the responsivity of each spectrometer module; the correction of nonlinearity can be accomplished as:

$$L^*_{\mathrm{cor},i} = \frac{L^*_{\mathrm{meas},i}}{\Re_{GL}(N_{\mathrm{meas},i})\Re_{IT}(t_{\mathrm{int}})} - L^*_{0,i} = \frac{L^*_{\mathrm{phot},i} + L^*_{0,i}}{\Re_{GL}(N_{\mathrm{meas},i})\Re_{IT}(t_{\mathrm{int}})} - L^*_{0,i} \tag{9}$$

Here it has been assumed that the nonlinear correction does not have a significant impact on L^*_0, therefore the same value has been used for both the corrected and the non-corrected dark signals.

2.4 Validation

In a pixel with a perfectly linear responsivity, $N_{\text{phot},i}$ is a linear function of the number of photons impinging on the pixel during the collection phase. This way, the rate of the gray level measured to any variable that modifies the amount of collected photons, e.g. integration time or radiant flux, would be constant. For this reason, in order to validate the GLIT-NL correction model, we assessed its ability to reduce the variability of this ratio, represented by $L^*_{\text{meas},i}$. On one hand, we used different integration times under a constant radiance; on the other, we also used a constant integration time under different radiance levels. In this second case, $L^*_{\text{meas},i}$ was calculated as the ratio of $N_{\text{phot},i}$ to the corresponding luminance value set in the light source (Table 2).

Table 2. Validation Scheme Summary

Tested datasets			
Dataset	Radiance Source	Modified variable	
GLIT-NL experiment	10 W tungsten bulb	Integration time	
FSF Inter-comparison	Hoffman Engineering LS-65-8D (Tungsten) Luminance/radiance standard source	Radiance	
Ocean Optics Lamp	Mercury-argon calibration source	Integration time	
Correction models compared			
Model	Calibration dataset	tint range (ms)	Correction functions
GLIT-NL	GLIT-NL experiment	4 - 741	$\mathfrak{R}$IT, $\mathfrak{R}$GL
OOLIT	GLIT-NL experiment	4 - 741	$\mathfrak{R}$GL
OOHIT	Pacheco-Labrador and Martin (2014)	50 - 1350	$\mathfrak{R}$GL

The performance of the GLIT-NL method was compared with the nonlinearity correction method commonly applied to field spectroradiometers and proposed by OceanOptics (OOINL) (OceanOptics 2012). This method only takes $\mathfrak{R}_{GL}$ into account. Moreover, in order to assess the impact of the integration-time-related nonlinearities on this method, we determined two different $\mathfrak{R}_{GL}$ correction functions, each based on a different experimental dataset (Table 2). The first correction function, from now on called Ocean Optics correction using High Integration Times (OOHIT), was established by using spectra that had been acquired with integration times much larger than the readout time of the sensors. OOHIT was calibrated in a previous work (Pacheco-Labrador and Martin 2014) using the same experimental setup and instrumentation; the minimum integration time was 50 ms. A second correction model, Ocean Optics correction using Low Integration Times (OOLIT), was established by applying the OOINL method to the data acquired for the GLIT-NL calibration dataset. In this case, the minimum integration time was 4 ms and data had to be smoothed using RLOWESS (Cleveland 1979) prior to the model fit.

The three models GLIT-NL, OOHIT and OOLIT were used to correct three different datasets. Firstly, the correction model was applied to the same data used for characterization of GLIT-NL, previously described. Secondly, the correction was applied to spectra acquired with the Unispec DC from a Hoffman Engineering LS-65-8D Luminance/radiance standard source at the NERC Field Spectroscopy Facility, University of Edinburgh. In this experiment, the integration time was kept constant at 122 ms, and the power of the radiance source was changed between 171.3 cd/m^2 and 3426.2 cd/m^2. In this case L^*_{meas} was calculated as the ratio of $N_{phot,i}$ to the corresponding luminance set in the light source. This way, the possible effect of

supraresponsivity (Ferrero et al. 2005), not directly considered in the GLIT-NL model, was at least partly assessed. Additionally, corrections were also applied to a set of narrow-band spectra that were acquired using a mercury-argon calibration source (Ocean Optics, Dunedin, FL, USA) with different low integration times: 4 ms, 6 ms and 7 ms, to avoid saturation. The models that describe $\mathfrak{R}_{GL}$, Eq. (6), and B, Eq. (8), rely on the assumption that the behavior of all the pixels is the same, though differences could exist. Since the emission spectra of the mercury-argon lamp and of the tungsten lamps used in the other experiments are very different, this allowed testing if this assumption could be accepted.

3. RESULTS

3.1 Dark signal characterization

A dark signal model was fit for each pixel. For the pixels in modules 1 and 2 the coefficients of determination (R^2) were 0.995 and 0.994 respectively. Relative Root Mean Squared Error (RRMSE) was 2.83 % in module 1 and 2.53 % in module 2. Figure 3 shows the different models for a single pixel belonging to module 2. The predicted bias and dark signal (a) and the dark readings (b) are depicted as a function of the integration time for three different temperatures. As can be observed from the figure, the bias decreases with the temperature and is usually larger than N_0. The dark signal ($N_{bias} + N_0$) increases with the integration time and also (and to a larger extent) with the temperature.

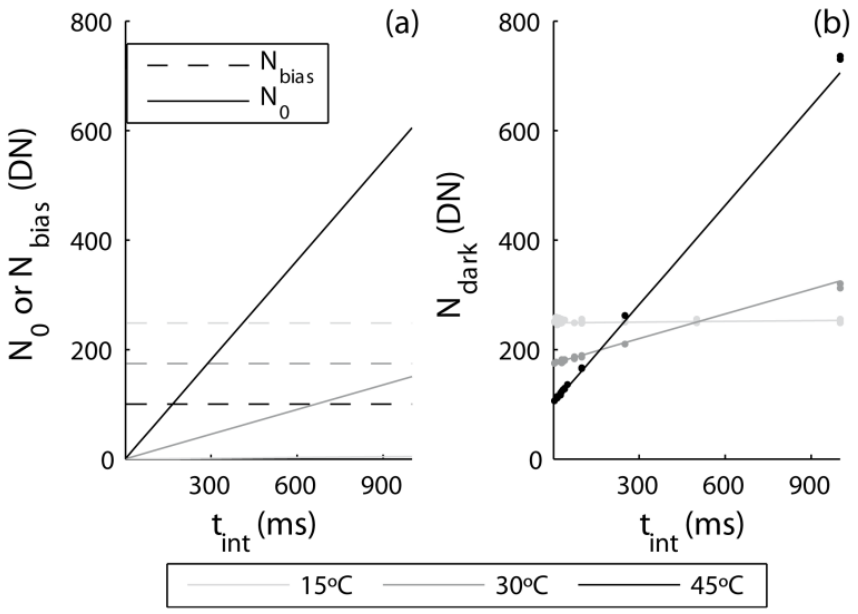

Figure 3. (a) Predicted dark current and electronic bias and (b) predicted and measured total dark signal versus integration time at different temperatures. Modeled data are depicted with lines, and measurements with dots. The simulations correspond to pixel 128 of module 2.

3.2 Nonlinearity

The spectra acquired for the nonlinearity characterization practically covered the dynamic range of the spectroradiometers. Maximum N_{meas} values were located at pixel 126 in module 1 and at pixel 128 in module 2. For the rest of the pixels, gray levels decreased towards the sensor's ends to almost dark signal values. The function $\mathfrak{R}_{GL}$ characterized from the residuals in the fit of the $\mathfrak{R}_{IT}$ correction function. For $\mathfrak{R}_{GL}$, the RRMSEs of the fit were 0.30 % and 0.40 % in modules 1 and 2, respectively. Figure 4 shows $\mathfrak{R}_{GL}$ fitted in module 2 vs. N_{meas}, for both the GLIT-NL curve and measured data. Moreover, the data and the curves of the models OOHIT and OOLIT are also shown. The three curves decrease slowly across most of the dynamic range and then experience

a sudden drop at its upper end. The responsivities estimated by the OOHIT and the OOLIT models are lower than that predicted by GLIT-NL. Moreover, OOLIT predicts a sudden initial drop of $\mathfrak{R}_{GL}$ at the lower end of the radiometric range. This results in OOLIT yielding lower values than the other two functions throughout the radiometric range under study.

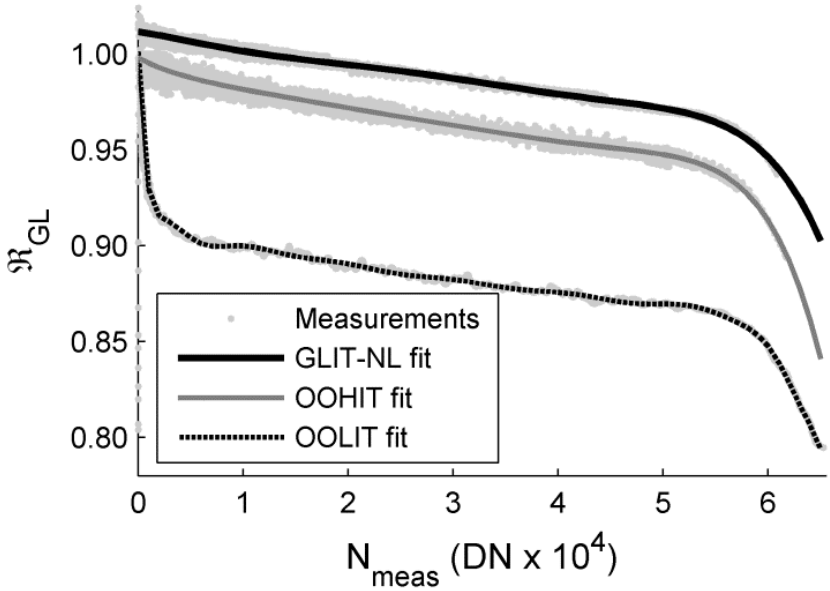

Figure 4. $\mathfrak{R}_{GL}$ correction functions in module 2, computed using three different methods

The fit of the function $\mathfrak{R}_{IT}$ was initially affected by the nonlinearity related to the gray level. However, the $\mathfrak{R}_{GL}$ correction led to an increase of the fitting accuracy and eventually the mean RRMSE was as low as 0.32 % and 0.39 % in modules 1 and 2, respectively. Figure 5a shows parameter *B* vs. the pixel position in the spectrometer of module 2. Negative values are seen in both ends of the array, where the signal is too noisy to enable a reliable fitting. Figure 5b shows the relationship between *B* and

$L^*_{\text{measGLcor}}$. B grows rapidly at first and then levels off to become asymptotic to a saturation level. RRMSEs were 8.98 % and 9.37 % in modules 1 and 2, respectively.

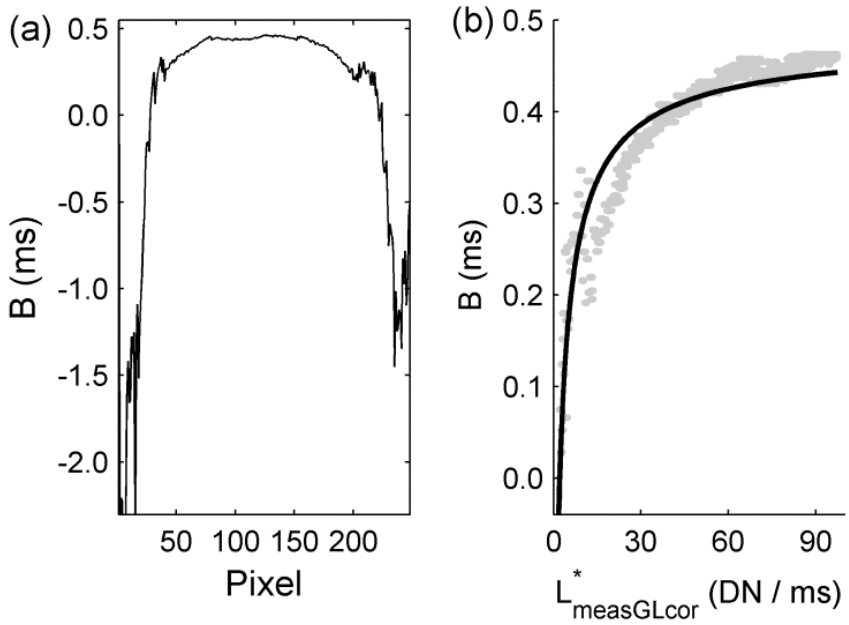

Figure 5. Estimated B for each pixel in module 2 (a) and B modeled as a function of $L^*_{\text{measGLcor}}$ (b) in module 2

3.3 Validation

Figure 6 (left column) shows $L^*_{\text{phot},i}$ spectra corresponding to the three validation datasets in module 2 (Table 2). An assessment of the performance of the three different methods is included in the same figure (right column). Figures 6a and 6b show the same data used for the GLIT-NL calibration, Figures 6c and 6d correspond to the spectra acquired with a fixed integration time and varying light source's luminance -notice that $L^*_{\text{phot},i}$ is in DN cd^{-1} m^2-, and Figures 6e and 6f show the mercury-argon lamp spectra for three different integration times. Figures 6a, 6c and 6e depict $L^*_{\text{phot},i}$ spectra both with and without GLIT-NL correction.

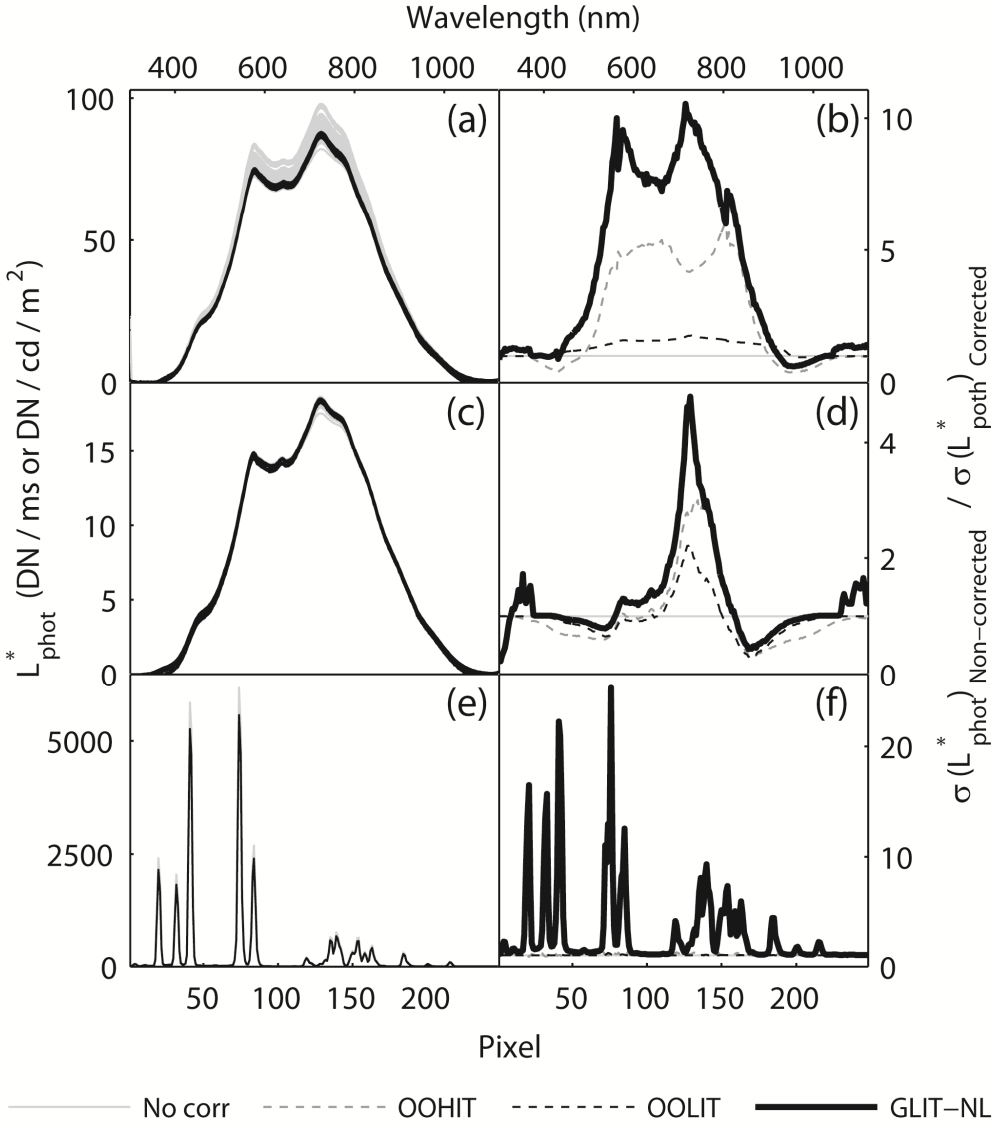

Figure 6. Left: $L^*_{phot,i}$ spectra with and without GLIT-NL correction for the different validation datasets: (a) calibration, (c) FSF-NERC lamp, and (e) mercury-argon lamp. $L^*_{phot,i}$ is given in DN/ms in (a) and (e) and in DN cd^{-1} m^2 in (c). Right: The curves represent, for each pixel, the ratio between the standard deviation of the non-corrected data and the standard deviation of the data that has been corrected with OOHIT, OOLIT or GLIT-NL. (b) corresponds to the calibration dataset, (e) to the FSF-NERC lamp, and (d) to the mercury-argon lamp.

Similarly, Figures 6b, 6d and 6f show, for these $L^*_{\text{phot},i}$, the ratio of the non-corrected to the corrected standard deviations for each pixel. This ratio is a good indicator of the improvement achieved by the correction carried out with the GLIT-NL, OOLIT and OOHIT models, respectively. As can be inferred from the figure, the GLIT-NL method significantly reduces $L^*_{\text{phot},i}$ variation in each pixel, and this effect is observed for the different datasets. The comparison between GLIT-NL and the models that only characterize $\mathfrak{R}_{\text{GL}}$ reveals that the former achieves a better correction of the nonlinearities, both using the calibration dataset (Figure 6b) and also with independent data (Figures 6d and 6f). The standard deviation of $L^*_{\text{phot},i}$ was reduced in each validation up to 10.54, 4.78 and 25.35 times (Figures 6b, 6d and 6f, respectively) by the GLIT-NL correction; whereas the maximum drop amounted to only 6.27, 2.99 and 1.29 times, respectively, with OOHIT and to 1.76, 2.23 and 1.23 times when using OOLIT.

4. DISCUSSION

In this work, we analyzed the nonlinearity in two NMOS sensors integrated in a Unispec DC spectroradiometer. The dependence of responsivity on gray level is usually characterized and corrected in the sensors integrated in field spectroradiometers. Nonetheless, results proved that responsivity was also affected by the integration time set. This phenomenon had been previously reported in CCD imager sensor (Ferrero et al. 2006). In both cases, it was concluded that the phenomenon was due to the leakage of photo-generated electrons in the photodiode during the readout phase; these electrons would be added to those generated during the integration time. However, a full characterization was not possible in (Ferrero et al. 2006) because the effect was dependent on three factors: (1) the radiant power's spectral distribution; (2) the lens'

numerical aperture -due to the variation of the inclination distribution of the rays- and (3) the pixel-to-pixel charge transfer along the sensor columns. The first two factors would influence the geometry of the irradiation and absorption on each pixel (i.e., the pixel region that is irradiated) and, therefore, would affect the distribution of the photo-generated electrons in the detector bulk. The third factor would not allow the leakage effect to be characterized in each individual pixel. On the contrary, the NMOS sensors characterized in this work presented certain features that allowed the characterization of the dependency of responsivity on both, the gray level and the integration time: (1) each pixel is irradiated by a narrow spectral band (2) the spectrometer's slits and entrances would produce a constant numerical aperture, and (3) no charge is transferred across neighboring pixels because it is read out separately from each individual pixel. The two first factors would produce a constant angular distribution of radiation on the sensor, so that changes in the irradiated area would be minimal. Irradiation geometry could still be affected by the temperature due to spectral calibration dependencies (Maleki and Petersen 1997), and by sharp changes in the radiant power's spectral distribution with each pixel waveband. However, these changes could be considered negligible due the spectral features of the sensors characterized. The third factor makes possible the characterization of the pixels on an individual basis, since the number of photoelectrons is not influenced by the number of photoelectrons of adjacent pixels.

Though the two first factors are common to the most of the linear sensors usually integrated in field spectroradiometers, the third is not usually applicable since these are most frequently CCDs. Therefore, the characterization and correction proposed in this work could not be extended to these sensors. Nonetheless, the understanding of the phenomenon is still valuable and its presence should be kept in

mind. As shown, this type of nonlinearity goes unnoticed unless very low integration times, close to the readout time of the sensor, are used in the nonlinearity characterization. Moreover, the responsivity of a large number of pixels must be studied across the sensor array. Thus, this effect is unlikely to be detected by the commonly applied OOINL algorithm (OceanOptics 2012), which only includes 9 pixels in its nonlinearity characterization procedure. Such small sample could lead to confound $\mathfrak{R}_{IT}$ with noise in those pixels with low gray level. On the contrary, when a large number of pixels is used to characterize nonlinearity, as it was the case in the present study, different pixel-position-related trends can be observed, revealing that this nonlinearity is not simply noise or sensor unevenness, but a systematic effect (Figure 4).

This phenomenon had not been observed in previous nonlinearity characterization experiments carried out in the laboratory because low irradiance levels and typically large integration times had been used. Though the influence of the integration time on the nonlinearity of the sensor can be unnoticed, it still can influence the characterization of the gray-level-related nonlinearity, as happened in Pacheco-Labrador and Martin (2014). As shown in Figure 4, when this factor is not accounted for, the dependency of responsivity on the gray level is overestimated. This could be explained because, in the OOINL method, responsivity values are calculated by normalizing the L^*_{phot} to each pixel's maximum L^*_{phot}, while $\mathfrak{R}_{IT}$ induces an increase of L^*_{phot} for low integration times (Figure 2). As expected, the overestimation of the effects of nonlinearity related with the gray level was more pronounced in the OOLIT than in the OOHIT model (Pacheco-Labrador and Martin 2014), which is consistent with the hyperbolic dependence of $\mathfrak{R}_{IT}$ on the integration time.

In the Unispec DC, the integration time can be set between 4 and 4,000 ms, whereas the sensor's readout time ranges between 2.5 and 3.5 ms (PPSystems 2013). Even though it is in fact lower since it has to be divided by the number of pixels in the sensor, -ranging then between 9.8 ns and 13.7 ns in each pixel-, this readout time is large enough to induce a significant nonlinearity in the measurements. In other commercially available field spectroradiometers the integration time can also be set to be close to the readout time (OceanOptics 1996, 2001), which can lead users to include this bias effect in the measurements without being aware of it.

The GLIT-NL method characterizes the function $\mathfrak{R}_{GL}$ from the residuals in the fit of $\mathfrak{R}_{IT}$. This is possible since these residuals are mainly produced by the dependency of responsivity on the gray level. However, like others methods (OceanOptics 2012; Pacheco-Labrador and Martin 2014), the GLIT-NL assumes that the response of all the pixels of a sensor is the same. This would introduce some uncertainty in the correction procedure; however, validation shows that the differences between pixels are less relevant than the corrected nonlinearities. Other works have also reported nonlinearities independent of the wavelength in photodiode arrays (Saber et al. 2011). The calibration of a model for each sensor pixel would require that the full dynamic range was completely covered for all the pixels during the characterization experiment. Though GLIT-NL does not characterize each pixel separately, this method is experimentally affordable and easy to implement in most spectroscopy laboratories.

In the GLIT-NL model, B represents the pixel's charge leakage rate between the detection and the register phases multiplied by the readout time. Results suggest that B varies with the radiant flux impinging on each pixel, reaching a saturation level above a given radiant flux level, as if the charge leakage rate would depend on the

photoelectrons generated during the readout rate until a given density of electrons is reached. For this reason, a saturation function was chosen to characterize the relationship between *B* and the "instrumental radiance" Eq. (8).

Since the characterization method is based on the residuals of one of the models fit, a robust validation scheme has been proposed to demonstrate that this is not just a way of improving the fit of experimental data. Therefore, the performance of the GLIT-NL method has been tested with datasets of different characteristics: On one hand, we used the data acquired for the characterization of the nonlinearities; on the other, we also used independent data acquired using a different methodology or from a radiance source with a very different emission spectrum curve (Table 2). In all the cases, the performance of GLIT-NL method has been compared with other correction models. The method proposed in this work outperformed those methods that only correct for $\mathfrak{R}_{GL}$. As show in Figure 6, validation was carried out using different radiance levels, the highest levels being reached with the mercury-argon lamp. It is worth pointing out that this is not a trivial issue, since radiance level determines the integration time to be selected and the value of *B*, but the radiance levels found in the field and in the laboratory can differ significantly. For instance, the maximum "instrumental radiance" levels reached by the tungsten lamps in the experiments described ranged between 60 DN/ms and 100 DN/ms, whereas in the case of the mercury-argon lamp they exceeded 5,000 DN/ms. Field measurements acquired under solar irradiance during a Summer clear-sky day can reach maxima L^*_{meas} between 1,000 DN/ms and 3,000 DN/ms with integration times between 19 ms and 39 ms. These low integration times and high radiance levels could potentially induce significant deviations in the acquired spectra. Therefore, as shown in the validation, methods that only account for $\mathfrak{R}_{GL}$ may not always be successful at

correcting nonlinearities in field measurements. GLIT-NL does not correct for supraresponsivity, which depends on the factor $(N\text{-}N_0)\times t_{\text{int}}$ (related with irradiance), since this effect did not become evident for the range tested with our spectroradiometer, but a very similar methodology may be developed if required.

Several approaches have been used to characterize nonlinearity in radiometric instrumentation. Usually, the response to different irradiance levels have been characterized using methods based on the superposition of sources, but also others (Saber et al. 2011; Schaepman and Dangel 2000). In the case of field spectroradiometers, different integration times are frequently used to achieve a range of signal that allows the characterization (OceanOptics 2012; Pacheco-Labrador and Martin 2014). In these cases, results show a decrease of linearity as the signal gets close to saturation, due to different reasons (ADC, supraresponsivity…) (1993). However, the impact of the integration time has not been so usually analyzed. Saber et al. (2011) also found a decrease of linearity at larger integration times, which was interpreted as a loss of photoelectrons during the storage of the charge.

The Unispec DC and other field spectroradiometers are frequently used to measure reflectance factors and sometimes also radiances. Reflectance factors are obtained as the ratio of two measurements over the same pixel. This means that nonlinearities could mutually cancel out if they were of similar magnitude in each pixel. However, in some cases, the signal differences between the down-welling irradiance (using reference panels and/or cosine receptors) and the up-welling radiance (which is a function of the down-welling irradiance and the fraction of it reflected by the measured target), could lead to different nonlinearity magnitudes that would not cancel out during the calculation of reflectance factors. As discussed in a previous work (Pacheco-

Labrador and Martin 2014), nonlinearities could play an especially relevant role in certain applications where both, the nonlinearities and the variable of interest, depend on the irradiance level. In the context of remote and proximal sensing, examples include the quantification of radiance; the study of short-term vegetation stress by measuring slight reflectance changes related to the Xanthophyll cycle (Gamon et al. 1992) and sun-induced fluorescence (Meroni et al. 2009); or the characterization of the bidirectional reflectance distribution function. In all these cases the measured radiance would determine the integration time to be selected and the gray level of each pixel -and, therefore, its nonlinearity. However, the integration time and the gray level would be also related to down-welling irradiance, illumination and observation angles and possibly to the vegetation physiology as well.

5. CONCLUSIONS

The GLIT-NL method is proposed to characterize nonlinearities related with the gray level and the integration time in NMOS sensors integrated in MMS-1 spectrometers of a Unispec DC spectroradiometer. The method has been robustly validated, and it has been proved that linearity is better achieved when the dependencies on the integration time are characterized and corrected. The source of this nonlinearity is the addition of spurious electrons due to pixel irradiation during the readout phase. Therefore, it could potentially affect other sensors not tested here, as in Ferrero et al. (2006). Pixel-to-pixel charge transfer in CCD sensors makes the application of this method impossible; however, users still should be aware of the phenomenon and avoid the use of integration times that are close to the sensor's readout time. GLIT-NL improves the instrumentation performance under large irradiance levels, when

integration times close to the readout time must be set to avoid saturation. These conditions can be found both outdoors and in the laboratory. Therefore, the quantification of radiometric variables, the measurement of reflectance factors, and the characterization of sensors could potentially be improved by this method. The present work's findings stress the need to match the radiance levels used for field spectroradiometers' characterization with those later found outdoors, so as to obtain reliable field measurements.

ACKNOWLEDGMENTS

We would like to acknowledge PP Systems' technical staff for their support and the information they provided us with regarding Unispec DC. The authors are also very grateful to Mr. Tommaso Julitta (University of Milano-Bicocca), Dr. Alasdair MacArthur (FSF-NERC, University of Edinburgh), Mr. Chris MacLellan (FSF-NERC, University of Edinburgh), and all the Cost Action ES0903-EUROSPEC and FSF-NERC colleagues that participate in the experiments carried out at the FSF-NERC (Edinburgh). We also thank Dr. Joaquín Campos and Dr. Alicia Pons from the "Daza de Valdés" Optics Institute (CSIC, Spain) for their valuable advice. Finally, we would like to acknowledge the contribution of those SpecLab colleagues who participated in the laboratory works.

This research has been funded by the BIOSPEC project "Linking spectral information at different spatial scales with biophysical parameters of Mediterranean vegetation in the context of Global Change" (http://www.lineas.cchs.csic.es/biospec) (CGL2008-02301/CLI, Ministry of Science and Innovation) and the FLUχPEC project "Monitoring changes in water and carbon fluxes from remote and proximal sensing in a

Mediterranean "dehesa" ecosystem" (http://www.lineas.cchs.csic.es/fluxpec) (CGL2012-34383, Ministry of Economy and Competitiveness). Pacheco-Labrador, J. was sponsored by the CSIC JAE-Predoc Fellowship Program (BOE 185-14853), which is co-funded by the European Social Fund.

REFERENCES

Boivin, L.P. (1993). Automated Absolute and Relative Spectral Linearity Measurements on Photovoltaic Detectors. *Metrologia, 30*, 355–360

Cleveland, W.S. (1979). Robust Locally Weighted Regression and Smoothing Scatterplots. *Journal of the American Statistical Association, 74*, 829-836

Ferrero, A., Campos, J., & Pons, A. (2006). Apparent violation of the radiant exposure reciprocity law in interline CCDs. *Applied Optics, 45*, 3991-3997

Ferrero, A., Campos, J., Pons, A., & Corrons, A. (2005). New model for the internal quantum efficiency of photodiodes based on photocurrent analysis. *Applied Optics, 44*, 208-216

Gamon, J.A., Coburn, C., Flanagan, L.B., Huemmrich, K.F., Kiddle, C., Sanchez-Azofeifa, G.A., Thayer, D.R., Vescovo, L., Gianelle, D., Sims, D.A., Rahman, A.F., & Pastorello, G.Z. (2010). SpecNet revisited: bridging flux and remote sensing communities. *Canadian Journal of Remote Sensing, 36*, S376-S390

Gamon, J.A., Peñuelas, J., & Field, C.B. (1992). A narrow-waveband spectral index that tracks diurnal changes in photosynthetic efficiency. *Remote Sensing of Environment, 41*, 35-44

Hamamatsu (2010). NMOS linear image sensor S8380/S8381 series. NMOS linear image sensors with IR sensitivity. In K.K. Hamamatsu Photonics (Ed.). Hamamatsu City, Japan: Hamamatsu Photonics, K. K.

Hamamatsu (2011). Characteristic and use of NMOS linear image sensors. Technical Information SD-26. (p. 56). Hamamatsu City, Japan: Hamamatsu Photonics, K. K.

Janesick, J.R. (2001). Chapter 6. Charge Measurement. *Scientific charge-coupled devices* (pp. 516-519). Bellingham, USA: Society of Photo-optical Instrumentation Engineers

Kuusk, J. (2011). Dark Signal Temperature Dependence Correction Method for Miniature Spectrometer Modules. *Journal of Sensors, 2011*

Maleki, M., & Petersen, J.C. (1997). Wavelength calibration of a fiber-optical spectrum analyzer: temperature dependence. *Applied Optics, 36*, 4451-4455

Meroni, M., Rossini, M., Guanter, L., Alonso, L., Rascher, U., Colombo, R., & Moreno, J. (2009). Remote sensing of solar-induced chlorophyll fluorescence: Review of methods and applications. *Remote Sensing of Environment, 113*, 2037-2051

Milton, E.J., Schaepman, M.E., Anderson, K., Kneubühler, M., & Fox, N. (2009). Progress in field spectroscopy. *Remote Sensing of Environment, 113, Supplement 1*, S92-S109

OceanOptics (1996). 2048-pixel CCD Linear Image Sensor (B/W). In. Tokyo, Japan: Sony

OceanOptics (2001). TOSHIBA CCD LINEAR IMAGE SENSOR CCD(Charge Coupled Device) TCD1304AP. In. Tokyo, Japan: Toshiba

OceanOptics (2012). OOINLCorrect Loading Non-Linearity Correction Coefficients Instructions. In O.O. Inc (Ed.) (p. 6). Dunedin, Florida, USA: Ocean Optics Inc

Pacheco-Labrador, J., & Martin, M.P. (2014). Nonlinear Response in a Field Portable Spectroradiometer: Characterization and Effects on Output Reflectance. *Geoscience and Remote Sensing, IEEE Transactions on, 52*, 920-928

PPSystems (2013). Personal communication. In. Amesbury, MA, USA

Saber, G.R.S., Fox, N.P., Theocharous, E., Sun, T., & Grattan, K.T.V. (2011). Temperature and nonlinearity corrections for a photodiode array spectrometer used in the field. *Applied Optics, 50*, 866-875

Schaepman, M.E., & Dangel, S. (2000). Solid laboratory calibration of a nonimaging spectroradiometer. *Applied Optics, 39*, 3754-3764

Stevens, E.G. (1991). Photoresponse nonlinearity of solid-state image sensors with antiblooming protection. *Electron Devices, IEEE Transactions on, 38*, 299-302

Stock, K.D. (1986). Si-photodiode spectral nonlinearity in the infrared. *Applied Optics, 25*, 830-832

CHAPTER 3

Characterization of a Field Spectroradiometer for Unattended Vegetation Monitoring. Key Sensor Models and Impacts on Reflectance

---

Published paper: Pacheco-Labrador, J., & Martín, M. (2015). Characterization of a Field Spectroradiometer for Unattended Vegetation Monitoring. Key Sensor Models and Impacts on Reflectance. *Sensors*, 15, 4154-4175

Javier Pacheco-Labrador[1], and M. Pilar Martín[1]
[1] Environmental Remote Sensing and Spectroscopy Laboratory (SpecLab)
Instituto de Economía, Geografía y Demografía; Consejo Superior de Investigaciones Científicas (CSIC)
C/ Albasanz 26-28, 28037 Madrid, Spain

Manuscript Received: 20 October 2014. Accepted: 6 February 2015. Published: 11 February 2015.

ABSTRACT

Field spectroradiometers integrated in automated systems at Eddy Covariance (EC) sites are a powerful tool for monitoring and upscaling vegetation physiology and carbon and water fluxes. However, exposure to varying environmental conditions can affect the functioning of these sensors, especially if these cannot be completely insulated and stabilized. This can cause inaccuracy in the spectral measurements and hinder the comparison between data acquired at different sites. This paper describes the characterization of key sensor models in a double beam spectroradiometer necessary to calculate the Hemispherical-Conical Reflectance Factor (HCRF). Dark current, temperature dependence, nonlinearity, spectral calibration and cosine receptor directional responses are modeled in the laboratory as a function of temperature, instrument settings, radiation measured or illumination angle. These models are used to correct the spectral measurements acquired continuously by the same instrument integrated outdoors in an automated system (AMSPEC-MED). Results suggest that part of the instrumental issues cancel out mutually or can be controlled by the instrument configuration, so that changes induced in HCFR reached about 0.05 at maximum. However, these corrections are necessary to ensure the inter-comparison of data with other ground or remote sensors and to discriminate instrumentally induced changes in HCRF from those related with vegetation physiology and directional effects.

Keywords: Spectroradiometer; automated system; characterization; sensor model; dark current; nonlinearity; temperature dependence; spectral calibration; cosine directional response; hemispherical-conical reflectance factor.

1. INTRODUCTION

Linking gas exchange measurements taken at single-point EC sites with spatial information provided by remote sensing is key to globally quantify and monitor the "breathing" of the planet (Gamon et al. 2006b). However, the connection between these data sources is challenging due to the existence of spatial and temporal mismatches. Unattended ground-set optical sensors have the advantage of overcoming the temporal mismatch existing between the continuous micrometeorological measurements acquired by the EC systems and the periodic overpass of remote sensors. This way, information relative to the optical properties of vegetation can be directly related with the biospheric carbon and water fluxes, and used to upscale the flux information from site to local, regional and global scales (Gamon et al. 2010; Gamon et al. 2006b). Though the use of single or multi-spectral sensors at EC sites is more frequent due to their low cost and easy installation (Balzarolo et al. 2011), hyperspectral sensors (spectroradiometers) are being gradually installed at these sites (Balzarolo et al. 2011; Gamon et al. 2010). These sensors sample radiation in narrow and overlapping bands continuously arranged along the spectral domain, typically covering the visible and Near Infrared (NIR) regions. On one hand, such detailed optical information can be related with the physiological and biochemical status of vegetation on the other it can be flexibly matched with the spectral bands of other remote sensors (Hilker et al. 2010a; Hilker et al. 2012; Hilker et al. 2009b).

However, though information provided by spectroradiometers is rich and detailed, large uncertainties can affect the quantities of these spectral measurements (Kostkowski 1997; Milton et al. 2009). This can be specially an issue in the case of unattended outdoor systems, which may face wide ranges of environmental conditions

in terms of temperature, irradiance or illumination geometry, among others. These factors can produce changes in the radiometric quantities and in the computed reflectance factors which are not related with the optical properties of the target covers. Among the instrumental sources of uncertainty that can affect field spectroradiometers there are: the dark current, nonlinearity, temperature dependence, spectral calibration or the directional response of the cosine receptors.

The dark current (DC) is a residual electrical current produced by a photosensitive device when this is not illuminated. It varies with the sensor's temperature (T) and the integration time (t_{int}) (Kuusk 2011); which is the period while radiation is sampled in the sensor. The dark current is added to the photocurrent produced by the radiation, and its impact is larger the lower the photogenerated signal in the pixel.

The nonlinearity (NL) is a variation in the proportionality between the radiance sampled and the output signal generated by the instrument. Nonlinearity can be related with the gray level measured in each pixel; this makes less comparable the measurements taken under different radiation levels, measurements of targets of different bright, and for the different pixels of the array (Pacheco-Labrador and Martin 2014; Saber et al. 2011). Moreover, nonlinearity can be also related with the integration time when this is close to the sensor's readout time (Ferrero et al. 2006). This artifact had been previously reported but not corrected in CCD cameras (Ferrero et al. 2006); however a correction method valid for NMOS sensors was recently proposed by Pacheco-Labrador et al. (2014).

The energy bandgap of semiconductors, and therefore their photoresponse, is inversely related with their temperature. This phenomenon is known as temperature

dependence (TD), and especially affects the near infra-red region in the case of silicon photodiodes (Markham et al. 1995; Starks et al. 1995). Heat can also slightly modify the spectrometer dimensions and consequently the center and width of the spectral bands; the spectral range within each pixel is illuminated. The spectral calibration (SC), which is the function that relates the center of these bands with each pixel, can show thus a dependence on temperature. The accuracy and precision of SC is key when integrating information of different sensors or for fine resolution applications (Anderson et al. 2006; Bachmann et al. 2012; Guanter et al. 2006)

Finally, in the case of the sensors that sample hemispherical irradiance using cosine diffusers, the directional response of the cosine receptor (CR) can be also an issue. Ideally, the CR is the cosine of the illumination zenith angle (θ_s); however, deviations from this behavior would introduce artifacts in the measurement of irradiance. The correction would require accounting for the fractions of diffuse and direct radiation in the environment (Meywerk and Ramanathan 1999).

Some of the abovementioned instrumental artifacts could be controlled, e.g., stabilizing the temperature of the instrument (Daumard et al. 2010; Drolet et al. 2014) but this might not always be possible. Also others are inherent to the instrument design so they cannot be prevented but should be characterized (e.g., nonlinearity, or directional response of cosine receptors). Some of these artifacts have already been considered and corrected in automated systems in different ways (Drolet et al. 2014; Gamon et al. 2006a; Hilker et al. 2007; Meroni et al. 2011; Middleton et al. 2013), however to the best of our knowledge a full characterization accounting for all the factors identified in this work has not been previously reported.

The aim of this work is characterizing the instrumental responses of a field spectroradiometer integrated in an automated system currently installed in an EC site, to allow the correction of the Hemispherical-Conical Reflectance Factor (Nicodemus et al. 1997). This would help to improve the inter-comparison of data, the upscale of spectral information and the separation between observed changes in the optical properties of vegetation caused by instrumental factors from those directionally, phenologically, and physiologically induced.

2. MATERIALS AND METHODS

2.1 Instrumentation

We describe the characterization of a commercial double beam field spectroradiometer (Unispec DC (SN 2038), PP Systems, Amesbury, MA, USA). This instrument allows calculating HCRF by simultaneously sampling up-welling (channel 2) and down-welling (channel 1) radiation. Channel 2 is a bare optical fiber (UNI685-6, PP Systems) whereas channel 1 is an optical fiber but with a cosine receptor (UNI686-6 + UNI435, PP Systems). Each channel is equipped with a Monolitical Miniature Spectrometer 1 (Carl Zeiss, Inc., Thornwood, NY, USA), composed by a fixed grating and a silicon diode array S8381-256Q NIR-enhanced sensor (Hamamatsu Photonics K.K., Tokyo, Japan). The Unispec DC operates in the Visible-NIR (300–1100 nm) with a radiometric resolution of 16 bits, a nominal bin size of 3.3 nm and < 10 nm of spectral resolution (Full Width at Half Maximum, FWHM). The instrument does not have shutters to automatically record dark current but provides temperature readings through a temperature sensor inside the spectroradiometer which can be used to model DC (Hilker et al. 2007).

This spectroradiometer has been installed in the field as the core instrument of an AMSPEC system (Hilker et al. 2007; Hilker et al. 2010b), in the Majadas del Tiétar FLUXNET site (www. fluxnet.ornl.gov), Cáceres, Spain (denominated AMSPEC-MED system). These systems can continuously sample canopy spectra at different viewing and illumination angles in order to characterize the canopy bidirectional reflectance distribution function and estimate Light Use Efficiency (LUE) and other biophysical variables (Hilker et al. 2009a; Hilker et al. 2008; Hilker et al. 2010a). The AMPSPEC-MED system is powered by solar panels. Power constrains do not allow stabilizing the instrument temperature as in other unattended systems (Daumard et al. 2010; Drolet et al. 2014), thus fans are used instead when air temperature goes over 30 °C.

In the EC site, diffuse-to-global radiation ratios (*DGr*) are continuously measured and integrated every ten minutes by a SPN1 Sunshine Pyranometer (Delta T Devices, Cambridge, UK). This instrument samples global and diffuse irradiance between 400 and 2800 nm. As in our study spectral *DGr* is needed to correct CR, this has been modeled using an ASD Fieldspec® 3 spectroradiometer (Analytical Spectral Devices Inc., Boulder, CO, USA), with a spectral range (350 to 2500 nm) close to the pyranometers's one, and a calibrated Spectralon® panel (Labsphere Inc., North Sutton, NH, USA).

Prior to field deployment, the Unispec DC was characterized in the Environmental Remote Sensing and Spectroscopy Laboratory (SpecLab-CSIC, Spain). As in the AMSPEC-MED, the Unispec DC User Interface Computer was bypassed and the instrument was controlled through a RS-232 connection using a fit-PC2i computer (CompuLab, Yokneam, Israel); and controlled using a Matlab routine (Hilker et al. 2007; Hilker et al. 2010a). For the characterization in the laboratory, an ASD RTS-3ZC

integrating sphere (Analytical Spectral Devices Inc.) was used as homogenous light source. The sphere's inner surface coating is highly reflective (> 95 % Zenith Polytetrafluoroethylene (PTFE), Sphereoptics Hoffman LLC, Contoocook, NH, USA); and it is illuminated by a 10 W quartz-tungsten-halogen bulb powered by a stabilized source. A collimated beam is sent through one of the ports of the sphere and reflected by a 99 % Zenith PTFE in front of it. Radiation is scattered in all directions and measured through a second open port, normal to the collimated beam, where both Unispec DC optical fibers are aimed.

A mercury-argon calibration source (Ocean Optics, Dunedin, FL, USA) and a 250 W quartz-tungsten-halogen bulb irradiance source (OSRAM GmbH, Munich, Germany) have been used for spectral calibration and the characterization of the cosine receptor directional response respectively. The spectroradiometer temperature was regulated using a drying oven Raypa DOD-90 (R. Espinar, Terrasa, Spain) and a fridge CTP 31213 (Lieberh, Ochsenhausen, Germany).

2.2 Experimental setup

This section describes the experiments and measurements carried out in order to characterize the Unispec DC spectroradiometer responses under different environmental conditions and instrument settings.

2.2.1 Dark current

DC was characterized as a function of the integration time and the sensor's temperature. The optical fibers connected to the instrument were covered to block the entrance of light. Like in the other experiments described in this work, where the

instrument temperature was modified, the spectroradiometer was first cooled down in the fridge. Then the experiment started and measurements were done while it was warmed up in the oven. Once it reached a maximum temperature, the instrument was cooled down at environmental conditions, while a second set of measurements was taken. In the cold down experiments the instrument never reached temperatures as low as those used at the beginning of the warm up since cooling was not forced. This way, two different models were adjusted both for the warm-up and the cool-down processes. DC measurements started when sensor temperature was 9.5 °C, when it reached 45.4 °C the instrument was cooled down to 24.2 °C (Table 1).

Table 1. Summary of the calibration experiments carried out with the Unispec DC spectroradiometer. In the third column: Wp = Warm-up model. Cd = Cool-down model. St = Stable temperature.

Experiment	t_{int} (ms)	T (°C)	Recorded Spectra
Dark current	4 , 10, 15, 20, 25, 30, 35, 40, 50, 75, 100, 250, 500, 1,000	Wp: [9.5, 45.4] Cd: [45.4, 24.2]	3840
Nonlinearity	4, 6, 9, 11, 13, 15, 17, 18, 20, 22, 24, 25, 27, 29, 31, 33, 34, 36, 38, 71, 105, 139, 172, 206, 240, 273, 307, 341, 375, 408, 442, 454, 476, 509, 543, 577, 610, 644, 676, 741	St: [22.7, 23.9]	419
Temperature dependence	190, 283, 376, 469	Wp: [13.9, 46.1] Cd: [46.1, 25.6]	1102
Spectral calibration	7	Wp: [15.6,48.3] Cd: [48.3,18.3]	430
Cosine directional response	400	St: [26.4,29.3]	200

Meanwhile measurements were continuously taken, randomly varying the t_{int} between 4 and 1,000 ms. Similarly as the instrument operates in the field, the integration time was first set and then the number of scans averaged was selected so that the full measurement took a time equal or shorter than 2 s. This configuration was also applied to the others experiments.

2.2.2. Nonlinearity

For the NL characterization, the spectroradiometer was warmed up at environmental temperature until the sensor's *T* was stable (notice that the range presented in Table 1 is due to random noise of the *T* sensor). Optical fibers for channels 1 and 2 were aimed into the integrating sphere port. Ten measurements of the radiance source were taken at 40 different and randomly selected integration times, ranging between 4 ms and 741 ms (Table 1).

2.2.3. Temperature dependence

The temperature dependence of the Unispec-DC was characterized by collecting measurements while the instrument was warmed up and cooled down. In this experiment, *T* started at 13.9 °C and was increased up to 46.1 °C; then the instrument was cooled at environment temperature up to 25.6 °C. In this case, the optical fibers were also aimed into an open port of the integrating sphere. Measurements were continuously acquired at four different integration times (Table 1); every time that a new integration time was set five spectra were taken.

2.2.4. Spectral calibration

The spectral calibration experiment was repeated at different temperatures in order to assess any significant influence of *T*. In this case the instrument was warmed up from 15.6 °C to 48.3 °C and then cooled to 18.3 °C. We alternately plugged the optical fibers of channels 1 and 2 into the mercury-argon source and took ten measurements using always the same integration time.

2.2.5. Cosine receptor directional response

The cosine receptor directional response was characterized by rotating the Unispec DC's cosine receptor in front of a fixed light source between 0° and 90°, at 10° steps. The experiment was done twice, rotating the cosine head 90° over its central axis in order to acquire measurements at different zenith angles in two perpendicular planes of the cosine head. The experiment was carried out in a dark room in order to minimize diffuse radiation. In each position of the cosine receptor, five measurements of the global radiation were acquired first, then the cosine diffuser was shaded using a small opaque plate, and five measurements of the diffuse radiation were recorded. During the experiment the sensor temperature was stable, ranging randomly between 26.4 °C and 29.3 °C.

2.2.6. Diffuse-to-global radiation ratio

Spectral *DGr* is needed for applying the CR correction. However, quite typically diffuse-to-global radiation ratio is only provided by broadband meteorological sensors in the field ($DGr_{broadband}$). In this study we use an ASD Fieldspec® 3 spectroradiometer

to model spectral DGr and $DGr_{broadband}$ by acquiring irradiance measurement under different sky conditions between 350 and 2500 nm. Modeled ratios are later used to predict the spectral *DGr* in the Unispec DC from the broadband measurements of the SPN1 sensor in the field. Global irradiance was measured using a calibrated Spectralon® panel, whereas diffuse radiation was measured shading the same panel with an opaque plate alternately (Rollin et al. 2000). High zenith angles were avoided to minimize the effects of panel anisotropy (Rollin et al. 2000). Since diffuse and global measurements were not simultaneous, global irradiance was linearly interpolated to the timestamps of the diffuse measurements. Then *DGr* was calculated by dividing the diffuse irradiance by the interpolated global irradiance.

2.3. Sensor models

This section describes the models adjusted to the experimental data that describe the responses of the sensor to radiation as a function of the different variables modified during the experiments.

2.3.1. Dark current

The dark current can be characterized as a variable proportional to the integration time and quadratically dependent of the temperature (Kuusk 2011). In addition, during the experiment we found a negative trend of the measured dark signal (N_{dark}) with the temperature at low integration times. This suggested that the recorded spectra could be actually composed by electrons thermally generated in the photodiode (N_0) plus an electronic bias (N_{bias}) inversely proportional to temperature (Hamamatsu 2011; Pacheco-Labrador et al. ; Pan et al. 2012). Consequently we characterized N_{dark} as

the addition of both signals, as described in Eq. (1). Coefficients a and b in Eq. (1) were fitted per each pixel (i) of each Unispec-DC channel by using ordinary least squares regression. Hysteresis (Kuusk 2011) was accounted for by fitting one model for the warm-up and another for the cool-down processes separately:

$$N_{\mathrm{dark},i} = N_{bias,i}(T) + N_{0,i}(t_{\mathrm{int}}, T) = \left(b_{0,i} + b_{1,i}T\right) + t_{\mathrm{int}} \cdot \left(a_{0,i} + a_{1,i}T + a_{2,i}T^2\right) \quad (1)$$

For every spectrum N_{bias} was first removed so that the measured signal (N_{meas}) later processed is the addition of the signals produced by the photocurrent (N_{phot}) and N_0.

2.3.2. Nonlinearity

In field spectroradiometers nonlinearity is usually characterized as a function of the gray level measured (OceanOptics 2012). However, a second source of nonlinearity has been found in this instrument and has been characterized using a new methodology; a complete description can be found in Pacheco-Labrador et al. (2014). This method characterizes the responses of the instrument to both sources of nonlinearity simultaneously from the measurements of a single experiment. The second NL is related with the integration time, and is described as a leakage of electrons from the pixel to the output line during the readout phase (Ferrero et al. 2006). This is represented by the function $\Re_{\mathrm{IT}}$ (Eq. 2), where linearity is proportional to the total amount of electrons leaked during the readout phase in each pixel (B_i) divided by the integration time set. In Pacheco-Labrador et al. (2014) was also shown that B_i increases with the radiance in the

pixel until a maximum level. Since this instrument has not a radiance calibration, B_i is defined as a function of a variable named "instrumental radiance" (Eq. 3), which is proportional to radiance after gray level-related nonlinearity has been corrected using $\mathfrak{R}_{GL}$. This variable, $L^*_{measGLcor,i}$, is calculated dividing N_{meas} by $\mathfrak{R}_{GL}$ and t_{int}:

$$\mathfrak{R}_{IT,i} = 1 + \frac{B_i\left(L^*_{measGLcor,i}\right)}{t_{int}} \tag{2}$$

$$B_i = C - \frac{D}{L^*_{measGLcor,i}} \cdot \log\left(1 + \frac{L^*_{measGLcor,i}}{D}\right) \tag{3}$$

2.3.3. Temperature dependence

Temperature dependence was characterized normalizing the sensor responses by the sensor responses measured at a given temperature. To avoid the influence of other variables, DC and NL corrections were first applied to N_{meas} resulting $N_{phot.}$ These corrections are later described in Section 2.4. TD was then calculated as the ratio between N_{phot} measured at different T and the N_{phot} linearly interpolated to a reference T arbitrarily selected (30 °C) as in Eq. (4). In order to minimize the impact of noise in the pixels where signal-to-noise ratio was low, TD was smoothed with a robust local regression using weighted linear least squares (RLOWESS) method (Cleveland 1979) A fifth degree polynomial was fit for each pixel of each sensor relating TD and T:

$$TS_i = \frac{N_{phot,i}}{N_{phot,i_{30°C}}} \tag{4}$$

2.3.4. Spectral calibration

Experimental data were first corrected using the sensor models previously described and the method described in the Section 2.4. Then spectral calibration measurements were used to fit a second degree polynomial that assigns wavelength units to the pixels of each sensor. This polynomial included also a temperature factor to account for the temperature related spectral shifts. In the spectra recorded several emission lines whose wavelength is known were selected. The center of the emission lines was calculated as the mean of a normal distribution fit on each selected emission line of the spectra; however, if the coefficient of determination was lower than 0.9, these emission lines were discarded. Eventually, only the emission lines that remained were used to adjust the model.

2.3.5. Cosine receptor directional response

Prior to any other calculation, measurements were corrected as described in Section 2.4 using the models previously adjusted. CR was characterized using exclusively the direct radiation measured during the experiment. Therefore, residual diffuse radiation was subtracted from global radiation to characterize the cosine response using only direct radiation. CR was characterized as the ratio between the direct radiation measured at each angle normalized by the direct radiation at nadir. As defined in Eq. (5), a correction factor $\beta_i(\theta_s)$ was calculated as the difference between the cosine of the illumination angle and CR (Meywerk and Ramanathan 1999). In each pixel, a seventh degree polynomial was fit to model the correction factor β_i as a function of θ_s:

$$\beta_i(\theta_s) = \cos(\theta_s) - {N_{\text{phot direct},i}(\theta_s)}/{N_{\text{phot direct},i}(0)} \quad (5)$$

2.3.6. Diffuse-to-global radiation ratio

The spectral *DGr* in each band of the channel 1 of the Unispec DC was modeled as a function of the broadband *DGr* measured in an EC tower by a single-band SPN1 Sunshine Pyranometer. For that, the $DGr_{\text{broadband}}$ was simulated from the global and diffuse irradiances measured with the ASD Fieldspec® 3 integrating the spectral irradiance between 400 and 2,500 nm weighted by the nominal spectral response of the SPN1 sensor (Wood et al. 2007). The 283 *DGr* spectra generated were resampled to the spectral bands previously estimated for the channel 1 of the Unispec DC using the spectral convolution method (Meroni et al. 2010) and the nominal spectral resolution of the instrument, < 10 nm. The Unispec DC itself was not used since the *DGr* measurements acquired with the cosine receptor would have been affected by the directional response of the diffuser, for whose correction the *DGr* is needed. Then the simulated spectral *DGr* of each pixel of the Unispec DC (DGr_i) was characterized as a linear function of the simulated $DGr_{\text{broadband}}$ (Eq. 6):

$$DGr_i = a_{0,i} + a_{1,i} \cdot DGr_{broadband} \quad (6)$$

2.4. HCRF correction

We used the described sensor models adjusted in the laboratory in order to correct spectral measurements provided by the Unispec DC integrated in an outdoors automated system. A summary of the corrections applied is shown in the Scheme 1; any

spectra quantified in digital numbers units, at different stages of the correction, is represented in a general way by the variable N and a subscript related with the correction level.

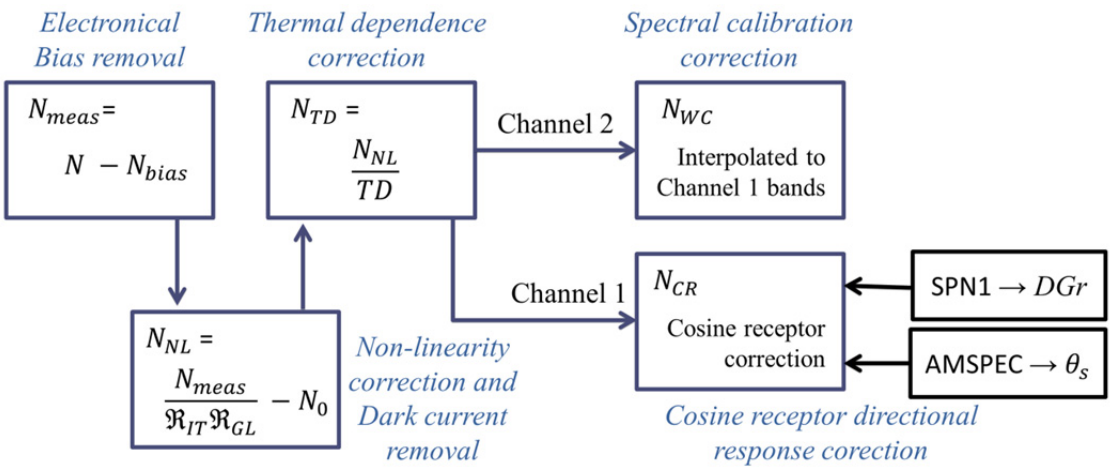

Scheme 1. Summary of the corrections performed to the spectral data acquired by the Unispec DC spectroradiometer.

In this paper, we present the corrections applied to the spectra acquired by the AMSPEC-MED system in a single viewing position between the 1 August 2013 and the 15 June 2014. Spectra were taken with a viewing azimuth and zenith of 190 ° and 40 ° respectively. Saturated and corrupted spectra were removed and eventually 3730 measurements were selected. For this dataset, sensor's temperature ranged between 1.2 °C and 44.4 °C, integration time was set between 8 and 4,000 ms, θ_s ranged between 16.8 ° and 77.8 °, and $DGr_{broadband}$ integrated every ten minutes by the SPN1 sensor ranged between 0.063 and 0.986. All the spectra were originally acquired in raw Digital Numbers (DN) for each channel.

The correction began estimating N_{bias} and N_0 from Eq. (1) so that N_{bias} was subtracted from the original digital numbers to obtain N_{meas}. Then NL correction was applied to those pixels where the signal was larger than N_0, which was removed afterwards (Eq. 7); this way, N_{NL} was calculated. After that, we estimated TD for each pixel as a function of T, and normalized N_{NL} to the sensor's response at 30 °C (Eq. 8), resulting N_{TD}. Next, since the spectral calibration of each channel is different, we resampled N_{TD} spectra of channel 2 to the center bands of channel 1 using linear interpolation (N_{SC}). For those corrections where two models (warm-up and cool-down) had been calibrated, the daily trend of temperature was used to decide which model would be used:

$$N_{\text{NL},i} = \frac{N_{meas,i}}{\Re_{GL}(N_{meas,i})\Re_{IT}(t_{int}, L^*{}_{measGLcor,i})} - N_{0,i} \tag{7}$$

$$N_{TD,i} = {N_{NL,i}}/{TD_i(T)} \tag{8}$$

Finally, we applied the CR correction to N_{TD} spectra of channel 1 following the methodology described in (Meywerk and Ramanathan 1999). First, we linearly interpolated the $DGr_{\text{broadband}}$ (integrated every 10 minutes by the SPN1) to the timestamp of each spectrum. Then we used the interpolated values to estimate the DGr_i in each spectral band using the previously adjusted model (Eq. 6). The sun zenith angle is calculated by the AMSPEC routine (Reda and Andreas 2003) and provided with the spectra metadata (Hilker et al. 2008). The correction factor β_i and the DGr_i are used to correct the instrumental irradiance as defined in Eq. (9):

$$N_{CR,i_{Ch\,1}} = N_{TD,i_{Ch\,1}} \cdot \left[1 - DGr_i \cdot \int_1^0 \beta_i(\theta_s)\,\theta_s d\theta_s - (1 - DGr_i) \cdot \beta_i(\theta_s)\right] \tag{9}$$

Finally, reflectance is calculated using the cross-calibration method (Gamon et al. 2006a), where the channels' ratio is corrected using the measurement of a calibrated white reference panel (while channel 1 measures down-welling irradiance) as in Eq. (10), where $\rho_{\text{Reference}}$ is the absolute reflectance correction factor of the reference panel:

$$\rho_{DBM,i} = \frac{\left(N_{WC,i_{Ch\,2}}\right)_{\text{Target}}}{\left(N_{CR,i_{Ch\,1}}\right)_{\text{Target}}} \cdot \frac{\left(N_{CR,i_{Ch\,1}}\right)_{\text{Reference}}}{\left(N_{WC,i_{Ch\,2}}\right)_{\text{Reference}}} \cdot \rho_{\text{Reference},i} \tag{10}$$

3. RESULTS

3.1. Dark current

Measured dark signal ranged between 81 and 829 and between 99 and 797 DN in channels 1 and 2 respectively. At low t_{int} we observed a negative trend of the dark signal with T, which led us to model N_{dark} as defined in Eq. (1). Errors in the fitting were low, Relative Root Mean Squared Errors (RRMSE) in the warm-up and cool-down models were 2.83 % and 3.45 % in channel 1 and 2.53 % and 4.46 % in channel 2 respectively.

Figure 1a separately depicts the modeled N_0 and N_{bias} in a pixel of channel 1 predicted by the warm-up model. As shown, N_{bias} linearly decreases with T and N_0 is weaker than N_{bias} at low temperatures. Figure 1b shows the predicted and measured N_{dark} for the same pixel; as can be seen, the dark signal increases with the temperature at large integration times, and decreases at low integration times.

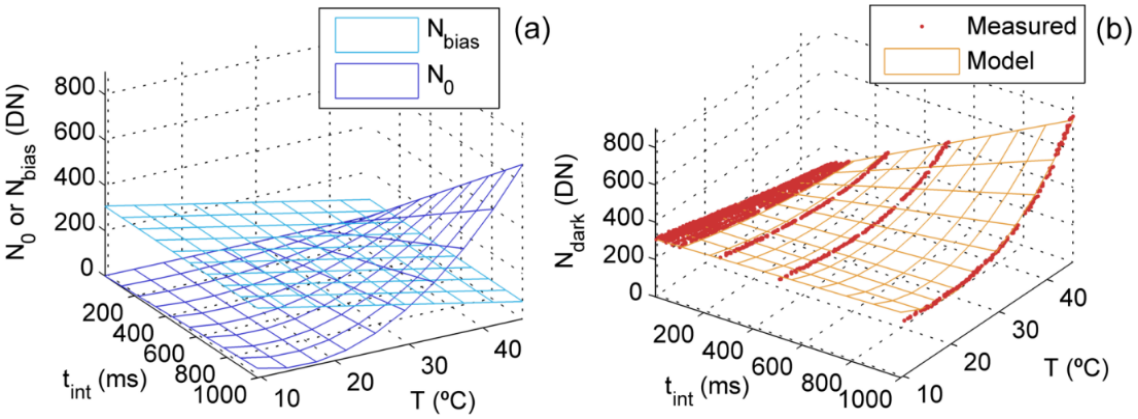

Figure 1. Channel 1's dark signal models in pixel 170 of sensor while warming up: (a) Modelled dark current (N_0) and electronic bias (N_{bias}); (b) Modelled and measured dark signal (N_{dark}).

3.2. Nonlinearity

NL measurements covered the full sensor's radiometric range and also used very low t_{int}; this allowed adjusting the models $\mathfrak{R}_{GL}$ and $\mathfrak{R}_{IT}$ (Pacheco-Labrador et al. 2014). Figure 2 shows the predicted and measured values for each one of the corrections functions corresponding to channel 1. Figure 2a depicts $\mathfrak{R}_{GL}$, which slightly decreases with the gray level measured up to dropping above 50,000 DN. RRMSEs of the fit were 0.30 % and 0.40 % in channels 1 and 2 respectively. Figure 2b shows the predicted and measured values of $\mathfrak{R}_{IT}$, in this case RRMSEs were 0.22 % in channel 1 and 0.24 % in channel 2. As can be seen, $\mathfrak{R}_{IT}$ asymptotically increases with $L^*_{measGLcor}$ up to a maximum value at low t_{int}, and drops quickly as the t_{int} increases.

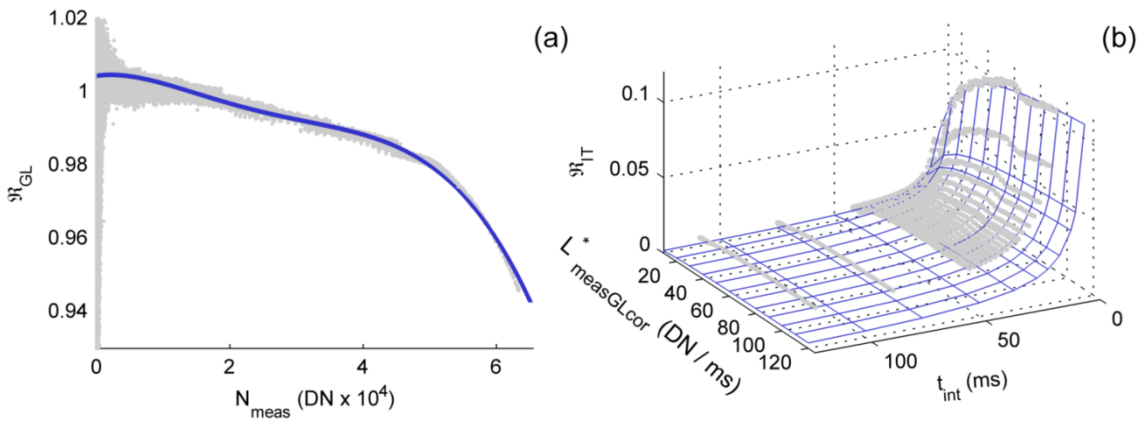

Figure 2. Channel 1's nonlinearity models: (a) NL model related with the gray level ($\mathfrak{R}_{GL}$); (b) NL model related with the integration time ($\mathfrak{R}_{IT}$).

3.3. Temperature dependence

Measured TD ranged between 0.90-1.21 in channel 1 and 0.86-1.19 in channel 2 (95 % confidence). Pixels in the extremes of the sensors, especially in the ultraviolet region, were very noisy due to the low signal. Figure 3a shows the adjusted models in channel 1. As can be seen, the sensitivity of the sensors varied with the temperature, especially in those pixels corresponding to the largest wavelengths, above pixel 120 (~700 nm), where the sensitivity increased with *T*. Predictive models were precisely fit, though noise was large in the extremes of the sensor array. Between 400 and 1,000 nm RRMSEs for the warm up and the cool down models were 0.155 % and 0.094 % in channel 1 and 0.160 % and 0.087 % in channel 2 respectively. Figure 3b shows the hysteresis of temperature dependence for different pixels.

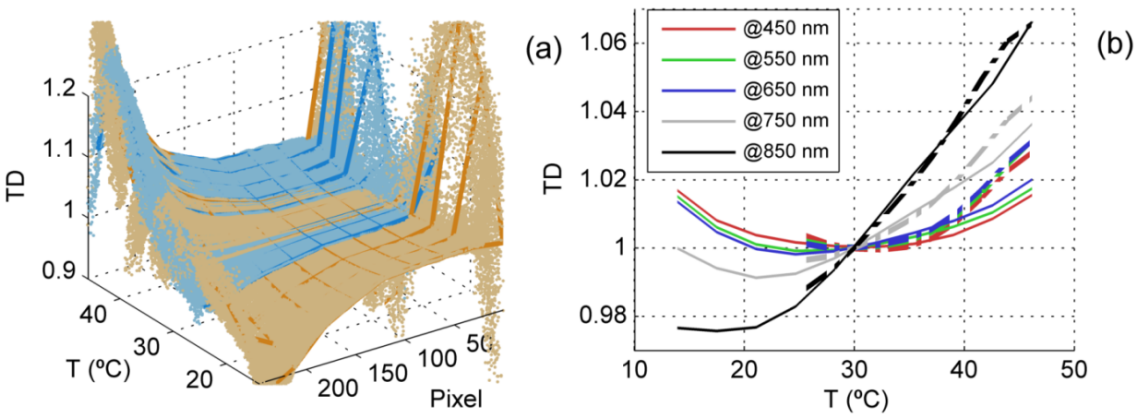

Figure 3. Temperature dependence models in channel 1: (a) Warm-up model and data (in orange) cool-down model and data (in blue). (b) Warm-up (thin solid lines) and cool-down models (thick dashed lines) for pixels close to different wavelengths.

3.4. Spectral calibration

In order to locate the center of the emission peaks in the sensor array, a normal distribution function was fit to the emission lines of the mercury-argon lamp. However, for the spectral calibration, only those emission lines where correlation coefficient of the fit was high were used. This way, nine and eight lines were selected for channel 1 and channel 2 respectively (Figure 4).

Center band position showed a small decreasing trend with *T*, with slopes ranging between -0.0048 nm/°C and -0.0006 nm/°C. For each sensor a second order polynomial was fit relating a center wavelength to each pixel of the array. The effect of temperature was tested including this variable in the models. Differences found between the wavelengths predicted by each model ranged between -0.081 and 0.075 nm in channel 1 and -0.098 and 0.094 nm in channel 2. Therefore, considering the spectral features of the sensors and the noise of the temperature readings, *T* was not included in the spectral calibration models. A second degree polynomial was fit relating the pixel

position and the corresponding spectral band; Root Mean Squared Errors (RMSE) of the models were 0.920 and 0.714 nm in channel 1 and 2 respectively. RMSEs were larger in the NIR, where emission lines were wider and noisier than in the visible. Spectral ranges estimated for channels 1 and 2 respectively were 301.13-1,122.98 nm and 300.10-1,122.16 nm.

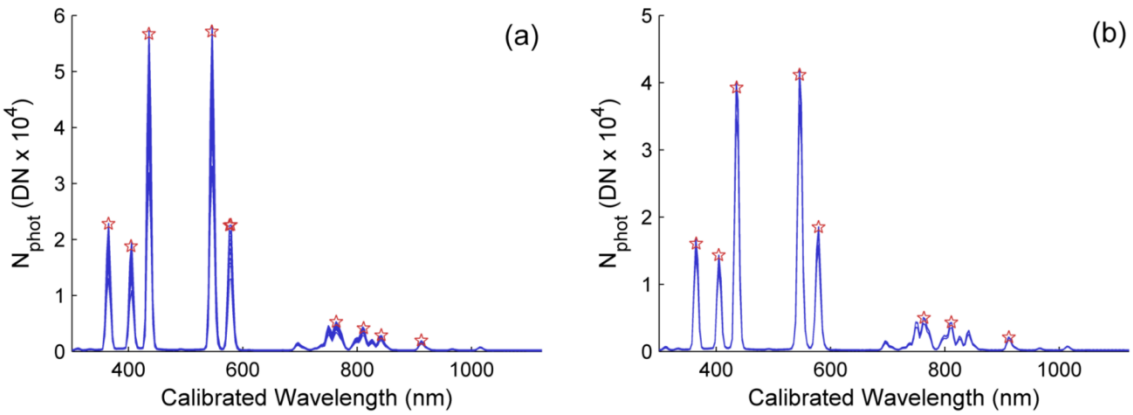

Figure 4. Mercury-argon lamp emission lines spectra. The bands selected for the spectral calibration of each channel are marked with a star. (a) Channel 1; (b) Channel 2.

3.5. Cosine receptor directional response

Figure 5 shows the correction factor $\beta_i(\theta_s)$ calculated as the difference between the ideal and the measured cosine response.

The cosine receptor overestimated irradiance at wavelengths lower than 700 nm. This threshold shifted to above 850 nm as the illumination angle increased. Maximum differences from an ideal cosine response were between -0.156 and 0.169 in the range 400-1100 nm, and were largest at the middle angles, around 60 °. A polynomial model

was fit for each pixel with an overall RRMSE of 1.03 %. Diffuse radiation fraction was lower than 2.14 % in the range 400-1,000 nm with the illumination at nadir.

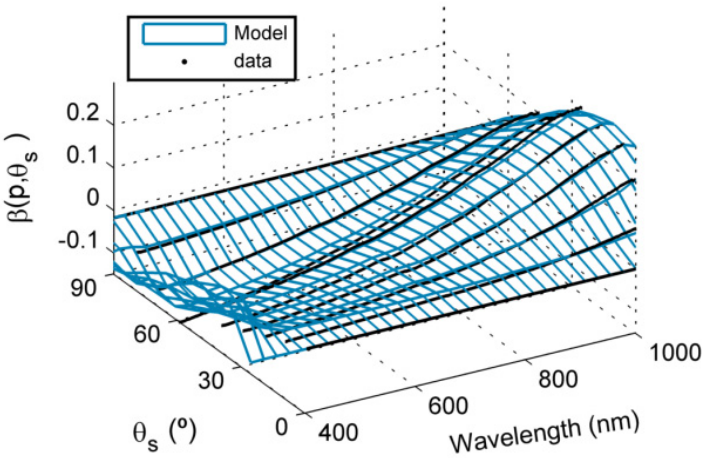

Figure 5. Cosine receptor directional response correction factor $\beta(\theta_s)$. Fit model and measured data.

3.6. Diffuse-to-global radiation ratio

For each band of the channel 1, a linear model was fit to predict the spectral *DGr* from the $DGr_{broadband}$. Figure 6a shows the slope and the offset of each model and Figure 6b depicts the measured and the modeled *DGr*. As can be seen, spectral *DGr* is lower in the atmospheric absorption bands; these features are noticeable in the offset of the models, which decrease from the Visible to the NIR. On the contrary, the slope of the models increases towards the NIR. Mean RRMSE in the prediction of spectral DGr_i was 1.21 %.

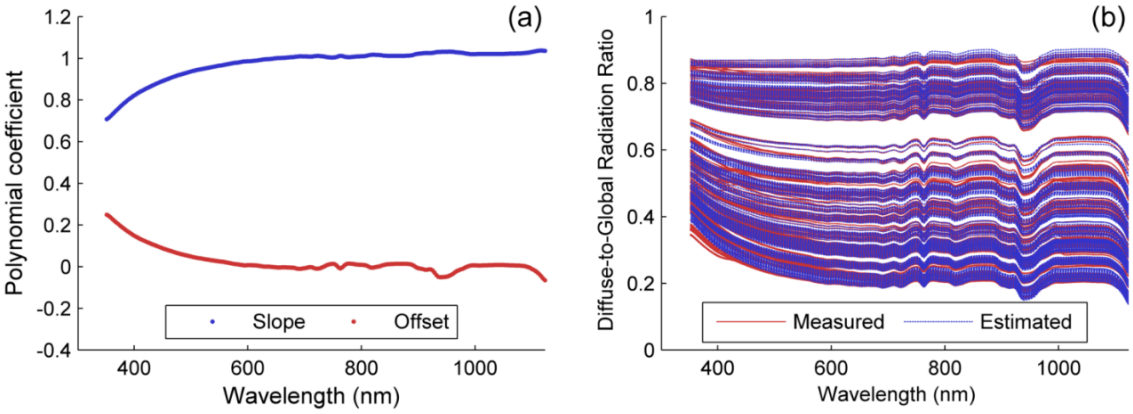

Figure 6. (a) DGr linear model coefficients. (b) Measured and estimated spectral *DGr*.

3.7. HCRF correction

In order to assess the influence of each correction both on the digital numbers and the reflectance factor spectra, we corrected a dataset of measurements acquired by the AMSPEC-MED system for almost ten months, under very different environmental conditions. The changes introduced by each step of the correction (Scheme 1) respect to the previous step were analyzed; and also the differences between the raw and the completely corrected values are also calculated. Results of this analysis are summarized in Figure 7, where the 99 % confidence intervals of the changes introduced in this dataset are shown. Figure 7a,b show the differences observed in the DN spectra (N) of channels 1 and 2 respectively. In this figure we have merged the removal of the dark current and the electronic bias in order to assess independently the impact of the dark signal. However, it must be noticed that N_{bias} is removed in the first step of the correction whereas N_0 is removed after the nonlinearity correction (Scheme 1). As can be observed, in channel 1, the largest changes in N were produced by the temperature dependency correction. These were mainly negative in the Visible region, and became more clearly positive in the NIR. CR corrections also introduced large variations, with

positive differences below 780 nm, and negative above 800 nm. Nonlinearity correction produced changes in *N* of lower magnitude than TD and CR, which where related with the measured DN value when positive. All the corrections applied together led to increases and decreases of *N*. The increases were larger than the decreases in the visible region and decreases were larger in the NIR. In channel 2 the temperature dependence correction also produced the largest variations; these were maxima above 700 nm with a positive effect. NL correction mainly produced decreases of DN, though increases were registered between 710 and 860 nm, where the signal was also maximum. The spectral calibration correction led to irregular differences that peaked around the atmospheric absorption features. These were maximum around 756 nm, close to the atmospheric O_2-A absorption band. In the overall, corrections in channel 2 produced a decrease of *N* in the Visible region and increases and decreases in the NIR, where the first were of larger magnitude. In both channels, DC correction produced a moderated decrease in *N*.

Figure 7c similarly shows the changes introduced in HCRF by each correction. HCRF calculation is limited to the spectral region between 400-1,000 nm due to the noise found in the models out of this range. DC correction slightly modified the HCFR, producing small decreases below 735 nm and larger differences, both positives and negatives, above this wavelength. NL produced small decreases of HCRF in all the spectral range, but in the range 720 nm to 900 nm, where some increases were also registered. TD correction produced small changes below 700 nm in HCRF, but above this point, large increases were registered. SC correction produced peaky changes around the atmospheric absorption bands, mainly located in the NIR such as 760 nm (O_2-A) and 820, 930 and 970 nm (H_2O). Variations introduced by the CR corrections were small and negative in the Visible; increases became larger and positive above 700

nm and were always positive above 800 nm. All the corrections together led to small decreases in HCRF between 400 and 700 nm, but these became larger and also positives in the NIR region.

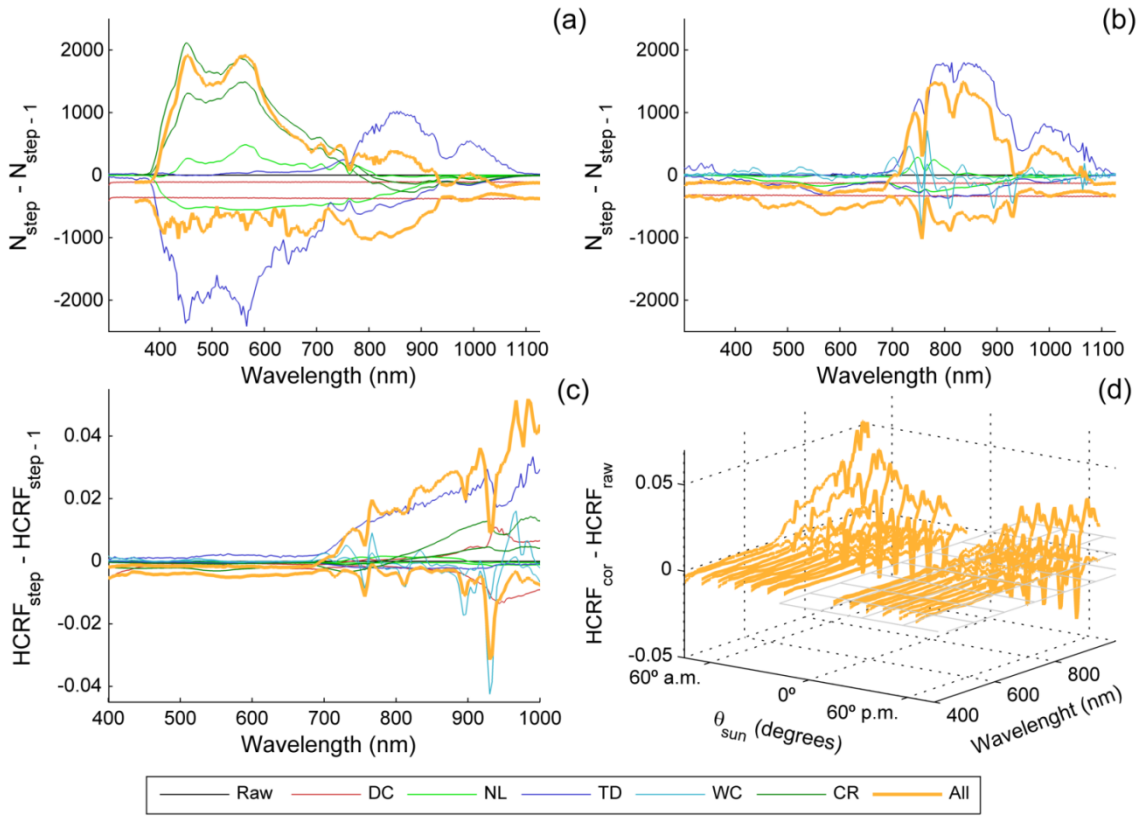

Figure 7. HCRF correction performed on 3730 spectra taken by the AMSPEC-Med system between the 1 August 2013 and 15 June 2014 in a single viewing position. Percentiles 99 % of the changes introduced by each step of the correction respect to the previous stage are shown: (a) DN spectra in channel 1; (b) DN spectra in channel 2; (c) HCRF spectra; (d) HCRF spectra grouped in 10 degrees wide ranges of θ_s.

Figure 7d depicts the percentile 99 % of changes introduced by all the corrections in HCRF grouped in different moments of the day. The dataset has been classified using ranges of θ_s with a width of 10 degrees and the time of the day (a.m. or

p.m.). As can be seen, the effects of the corrections are larger the larger is θ_s. The differences between the corrected and non-corrected HCRF were minimum at noon and larger in the morning than in the afternoon for the same elevation angles.

4. DISCUSSION

Different instrumental sources of error in the computation of HCRF have been characterized in laboratory under different temperatures and configuration settings. The Unispec DC spectroradiometer is not provided with a shutter that allows measuring dark current, however, it can be retrieved as a function of t_{int} and T. Hysteresis can be accounted for by using the T variations along the day to establish when the instrument is warming up or cooling down. Temperature ranges used were shorter for cooling experiment than for the warming up experiments, since cooling could not be controlled. However, models adjusted are still suitable to correct field data, since this is similar to what actually occurs outdoors; temperatures in the morning are lower than temperatures at the end of the afternoon. A similar characterization performed on a MMS 1 spectroradiometer also found quadratic and linear relationships between dark current and T and t_{int} respectively (Kuusk 2011). In that case, minimum t_{int} were larger than the ones used here, and the Front End Electronics that controlled the spectrometer was different; thus the presence of a bias or a negative trend like the one we found could not be compared. The authors have not a clear explanation for the reported bias inversely related with the temperature, but it might be explained by a change in the capacitance of the condensers related with the temperature. Though both N_{bias} and N_0 are eventually subtracted from the spectra, the separation is necessary for the correction of NL.

The nonlinearity correction method we used proved having a better performance during independent validations (Pacheco-Labrador et al. 2014), and would provide corrections more reliable than other methods under AMSPEC-MED operating conditions. This method corrects nonlinearity using the functions $\mathfrak{R}_{GL}$ and $\mathfrak{R}_{IT}$; the first of them is related with the electronics that process the analogical signal read from the sensor, and the second with a leakage of photocurrent generated during the readout. The AMSPEC-MED system automatically sets the t_{int} of each spectrum so that the signal in channel 1 reaches about 40,000 DN, this prevents reaching very high values, where the influence of $\mathfrak{R}_{GL}$ is large. However, t_{int} set under sunny conditions are low and measurements could be potentially affected by photocurrent leakage. The effects of nonlinearity in HCRF are, however, lower than those produced by other corrections. This can be explained on one hand because the t_{int} auto-adjustment is designed to keep measurements within a range of DN values where of $\mathfrak{R}_{GL}$ is low. On the other hand, the t_{int} is the same for both channels and both also reach high "instrumental radiances" (in DN/ms) (Pacheco-Labrador et al. 2014). Since the electron leakage (B_i) rapidly increases at low radiance levels, approaching asymptotically a maximum value (Figure 2b), $\mathfrak{R}_{IT}$ would be similar in channels 1 and 2 too, and would cancel mutually when DN spectra from these channels are divided to calculate HCRF (Eq. 10). However this cancellation might not occur in all the cases; for example, when measuring shaded targets the up-welling radiation channel might register low instrumental radiances, or in the case of sensors with a high spectral resolution, within atmospheric absorption lines. In that case, $\mathfrak{R}_{IT}$ could be different in each channel, leading to artifacts in HCRF, and also in LUE estimators as those derived from spectral indices such as the Photochemical

Reflectance Index (PRI) (Gamon et al. 1992) or Sun Induced Fluorescence (Meroni et al. 2009).

Within the range of temperatures registered during its characterization, the temperature dependency normalized at 30 °C varied less than 0.032 between 400 and the 700 nm, but above this region, variation exponentially increased up to 0.23 at 1,000 nm. This might be explained due to proximity to the band edge of the silicon, which is sensible to *T* (Saber et al. 2011). Compared with the other corrections the temperature dependence produced large changes in HCRF, especially in the NIR region. Unlike in the case of nonlinearity, differences between both channels did not seem to cancel out during the calculation of the reflectance factor. Changes introduced in the raw DN spectra were also large, and might be significant in the quantification of the measured radiation.

The spectral calibration showed a dependency on temperature; however, the magnitude of these observed drifts compared with the spectral characteristics of the sensor and the model errors suggested that it could be overlooked. Actually, the inclusion of *T* on the calibration models barely produced any difference in the calibrated wavelengths and was eventually removed. Spectral resolution and sampling interval of the Unispec DC are suitable for the characterization of vegetation reflectance and computation of different vegetation indices (Claudio et al. 2006; Gamon et al. 2006a; Sims et al. 2006); however, it cannot be used for other applications which require very high spectral resolution, such as sun induced fluorescence retrieval (Damm et al. 2011; Meroni et al. 2009). Though we discarded the influence of *T* on the spectral calibration, this might be still considered for instruments whose applications require very high spectral accuracy. Though we were able to characterize the spectral shift, we could not

measure the changes in the FWHM. However, considering the small shifts in the center wavebands in the case of this instrument and its application, we assumed that these should be also negligible.

The characterization of the cosine receptor's directional response allows correcting the down-welling radiation spectra taking into account the direct and diffuse fractions. (Milton and Rollin 2006) empirically inferred spectral irradiance from a reduced number of spectral bands; though estimations would not be reliable under passing clouds. A simple approach has been used here, since *DGr* is measured with a single broadband pyranometer in the EC site, this single value is used to infer the spectral *DGr*. The modelling was done using an ASD spectroradiometer with a spectral range slightly narrower than the one of the SPN1 sensor; however, irradiance in the spectral range not measured by the ASD is low, and should have little effect on the model. CR corrections rely also on the directional responses of the Spectralon® panel used for the modelling and the directional response of the SPN1 sensors. For this reason, large θ_s were avoided during the modelling of the *DGr* to minimize directional dependencies on the panel. Moreover, the directional response of the cosine receptor used in the AMSPEC system is known to be further from the ideal response when compared with the responses of other cosine heads (Julitta et al. 2013). For these reasons, we expect that this correction is able to improve the quality and inter-comparability of data. The CR correction applied relies on the assumption that the diffuse skylight is isotropic, and the $DGr_{\text{broadband}}$ provided is the average of ten minutes period; this can lead to uncertainties under heterotrophic and unstable sky conditions. However, data used to separate physiological from directional changes in PRI (Hilker et al. 2008) must be acquired under similar illumination conditions. Thus, unstable

conditions would force to reject these data even if *DGr* measurements were available all the time. Nonetheless, this correction introduced large changes both in the *N* and HCRF spectra; thus, CR correction should be regularly included and further research should be done to achieve reliable estimates of DGr_i. CR correction produced the second largest changes in the *N* spectra of channel 1, and also in the HCRF in the NIR.

The analysis of the effects of all the corrections across the day (Figure 7d) can be related mainly with two corrections. On one hand, the CR correction produces larger differences in the NIR region the larger is θ_s, since in this region the directional response is furthest from the cosine response than in the Visible. Moreover, the largest changes occur during the morning, this can be related to the temperature dependence correction. Due to power constrains, the instrument is not thermally stabilized, and starts operating as soon as it switches on in the morning. The largest changes of temperature are thus experimented in the first hours of the day, during which the instrument is warmed up by the circulating power and by the increasing environmental temperature. *T* varies less during the afternoon, when is stable and slightly decreases at the end. Thus, the temperature dependence correction, which is based on a reference of 30 °C, produces large changes in the NIR region during the first hours of operation.

The effects observed are limited to the spectroradiometer used for this work. Nonetheless, the instrument has been tested under a wide range of environmental conditions, showing how instrumental issues can operate and modify the measurements. Results suggest that similar characterizations should be applied to spectroradiometers integrated in outdoors unattended systems. Since characteristics of each instrument would be unique and the requirements of each application also different, the selection of which sensor models should be used and how should be experimentally adjusted could

vary. However, some of the methods proposed in this work could be either directly used or adapted to characterize other instruments. Additionally the reported impacts of each model on the spectral variables considered can help other users to take decisions about systems development, instrument configuration and data analysis. Corrections applied generated differences in HCRF close to 0.05 at maximum, partially due to cancelling effects and partially due to the configuration of the system. The largest changes occurred in the NIR bands, which are of relevance in the study of vegetation vigor, structure and sun induced fluorescence. Effects in the Visible bands were much lower, however, this not might happen all the times, depending on the instrument characteristics, configuration and targets measured. Effects on the quantification of radiance or irradiance would be related with the changes introduced in the digital numbers by the different corrections. However, the instrument lacks of radiometric calibration, and these could not be assessed. Moreover, maintenance of updated sensor models shall not be overlooked, and should be done as frequently as possible. However, dismantling automated systems can be resource and time consuming, and therefore methods for in-situ calibration, characterization or validation should be explored.

5. CONCLUSIONS

We have characterized the responses of a Unispec DC spectroradiometer integrated in an automated system (AMSPEC-MED) under a wide range of environmental conditions. Results show the impact of temperature, irradiance levels and illumination angle, and also the instrument settings on the spectral data acquired. Some of the effects partially cancelled out when raw spectra of each channel were divided to calculate HCRF, especially in the visible bands. For this reason and because some of the

artifacts operate more strongly in the NIR, corrections had larger effects in this region than in the Visible. Though the instrumental dependencies can be also characterized as done in this work, some of these can be controlled during the design of the automated systems. Results suggest that temperature stabilization would be highly recommendable. Moreover, the estimation of spectral *DGr* is not usual in this type of systems, and further research should be done since this information is needed for the CR correction and could be applied in the use of radiative transfer models. Additional efforts should be done to correct instrumental dependencies of sensors installed in outdoors automated systems, in order to ensure quality and comparability of data, and to assure the update of the sensor models.

ACKNOWLEDGMENTS

We are very grateful to all the SpecLab and CEAM colleagues who contributed to field and laboratory works, especially Ramón López for his contribution in the development of the AMSPEC-MED system. We also want to acknowledge Thomas Hilker (Oregon State University) for the support provided and the original AMSPEC codes and setup; and the PP Systems technical staff for the support and information provided about the Unispec DC. We also thank our colleagues for the Optics Institute (CSIC) Alejandro Ferrero, Joaquín Campos and Alicia Pons; and Jorge Pacheco-Labrador from the Technical University of Madrid for their contributions. Javier Pacheco-Labrador was sponsored by a JAE-Predoc grant (CSIC), co-funded by the European Social Fund. AMSPEC-MED has been funded by the BIOSPEC project "Linking spectral information at different spatial scales with biophysical parameters of Mediterranean vegetation in the context of Global Change"

(http://www.lineas.cchs.csic.es/biospec) (CGL2008-02301/CLI, Ministry of Science and Innovation) and the FLUχPEC project "Monitoring changes in water and carbon fluxes from remote and proximal sensing in a Mediterranean dehesa ecosystem" (http://www.lineas.cchs.csic.es/fluxpec) (CGL2012-34383, Ministry of Economy and Competitiveness).

REFERENCES

Anderson, K., Milton, E.J., & Rollin, E.M. (2006). Calibration of dual-beam spectroradiometric data. *International Journal of Remote Sensing, 27*, 975-986

Bachmann, C.M., Montes, M.J., Parrish, C.E., Fusina, R.A., Nichols, C.R., Li, R.-R., Hallenborg, E., Jones, C.A., Lee, K., Sellars, J., White, S.A., & Fry, J.C. (2012). A dual-spectrometer approach to reflectance measurements under sub-optimal sky conditions. *Optics Express, 20*, 8959-8973

Balzarolo, M., Anderson, K., Nichol, C., Rossini, M., Vescovo, L., Arriga, N., Wohlfahrt, G., Calvet, J.-C., Carrara, A., Cerasoli, S., Cogliati, S., Daumard, F., Eklundh, L., Elbers, J.A., Evrendilek, F., Handcock, R.N., Kaduk, J., Klumpp, K., Longdoz, B., Matteucci, G., Meroni, M., Montagnani, L., Ourcival, J.-M., Sánchez-Cañete, E.P., Pontailler, J.-Y., Juszczak, R., Scholes, B., & Martín, M.P. (2011). Ground-Based Optical Measurements at European Flux Sites: A Review of Methods, Instruments and Current Controversies. *Sensors, 11*, 7954-7981

Claudio, H.C., Cheng, Y., Fuentes, D.A., Gamon, J.A., Luo, H., Oechel, W., Qiu, H.-L., Rahman, A.F., & Sims, D.A. (2006). Monitoring drought effects on vegetation water content and fluxes in chaparral with the 970 nm water band index. *Remote Sensing of Environment, 103*, 304-311

Cleveland, W.S. (1979). Robust Locally Weighted Regression and Smoothing Scatterplots. *Journal of the American Statistical Association, 74*, 829-836

Damm, A., Erler, A., Hillen, W., Meroni, M., Schaepman, M.E., Verhoef, W., & Rascher, U. (2011). Modeling the impact of spectral sensor configurations on the FLD retrieval accuracy of sun-induced chlorophyll fluorescence. *Remote Sensing of Environment, 115*, 1882-1892

Daumard, F., Champagne, S., Fournier, A., Goulas, Y., Ounis, A., Hanocq, J.F., & Moya, I. (2010). A Field Platform for Continuous Measurement of Canopy Fluorescence. *Geoscience and Remote Sensing, IEEE Transactions on, 48*, 3358-3368

Drolet, G., Wade, T., Nichol, C.J., MacLellan, C., Levula, J., Porcar-Castell, A., Nikinmaa, E., & Vesala, T. (2014). A temperature-controlled spectrometer system for continuous and unattended measurements of canopy spectral radiance and reflectance. *International Journal of Remote Sensing, 35*, 1769-1785

Ferrero, A., Campos, J., & Pons, A. (2006). Apparent violation of the radiant exposure reciprocity law in interline CCDs. *Applied Optics, 45*, 3991-3997

Gamon, J.A., Coburn, C., Flanagan, L.B., Huemmrich, K.F., Kiddle, C., Sanchez-Azofeifa, G.A., Thayer, D.R., Vescovo, L., Gianelle, D., Sims, D.A., Rahman, A.F., & Pastorello, G.Z. (2010). SpecNet revisited: bridging flux and remote sensing communities. *Canadian Journal of Remote Sensing, 36*, S376-S390

Gamon, J.A., Cheng, Y., Claudio, H., MacKinney, L., & Sims, D.A. (2006a). A mobile tram system for systematic sampling of ecosystem optical properties. *Remote Sensing of Environment, 103*, 246-254

Gamon, J.A., Peñuelas, J., & Field, C.B. (1992). A narrow-waveband spectral index that tracks diurnal changes in photosynthetic efficiency. *Remote Sensing of Environment, 41*, 35-44

Gamon, J.A., Rahman, A.F., Dungan, J.L., Schildhauer, M., & Huemmrich, K.F. (2006b). Spectral Network (SpecNet)—What is it and why do we need it? *Remote Sensing of Environment, 103*, 227-235

Guanter, L., Richter, R., & Moreno, J. (2006). Spectral calibration of hyperspectral imagery using atmospheric absorption features. *Applied Optics, 45*, 2360-2370

Hamamatsu (2011). Characteristic and use of NMOS linear image sensors. Technical Information SD-26. (p. 56). Hamamatsu City, Japan: Hamamatsu Photonics, K. K.

Hilker, T., Coops, N.C., Coggins, S.B., Wulder, M.A., Brownc, M., Black, T.A., Nesic, Z., & Lessard, D. (2009a). Detection of foliage conditions and disturbance from multi-angular high spectral resolution remote sensing. *Remote Sensing of Environment, 113*, 421-434

Hilker, T., Coops, N.C., Hall, F.G., Black, T.A., Wulder, M.A., Nesic, Z., & Krishnan, P. (2008). Separating physiologically and directionally induced changes in PRI using BRDF models. *Remote Sensing of Environment, 112*, 2777-2788

Hilker, T., Coops, N.C., Nesic, Z., Wulder, M.A., & Black, A.T. (2007). Instrumentation and approach for unattended year round tower based measurements of spectral reflectance. *Computers and Electronics in Agriculture, 56*, 72-84

Hilker, T., Hall, F.G., Coops, N.C., Lyapustin, A., Wang, Y., Nesic, Z., Grant, N., Black, T.A., Wulder, M.A., Kljun, N., Hopkinson, C., & Chasmer, L. (2010a). Remote sensing of photosynthetic light-use efficiency across two forested biomes: Spatial scaling. *Remote Sensing of Environment, 114*, 2863-2874

Hilker, T., Hall, F.G., Tucker, C.J., Coops, N.C., Black, T.A., Nichol, C.J., Sellers, P.J., Barr, A., Hollinger, D.Y., & Munger, J.W. (2012). Data assimilation of photosynthetic light-use efficiency using multi-angular satellite data: II Model implementation and validation. *Remote Sensing of Environment, 121*, 287-300

Hilker, T., Lyapustin, A., Hall, F.G., Wang, Y., Coops, N.C., Drolet, G., & Black, T.A. (2009b). An assessment of photosynthetic light use efficiency from space: Modeling the atmospheric and directional impacts on PRI reflectance. *Remote Sensing of Environment, 113*, 2463-2475

Hilker, T., Nesic, Z., Coops, N.C., & Lessard, D. (2010b). A New, Automated, Multiangular Radiometer Instrument for Tower-Based Observations of Canopy Reflectance (AMSPEC II). *Instrumentation Science & Technology, 38*, 319-340

Julitta, T., Pacheco-Labrador, J., Rossini, M., Fava, F., & MacArthur, A. (2013). The EUROSPEC instrument inter comparison experiments in Edinburgh. In, *COST Action ES0903 "EUROSPEC" Final Conference*. Trento, Italy

Kostkowski, H.J. (1997). *Reliable Spectroradiometry*. La Plata, Md: Spectroradiometry Consulting

Kuusk, J. (2011). Dark Signal Temperature Dependence Correction Method for Miniature Spectrometer Modules. *Journal of Sensors, 2011*

Markham, B.L., Williams, D.L., Schafer, J.R., Wood, F., & Kim, M.S. (1995). Radiometric characterization of diode-array field spectroradiometers. *Remote Sensing of Environment, 51*, 317-330

Meroni, M., Barducci, A., Cogliati, S., Castagnoli, F., Rossini, M., Busetto, L., Migliavacca, M., Cremonese, E., Galvagno, M., Colombo, R., & di Cella, U.M.

(2011). The hyperspectral irradiometer, a new instrument for long-term and unattended field spectroscopy measurements. *Review of Scientific Instruments, 82*

Meroni, M., Busetto, L., Guanter, L., Cogliati, S., Crosta, G.F., Migliavacca, M., Panigada, C., Rossini, M., & Colombo, R. (2010). Characterization of fine resolution field spectrometers using solar Fraunhofer lines and atmospheric absorption features. *Appl. Opt., 49*, 2858-2871

Meroni, M., Rossini, M., Guanter, L., Alonso, L., Rascher, U., Colombo, R., & Moreno, J. (2009). Remote sensing of solar-induced chlorophyll fluorescence: Review of methods and applications. *Remote Sensing of Environment, 113*, 2037-2051

Meywerk, J., & Ramanathan, V. (1999). Observations of the spectral clear-sky aerosol forcing over the tropical Indian Ocean. *Journal of Geophysical Research: Atmospheres, 104*, 24359-24370

Middleton, E., Corp, L.A., & Cook, B.D. (2013). FUSION: Canopy Tower System for Remote Sensing Observations of Terrestrial Ecosystems. In, *White Paper*

Milton, E.J., & Rollin, E.M. (2006). Estimating the irradiance spectrum from measurements in a limited number of spectral bands. *Remote Sensing of Environment, 100*, 348-355

Milton, E.J., Schaepman, M.E., Anderson, K., Kneubühler, M., & Fox, N. (2009). Progress in field spectroscopy. *Remote Sensing of Environment, 113, Supplement 1*, S92-S109

Nicodemus, F.E., Richmond, J.C., Hsia, J.J., Ginsberg, I.W., & Limperis, T. (1997). Geometrical considerations and nomenclature for reflectance. In B.W. Lawrence, A.S. Steven & H. Glenn (Eds.) (pp. 94-145): Washington, DC: National Bureau of Standards, US Department of Commerce

OceanOptics (2012). OOINLCorrect Loading Non-Linearity Correction Coefficients Instructions. In O.O. Inc (Ed.) (p. 6). Dunedun, Florida, USA

Pacheco-Labrador, J., Ferrero, A., & Martín, M.P. (2014). Characterizing integration time and gray-level-related nonlinearities in a NMOS sensor. *Applied Optics, 53*, 7778-7786

Pacheco-Labrador, J., & Martin, M.P. (2014). Nonlinear Response in a Field Portable Spectroradiometer: Characterization and Effects on Output Reflectance. *Geoscience and Remote Sensing, IEEE Transactions on, 52*, 920-928

Pan, C., Weng, F., Jaross, G., Wu, X., Haken, M., Flynn, L., Janz, S., Caponi, M., Kowalewski, M., & Buss, R. (2012). OMPS early orbit dark and bias evaluation and calibration. In, *Geoscience and Remote Sensing Symposium (IGARSS), 2012 IEEE International* (pp. 1092-1095)

Reda, I., & Andreas, A. (2003). Solar position algorithm for solar radiation applications. (p. 56). 1617 Cole Blvd., Golden, CO 80401, USA: National Renewable Energy Laboratory (NREL)

Rollin, E.M., Milton, E.J., & Emery, D.R. (2000). Reference panel anisotropy and diffuse radiation - some implications for field spectroscopy. *International Journal of Remote Sensing, 21*, 2799-2810

Saber, G.R.S., Fox, N.P., Theocharous, E., Sun, T., & Grattan, K.T.V. (2011). Temperature and nonlinearity corrections for a photodiode array spectrometer used in the field. *Applied Optics, 50*, 866-875

Sims, D.A., Luo, H., Hastings, S., Oechel, W.C., Rahman, A.F., & Gamon, J.A. (2006). Parallel adjustments in vegetation greenness and ecosystem CO2 exchange in

response to drought in a Southern California chaparral ecosystem. *Remote Sensing of Environment, 103*, 289-303

Starks, P.J., Walter-Shea, E.A., Schiebe, F.R., & Markham, B.L. (1995). Temperature Sensitivity Characterization of a Silicon Diode Array Spectrometer. *Remote Sensing of Environment, 51*, 385-389

Wood, J., Potter, E., Nobbs, S., & Webb, N. (2007). *User Manual for the Sunshine Pyranometer type SPN1*. Cambridge, UK: Delta-T Devices

CHAPTER 4

Hemispherical-Directional Reflectance Distribution Function Modeling and Unmixing in a Mediterranean Tree-grass Ecosystem Using a Tower-Based Automated Multi-Angular Spectrometer

ABSTRACT

The development of automated multi-angular hyperspectral systems has brought new opportunities but also new challenges for the characterization of the Bidirectional Reflectance Distribution Function (BRDF) in a continuous basis. In this study we describe the setup of one of these systems (AMSPEC-MED) in a Mediterranean tree-grass ecosystem and the modeling of directional effects. We model the Hemispherical-Directional Reflectance Distribution Function (HDRDF) in order to account for the effects of diffuse radiation on the estimation of BRDF. This required integrating data from several days in order to increase variability of sky conditions. In addition, a 3D modeling of the observed scene is used to unmix the HDRDF of the two components of the ecosystem, trees and grass covers. To do so, optics and observation geometry were characterized. For model inversion, Tikhonov regularization and least squares solutions were compared. Estimates of HDRDF were up-scaled and compared with the MODIS BRDF product (r^2 = 0.86); and also were compared with grass hand held spectral measurements (r^2 = 0.89). Despite of uncertainties in the estimation of diffuse irradiance and the modeling of the observed scene the HDRDF unmix was reasonably achieved. Results prove the potential of multi-angular automated proximal sensing for the study of vegetation and the correction of directional effects from different sources. Further systems should consider new approaches to improve the measurement of spectral diffuse down-welling flux, to model scene heterogeneity and to explore optimal datasets and sampling schemes.

Keywords: BRDF, HDRDF, diffuse irradiance, unmix, automated proximal sensing, AMSPEC-MED, Unispec DC, tree-grass, MODIS.

1. INTRODUCTION

The BRDF relates the incoming radiation flux that reaches a given surface from a direction in the hemisphere to the reflected one in another direction (Nicodemus et al. 1977). This function is defined as the ratio between two infinitesimals and since these do not exist, BRDF cannot be measured (Nicodemus et al. 1977). However, this function is characteristic of each surface, and thought it cannot be directly measured its estimation is of large importance in remote sensing science (Lucht et al. 2000; Schaepman-Strub et al. 2006). BRDF serves to estimate albedo, which is the ratio of the reflected and incoming radiant fluxes by a surface unit from/to the whole hemisphere (Nicodemus et al. 1977). Albedo quantifies the energy absorbed by the earth, allowing the computation of the energy balance (Dickinson et al. 1990; Vermote et al. 1997). It cannot be measured from satellites since a remote sensor only samples the radiation flux within a small solid angle; however albedo can be computed integrating the BRDF (Lucht and Roujean 2000; Nicodemus et al. 1977). Moreover, BRDF allows the directional normalization of the reflectance factors, making comparable observations acquired at different sun-view geometries (Lucht and Roujean 2000). Also, since BRDF is an intrinsic characteristic of each surface, it can be used for land cover classification. Though directional and spectral information are in part redundant, their combination still could increase the degree of freedom available to discriminate different elements (Lucht and Roujean 2000). Several works have improved the classification accuracy by including information in the directional domain (Brown de Colstoun and Walthall 2006; Dupigny-Giroux 2007), by normalizing spectral information prior to classification (Colgan et al. 2012) or directly adding albedo to the classifier (Kuusinen et al. 2013; Roy et al. 2002).

BRDF products have multiple applications in the study of vegetation terrestrial ecology (Asner et al. 1998; Fassnacht and Koch 2012). The contrast between the hot and the dark spots of different vegetation indices or at several angles in the solar plane has been related with vegetation structure parameters such as Leaf Area Index (LAI) (Hasegawa et al. 2010), clumping index (Chen et al. 2003), canopy height (Wang et al. 2011) and roughness (de Wasseige and Defourny 2002). The difference between the Photochemical Reflectance Index (PRI) value in the hot and the dark spot has also been related with physiological variables such light use efficiency (Hall et al. 2008; Hilker et al. 2008a). Other authors have used the BRDF or multi-angular observations to invert complex radiative transfer models and derive biophysical parameters of vegetation (Durbha et al. 2007; Liu et al. 2007; Qi et al. 2000); to determine the sun-view geometries most sensitive to biophysical variables (Byambakhuu et al. 2010) or to get rid of directional effects prior to their estimation (de Abelleyra and Verón 2014).

BRDF is usually retrieved by inversion of linear semi-empirical kernel-driven models to compromise between complex radiative transfer and purely empirical models (Pokrovsky et al. 2003b; Wanner et al. 1997). These kernel-driven models consist on a linear combination of mathematical functions that represent the major BRDF features. They are computationally cheap to invert, need no prior knowledge of the pixel contents, and require only a limited number of remote observations since usually a few kernel parameters must be estimated. Even though they are based on substantial simplifications, they acceptably represent the BRDF of land covers (Roujean et al. 1992; Wanner et al. 1997). However, much of the physics of the phenomenon is retained is also questioned (Lucht and Roujean 2000). Usually, these semi-empirical models linearly combine functions that describe the isotropic, geometric and volumetric

scattering depending on illumination and viewing geometry and, in some cases, on parameters that describe properties of the observed surface (Roujean et al. 1992; Wanner et al. 1995). The isometric kernel is a constant that represents the Bidirectional Reflectance Factor (BRF) observed and illuminated from nadir. The geometric-optical kernel characterizes the shadows and occlusion produced by the vegetation canopy in the scene based on the areas of background and canopy viewed, shaded and sunlit (Roujean et al. 1992; Wanner et al. 1995; Xiaowen and Strahler 1985, 1992). Based on the Ross theory (Ross 1981), the volumetric kernel represents the directional scattering of a medium of facets randomly distributed, simulating the leaves (Roujean et al. 1992; Wanner et al. 1995). The pixel boundary problem is overcome by assuming no pixel-to-pixel variance around the modelled pixel (Xiaowen and Strahler 1985). Therefore, kernel models describe scattering in pixels where texture is fine enough to assume homogeneity at the observing scale, and minimum variance with respect to the surrounding pixels. However, this does not mean that heterogeneous pixels cannot be modeled; in fact that is one of the advantages of linear models (Lucht and Roujean 2000; Wanner et al. 1995). Model parameters provide information about the control of each scattering type on the BRDF of the observed pixel (Roujean et al. 1992), however they lack of physical meaning and their interpretation must be carefully considered (Lucht and Roujean 2000).

A limited number of satellite missions provide multi-angular observations simultaneously, sequentially or within several days to generate standard BRDF and/or albedo products in a continuous basis, such as Moderate Resolution Imaging Spectro-radiometer (MODIS) (Schaaf et al. 2002), Advanced Very High Resolution Radiometer (AVHRR) (O'Brien et al. 1998), Polarization and Directionality of Earth Reflectance

(POLDER) (Bacour and Bréon 2005; Hautecœur and Leroy 1998), Multi-Angle Imaging Spectra-Radiometer (MISR) (Diner et al. 2005), Compact High Resolution Imaging Spectrometer (CHRIS) (Guanter et al. 2005), VEGETATION (Duchemin et al. 2002; Duchemin and Maisongrande 2002), Meteosat (Pinty et al. 2000) or Meteosat Second Generation (MSG) (Pokrovsky et al. 2003a; Proud et al. 2014). In addition, multi-angular imagery acquired from planes (Colgan et al. 2012; Weyermann et al. 2014), Remotely Piloted Aircraft Systems (RPAS) (Burkart et al. 2015; Roosjen et al. 2015) and proximal sensing (Abdou et al. 2001; Sandmeier 2000) can also retrieve BRDF. However, these measurements are mostly limited to sporadic field campaigns. One of the challenges of multi-angular proximal sensing has been the location of the sensor at the desired geometries. For example, goniometers locate the sensor at a specific observation angles while aiming at the same target. However height constrains have limited their use to the measurement of low canopies, such as grasslands (Chopping 2000; Chopping et al. 2004), crops. (Schopfer et al. 2008; Strub et al. 2003), shrubs lichens and moss (Peltoniemi et al. 2005; Suomalainen et al. 2009b), and non-vegetated covers such as soils, stones, ice or snow (Marks et al. 2015; Peltoniemi et al. 2009; Suomalainen et al. 2009a). In order to measure taller canopies and larger targets, field spectroradiometers have been also mounted on helicopters (Kimes et al. 1986) or cranes (Thomas et al. 2004). Recently, RPAS have brought new possibilities on terms of sensor location. Multi-angular observations have already been carried out from such platforms using cameras (Bendig et al. 2015; Hakala et al. 2010; von Bueren et al. 2015) and spectroradiometers (Burkart et al. 2015; Burkart et al. 2014; Roosjen et al. 2015; von Bueren et al. 2015). However RPAS show some limitations related with power constrains, payload, wind speed or legislation thus currently measurements are

mainly limited to dedicated research field campaigns (Colomina and Molina 2014; Lei et al. 2013; Salamí et al. 2014).On the other hand, in the last years the development of tower-based automated multi-angular hyperspectral systems is also increasing (Hilker et al. 2007; Hilker et al. 2010b; Huber et al. 2014; Leuning et al. 2006; Middleton et al. 2013). These systems are closely related with the study of vegetation physiology and ecosystem-atmosphere flux exchanges and thus usually installed in towers where such fluxes are measured using the eddy covariance technique (Baldocchi 2003). These systems provide new opportunities to validate and compare BRDF estimates with satellite observations (Hilker et al. 2010a; Hilker et al. 2009b).

It is noticeable that multi-angular proximal sensing does not measure the BRF but a different quantity that is used as a proxy, the Hemispherical-Conical Reflectance Factor (HCRF) (Schaepman-Strub et al. 2006). Cosine heads or Lambertian panels provide measurements of the down-welling radiation flux in the sky hemisphere. This includes, not only of the direct, but also the diffuse radiation generated in the atmosphere and in the scene. Optics sampling the up-welling radiation flux usually capture radiance within a relatively wide Field of View (FOV), which makes this component, in the simplest case, conical and can only be assumed directional if FOV is very narrow (Marks et al. 2015).

Automated systems can operate under wide ranges of diffuse-to-global radiation ratio (δ_{dif}) (Hilker et al. 2008a); whereas datasets acquired in sporadic field campaigns or remote observations are usually limited to clear sky conditions, when δ_{dif} is generally low. Nonetheless, diffuse radiation influences the reflectance factors measured (Kriebel 1975, 1978) and affects the estimation of BRDF (Hilker et al. 2008a; Martonchik 1994). A simple alternative adopted in some automated multi-angular systems has been

filtering or classifying data by sky conditions prior to the characterization of surface directional responses (Hilker et al. 2009a; Hilker et al. 2008a). However, diffuse radiation can be accounted for during the retrieval of BRDF if it is modeled or measured (Lyapustin and Privette 1999; Martonchik 1994); which can be understood as modeling the Hemispherical-Directional Reflectance Distribution Function (HDRDF) (Cierniewski et al. 2004).

Most automated multi-angular systems that have provided BRDF estimates have operated in dense forests largely homogeneous (Hilker et al. 2007; Hilker et al. 2010b), so that the same BRDF was assumed for the whole stand. However, scene heterogeneity might be a problem for multi-angular proximal sensing since changes in the composition of the patches observed at different geometries would be mixed with the directional effects. In these situations BRDF retrieval would not be straight forward. Heterogeneity is also a challenge for remote sensing as usually coarse spatial resolutions integrate the signals of the different elements of the scene. This complicates the interpretation of data (Abdou et al. 2001) and leads to errors in the estimation of biophysical parameters of vegetation (Sjöström et al. 2009). In response to this problem, different techniques have been used to disentangle the contributions of the different elements in the pixel, such as spectral unmixing analysis (Guerschman et al. 2009), classifying high spatial resolution imagery (Boggs 2010; Detto et al. 2006) or analyzing the responses of the different vegetation types to rainfall (Scanlon et al. 2002). On the contrary, proximal sensing usually deals with scene elements which are similar or larger than the pixel size. This makes necessary adopting strategies that ensure a representative sampling of the study area or the pixel; but also that allow a characterization of the different elements that compose the scene (Wang et al. 2005; Webster et al. 1989). Such

adequate sampling is needed to up-scale the optical signals and to relate them with ecosystem processes, which can be dynamic in time and space as in example gas exchanges with the atmosphere (Balzarolo et al. 2011; Gamon et al. 2010; Gamon et al. 2006b). Hand held spectroscopy can address these issues with a suitable sampling design (Wang et al. 2005); however, automated systems are usually fixed and only sample a given fraction of the area of interest. Limited experiences have been reported in the literature where automated systems have been able to tackle spatial issues. In some cases, the full system has been moved using a tram to sample the scene variability (Gamon et al. 2006a). In others, image sensors like phenological cameras, limited to a few spectral bands, have been used to identify and monitor patches of different vegetation types (Ahamed et al. 2012; Julitta 2015). To the best of our knowledge, only two multi-angular automated hyperspectral systems have been installed in heterogeneous ecosystems. The first was an AMSPEC located in a beetle infested lodgepole pine stand in Canada (Hilker et al. 2009a). In this case the observations were stratified in different classes of disturbance prior to retrieve BRDF. The second case was the DAFIS system installed in a semi-arid savanna in Senegal (Huber et al. 2014), where observations were limited to the dominant cover, the grass. However none of these automated systems have addressed the heterogeneity at intra-pixel scale.

As shown, heterogeneity complicates the remote and proximal observation of Earth surfaces and consequently the study of some types of ecosystems is inherently complex. Among them, mixed tree-grass and shrub-grass vegetation associations present one of the most wide and extensive distributions; e.g. tree-grass ecosystems occupy nearly a quarter of the terrestrial surface (27 million km^2). These systems are characterized by a complex horizontal and vertical structure where species with

different ecological strategies are mixed. Moreover they frequently experiment also a large temporal variability related to drought, seasonality, fire, herbivory and land use change. Therefore they present features inherently difficult to measure with remote sensing and represent in ecosystem and Earth system models (Hill et al. 2011). These systems face severe pressures from land use change and climate change as well as are vital for a livestock production that supports the livelihoods of more than 600 million people in development regions, where food security and livelihoods are vulnerable to climate variability, drought, degradation and famine (Hill et al, 2011; MEA 2005). Thus, despite of the importance of tree-grass ecosystems in Earth processes and human well-being these still represent a gap in Earth Observation science and land surface modeling. Their role in the climate system and feedbacks with the atmosphere are not well understood; as well as the consequences that land cover and land use change in these areas will have for ecosystems function and human beings (Hill et al. 2011).

This study describes the setup of an automated multi-angular spectrometer hyperspectral system (AMSPEC-MED) installed in a Mediterranean tree-grass ecosystem. Multi-angular observations acquired by the system from August 2013 to June 2015 were used to unmix the HDRDF of the two main ecosystem components (tree and grass), based on estimates of spectral diffuse radiation and a 3D model of the ecosystem.

2. METHODS

2.1 Study site

The AMSPEC-MED was installed on a tower adjacent to a flux tower in July 2013 in Las Majadas del Tietar, Cáceres, Spain (39 º 56 ’ 29 ’’N, 5 º 46 ’ 24 ’’W) at 259

m above sea level. The site is part of the FLUXNET (http://fluxnet.ornl.gov/site/440, last accessed 16 July 2015), Figure 1. A Continental Mediterranean climate causes hot and dry Summers that reach over 40 ºC, much above the 16.7 ºC annual average, and concentrate only 6 % of the annual 572 mm rainfall (Casals et al. 2009). This site is a tree-grass ecosystem, also known as "dehesa", where annual grasses peak in Spring, senesce by the beginning of the Summer and recover moderately with Autumn rains, before going dormant in Winter. Holm oak trees (*Quercus ilex* subsp. *ballota* L.) cover 20 % of the ground. Around the AMSPEC-MED, mean distance between them is 16 m.

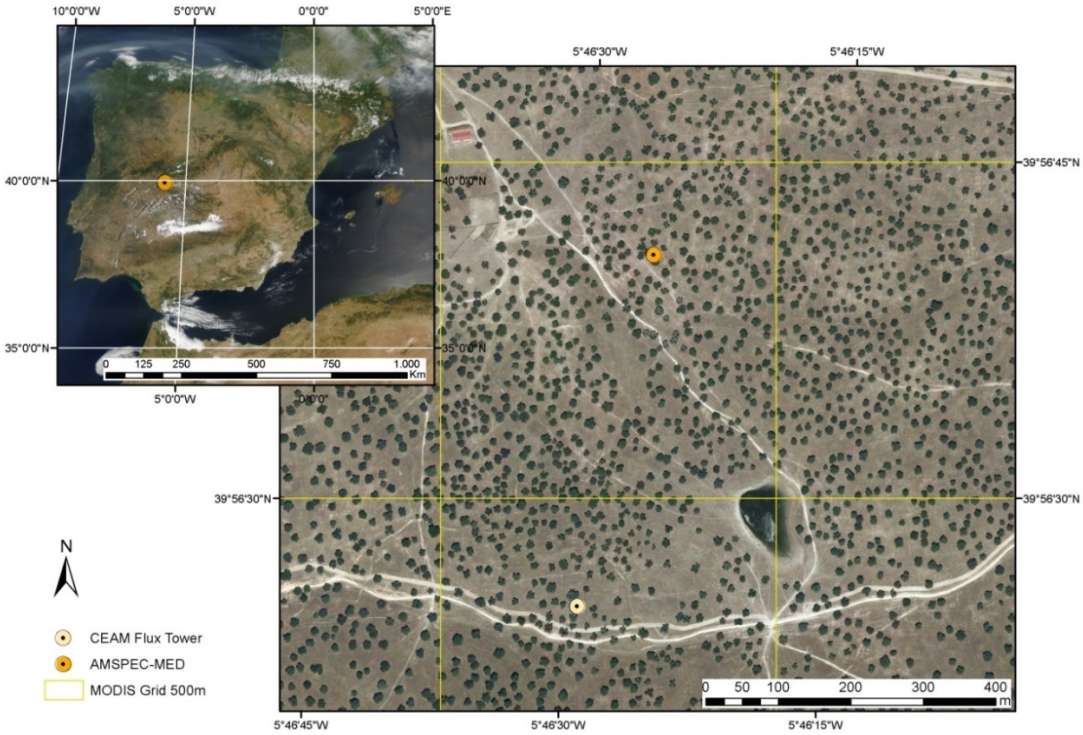

Figure 1. AMSPEC-MED location in the Majadas del Tietar study site

2.2 The AMSPEC-MED system

2.2.1 Components

The AMSPEC-MED is a modified version of the AMSPEC-II (Hilker et al. 2010b) that measures HCRF at different view angles in a continuous basis. It is divided in ground, tower and sensor modules (Figure 2). The ground module contains a CR3000 Micrologger® (Campbell Scientific Inc, Logan, UT, USA) that switches the system on and off, and a MultiConnect® rCell MTR-H6-B16-EU modem (Multi-Tech Systems Inc, Mounds View, MN United States) to transfer data via mobile phone connection. It is plugged to a set of batteries that accumulate energy generated by solar panels situated around the tower. The tower module is insulated in an electronic box at 8 m above the ground and connects to the ground module via Ethernet line. The power cable connects with a relay system that controls the power supply and distribution to the other components. A fit-PC2i computer (CompuLab Ltd., Yokneam Elite, Israel) controls data acquisition, storage and transfer via Ethernet connection with the router. There is also a Pan-Tilt Unit (PTU) D-46 controller (Directed Perception, Burlingame, CA, USA) that communicates with the computer via RS-232 through a micro USB converter. The hyperspectral sensor is a Unispec DC spectrometer (SN 2038, PP Systems, Amesbury, MA, USA), it communicates via RS-232 with the fit-PC2i. Unispec DC is a dual-channel system with two sensors featuring 256 spectral bands with an interval sampling of 3.3 nm and Full Width Half Maximum (FWHM) lower than 10 nm. The channel 1 is a 6 m optical fiber and a cosine diffuser (UNI686-6 + UNI435, PP Systems) which samples the down-welling radiation flux. Channel 2 consists of a 6 m optical fiber (UNI686-6, PP Systems) plus a 1 m extension (HPCS600IRT-1m, LEONI Fiber Optics GmbH, Berlin, Germany) linked by a SMA-

905/SMA-905 connector (LEONI). A thermostat controls two fans inside the tower module box, one on each side, which refrigerate it when air temperature exceeds 30 ºC.

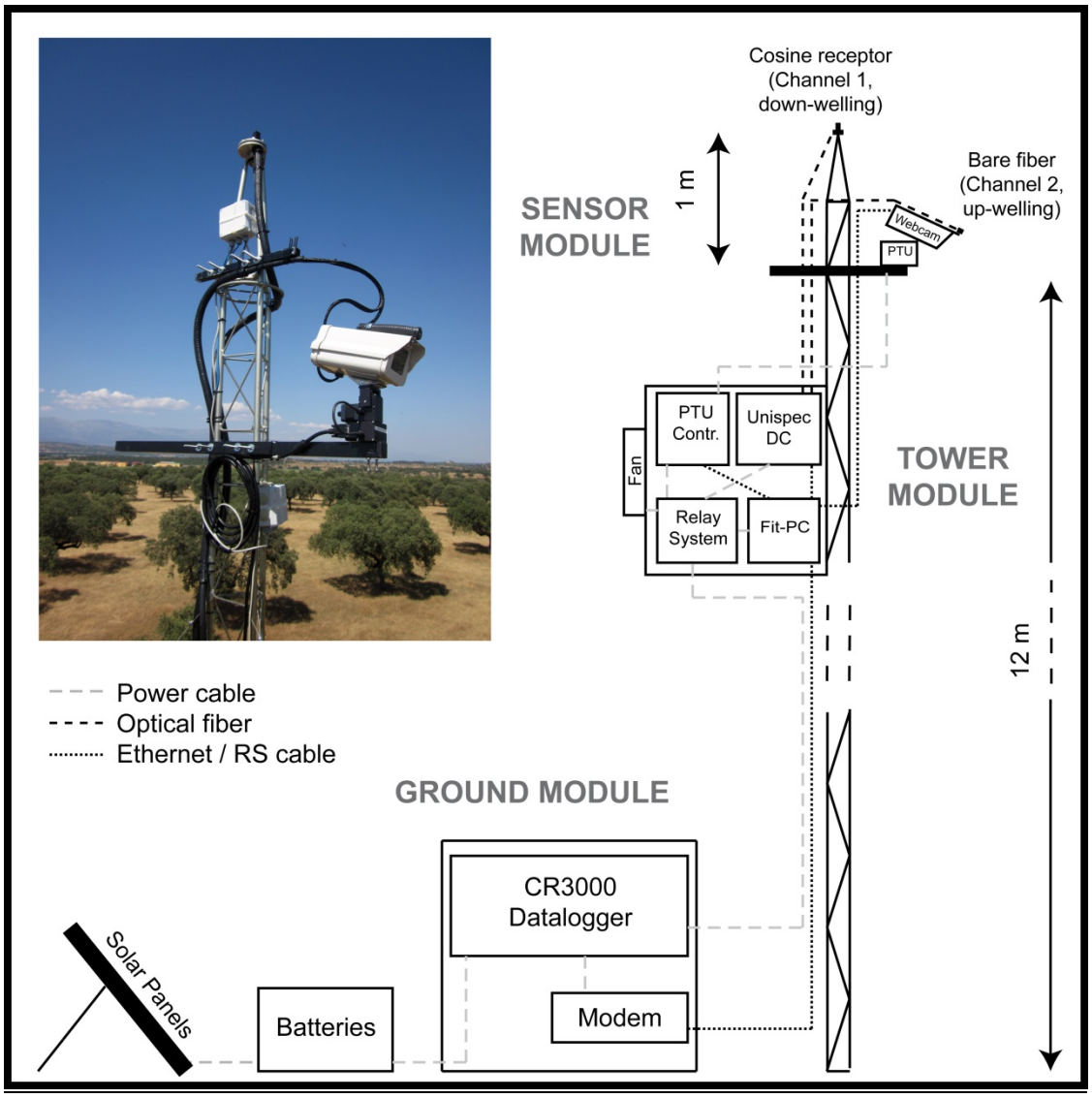

Figure 2. Main connections and module components for the AMSPEC-MED.

The sensor module is located on a horizontal arm, 40 cm distant from the tower and 12 m above the ground. A weatherized PTU D46- 17.70W (Directed Perception, Burlingame, CA, USA) installed on the arm communicates with the controller in the tower module with a RS-485 cable. The PTU holds a box with a NetCam SC 5MP

webcam, connected with the fitPC2i computer via Ethernet. The tip of the optical fiber attaches to the top of this box and connects to the channel 2 of the Unispec DC. Moreover, the cosine diffuser is located on top of the tower at 13 m, so that no other elements can shade the sky hemisphere.

2.2.2 Operation

Since the system is powered by solar panels, the datalogger in the ground module switches on and off the AMSPEC-MED when the sun elevation angle goes above and below 20 º respectively. When powered up, the PTU performs a starting/reset sequence moving to the extremes of the horizontal and vertical rotations for calibration. Meanwhile the fitPC2i computer starts up and initializes the compiled executable that controls the webcam, the PTU and the Unispec DC. This is a modified version of the Matlab® (Matworks, Natick, MA, USA) code used by Hilker et al. (2010b). The control routine initializes and configures the Unispec DC, sets communication rates, integration time and number of scans to average. Unlike in previous versions of the AMSPEC (Hilker et al. 2007; Hilker et al. 2010b), the integration time is configured here to optimize the signal in each measurement. Initially, the integration time is the minimum allowed by the instrument (4 ms) and the number of scans to average is a function of integration time, so that a measurement takes 2 s or less. The computer also communicates with the PTU to set speed, acceleration, power and rotation limits. When both PTU and Unispec DC are ready, a sequence of rotations to measure starts. First, the PTU moves to a pre-determined position. If requested, the webcam acquires an image, cuts out a 400 x 400 pixels central window and stores it as a 4D variable. Eventually, the Unispec DC takes a measurement and attempts an integration time

optimization. If the maximum Digital Number (DN) recorded in channel 1 is not in the range 40,000 ± 2,000 DN, a new integration that corrects for the difference is set. This maximizes the signal-to-noise at the same time that keeps the signal in the linear range of the instrument, as described in previous chapters. If signal saturates, it selects a pixel to set a new integration time where solar irradiance usually produces DN values about 2.7 times lower than the maximum. The instrument attempts three times the optimization so that the measurements do not stop under changing illumination conditions and continues otherwise. Moreover, if a measurement is corrupted or incomplete it is also repeated three times. If despite of these repetitions, a correct measurement is not completed the Unispec DC is switched off and restarted. Once the spectral measurement is acquired, the PTU moves to the next position.

Spectrodirectional measurements of channels 1 and 2 are organized in periods of 30 min, in which the PTU drives to "solar" and to "regular" sequences of measurements (Hilker et al. 2010b). In the "regular" sequence, the PTU fixes one of the five predefined zenith angles ϵ [40 º, 49 º, 56 º, 63 º 69 º], and scans in the azimuthal direction between 20 º and 330 º at 10 º intervals. After this, it increases the zenith angle and repeats the azimuth scan inversely. The sequence is repeated until the end of the 30 minutes period; then data are stored in a Matlab® structure format and the PTU calibrates itself. At the beginning of each period, the PTU performs a "solar" sequence driving to the sun zenith angle for the same azimuthal positions used in the "regular" sequence (Hilker et al. 2010b).

In addition to the spectral data, AMSPEC-MED stores the Universal Standard Time of acquisition, scan type ("regular"/"solar"), integration time, number of scans averaged, sensor voltage and temperature, and view and sun zenith and azimuth angles.

The input angles provided to the PTU and the actual returned ones usually differ in few tenths of degrees, so both are recorded. The algorithm described in Reda and Andreas (2004) is used to calculate the sun angles. Spectral data are back-up in a server via mobile phone connection every day at noon. The fitPC2i separately stores the webcam images once a day, during the 30 minutes period at noon, due to storage and data transfer limitations. Images are manually downloaded from the ground module using the Ethernet connection during maintenance activities. Every afternoon, AMSPEC-MED stops before sun zenith reaches 20 º and stores the last dataset acquired, the PTU returns to a safe position, and the data logger powers off the complete system.

2.2.3 System characterization and models

As described in chapter 3, in order to adequately calculate the HCRF, sensor models were adjusted in the laboratory to correct the Unispec DC measurements for dark current, nonlinearity, temperature dependence, spectral calibration and the directional response function (DRF_λ) of the cosine diffuser, where λ denotes spectral (Pacheco-Labrador and Martín 2015). Consequently, AMSPEC-MED radiometric quantities were independent of environmental conditions such as temperature, sun zenith, irradiance level, diffuse down-welling radiation, and integration time. In addition, a model predicted spectral δ_{dif} from a broadband SPN1 Sunshine Pyranometer (Delta T Devices, Cambridge, UK) installed in the flux tower (Pacheco-Labrador and Martín 2015). This variable serves to correct the directional response of the cosine diffuser and to model HDRDF.

During an inter-comparison experiment of different spectroradiometers organized by the COST Action ES0903 EUROSPEC in the NERC Field Spectroscopy

Facility at the University of Edinburgh, United Kingdom, the FOV and the DRF_λ of the Unispec DC downward-looking optical fiber was characterized (Julitta 2015). This inter-comparison aimed to test the performance of different commercial field spectroradiometers. The FOV was mapped by measuring a miniature halogen lamp mounted on a movable carriage at different positions following MacArthur et al. (2012) (Figure 3). Due to technical issues, the lamp could not be rotated at each position, so that the same part of the incandescent filament could be observed by the spectroradiometer. This produced an occlusion of the portion of the lamp filament observed, which was noticeable in the DRF_λ shapes (Julitta 2015). In order to minimize this problem, we selected the maximum values in the axial section of the FOV map and rotated them 360º around the FOV axis.

The deviation of the fiber with respect to the direction where the PTU drives and its orientation and rotation was estimated similarly as the characterization of the FOV and the DRF_λ. In this case, an experimental setup was mounted at the Environmental Remote Sensing and Spectroscopy Laboratory (SpecLab-CSIC), Madrid, Spain in which the fiber response was measured with a 1W white LED light on a movable carriage (Figure 3). The sensor module was deployed at the laboratory, and the PTU aimed horizontally. The frame holding the movable carriage was placed normal to the PTU aiming direction and the LED carefully positioned in front of the optical fiber with a laser. The LED was moved horizontally and vertically at 5 cm steps to map the FOV over the frame. The distance between the starting position of the LED and the center of the FOV map determined the actual direction where the fiber aimed.

Figure 3. On the left, experimental set-up for the DFR characterization at the NERC Field Spectroscopy Facility at the University of Edinburgh, University of Edinburgh. On the right, experimental setup to characterize the optical fiber deviations at SpecLab-CSIC, Madrid.

Once the AMSPEC-MED sensor module was later installed at Las Majadas site, zenith and azimuth deviations of the arm that holds the PTU from North and nadir were measured. Zenith deviation was measured along and across the arm alignment using a digital level S-Digit min (Geo-FENNEL GmbH, Baunatal, Germany) with a precision of ± 0.1 º. The azimuth deviation was measured placing an aligned 25 mW laser parallel to the arm and measuring the laser ray path with a GPS Leica 1200 (Leica Geosystems AG, St. Gallen, Switzerland). The laser aimed forwards and backwards and the slope of the linear model fit to the GPS coordinates determined the azimuth angle and 9 points were measured within a segment of 78.5 m. Coordinates of the base of the tower were also acquired to later determine the PTU position, whose position relative to the tower was known. All these measurements defined the actual Cartesian reference coordinate system of PTU and were used to estimate the actual observation angles.

2.2.4 Ecosystem and observation models

Airborne laser scanning (ALS) data acquired over the study area in 2010 and provided by Spanish National Plan for Aerial Orthophotography (PNOA) were used to build a tree dimensional model of the scene observed by the AMSPEC-MED. The average laser density was 0.96 points/m^2, but areas with no overlapping flight lines contained only 0.41 points/m^2. Ground and tree canopy points were classified with TerraScan (Terrasolid Ltd., Finland). Taking into account this classification, a Digital Ground (DGM) and a Surface (DSM) Model were generated using 0.5 m pixels and filling gaps up to 20 pixels. The area modeled was a rectangle of 500 x 400 m approximately. The size was determined from the observation angles of a "regular" sequence and the AMSPEC-MED was located on the North of it, since observations in this direction are occluded by the tower itself. In this area 545 trees were selected and individual crowns discriminated. For each one an ellipsoid was fit using the Matlab® package developed by Levente Hunyadi (http://www.mathworks.com/matlabcentral/fileexchange/45356-fitting-quadratic-curves-and-surfaces, last accessed 24th June 2014). Moreover, GPS measurements were used to represent the shape and location of the polluting non-vegetation elements of the scene: the solar panels, the ground module housing, the fence around the tower or and road nearby. The 3D location of the AMSPEC-MED tower module was also derived from the GPS coordinates and the known dimensions of the structure.

Based on this 3D model, a ray-casting model simulated the Unispec DC FOV to determine the contribution of trees and grasses, both sunlit and shaded, in each observation of the AMSPEC-MED. A cone of vectors was generated from a dense regular grid of coordinates within the FOV. The interval between these coordinates was

selected so that the average of all the vectors was equal to the central vector of the cone. The position of the PTU in the 3D model was determined knowing the height and azimuth direction of the arm and the distance between the mast and the PTU. Prior to model each observation, the azimuth and zenith angles provided by the PTU were transformed to the Cartesian reference coordinate system to determine the actual aiming direction of the PTU and translate the position of the optical fiber tip on it. Then the cone of vectors that describe the FOV were translated to each PTU position and rotated considering also the deviation of the optical fiber respect to the PTU aiming direction.

Once the FOV was set, each vector was projected on the DGM and the 3D coordinates calculated. All the vectors were initially classified as "sunlit grass". Then the ellipsoids representing the trees located within and around the FOV were selected and the vectors that intercepted these ellipsoids were classified initially as "sunlit trees"; the coordinates of interception replaced the original coordinates projected on the DGM. At this point we discarded any observation with polluting elements within the FOV like a fence, solar panels or a road nearby; as well as any observation that unexpectedly might reach out of the 3D model. If the measurement was not discarded, we used the sun angles to determine the shadow fraction of each cover. All the ellipsoids that might cast a shadow within the FOV were selected; these were those within the FOV projected on the ground and within a distance from it estimated from the sun elevation angle and the maximum tree height. All the points intercepting grass and trees were projected towards the sun; Those which intercepted any of the selected ellipsoids and whose distance to sun was larger or equal to that of the ellipsoid, were classified as "shaded grass" or "shaded tree" respectively. Shades in the trees could be produced by their own crowns or by other tree crowns. For each 30 minutes sequence of measurements, a

Matlab® structure variable type was generated to store the FOV vectors with the corresponding interception coordinates, sunlit/shadow and tree/grass classification; and all the geometric variables of each observation.

To determine the contribution to the observation (α) of each one of the four categories, we calculated the fraction of vectors of the FOV that intercepted each category weighted by the DRF_λ of the optical fiber. To do so, a weight was assigned to each vector of the FOV interpolating the DRF_λ measurements. Since DRF_λ is different for each band fractions are actually not estimated in this phase, but when later, during the modeling of the HDRDF. Similarly observation zenith and azimuth angles of each category were calculated as the mean angles of the vectors that intercepted each surface, also weighted by the DRF_λ of the optical fiber.

2.2.5. Data processing

Spectra recorded by each Unispec DC channel were used to calculate the HCRF in a daily basis. For every measurement, sensor temperature, integration time and the raw signal in DN were used to correct dark current, nonlinearity and temperature dependence as described in chapter 3 and Pacheco-Labrador and Martín (2015). During the process, saturated spectra were filtered out. Then the spectral calibration model of each channel was used to linearly interpolate channel 2 spectra to the corresponding wavelengths of channel 1. Sun zenith angle and spectral δ_{dif} were used to correct the directional response of the cosine diffuser in channel 1. Spectral δ_{dif} was calculated using the model fit in Pacheco-Labrador and Martín (2015) interpolating the measurements averaged every 10 minutes by the SPN1 pyranometer located in the flux tower. Data were filtered in a daily basis; measurements acquired 4 hours after the last

rain event and reflectance outliers were removed. Then the calculated δ_{dif}, HCRF and the corrected spectra in DN of both channels were stored.

In a second phase, the 3D and the ray casting models simulated the contents of each observation. For each ray in the FOV the interception coordinates with the vegetation and type of cover (grass/tree, sunlit/shaded) were stored. However, if the absolute difference between the input and the output angles of the PTU was larger than 0.2 º, or if the FOV included polluting surfaces as described in section 2.2.4; the observation was not analyzed.

The third phase was the modeling of HDRDF; that made use only of observations for which both, HCRF and FOV contents were available. At this stage, the contribution of the different covers and the average observation angles were calculated using the DRF_{λ} of the optical fiber for each band. HCRF, δ_{dif}, contributions and observation and illumination angles were used for the retrieval of HDRDF using the methods described in the following section.

2.3. HDRDF and BRDF modeling

This section describes the HDRDF model and inversion method. This model is tested against synthetic data, the AMSPEC-MED measurements, and independent measurements both proximal (hand held spectroscopy) and remote (a BRDF product). A summary of the abovementioned analyses and the datasets used in each case can be found in the Figure 4.

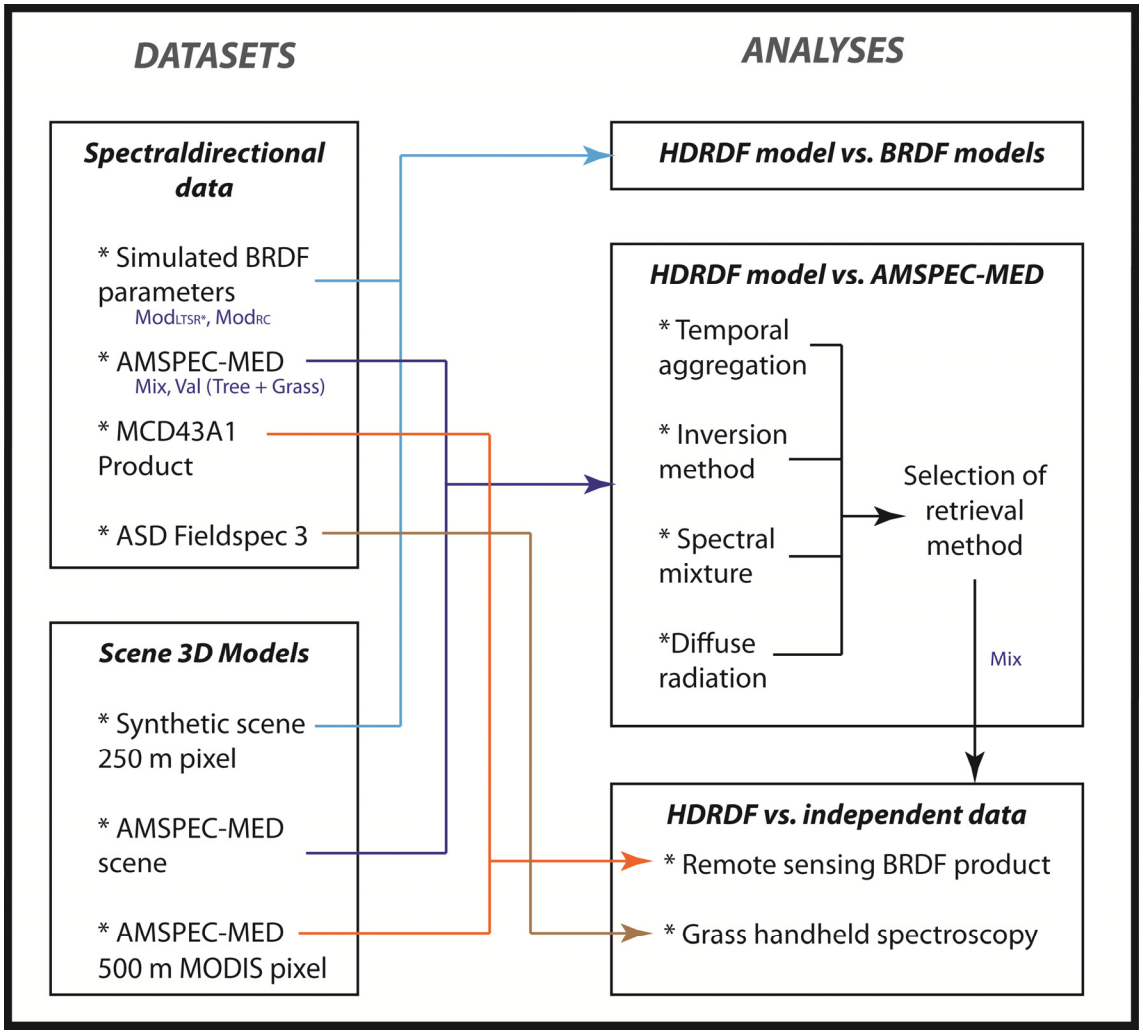

Figure 4. Summary of the analyses and datasets used to test the HDRDF model.

2.3.1 Model definition

Up to now, multi-angular automated tower-based systems used for BRDF retrieval have been deployed in ecosystems that were homogeneous (Hilker et al. 2008a; Hilker et al. 2010a; Leuning et al. 2006) or where pure observations of the different covers could be identified (Hilker et al. 2009a). In these cases, it was possible assuming that the differences between the observations of different patches of the same cover were exclusively due to directional effects. This is therefore equivalent to observing the

same pixel from different directions; which is the base of the multi-angular tower-based systems. In the case of the AMSPEC-MED, pixel heterogeneity at the viewing scale makes not possible assuming that the same cover is observed from different directions. Differences between observations are partly due to the fact that different covers are seen every time. AMSPEC-MED rather observes small areas within a pixel where only parts or a few individual elements are present but it does not observe a representative sample of the pixel. Thus a priori information of such contents is needed to model the directional effects. For this reason, we developed a 3D model of the ecosystem and a ray casting model of the AMSPEC-MED FOV. These were used to estimate which the elements of the ecosystem were present in each observation and their corresponding contributions to the sensor signal. A linear kernel-driven model is proposed to separate the isotropic, volumetric and geometric scattering of the two covers (j) described in the ecosystem: trees and grass. The contributions of each cover (αj) predicted by the 3D model were used as weight in a linear combination of semi-empirical kernel functions (Eq. 1).

$$\rho(\theta_v, \theta_s, \phi) = \sum_{j=1}^{m} \left(\alpha_j \left(k_{\mathrm{iso},j} + k_{\mathrm{geo},j} K'_{\mathrm{geo},j} + k_{\mathrm{vol},j} K'_{\mathrm{vol},j} \right) \right) \tag{1}$$

where m is the number of different covers observed. θ_v, θ_s and ϕ stand for the view zenith angle, the sun zenith angle and the relative view-sun azimuth respectively. $K'_{\mathrm{geo},j}$ and $K'_{\mathrm{vol},j}$ are the geometric and the volumetric kernel functions and $k_{\mathrm{iso},j}$, $k_{\mathrm{geo},j}$ and $k_{\mathrm{vol},j}$ are the model parameters or weights for the isotropic, geometric and volumetric coefficients respectively.

In addition, since the AMSPEC-MED system operates under a wide range of sky conditions, the model accounted for the diffuse (δ_{dif}) and direct (1 - δ_{dif}) fractions of incoming irradiance. This way, it would not be necessary to classify the measurements in different sky condition groups as previously done for other AMSPEC dataset (Hilker et al. 2008a). In all the cases, δ_{dif} is assumed isotropic. This is a common assumption in radiative transfer and BRDF analysis. It is actually an approximation; however, it makes feasible the computation while it still takes into account the most of the effect (Lucht et al. 2000; Pinker and Laszlo 1992). Therefore, our model actually represents the HDRDF based on the BRDF and the integrated components of the BRDF that account for the directional response to diffuse isotropic irradiance.

In order to model the geometric component of scattering, we substituted the typically used geometric-optical kernel functions by a new function ($K'_{\mathrm{geo_{RC},}j}$) that describes occlusion and shading from the contributions estimated by the 3D model as follows (Eq. 2):

$$K'_{\mathrm{geo_{RC},}j} = f\left(\alpha_{\mathrm{sl},j}, \alpha_{\mathrm{sh},j}, \delta_{dif}\right) = \frac{\left(\alpha_{\mathrm{sl},j} + \alpha_{\mathrm{sh},j} \cdot \delta_{\mathrm{dif}}\right)}{\alpha_j} - 1,\ K'_{\mathrm{geo_{RC},}j} \epsilon [0, -1] \qquad (2)$$

where $\alpha_{\mathrm{sl},j}$ and $\alpha_{\mathrm{sh},j}$ stand for the sunlit and the shaded contribution of each element, so that $\alpha_j = \alpha_{\mathrm{sl},j}.+ \alpha_{\mathrm{sh},j}$. The function accounts for δ_{dif} similarly as described in Hall (2011). Like other geometric-optical kernels, the function acquires negatives values (ranges between 0 and -1) describing a decrease of the reflected radiance as shadow fraction increases in the observation (Wanner et al. 1995; Xiaowen and Strahler 1985). It predicts minimum values for a shaded pixel under pure direct irradiance that would increase as diffuse irradiance illuminates shaded areas. Therefore, kernel values are the

same for a completely sunlit area ($\alpha_{\mathrm{sh},j}$=0) that is observed under a "black-sky" (δ_{dif} = 0) than for any observation under a "white-sky" (δ_{dif} = 1). Unlike other geometric-optical models, this function depends exclusively of the modeled scene, and there is not necessarily neither reciprocity nor symmetry at both sides of the solar plane (Lucht and Roujean 2000; Lucht et al. 2000; Pokrovsky and Roujean 2003a).

The volumetric scattering was modeled using Ross kernels (Roujean et al. 1992; Wanner et al. 1995). After different tests, we selected the Ross-thick kernel (Roujean et al. 1992) for both grass and tree covers. In their original *formulae* these functions only describe the bidirectional scattering; however these can be integrated over the hemisphere of view or illumination angles becoming exclusively dependent on θ_{s} or θ_{v} respectively. This has been done for the computation of black-sky albedo (Lucht et al. 2000) or emittance (Snyder and Zhengming 1998). In order to model HDRDF Cierniewski et al. (2004) used the integrated forms of the kernel functions over the illumination hemisphere to calculate HDRF under isotropic diffuse illumination; these integrated forms only depend on θ_{v} (Eq. 3).

$$h_k(\theta_{\mathrm{v}}) = \frac{1}{\pi}\int_0^{2\pi}\int_0^{\pi/2} K(\theta_{\mathrm{s}}, \theta_{\mathrm{v}}, \phi)\sin(\theta_{\mathrm{s}})\cos(\theta_{\mathrm{s}})\, d\theta_{\mathrm{s}} d\phi \tag{3}$$

Later, the hemispherical-directional form of the kernel can be linearly mixed with the bidirectional kernel as a function of the diffuse and the direct irradiance components both in the sunlit and shaded fractions (Eq. 4).

$$K'_j = \frac{\alpha_{\mathrm{sl},j}}{\alpha_j}\Big((1-\delta_{\mathrm{dif}})K\big(\theta_{\mathrm{s}}, \theta_{\mathrm{v,sl},j}, \phi_{\mathrm{sl},j}\big) + \delta_{\mathrm{dif}} h_k\big(\theta_{\mathrm{v,sl},j}\big)\Big) + \frac{\alpha_{\mathrm{sh},j}}{\alpha_j}\delta_{\mathrm{dif}} h_k\big(\theta_{\mathrm{v,sh},j}\big) \tag{4}$$

The first term represents the contribution of the sunlit area of a given cover (sl,j) illuminated by direct and diffuse radiation, whereas the second is the contribution of the shaded area (sh,j) exclusively illuminated by diffuse radiation.

From, Eq. 2 and 4 each observation was described as follows (Eq 5):

$$\begin{aligned}\mathrm{HDRF} = {} & \alpha_{\mathrm{G}} k_{\mathrm{i,G}} + \alpha_{\mathrm{G}} k_{\mathrm{geo}_{RC},\mathrm{G}} K'_{\mathrm{geo_{RC},G}} + \alpha_{\mathrm{G}} k_{\mathrm{vol_{RT},G}} K'_{\mathrm{vol_{RT},G}} \\ & + \alpha_{\mathrm{T}} k_{\mathrm{i,T}} + \alpha_{\mathrm{T}} k_{\mathrm{geo}_{RC},\mathrm{T}} K'_{\mathrm{geo_{RC},T}} + \alpha_{\mathrm{T}} k_{\mathrm{vol_{RT},T}} K'_{\mathrm{vol_{RT},T}}\end{aligned} \tag{5}$$

where subscripts “G” and “T” stand for grass and tree respectively, “$\mathrm{geo_{RC}}$” stand for the geometric-optical ray casting model and “$\mathrm{vol_{RT}}$“ indicates the volumetric Ross-thick kernel. Though this model predicts HDRF, BRF values can be also computed by setting δ_{dif} to 0.

As described in Eq. 5, HDRF was modeled as a linear combination of six kernels weighted by their contribution the corresponding covers to the observation. This allows the retrieval of the HDRDF model parameters k from observations that include significantly different fractions of each cover and acquired under different sky conditions. The simplification done here is that the quantity measured by the AMSPEC-MED, the HCRF, can be used as a proxy of HDRF in the inversion. This has been previously done in other AMSPEC systems (Hilker et al. 2009a; Hilker et al. 2008a). HDRDF is connected to BRDF as both functions share the same parameters and BRDF equals HDRDF when $\delta_{\mathrm{dif}} = 0$.

2.3.2 Model inversion and quantification of uncertainties

From Eq. 5 we deduce that for any set on n AMSPEC-MED observations for which the optical properties of vegetation can be assumed invariant, the following linear system can be built:

$$b = \mathrm{A}\,x + \varepsilon \tag{6}$$

where b is a n-by-1 matrix with the HCRF values measured by the AMSPEC-MED, A is a n-by-6 matrix containing the kernel function values where $n >> 6$, x is a 6-by-1 matrix with the corresponding coefficients (k) and ε would be a n-by-1 matrix with the associated errors. Thought linear systems are readily invertible, the sensitivity of system solutions to perturbation (ill-conditioning) and the existence of several solutions due to dependences between the columns of matrix A (ill-posedness) must be taken into account. Several works deal with these issues in the retrieval of BRDF parameters from linear models (Cui et al. 2014; Pokrovsky et al. 2003b; Pokrovsky and Roujean 2003a, b; Wang et al. 2007). Though in the case of multi-angular remote observations the ill-posedness is related with the lack of observations or even the underdetermination of the system; AMSPEC systems usually sample so much data that systems are largely overdetermined (Hilker et al. 2008a). However, condition numbers can be large so that model coefficients can be extremely sensitive to perturbation. To avoid these problems, additional conditions can be imposed to the minimization of the sum of squares using techniques such as Tikhonov regularization (Tikhonov and Arsenin 1977); where together with the sum of squares of residuals, the sum of squares of the solution is also minimized (Eq. 7):

$$x_\beta = \text{argmin}\{\|\text{A}x - b\|_2^2 + \beta^2\|L(x - x^*)\|_2^2\} \tag{7}$$

where x_β is the regularized solution, β is the weight given to the minimization of the solution Euclidean norm, L is the identity matrix or a derivative operator and x^* can be included as an initial estimate of the solution. Eq. (7) can be rewritten as a least squares problem (Eq. 8):

$$x_\beta = \text{argmin}\left\{\left\|\begin{bmatrix}\text{A}\\ \beta\text{L}\end{bmatrix}x - \begin{bmatrix}b\\ \beta\text{L}x^*\end{bmatrix}\right\|_2\right\} = \|\text{C}x - d\|_2^2 \tag{8}$$

The problem can be summarized with the new matrices C and d analogous to A and b respectively. As can be seen in Eq. (7), the coefficient β controls the balance between the two errors that determine the regularized solution, the perturbation error and the regularization error. The L-curve method can be used to select an optimal balance between both errors by looking for the maximum curvature log-log relationship between the norm of the error and the norm of the solution (Hansen 1992). Tikhonov regularization was used to retrieve HDRDF parameters using the Matlab® package developed by Hansen (2007), available at http://www.mathworks.com/matlabcentral/fileexchange/52-regtools (last accessed, 21st April 2015). Problems were solved in the "standard form" (L = I_n) and no initial estimate of the solution (x^*) was provided. In addition, we also computed the ordinary least squares (OLS) solution for comparison.

In a least squares problem the uncertainty half-band associated to the vector of coefficients ($\delta_{\hat{x}}$) can be derived using information present in the diagonal of the covariance matrix of the matrix of predictors ($[(A^TA)^{-1}]_{qq}$, where "q" is the row or column number) and the error variance (σ^2) (Van De Geer 2005). As shown in Pokrovsky and Roujean (2003a), confidence intervals can be established from the inverse Student's cumulative distribution value ($T_{inv}(1- \gamma/2, v)$) for a given significance level (γ) and degree of freedom (v) (Eq. 9) and propagated to produce the uncertainty half-band of the predicted directional reflectance ($\delta_{\hat{y}}$) from a given set of predictors (Z) (Eq. 10), where A can also be the C matrix in Eq. (8).

$$\delta_{\hat{x}} = T_{inv}\left(1 - \frac{\gamma}{2}, v\right)\sqrt{\sigma^2[(\mathrm{A^TA})^{-1}]_{qq}} \tag{9}$$

$$\delta_{\hat{y}} = T_{inv}\left(1 - \frac{\gamma}{2}, v\right)\sqrt{\sigma^2 \mathrm{Z}^T[(\mathrm{A^TA})^{-1}]_{qq}\mathrm{Z}} \tag{10}$$

Though this analysis can be extended to the regularized solutions, it must be considered that, in this case, the estimation of uncertainty is only an approximation, since a bias might exist between the real solution (x) and the estimated solution (x_β) which is not easily taken into account (Kasper et al. 2002).

2.3.3 Model performance: comparison with remote sensing BRDF models

In this work, we propose the substitution of the geometric-optical kernels by a direct estimation of the observed sunlit and shaded fractions of each ecosystem layer. Moreover, we account for irradiance using the integrated form of the volumetric kernel

functions, and adding the diffuse radiation to the shaded fractions predicted by the 3D and the ray casting models. In this section, we analyze the changes introduced in the HDRDF shape by these modifications and compare the proposed model with a BRDF model typically used in remote sensing products. To do so, we used the ecosystem 3D model to simulate remote observations of an artificial scene where spheroid trees were randomly distributed. Crown relative height and shape were defined using the AMBRALS (Wanner et al. 1997) standard values $h/b = 2$ and $b/r = 1$ (Lucht et al. 2000; Schaaf et al. 2002). The scene was theoretically observed from a remote sensor with a small instantaneous FOV (0.3545 mrad) resulting in a diameter of 250 m at nadir, analogous to MODIS bands 1 and 2. In this case the FOV was made of a cone of 6957 vectors that equally contributed to the signal. Sun was located at three different zenith angles 30 º, 45 º and 60 º. For each illumination angle, the contributions of each cover, -sunlit and shaded- in the simulated scene were estimated for 121 observation angles homogeneously distributed in the hemisphere every 15 º; view zenith was limited to 75 º. The estimated contributions were used to simulate BRF ($\delta_{dif} = 0$) and HDRF ($\delta_{dif} = 0.5, 1$) from Eq. (5). For that, a sample of 500 vectors containing the model parameters k was randomly generated, always with the condition that the modeled reflectance factors would be comprised between 0 and 1.

In order to compare our model with other BRDF models commonly used in remote sensing (Wanner et al. 1997), the simulated BRF ($\delta_{dif} = 0$) and HDRF ($\delta_{dif} = 0.5, 1$) were used to adjust the parameters of a linear model that includes the widely used Li-Sparse-Reciprocal (Lucht 1998) and Ross-thick kernels known as RTLSR BRDF model. One of the assumptions frequently found in the geometric-optical models is that the canopy and the background are equally bright (Roujean et al. 1992; Wanner et al.

1995; Xiaowen and Strahler 1985). Since we selected the same kernel function (Ross-Thick) for both covers, any linear combination of different covers' BRDF would be directly comparable with the RTLSR model; this dataset was labeled as Mod_{TkTk}. However, the model proposed (Eq. 5) allows combining BRDFs described by different functions. In order to assess the impact of this feature we also generated a second dataset where the volumetric kernel of grass was the Ross-thin function instead of the Ross-thick (Wanner et al. 1995). This function describes the volumetric scattering of canopies with low LAI values. This second dataset was not directly comparable with the RTLSR model since canopy and background directional responses were described by different functions, and it was labeled as Mod_{TnTk}

BRF values were used to assess the effect of mixing covers with different bright in the retrieval of BRDF; whereas HDRF values were used to assess the effect of isotropic diffuse radiation. This way, both features of the model could be separately analyzed and also combined. Notice that, in these analyses, atmospheric correction and related errors were omitted and therefore we assumed that irradiance and radiance at the top of the canopy were perfectly known.

2.3.4 Model performance: comparison with real observations

The performance of the model was also tested using the AMSPEC-MED measurements to retrieve HDRDF. For that, we selected all the measurements available between 1st August 2013 and 30th May 2014. Since the proposed model deals with different sky conditions, we evaluated the need of aggregating data during a single day or for larger periods in order to improve the distribution of δ_{dif} values available for model inversion. Thus, we retrieved HDRDF using data selected from a single day

(TW0) and within three time windows around each day of the period of ± 1, ± 2 and ± 3 days around it (TW1, TW2 and TW3 respectively). Additionally, the performance of the inversion methods (OLS and Tikhonov regularization) was also tested in order to determine if any of them could provide more robust estimates of the model parameters. Then we analyzed the two main features of the modeling approach proposed: unmixing directional responses of different covers and accounting for diffuse radiation. To assess the unmixing we compared the HDRDF retrievals using different datasets: the first included all the observations where the different covers of the ecosystem were mixed ("Mix"); the following were mono-angular observations of pure grassland ("Grass") or tree crowns ("Tree"). Pure observations were not included in the "Mix" dataset, but used together as a validation dataset ("Val") to test the retrievals performed using "Mix". Finally, we compared the retrieval of HDRDF which accounts for diffuse radiation, with the direct retrieval of BRDF which assumes $\delta_{\mathrm{dif}} = 0$.

In order to assess the results these analyses we calculated the Root Mean Square Error (RMSE) of the adjusted models. We also assessed the smoothness of model parameters and the derived HDRF and BRF time series; inferring that noise in the series was due to dependences of the results on data availability and random errors. In order to maximize these effects, HDRF and BRF were also computed at geometries not observed by AMSPEC-MED, and therefore where models are not constrained by measurements. Also, parameter uncertainties were propagated to predicted reflectance factors and considered in the evaluation. Additionally, the presence of model parameters with negative values was interpreted as a bad performance of the models. Even though kernel-driven models are not completely physical, they are conceived so that reflectance factors result of the positive addition of the kernel values (Lucht and Roujean 2000),

and therefore some physical consitency is expected. Though negative values could appear when confidence intervals are considered (Pokrovsky and Roujean 2003a) these can be also be produced by ill-posedness and/or ill-conditioning of the inverse problem.

Results of the analysis described in this section were used to select the most reliable methodology for the HDRDF retrieval using data acquired by the AMSPEC-MED system. This method was used to retrieve HDRDF parameters with the associated uncertainties at the different spectral bands between August 2013 and June 2015. From these, daily BRF and HDRF values normalized to standardized sun-view geometry and sky conditions would be generated and used for the analysis of time series of comparable spectral data.

2.3.5 Comparison with remote BRDF products and hand held field spectroscopy

After selecting an adequate methodology the directional analysis (section 2.3.4), grass and tree HDRDF model parameters were retrieved between the 1st August 2013 and the 15th May 2015, and used to upscale BRF at the ecosystem level. These estimates were compared with those predicted by the BRDF parameters provided by the MCD43A1 BRDF/Albedo Model Parameters Product. For this comparison, we simulated remote observations of the ecosystem using the methodology described in section 2.3.3. In this case, the FOV was modified to produce a 500 m pixel to match the resolution of the MCD43A1. The number of vectors (6957) was kept in order to reduce computing effort after checking that this had no impact on the cover contributions estimated. The scene was simulated using the 3D model derived from airborne LiDAR data (section 2.2.4). Since this model only covered an area about 500 x 400 m, the central square of 300 x 300 m was replicated 49 times in order to cover the area that

could be observed by a MODIS 500 m pixel at the same angles as described in section 2.3.3. The contributions of each cover and the shadow fractions were estimated at θ_s = 30 º, 45 º and 60 º; and a Gaussian DRF_λ of the sensor was assumed. The contributions simulated and the HDRDF parameters estimated from the AMSPEC-MED observations were used to compute BRF values of the scene. All the MCD43A1 images acquired over the study site and available from 1st August 2013 and the 15th May 2015 were downloaded from http://e4ftl01.cr.usgs.gov. The MODIS Reprojection Tool (Dwyer and Schmidt 2006) was used to extract the parameter values from the pixel in where the AMSPEC-MED is located. These and the RTLSR model were used to compute BRF at the same sun and view angles used in the simulated scenes. BRF values predicted by the MCD43A1 and the AMSPEC-MED were compared. For the comparison, MODIS Band 1 data was used and the Unispec DC spectral bands were convolved to MODIS Band 1 by using the averaged spectral response of Terra and Aqua sensors available at http://mcst.gsfc.nasa.gov/calibration/parameters, last accessed 1st July 2015.

We also compared grass field spectra acquired in the Majadas del Tiétar site with the AMSPEC-MED HDRF estimates at the same θ_s and δ_{dif}. Hand held spectra were acquired at nadir in 25 x 25 m plots with an ASD Fieldspec® 3 in eight campaigns ± 2 h around solar midday, resulting in a total of 132 spectra. Measurements were taken with a bare optical fiber with a FOV of approximately 25 º.

3. RESULTS

3.1. AMSPEC-MED characterization and models

In this section, we describe the outcomes of the characterization of the different features of the system. A complete characterization of the Unispec DC spectrometer

was already described in Chapter 3 and Pacheco-Labrador and Martín (2015). Thus only results corresponding to the system geometry are described here.

The DRF_λ characterization of the downward-looking optical fiber revealed that the FWHM ranged between 22.79 º and 28.84 º in the range 400-1,000 nm. Actually, radiation flux was sampled within solid angles between 34.05 º and 39.64 º (accumulated DRF_λ larger than 0.05). DRF_λ showed a top-hat shape and the DRF_λ became narrower and sharper towards the Near Infrared (NIR). Figure 5 shows the DRF_λ weights of the modeled FOV for three different bands.

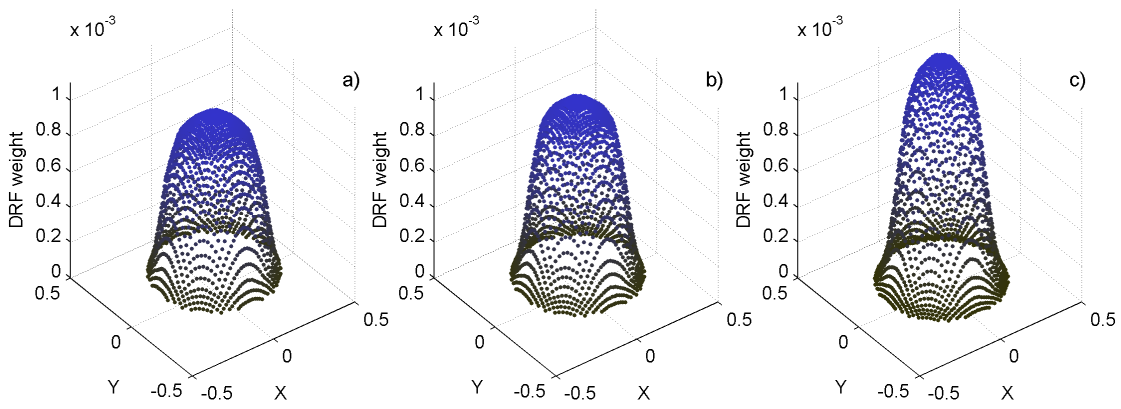

Figure 5. FOV DRF weights at 500 (a), 700 (b) and 900 nm (c). Each value corresponds to one of the vectors that represent the FOV of the AMSPEC-MED.

The observation direction of the optical fiber was found also biased respect to the direction driven by the PTU. The optical fiber aimed 0.44 º above and 0.41 º to the right side of the direction driven by the PTU. In the field, the orientation of the pole that holds the PTU was determined with an aligned laser and a GPS. The pole and therefore the relative zero azimuth reference of the PTU was at 173.72 º. The pole was inclined respect to the horizontal plane 0.33 º in the east-west direction and -0.27 º in the north-

south direction. All these angles were later considered to determine the actual orientation of the FOV. The characterization proved not to be trivial. The correction of the tower inclination and the optical fiber deviations produced differences between 1.47 º and 9.44 º in the azimuth view angles and between -3.12 º and 3.69 º in the zenith view angles for the observations of a "regular" sequence of measurements.

3.2. Ecosystem and observation models

Figure 6 shows an example of an 84 x 84 m scene generated with the 3D model and the points intercepted by the FOV vectors used for the analysis of the AMSPEC-MED data. A similar scene was generated for each AMSPEC-MED measurement in order to determine the contributions of the different covers observed. In a "regular" sequence (186 observations at different geometries), the average contribution of grasses and trees is approximately 70.5 and 29.5 % respectively. Shadow fractions vary depending on the sun position. Among the observation angles set in the "regular" sequence only one of the measurements included exclusively grass, at azimuth 84.63 º and zenith 45.32 º. The purest observation of a tree crown included ~97.5 % of tree cover within the FOV, at the azimuth 168.53 º and zenith 39.58 º. This measurement was assumed as pure in further analyses.

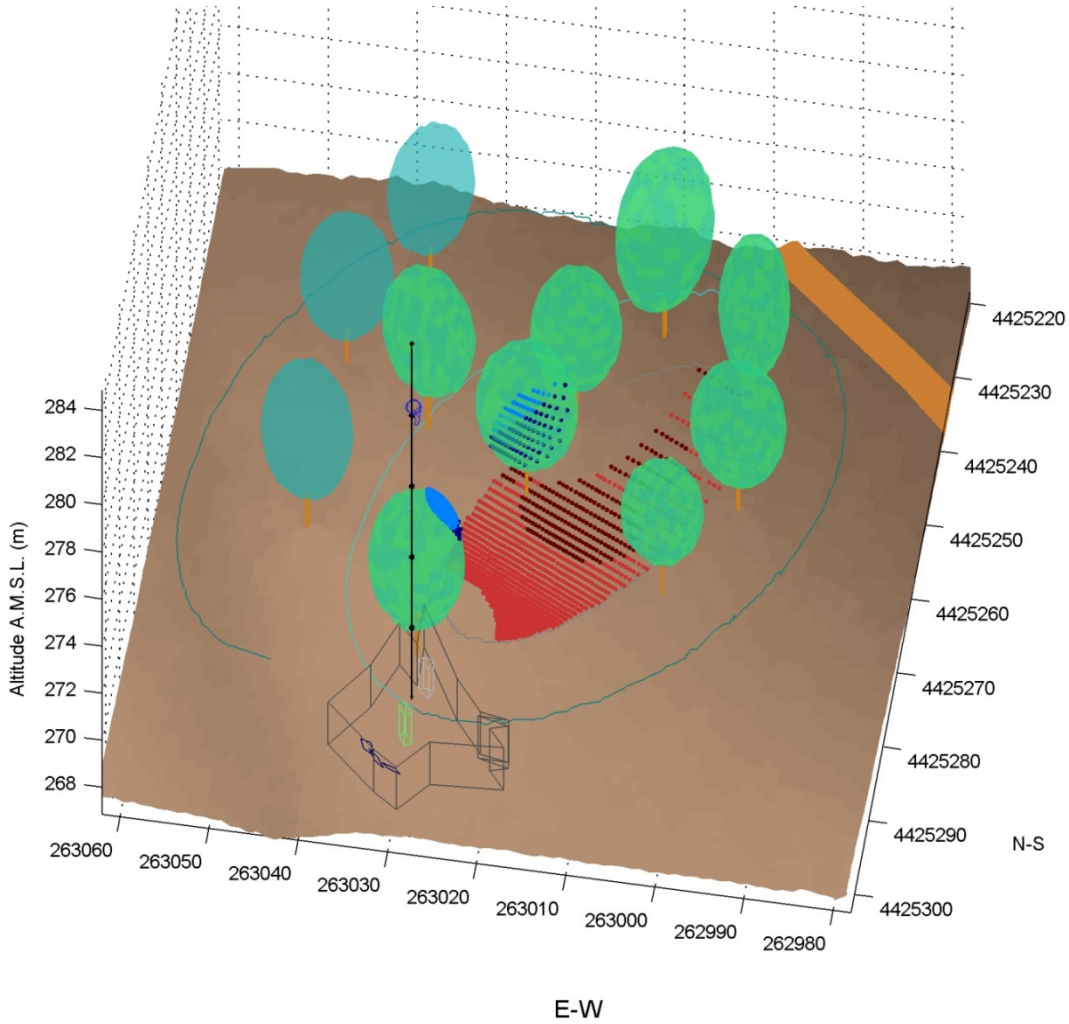

Figure 6. Example of a modeled AMSPEC-MED FOV and scene at ϕ = 206.1 º, θ_v = 57.7 º, θ_s =.60 º. Blue and red dots show the interceptions of the simulated FOV vectors. Darker tones used for shaded and brighter for sunlit areas. Tree crowns were selected to detect any interception with the FOV rays; those in turquoise were tested for producing shades in the FOV. The road on the south in bright brown, and the fence and structures nearby in grey were also represented.

3.3. Model performance: comparison with remote sensing BRDF models

Figure 7 shows one of the artificial scenes simulating observations from a 250 m MODIS pixel as described in 2.3.3; tree crowns and FOV rays interceptions are shown.

Also, threes selected to test shadow casting or interception out of the FOV can be seen in the surroundings of the doted area. In this case, the 28.33 % and the 39.79 % of the rays intercepted sunlit and shaded grass respectively, while 23.98 % and 7.91 % captured sunlit and shaded tree crowns.

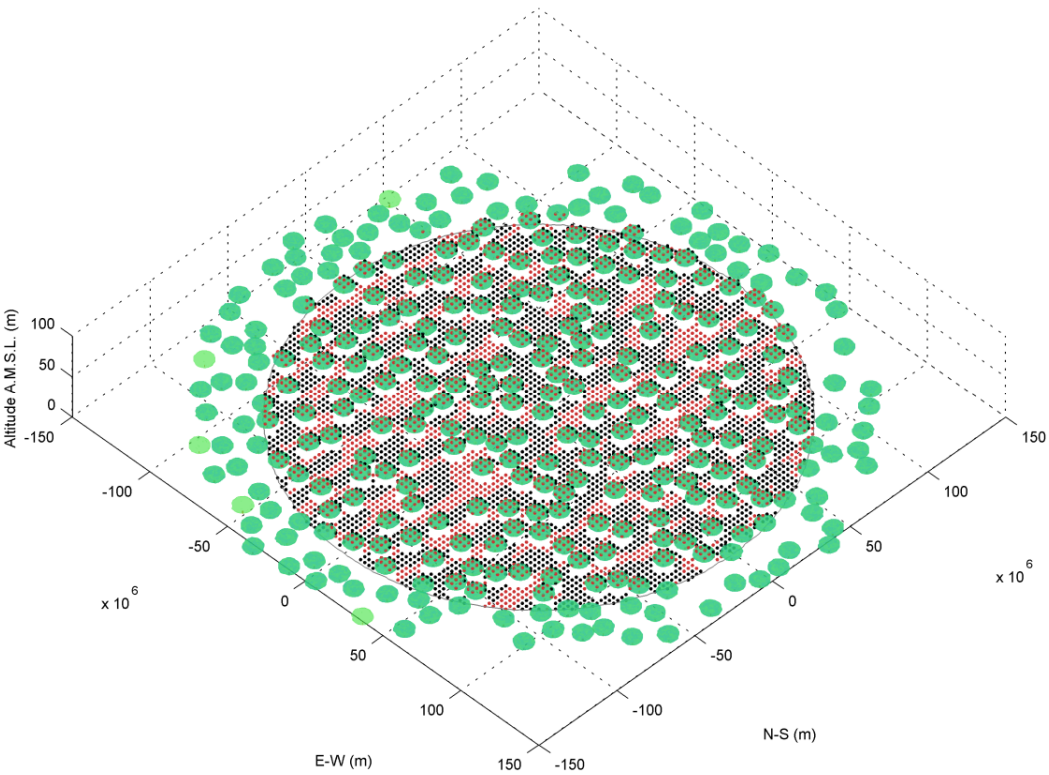

Figure 7. 3D simulated scene for a MODIS 250 m pixel at ϕ = 0.0 º, θ_v = 0.0 º, θ_s =.60.0 º. Red dots represent viewed sunlit grass or tree crowns and black dots the view shaded covers.

Figure 8 shows the different contributions estimated in the principal plane (a-c) and in the cross principal plane (d-f) for different zenith illumination angles: 30 º (a, d), 45 º (b, e) and 60 º (c, f). The total sunlit (α_{sl}) and total shaded (α_{sh}) fractions including all the covers are also shown. For comparison, the corresponding Li-Sparse-Reciprocal

and the Li-Dense-Reciprocal kernel values (Lucht 1998) are presented in an arbitrary scale. As can be seen, the total sunlit fraction resembles the Li-Sparse-Reciprocal kernel values at low observation zenith angles, but large angles the decrease is not as much abrupt and slightly behaves like the Li-Dense-Reciprocal kernel. The ray casting model is able to reproduce the "hot spot" in the backward direction, where no shaded surfaces are observed. Also the symmetry at both sides of the cross principal plane is reasonably achieved.

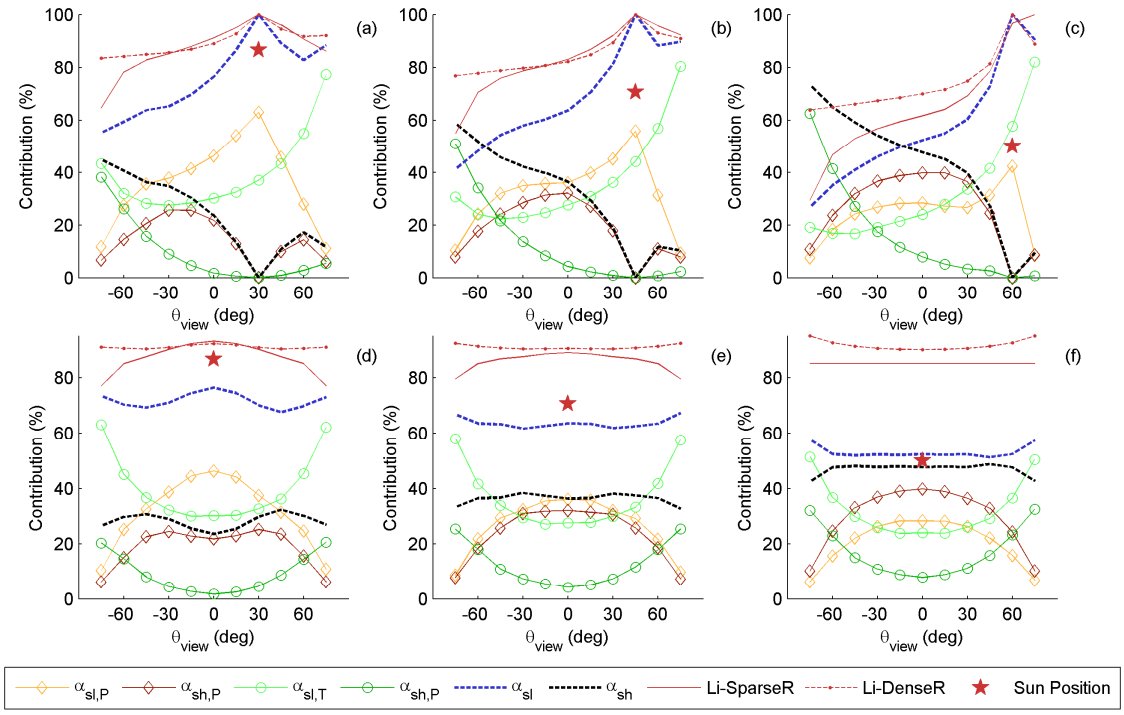

Figure 8: Contributions of the tree/grass sunlit/shaded covers and total sunlit and shadow fractions simulated with a 3D model for multi-angular remote observations. Values shown correspond to observations located in the principal plane (a-c) and in the cross principal plane (d-f) for different zenith illumination angles: 30 º (a, d), 45 º (b, e) and 60 º (c, f). Sun zenith angle and scaled values of the Li-Sparse-Reciprocal and Li-Dense-Reciprocal kernel values (b/r = 1, h/b = 2) are shown in all the cases.

The RTLSR BRDF model was fit to BRF and HDRF generated from the synthetic scene using the Mod_{TkTk} and the Mod_{TnTk} datasets. The corresponding Relative Root Mean Square Error (RRMSE) and the 95 % confidence intervals corresponding to the 500 samples simulated are presented in Table 1. In absence of diffuse radiation, RRMSE increased with θ_s and was always larger for the Mod_{TnTk} dataset. Under isotropic diffuse radiation the fit of each dataset works differently. At low θ_s Mod_{TkTk} is best fit under mid diffuse conditions (δ_{dif} = 0.5), and RRMSEs are always lower than under direct radiation and increases with θ_s. In the case of Mod_{TnTk}, the errors increase with δ_{dif} only at low illumination angles; but these are minimum at δ_{dif} = 0.5 at mid and high θ_s. Only at the highest illumination angle, RRMSEs are lower under completely diffuse radiation than under direct.

Table 1. RRMSE (%) of the fit of the RTLSR BRDF model to simulated BRF (δ_{dif} = 0) and HDRF (δ_{dif} = 0.5, 1) at different illumination angles; both mimicking the RTLSR model (Mod_{TkTk}) and representing covers of different BRDF (Mod_{TnTk}). Each dataset had 500 samples. Mean values and the 95 % confidence interval are presented.

θ_s	30 º		45 º		60 º	
δ_{dif}	Mod_{TkTk}	Mod_{TnTk}	Mod_{TkTk}	Mod_{TnTk}	Mod_{TkTk}	Mod_{TnTk}
0.0	6.2 ϵ [1.5, 12.7]	6.5 ϵ [2.0, 12.4]	7.7 ϵ [2.0, 14.5]	8.3 ϵ [2.4, 14.9]	8.2 ϵ [2.2, 15.7]	10.8 ϵ [4.1, 20.2]
0.5	5.2 ϵ [1.1, 11.0]	6.8 ϵ [2.1, 11.9]	6.8 ϵ [1.4, 15.0]	7.8 ϵ [2.3, 13.2]	7.0 ϵ [1.2, 15.8]	7.7 ϵ [2.6, 12.8]
1.0	5.3 ϵ [0.9, 12.1]	7.5 ϵ [1.8, 12.6]	7.1 ϵ [1.0, 16.8]	8.7 ϵ [2.0, 14.5]	7.4 ϵ [0.9, 18.3]	8.4 ϵ [2.1, 14.4]

Figure 9 shows the average BRF and HDRF simulated values and the values predicted by the adjusted RTLSR model. As can be seen, for the same θ_v the reflectance factors' slope in the principal plane is maximum under direct radiation (Figure 9a, d) and becomes flatter under full diffuse conditions (Figure 9c, f). Directional effects and absolute mean BRF and HDRF values are larger for Mod_{TnTk} (Figure 9d-f) than for Mod_{TkTk} (Figure 9a-c). For both datasets, RTLSR BRDF model fits reasonably when δ_{dif} = 0; however, this fit gets worse when δ_{dif} increases. In both datasets diffuse radiation led to an overestimation of the reflectance factors in the backward direction of the principal plane.

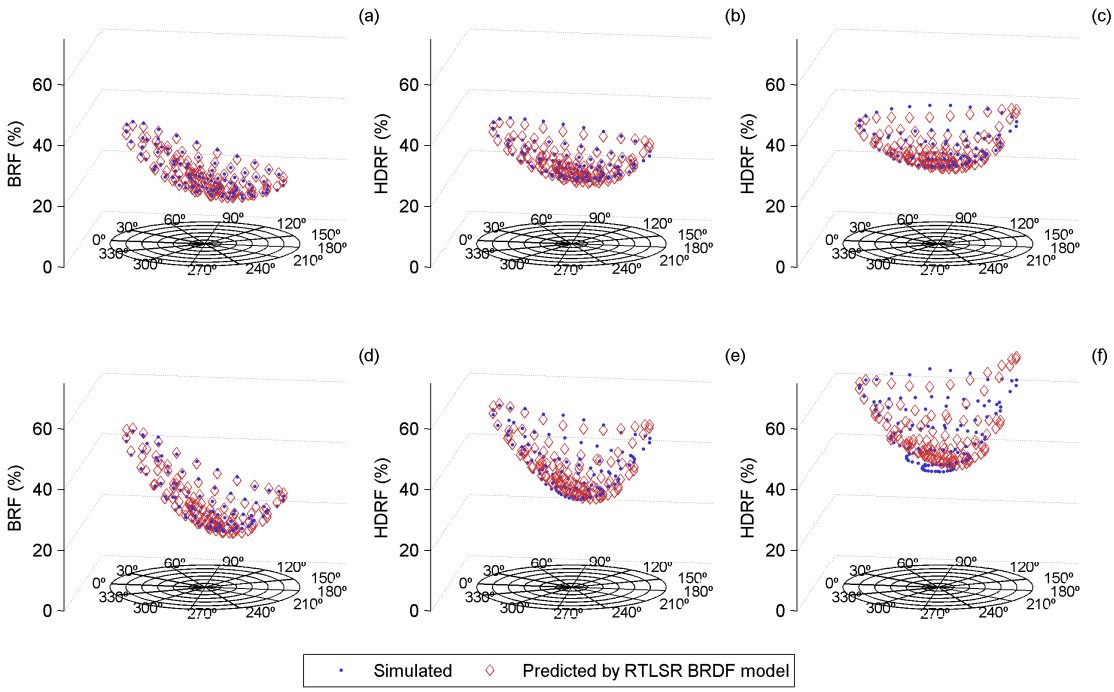

Figure 9. Average BRF and HDRF values derived from the synthetic 3D scene and the corresponding values predicted by the RTLSR BRDF model. In the bottom ϕ and θ_v are plotted every 30 º and 15 º respectively. In (a)-(c) values were simulated using Mod_{TkTk} model. In (d)-(f) values were simulated using Mod_{TnTk}. Diffuse radiation fraction

increases from left to right. In (a) and (d) $\delta_{dif} = 0$; in (b) and (e) $\delta_{dif} = 0.5$ and in (c) and (f) $\delta_{dif} = 1$. In all the cases, $\theta_s = 45$ º.

The mean values of the RTLSR parameters inverted by OLS from the Mod_{TkTk} and the Mod_{TnTk} datasets are shown in Table 2. Parameters differ for each dataset and δ_{dif} level. Diffuse radiation produced an increase of the isometric parameters and a decrease of the volumetric and the geometric ones. In fact, the parameters of the geometric kernel took negative values.

Table 2. Averaged RTLSR model coefficients retrieved over two simulated datasets of remotely observed reflectance factors and different illumination conditions. $\theta_s = 45$ º.

	Mod_{TkTk}			Mod_{TnTk}		
δ_{dif}	k_i	k_g	k_v	k_i	k_g	k_v
0.0	0.237	0.003	0.364	0.250	0.003	0.413
0.5	0.251	-0.024	0.351	0.280	-0.028	0.410
1.0	0.264	-0.050	0.339	0.310	-0.059	0.407

3.4. Model performance: comparison with real observations

3.4.1. Effect of the temporal aggregation of data

AMSPEC-MED multi-angular observations were used to retrieve HDRDF of the different components of the ecosystem between 1st August 2013 and 30th May 2014. In this period there were data available only for the 74.59 % of the days due to rain or technical failures. After data processing and filtering 300,498 observations were selected and used for the retrieval of HDRDF. Results of the data aggregation analysis are shown in Figure 10.

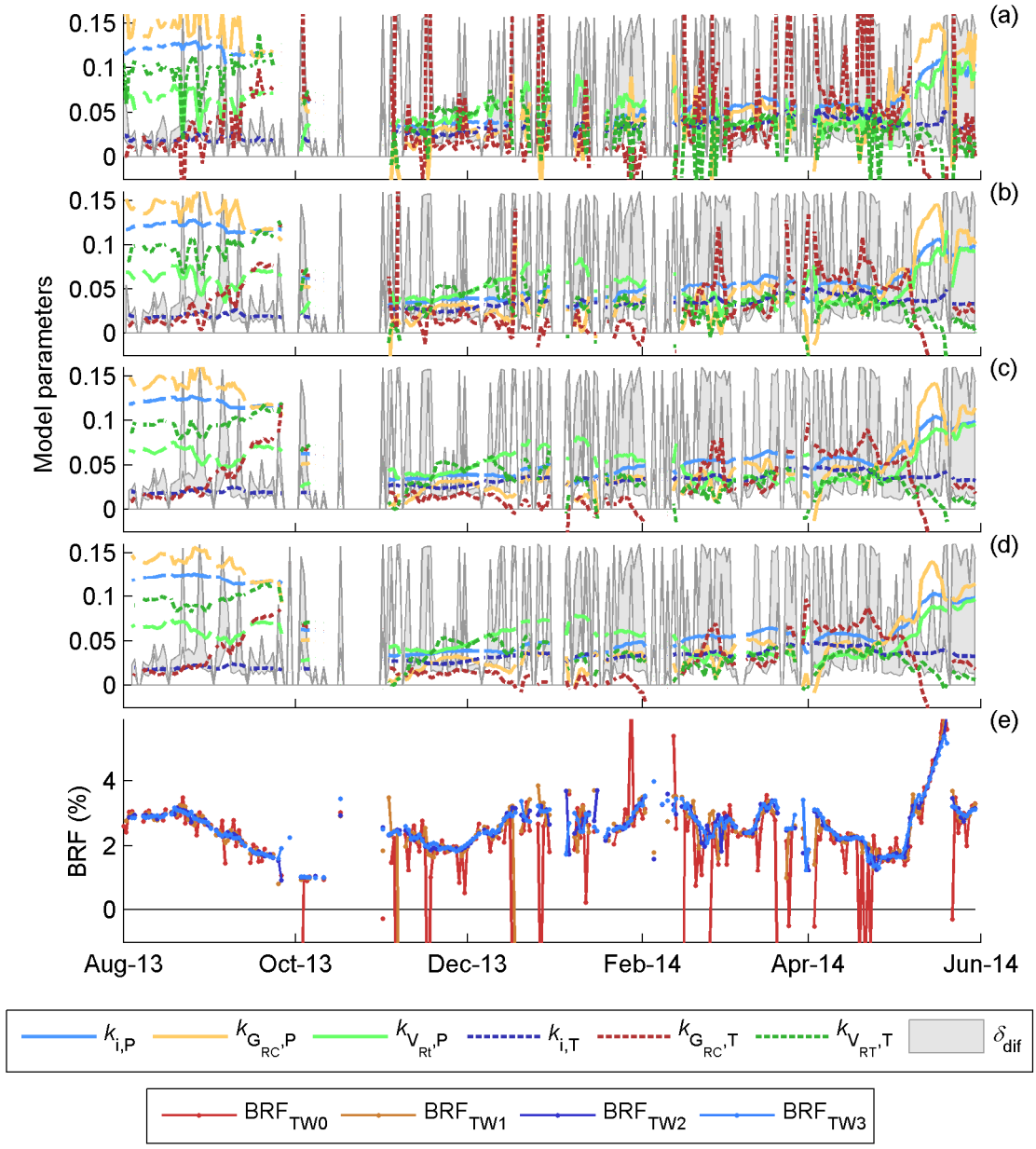

Figure 10: HDRDF model coefficients retrieved daily by ordinary least squares fitting @650 nm. Data acquired the same day (a), ± 1 (b), ± 2 (c) and ± 3 days (d). The ranges of daily δ_{dif} (between 0 and 1) are plotted scaled according to the y axis values. Predicted BRF (e) by the same model parameters for θ_s =45 º, θ_v =0 º, ϕ = 45 º, δ_{dif} = 0, $\alpha_{sl,P} = \alpha_{sh,P} = \alpha_{sl,T} = \alpha_{sh,T} = 0.25$.

Figure 10a-d shows the HDRDF model parameters corresponding to the 650 nm band. These were retrieved by OLS for from data aggregated in different time windows, as described in 2.3.4. Model parameters became less noisy along the period as the width of the time window increased. In the figure, the daily ranges of the δ_{dif} values are also shown. As can be observed, the coefficients seem to vary according to the values of δ_{dif} available. This effect is more acute the narrower is the time window used, as well as the presence of negative values in the retrieved parameters. Figure 10e shows the corresponding BRF estimates, predicted under sky conditions and sun-view configurations that were not measured by the system. Similarly, BRF noise and presence of negative values decrease as the time window width increases.

Table 3 shows the averaged uncertainties and sample size (n) of the retrievals of HDRDF for the different time windows. RMSEs shown correspond to the "Mix" dataset from where model is inverted and to the "Val" dataset used for validation purposes. In all the cases the systems were largely overdetermined; more than 1,000 observations were available, in average, for the narrowest time window. Table 3 shows the values corresponding to the model inversion using OLS, but results are similar using Tikhonov regularization. For the different time windows, no large differences were found between errors. RMSE slightly increased with the width of the time window. However, the maximum 95 % half band uncertainty was at TW0. Similar results were observed in other bands, both in the Visible and in the NIR regions.

Table 3. Time aggregation analysis results for the 650 nm band. Uncertainties expressed in reflectance (%) for the different time windows (TW). Predicted 95 % confidence half band ($\delta_{\hat{y}}$) corresponds to predicted values shown in Figure 10e.

	TW0	TW1	TW2	TW3
Mean n	1,330.6	3,560.2	5,725.6	7,854.4
$RMSE_{mix}$	1.36	1.37	1.39	1.42
$RMSE_{val}$	0.97	1.00	1.02	1.06
Predicted $\delta_{\hat{y}}$	2.03	1.89	1.89	1.92

3.4.2. Effect of inversion method

Figure 11 shows the model parameters retrieved by least squares (a, c) and Tikhonov regularization (b, d) for the narrowest (a, b) and the widest (c, d) time windows used. For both inversion methods, the width of the time window contributed to smooth coefficients across time, reducing the dependence of δ_{dif} data available for the inversion. Even for TW3, coefficients derived by OLS showed abrupt variations and largely negative values; however regularized solutions were less noisy.

Figure 11e shows the BRF computed from the coefficients above in the same graph, and the same sun-view configuration and sky conditions than in Figure 10e. TW0 led to noisier values than TW3 for both methods; OLS also produced negative values. Regularized BRF predictions reached larger and usually smoother values.

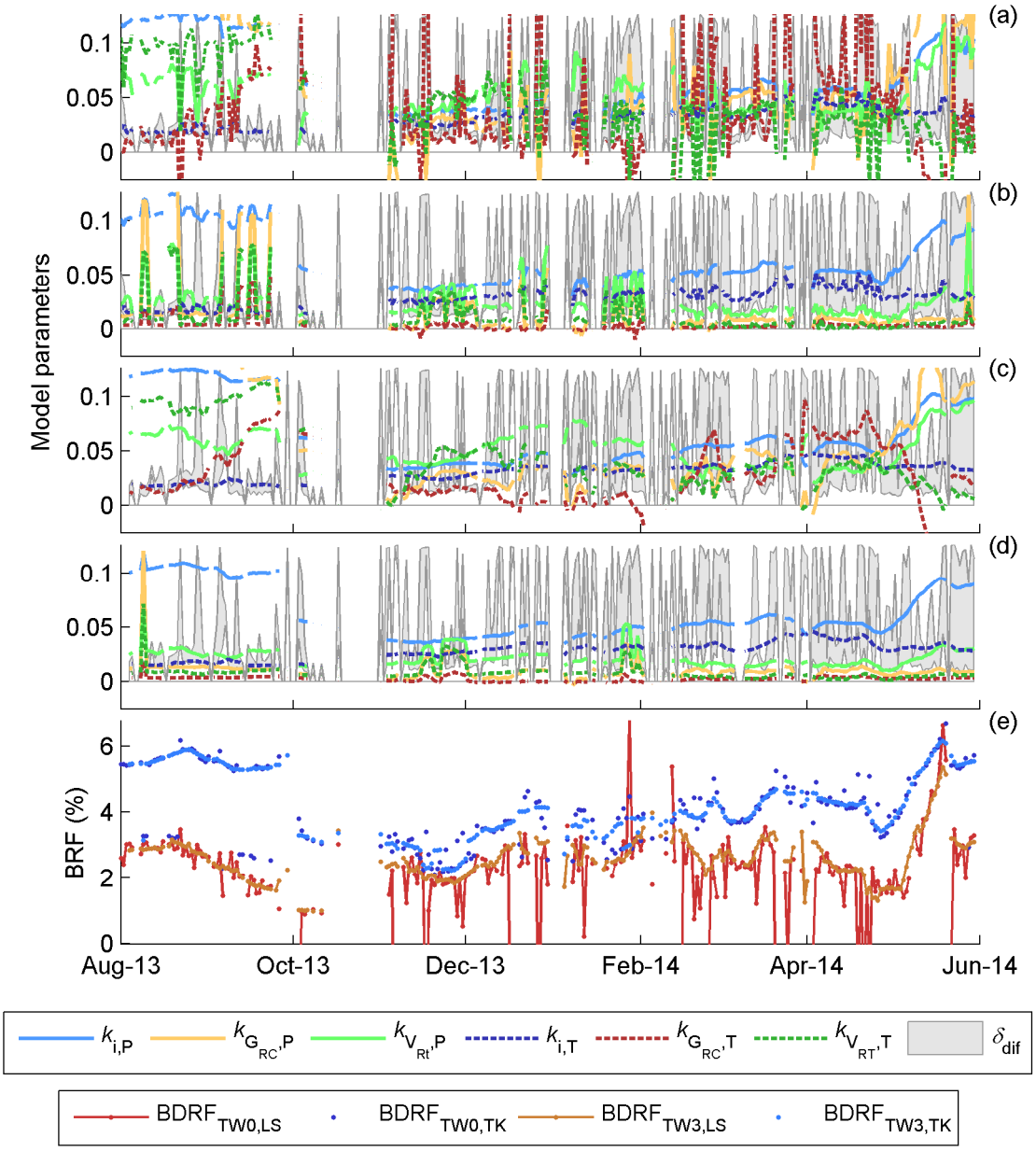

Figure 11: HDRDF model coefficients retrieved daily @650 nm for two different time windows and inversion methods. Model parameters corresponding to TW0, OLS (a); TW0, Tikhonov regularized (b); TW3, OLS (c); and TW3, Tikhonov regularized (d). The ranges of daily δ_{dif} (between 0 and 1) are plotted scaled according to the y axis values. Predicted BRF (e) for the coefficients shown above under θ_s =45 º, θ_v =0 º, ϕ = 45 º, δ_{dif} = 0, $\alpha_{sl,P} = \alpha_{sh,P} = \alpha_{sl,T} = \alpha_{sh,T}$ = 0.25.

Table 4 shows the mean RMSE and propagated uncertainties from the parameters retrieved with each method. Error variances and propagated uncertainties were larger for the regularized solutions; which also increased with the width of the time window. In the case of the OLS, mean RMSE increased with the width of the time window, whereas propagated uncertainties were maxima at TW0.

Table 4. Inversion method analysis results, @650 nm. Uncertainties expressed in reflectance (%). Predicted 95 % confidence half bands ($\delta_{\hat{y}}$) correspond to the BRF values shown in Figure 11e.

	TW0	TW1	TW2	TW3
Mean n	1323.6	3553.2	5742.9	7914.3
Ordinary least squares				
Mean fit RMSE	0.90	0.94	0.95	0.97
Predicted $\delta_{\hat{y}}$	2.03	1.89	1.89	1.92
Tikhonov regularization				
Mean fit RMSE	1.08	1.11	1.14	1.17
Predicted $\delta_{\hat{y}}$	2.12	2.18	2.23	2.30

3.4.3. Effect of the spectral mixture

In this section, we present the results of the unmixing of the HDRDF. We compare the HDRDF model parameters retrieved using datasets that include mixed and pure observations and the predicted BRF. In this case, in order to minimize the effect of other sources of noise, model parameters were retrieved using Tikhonov regularization and a time window of ± 3 days around each date. Figure 12a-c shows the model parameters retrieved using the “Grass”, “Tree” and “Mix” datasets.

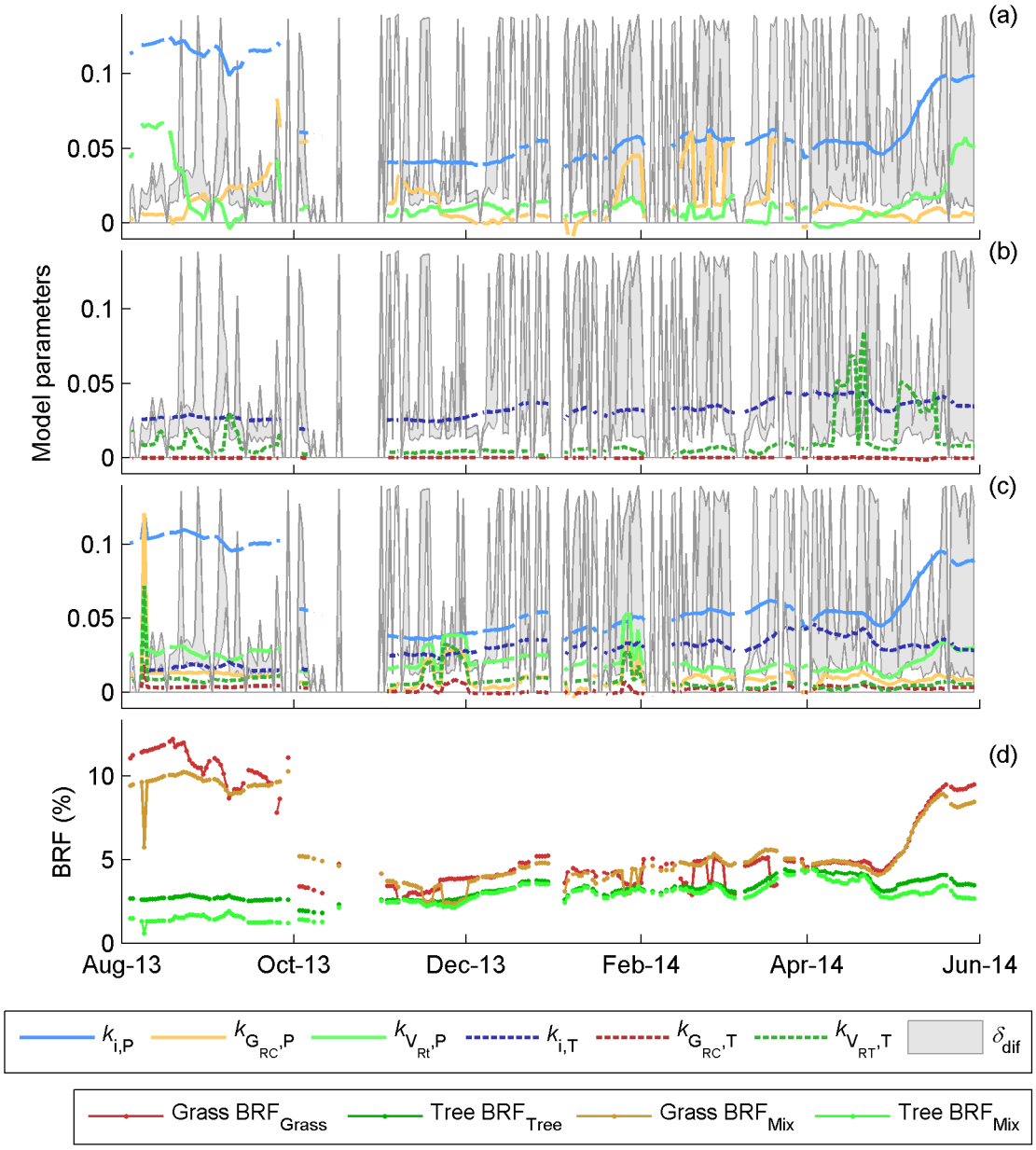

Figure 12: HDRF model coefficients retrieved daily by least squares fitting @650 nm. Parameter retrieval for a pure grass patch (a), pure tree crown (b) and a mix of grass and tree canopies (c). The ranges of daily δ_{dif} (between 0 and 1) are plotted rescaled according to the y axis values. Predicted BRF (d) for the coefficients shown above under θ_s =45 º, θ_v =0 º, ϕ = 45 º, δ_{dif} = 0, $\alpha_{sl,P}$ = $\alpha_{sh,P}$ = 0.5, $\alpha_{sl,T}$ = $\alpha_{sh,T}$ = 0.5.

As can be seen in the figure, negative parameters can be observed in the all cases. For each cover, the corresponding parameters retrieved from pure and mixed datasets showed different absolute values and also trends. These were noisier when retrieved from mon-angular pure observations. The isotropic parameters were more similar than the others in all the cases.

Figure 12d shows the grass and tree canopy BRF predicted by coefficients above in the same figure. BRF was computed under the same sun-view configuration and sky conditions than in Figure 10e, but corresponding to pure covers. As can be seen, there are differences between the predicted values of each cover depending on the dataset used to estimate the coefficients. Grass and trees BRF estimated from pure observations usually reached higher values than BRF derived from the "Mix" dataset. The largest differences were found in the Summer. Sudden changes appeared in grass BRF derived from the "Grass" and the "Mix" datasets, but these were less frequent in the case of "Mix" (Figure 12e).

Table 5 summarizes sample sizes and uncertainties related with each dataset. As shown, the sample sizes of the datasets with pure observations were considerably smaller than the one that included the remaining mixed observations available; thought in these cases the models were still largely overdetermined. These differences are explained because due to ecosystem heterogeneity and system configuration only one observation angle was sample pure patches of the two covers. Thus only the variation of illumination angles drives HDRDF. RMSE and half-band uncertainties propagated to the predicted BRF were larger when parameters derived from the "Mix" were used.

Table 5. Cover mix analysis results, @650 nm. Uncertainties expressed in reflectance (%). Predicted 95 % confidence half band ($\delta_{\hat{y}}$) corresponds to the values in Figure 12d.

	"Grass"	"Tree"	"Mix"
Mean *n*	89.1	108	7,926.3
RMSE	1.06	0.34	1.42
Predicted $\delta_{\hat{y}}$	1.82	1.05	2.30 ("Grass"); 2.30 ("Tree")

3.4.4. Effect of diffuse radiation

In this section we analyze the inclusion of diffuse radiation in the model. The retrieval of HDRDF as proposed in section 2.3.1 is compared with the retrieval of a pseudo-BRDF (BRDF*) where diffuse radiation is neglected assuming it equals 0. In order to minimize the effect of other sources of noise, model parameters were retrieved using Tikhonov regularization and a time window of ± 3 days around each date.

Figure 13 shows the model parameters retrieved neglecting diffuse radiation (a) and accounting for it (b). This is, forcing δ_{dif}.to 0 or using estimated values as described in 2.2.5 and Pacheco-Labrador and Martín (2015) respectively. Though in both cases parameters show smooth curves, the first methodology shows a larger dependence on δ_{dif} ranges. Abrupt changes and negative values in model parameters are larger and more frequent in BRDF*. Figure 13c-d show respectively BRF and HDRF values predicted from both methods with the same geometry and contributions than in Figure 12d, but full direct and full diffuse radiation were used in each case. As can be seen, when diffuse radiation is neglected, predictions largely depend on sky conditions. The largest differences between the estimates of each method can be noticed in the Summer; when also in some cases, BRDF* based predictions present sharp variations.

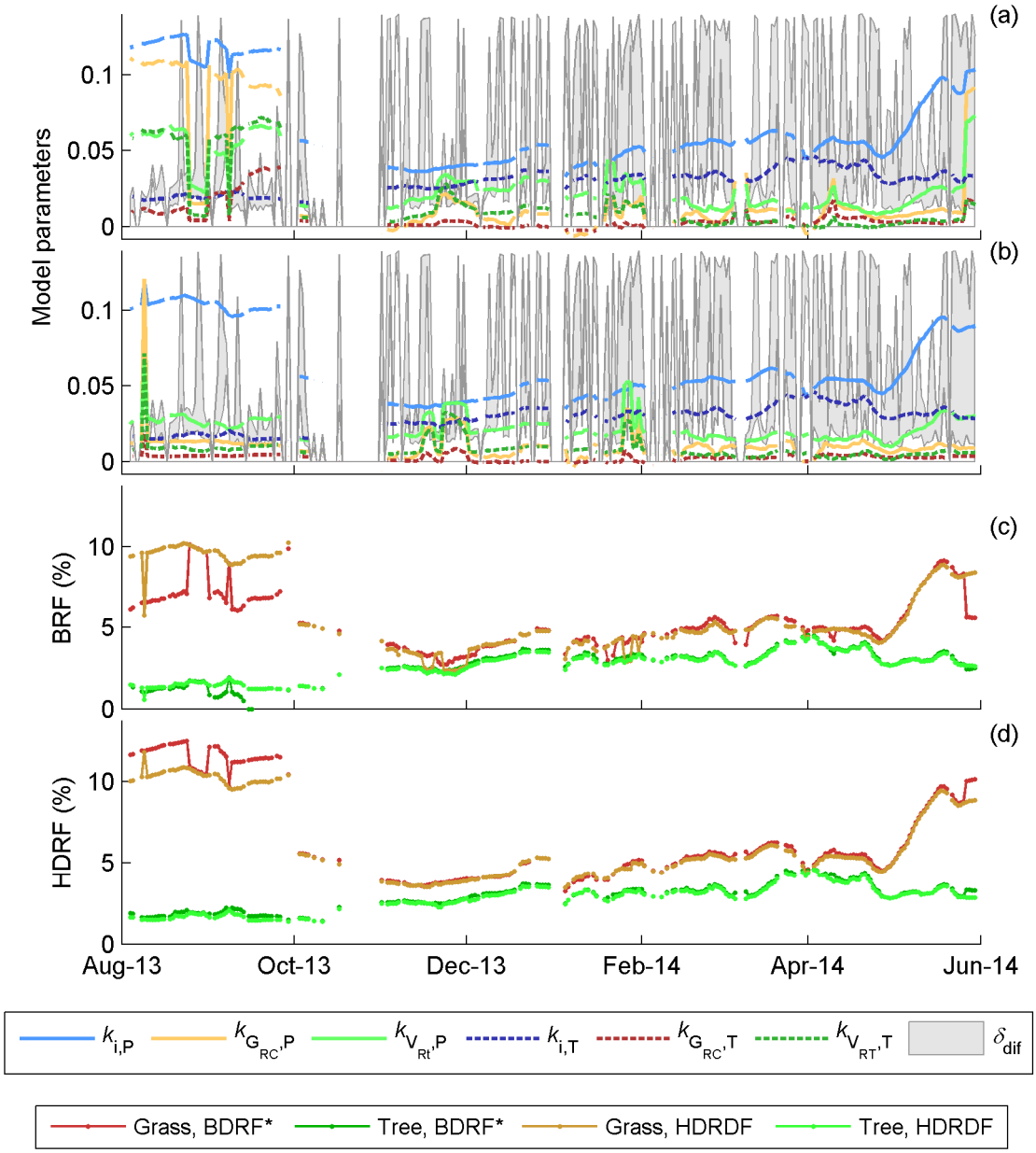

Figure 13: HDRF model coefficients retrieved daily by Tikhonov regularization @650 nm and predictions not (a) and taking (b) into account diffuse radiation. The ranges of daily δ_{dif} measured (between 0 and 1) are plotted rescaled according to the y axis values. (c) Predicted BRF values from coefficients in the same figure, δ_{dif} = 0. (d) Predicted HDRF values from coefficients in the same figure, δ_{dif} = 1. For the predictions θ_s =45 º, θ_v =0 º, ϕ = 45 º, $\alpha_{sl,P} = \alpha_{sh,P} = 0.5$, $\alpha_{sl,T} = \alpha_{sh,T} = 0.5$.

Table 6 shows the RMSE of the models fits corresponding to the datasets "Grass", "Trees", "Mix" and its validation dataset "Val". It also provides the 95 % half band uncertainties for the predicted BRF and HDRF shown in Figure 13c-d. As can be seen RMSEs were, in general, larger when diffuse radiation was included into the model. No large differences can be observed between the uncertainties in the prediction of BRF and HDRF, but these were still larger for the HDRDF-based estimates.

Table 6. Diffuse radiation analysis results, @650 nm. Uncertainties expressed in reflectance (%). Predicted 95 % confidence half band ($\delta_{\hat{y}}$) corresponds to the BRF and HDRF values shown in Figure 13c-d.

RMSE	"Grass"	"Trees"	"Mix"	"Val"
BRDF*	1.05	0.36	1.25	0.87
HDRDF	1.06	0.34	1.42	1.06
Predicted $\delta_{\hat{y}}$	BRF_{Grass}	BRF_{Tree}	$HDRF_{Grass}$	$HDRF_{Tree}$
BRDF*	2.12	2.12	2.12	2.12
HDRDF	2.30	2.30	2.30	2.30

3.4.5. Method selection and HDRDF retrieval

Previous analyses led to the selection of the most appropriate methodology to model the directional responses of vegetation from AMSPEC-MED observations. We decided modeling HDRDF using observations from mixed covers and aggregated in a time window of ± 3 days. The inversion selected was method was Tikhonov regularization, however, OLS solutions were always computed for comparison.

Figure 14 summarizes the performance of the method using the AMSPEC-MED data between the 1st August 2013 and 30th May 2015 corresponding to the 650 nm band.

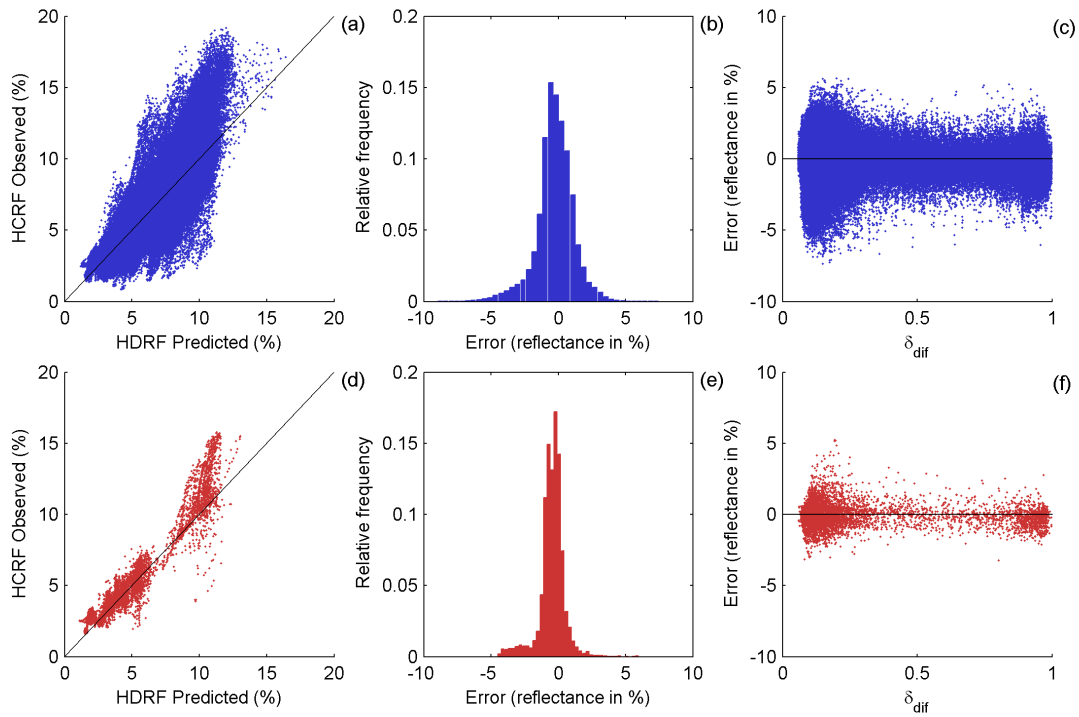

Figure 14: Model fit on the "Mix" (blue, a-c) and the validation (red, d-f) dataset @650 nm. From left to right, observed HCRF vs. predicted HDRF values (a, d), error histogram (b, e) and δ_{dif} vs. error (c, f).

From the predicted-observed scatterplots (a, c), the model seems to slightly underestimate the largest HDRF values, both, for validation and fit datasets. r^2 values were 0.76 and 0.92 respectively for the model fit and the validation datasets ($p < 0.05$ in both). The bias can be noticed in the error histograms (b, e), which are narrow and with the error still centered on 0. RMSE are 1.40 % and 0.96 % respectively. The largest errors were found under clear skies with low δ_{dif} (c, f).

Figure 15 shows the predicted HDRF and the 95 % uncertainty confidence intervals for different spectral bands frequently used in vegetation spectral indices.

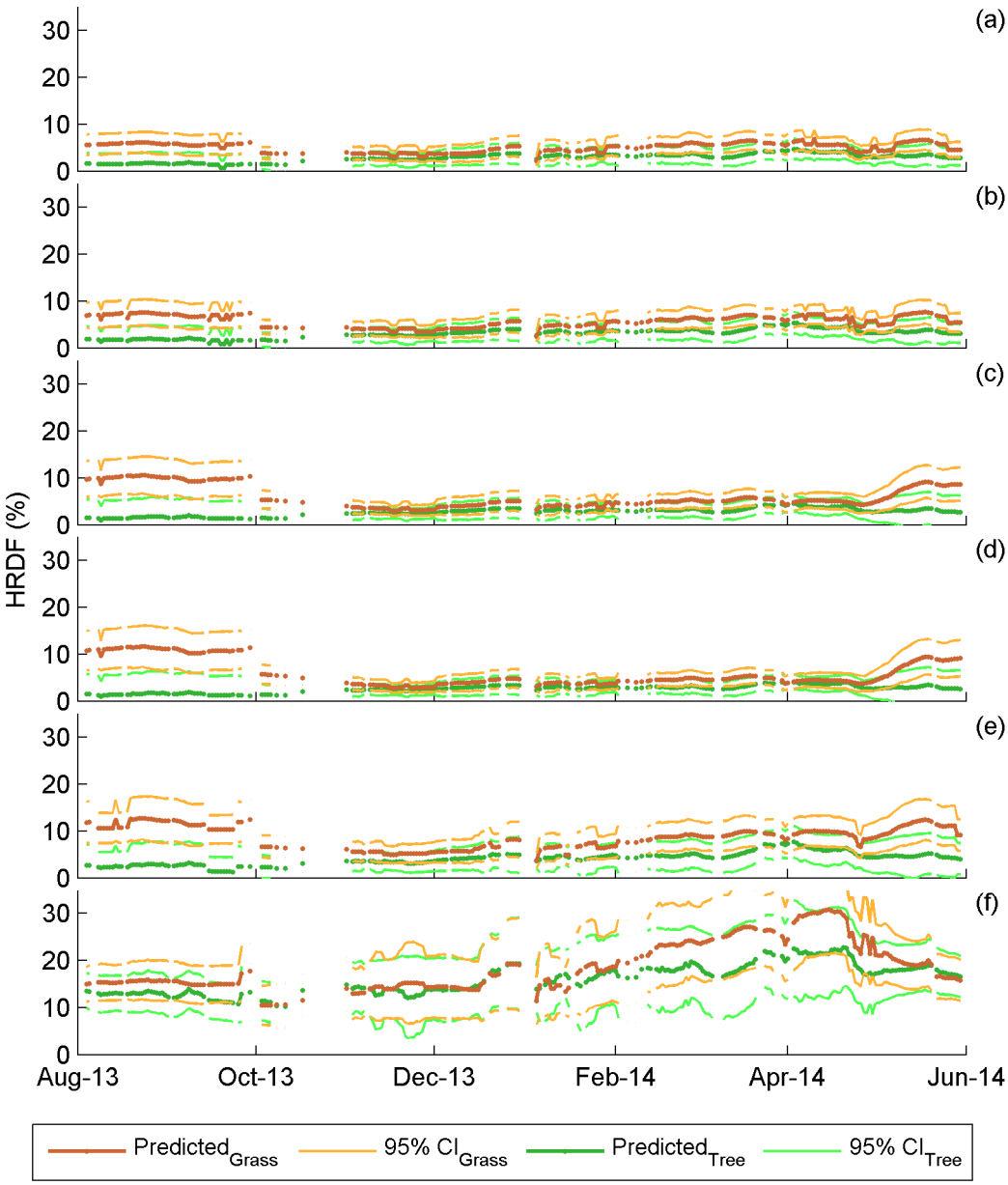

Figure 15: Predicted HDRF values and 95 % confidence intervals for 531 (a), 570 (b), 650 (c), 680 (d), 700 (e) and 800 nm (f) at θ_s =45 º, θ_v =0 º, ϕ = 45 º, $\alpha_{sl,P} = \alpha_{sh,P} = 0.5$, $\alpha_{sl,T} = \alpha_{sh,T} = 0.5$, $\delta_{dif} = 0.5$.

HDRF values were estimated for tree and grass covers separately and corresponds to a standardized observation where half of the contribution is shaded and δ_{dif} = 0.5. Thought the changes predicted across the period were smooth, still some

abrupt variations appeared in some of the bands, and confidence intervals included negative values. Uncertainties seem to become wider in the Summer, but in the case of the 800 nm band (Figure 15f) when contrarily to the other bands, the values of both covers are more similar.

3.5 Comparison with remote BRDF products and hand held field spectroscopy

Table 7 summarizes the results obtained from the comparison between AMSPEC-MED based estimates with other remote and proximal measurements. BRF up-scaled from AMSPEC-MED parametrized HDRDF and a 3D model is compared with BRF computed from the MOD43A1 parameters corresponding to band 1 of MODIS. Also, HDRF estimated is compared with hand held spectral measurements of grass. Though model parameters are derived from the AMSPEC-MED data using the methodology selected in section 3.4.5; OLS based estimates were also compared. As can be seen, OLS estimates got lager r^2 and lower RMSE than the regularized ones. For both inversion methods, errors increased and r^2 decreased with θ_s. The comparison of grass HCRF measurements with the predicted grass HDRF showed higher correlations and lower errors than in the comparison with the MCD43A1; OLS also achieved a better fit than Tikhonov regularization. In all the cases, relationships were significant ($p < 0.05$).

Table 7. Summary of the comparison of the AMSPEC-MED BRF and HDRF estimates with BRF derived from the MCD43A1 BRDF/Albedo Model Parameters Product and hand held HCRF. RMSE is expressed in reflectance (%).

	Ordinary Least Squares		Tikhonov Regularization	
	r^2	RMSE	r^2	RMSE
MODIS Band 1				
$\theta_s = 30$ º	0.86	2.07	0.84	2.32
$\theta_s = 45$ º	0.85	2.24	0.80	2.65
$\theta_s = 60$ º	0.76	3.00	0.66	3.69
ASD Fieldspec® 3, grass				
$\theta_v = 0$ º	0.89	1.85	0.85	2.10

Figure 16 shows the observed vs. predicted plots corresponding to the comparison with MODIS (a, b) at $\theta_s = 45$ ºand for the comparison with handheld grass measurements taken from nadir (c, d). The comparison with MODIS BRF shows an underestimation of the largest BRF values; which can also be observed in the comparison with hand held measurements of grass (c, d). In all the cases, the underestimation was slightly more acute for the regularized solutions than for OLS. In the comparison with MODIS, 121 different observation angles are compared for each date; in the figure, data corresponding to the nadir view are flagged in green; these show in general a better fit than the complete dataset.

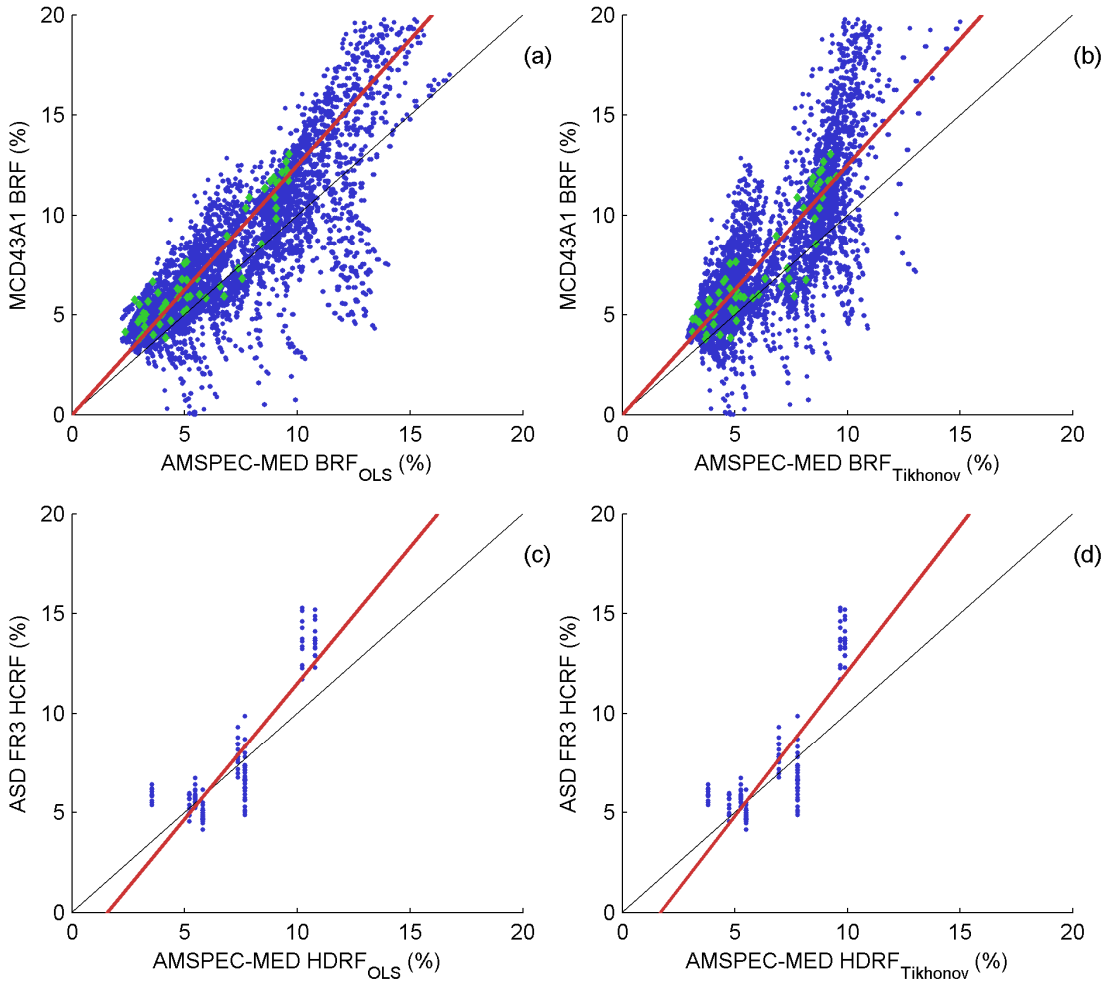

Figure 16. Comparison of ecosystem MCD43A1 BRF and AMSPEC-MED up-scaled BRF from OLS (a) and Tikhonov regularization (b) parameters; green diamonds corresponds to observations at nadir. Comparison of grass hand held measured HCRF and AMSPEC-MED predicted HDRF from OLS (c) and Tikhonov regularization (d) parameters.

4. DISCUSSION

4.1 AMSPEC-MED system and scene characterization.

AMSPEC-MED was be carefully characterized in order to correct the reflectance factors computed and to model and unmix the directional responses of the

different elements of the ecosystem. Different sensor models were developed for the correction of instrumental artifacts during the characterization of the spectroradiometer (Pacheco-Labrador et al. 2014; Pacheco-Labrador and Martín 2015; Pacheco-Labrador and Martin 2014). We found that, due to the combination of solar irradiance spectrum, optics transmittance and sensor quantum the maximum signal of the down-welling was close to 570 nm. Therefore this band could be more severely affected by gray-level-related nonlinearity than others (Pacheco-Labrador and Martin 2014). This could produce changes in the PRI due to increases in irradiance levels actually not related with changes in vegetation physiology. For this reason we included an integration time optimization in AMSPEC-MED which not only prevents from nonlinearity artifacts, but also maximizes the signal-to-noise ratio for every measurement. Since in the field site the power supply was limited and the spectroradiometer temperature could not be regulated, the characterization included dark current and temperature dependence models to correct data in the post-process.

The system integrates also information on δ_{dif} provided by a SPN1 sensor for the correction of the directional response of the cosine diffuser, and later for HDRDF modeling. However, uncertainties related to this approach might be important in some cases: First, because this is a broadband sensor from which spectral δ_{dif} values were estimated empirically. Second because the SPN1 sensor provides values integrated every 10 minutes; which are interpolated to provide estimates for each measurement of the AMSPEC-MED system. This might lead to errors when sky conditions rapidly change, e.g. under passing clouds. Nonetheless, such situations are already uncertain since, unlike assumed, diffuse radiation is largely anisotropic in a heterogeneous sky. In other circumstances these estimates might be closer to reality, and contribute to the

quality of data. Spectral diffuse radiation should be measured in automated systems; ideally using the same sensor of the system since this would provide diffuse and global irradiance values at the same wavelengths. Shadow band devices could be used to shade the spectrometer cosine receptor, as done by Barch et al. (1983). If that was not possible, multiband shadow band sensors as the one installed in FIGOS (Dangel et al. 2005) could provide better estimates of spectral δ_{dif} tan the SPN1 used in this work. If measurements of δ_{dif} could not be simultaneous to the acquisition of HCRF, at least alternate measurements or a frequency similar the one at which HCRF was acquired should be used. Nonetheless, systems based on cosine diffusers are not able to characterize the angular distribution of diffuse radiation, actually anisotropic (Lyapustin and Privette 1999). A different approach might be the one adopted by PARABOLA III (Bruegge et al. 2000) and later by FIGOS (Schopfer et al. 2008): measuring bi-conical radiation fluxes as a proxy of the bi-directional ones. All these methods would increase the complexity and the vulnerability of these systems, but might be worthy to ensure a better understanding of the effects of diffuse radiation and provide more accurate estimates of BDRF. Though in this work we adopted a very simple approach, the advantages of accounting for diffuse radiation could be noticed. An additional issue that could be taken into consideration is that diffuse irradiance generated in the atmosphere might differ from the diffuse irradiance reaching the observed surface. The latter can be increased by the scattering of adjacent objects and this would be more relevant at bands where albedo is higher and anisotropic depending on the scene structure (Courbaud et al. 2003). To account for this effect the inversion of scene radiative transfer models based on Monte Carlo simulation of photon transport might be used; however computational effort might be excessive in the case of operational automated systems.

We characterized the multi-angular system geometry in order to correctly determine the observation angles and the contribution of the different elements present in the FOV. In previous automated multi-angular systems, such a detailed termination of the FOV contents was not necessary since it was assumed that a single cover was observed (Hilker et al. 2008a; Leuning et al. 2006) or that observations could be stratified in homogeneous clases (Hilker et al. 2009a). However Hilker et al. (2008b) used an ALS to generate a canopy surface model and estimate the shadow fraction of each observation, though still in a homogeneous canopy. The effect of elements surrounding the FOV had not been previously characterized in multi-angular automated systems, though Huber et al. (2014) found that shadows casted by trees out of the observed area might explain some variations in grass anisotropy factor. In our case, the characterization of the DRF_λ of the Unispec DC optical fiber was undertaken; however it was not as accurate as needed due to a technical failure in the laboratory. To what extent has this affected the modeling of the viewed scene and of the BRDF is unknown. MacArthur et al. (2012) found that optics and entrance slits slightly modified the shape and DRF_λ of a field spectroradiometer and such details would have been missed in our case. However our approach was more realistic than assuming a homogeneous response. In addition, we discovered that the FOV was wider than reported by the manufacturer (in terms of FWHM) and delimited the solid angle from where most of the radiation flux is sampled. This was relevant for the characterization of the FOV contents and to avoid sampling radiance above the horizon at large θ_v.

4.2 HDRDF modeling and retrieval

The modeling of the directional effects proposed in this work includes two features that make it different from the kernel-based models most frequently used. On one hand, the geometric-optical scatter is substituted by a description of the viewed scene and the FOV. On the other hand, the model accounts for diffuse radiation.

Similarly to the geometric-optical kernels, the ray casting model used in this work estimates the occlusion and shading effects for each AMSPEC-MED observation; and also assumes single scatter and no transmittance of the scene elements (Roujean et al. 1992). However, several features make the approach different. First, contributions and angles of the different elements observed are weighted by the DRF_λ of the optical fiber. This is rarely done for non-imager sensors since it requires some knowledge about the contents of the pixel, though it is analogous to the point-spread function more frequently used in image analysis (Plaza et al. 2012). Its impact will depend on pixel heterogeneity and sensor DRF_λ (MacArthur et al. 2012), which would be reduced when observing a homogeneous area from a narrow solid angle. Since AMSPEC-MED system FOV width and scene heterogeneity were large, accounting for DRF_λ was necessary even if this could not be accurately determined. Second, geometric-optical models usually account for shades and occlusion based on the observed area of each cover observed and projected on the ground as a function of the sun-view geometry (Xiaowen and Strahler 1992). This does not account for the increase of the horizontal area per steradian within the FOV as a function of θ_v; which can be ignored for a homogeneous scene of fine grain observed by a narrow FOV. On the contrary, AMSPEC-MED model uses a ray casting approach with a constant vector density per solid angle, and estimates the different contributions based on the frequency of

interception of each cover. Therefore as θ_v increases, the sampling density per unit horizontal area becomes sparser, following in fact a Cauchy distribution (Eklundh et al. 2011). Moreover, when vectors intercept crowns in the FOV, sampling density varies according to the distance to the sensor optics and the surface curvature. However, it must be noted that the model do not integrate the contents of the area observed within the solid angle. AMSPEC-MED FOV is wide, observations are done at large θ_v and the grain of the scene respect to the observation scale is large. Therefore, despite of the computational effort, the proposed approach is more suitable than the use of area-based methods. An alternative would be projecting the observed areas on a plane normal to the observation direction. A simulation analysis was used to compare the contributions estimated by our model with the Li-Sparse and Li-Dense reciprocal kernels. The correlation between the predicted sunlit fraction and each of the functions at high or low θ_v respectively can be explained by the tree density crown of the synthetic image. The Li-Sparse model predicts no occlusion of tree crowns due to low density by simplifying the term $e^x \approx 1 + x$ in Eq. 30 of Wanner et al. (1995); which occurs at low θ_v. On the contrary at large θ_v occlusion happens and only the top of the crowns is observed, which increases the sunlit fraction observed as predicted by Li-Dense. An approach that deals with this issue is the Li-Transit kernel which combines the version of the Li-Sparse reciprocal kernel at low zenith angles and the Li-Dense function at large ones (Gao et al. 2000).

The estimation of the contribution of the different covers to the sensor signal in each observation is the basis for unmixing their directional responses. Some authors have previously used prior information for BRDF modeling and unmixing. In example, Asner et al. (1997) used spectral unmix analysis to determine sub-pixel canopy,

background and shadow fractions and invert a geometric-optical model of a simulated scene. You et al. (2015) used high resolution imagery to determine sub-pixel fractions of different covers within a MODIS pixel and unmixed the corresponding BRDF; whereas Román et al. (2011) used land cover type prior knowledge and high spatial resolution airborne multi-angular information to analyze the impact of scale and mix in the BRDF retrieval.

The second feature of the proposed approach is the inclusion of diffuse radiation by modeling HDRDF instead of directly BRDF, as proposed by Cierniewski et al. (2004). Methods to include diffuse radiation in BRDF modeling have been proposed and used (Dangel et al. 2005; Lyapustin and Privette 1999; Martonchik 1994). However, to our knowledge, these have not been used in automated tower-based mono and multi-angular hyperspectral systems. In spite of that, the effects of diffuse radiation on data acquired by these systems have been reported. In example, Meroni et al (2011) found that diffuse radiation could explain the disagreement of incoming irradiance and the cosine law. Huber et al. (2014) also found that diffuse irradiance might explain hihg forward scattering at high θ_s. Hilker et al. (2008a) found that shadow fraction had an effect on the BRDF shape of PRI under different sky conditions. In the same work, BRDF shapes related to different light use efficiency could only be determined by classifying data in different sky conditions groups. The relationship between the shadow fraction, the diffuse radiation and changes induced in PRI were later analyzed in Hall et al. (2011). On the other hand, Hilker et al. (2009a) filtered and removed cloudy data to avoid this influence in the BRDF analysis of several vegetation indices. Skawoska et al. (2015) found large variations in HCRF related with δ_{dif}. Results of this and other works support that even if impact of diffuse radiation can be small in remote sensing data, it is

relevant in the case of data acquired from proximal sensors. Most of the reported effects are related with large θ_s or cloudy situations but diffuse radiation might have significant effects in the visible region also under clear skies, where atmospheric scattering is strong (Kriebel 1996). Diffuse radiation increases the contribution of radiance coming from the shaded areas. Among other effects, diffuse radiation smooths the BRDF slope in the principal plane (section 3.3, this work) and increases the pixel bright (Sakowska et al. 2015). And as can be deduced by the hemispherical integrals of the kernel functions (Lucht et al. 2000), enhances the differences of scatter between low and large zenith angles. Diffuse radiation also affects the retrieval of BRDF parameters. Hilker et al. (2008a) also reported such effect on PRI BRDF; however since they analyzed a spectral index also related to plant physiology, their results are not directly comparable to the simulation done in this work. Results of the models comparison in section 3.3 showed that kernel-driven BRDF models can accommodate to HDRDF with errors comparable to those produced by disagreement between the BRDF model and the real BRDF observed. This could affect the normalization of reflectance factors. In our analysis the BRDF dark spot was overestimated under diffuse conditions, which should be taken into account prior to use the contrast between the dark and the hot spot to estimate vegetation properties.

The modeling of HDRDF proposed here is similar to the one suggested by Martonchik (1994). However, since δ_{dif} is estimated and assumed isotropic, no iterative inversion schemes are applied and the hemispherical integrals of the functions that represent the diffuse irradiance are precomputed. Different features of the approach proposed were tested using real data acquired by the AMSPEC-MED system. We concluded that aggregating data from several days increased the diversity of sky

conditions and better constrained the models. The maximum period of aggregation was a week, though no large differences were found when comparing to the 5-days aggregation period. In remote sensing, biophysical and optical properties of vegetation covers are not expected to show large changes within these periods. In fact, similar and larger periods are used to generate BRDF products from remote sensors (Hautecœur and Leroy 1998; Schaaf et al. 2002). After temporal aggregation some numerical instability persisted and consequently regularization techniques were tested. Tikhonov regularization provided solutions numerically more stable than OLS, and also estimates of HRDF and BRF smoother across time. The drawback of regularization is that uncertainties in the fit and the predictions were larger. Regularization is been often used for BRDF inversion (Asner et al. 1997; Cui et al. 2014; Pokrovsky and Roujean 2003a; Wang et al. 2007) but more frequently to overcome data scarcity. Automated multi-angular sensors produce large datasets, and new approaches might be explored for BRDF models inversion. In addition to ill-posedness and conditioning, other issues should be addressed, like the effect of the distribution of geometries and diffuse-to-global radiation ratios available for each inversion. Pokrovsky and Roujean (2003b) analyzed the issue of angular sampling scheme concluding that exhaustive sampling might not be always the best option whereas the optimal design was land cover dependent. Angular sampling might be optimized in these automated systems, taking also into account changes in the observed covers. However sky conditions cannot be controlled and schemes for the selection of optimal datasets should be explored.

The unmixing of the grass and tree canopy HDRDF was based on the estimates of their respective contributions in every multi-angular observation. To our knowledge, this had not been done before from a tower-based multi-angular system. Despite of the

uncertainties associated to the modeling of the FOV scene and sampling, separation was reasonably achieved. The multi-angular unmixing approach proved to be also more convenient for the estimation of HDRDF than the mono-angular observation of pure targets. The latter approach could be easier to deploy in a heterogeneous tree-grass ecosystem, but as proved in our comparison, the characterization of directional effects might not be properly constrained. AMSPEC-MED FOV is wide, so in a savanna ecosystem as the one under investigation, this allows acquiring measurements with different contributions of grass and trees. Uncertainties in the estimation of such contributions can be relatively large, but the wide FOV also homogenizes the errors in the different measurements. In addition, the internal heterogeneity of each cover is integrated. A wide FOV also requires assuming that the measured HCRF still can be a proxy of HDRF. Another alternative would be using a narrow FOV (Bruegge et al. 2000; Schopfer et al. 2008) where this assumption was more relaxed, and selecting angles to observe pure patches of each cover. This approach might also present technical problems related with the lenses when permanently installed outdoors and also a larger sensitivity to uncertainties in geometry of observation and intra-cover heterogeneity. In any case, in a tree-grass ecosystem it would be necessary to account for shadows casted from trees outside the FOV.

We compared modeling HDRDF vs. modeling BRDF, where $\delta_{\mathrm{dif}} = 0$ was assumed. Though differences in terms of error were not large between both methods, modeling HDRDF provided model parameters more independent from the illumination conditions. Results show that, despite of the uncertainties in spectral δ_{dif}, automated multi-angular proximal sensing should account for diffuse radiation if the robust normalization of reflectance factors or if any interpretation of the model parameters are

expected. In this work, errors in the model fit were larger under clear skies ($\delta_{dif} < 0.2$) and this might be explained by the anisotropy of diffuse radiation (Lyapustin and Privette 1999), maybe further from isotropy in absence of clouds; or by the assumed opacity of tree crowns. Since trees' clumping was not accounted for, this could produce an overestimation of shaded grass that would vanish under diffuse radiation; and an overestimation of tree contributions. A characterization of this clumping and tree crown transitivity might improve the estimates.

Uncertainties found in the estimation of the contributions of each cover and in the characterization of sky conditions, and also problems related with adequate distribution of data could partly explain the larger errors and instabilities in data. During the Summer in example sky was mainly clear and sometimes model was not well constrain even gathering data from several days. During this period also, the differences between trees and grass reflectances were maxima in the Visible, so that uncertainties in the modeling of FOV contents might have a larger impact in model inversion. Contrarily, in the Summer uncertainties were lower in the NIR, when differences between the reflectance factors of both covers were also smaller. This might be a problematic inherent in the study of tree-grass ecosystems, and others similar where vegetation types present behave spectrally different across the phenological cycle.

In the model proposed, up-scaling HDRDF and reflectance factors requires using a 3D model of the pixel up-scaled and is therefore not straightforward. A 3D model of a 500 m MODIS pixel was approximated and AMSPEC-MED BRF estimates were compared with values derived from the band 1 of MODIS MCD43A1 product. We observed an underestimation of the highest BRF values. This was confirmed when comparing HDRF estimates with field spectral measurements of grass canopy (Figure

16), and was also noticed during the fit of the HDRDF models (Figure 14). Uncertainties in the estimation of δ_{dif} or cover contributions, in the characterization of the FOV width and geometry, or a biased sampling scheme could explain the differences. However, correlation coefficients ($r^2 \in [0.66, 0.86]$) were still larger than those found in previous comparisons of AMSPEC systems in homogeneous ecosystems. Hilker et al. (2009b) found $r^2 = 0.74$ between tower-based and MODIS PRI in a Douglas fir forest. Also, Hilker et al. (2010a) compared PRI AMSPEC estimates with those derived from MODIS bands 11 and 12 obtaining r^2 ranging between 0.57 and 0.62 in a Douglas fir and between 0.51 and 0.63 in mature Aspen forest.

5. CONCLUSIONS

Automated tower-based hyperspectral systems are becoming more frequent nowadays; however several factors jeopardize the comparability of data and the analysis of surface properties. These systems operate under wide ranges of environmental conditions including air temperature, sun angles and diffuse fractions of down-welling flux. On one hand, instrumental artifacts can be prevented via system design and sensor models properly adjusted and updated. On the other, directional effects affecting these systems can be overcame retrieving the BRDF from multi-angular observations. Further efforts should be dedicated to the development of methodologies that make comparable the measurements of different systems. As shown, such approaches would not only depend on the sensor, but also on the scene observed and therefore he problematics and opportunities of these systems could be quite specific. Therefore, ad-hoc approaches rather than a standardization of the sensors used by the scientific community would achieve the comparability of data.

Further efforts will be needed in the modeling of the directional effects affecting these systems. Diffuse irradiance should be accounted for, and measurements of spectral δ_{dif} as simultaneous as possible to the acquisition of reflectance factors would be needed in order to model HDRDF. In some cases, spatial heterogeneity would be also an issue to address. In this study, we used a 3D model of the scene observed to unmix the directional functions of trees and grass; which was also necessary for up-scaling. This required a detailed characterization of the system optics and observation geometry. Similar approaches could be used and up-graded in tree-grass ecosystems and heterogeneous sites. In addition, automated multi-angular hyperspectral systems can provide enormous datasets; new methods to ensure robust model inversion and to select the most suitable angular and atmospheric datasets should be explored.

ACKNOWLEDGEMENTS

The authors of this work are very grateful to Mr. Ramón López, Mr. Jose Francisco Ivars Aparici and Dr. Arnaud Carrara, from the Centro de Estudios Ambientales del Mediterráneo (CEAM) for all the technical support during the installation and setup of the AMSPEC-MED system and for providing the SPN1 data. We would like to thanks Ms. Elia Durá, Ms. Pilar Echavarría, Mr. David Arango and Dr. Gorka Mendiguren from the Spanish National Research Council for the help provided with the field works and setup of the AMSPEC-MED system. We are also very grateful to all the colleagues from the COST Action ES0903 EUROSPEC that participated in the inter-comparison experiments at the NERC Field Spectroscopy Facility, especially to Dr. Tommaso Julitta and Dr. Alasdair MacArthur. Javier Pacheco-Labrador was sponsored by a JAE-Predoc grant (CSIC), co-funded by the

European Social Fund. AMSPEC-MED was funded by the BIOSPEC project "Linking spectral information at different spatial scales with biophysical parameters of Mediterranean vegetation in the context of Global Change" (http://www.lineas.cchs.csic.es/biospec) (CGL2008-02301/CLI, Ministry of Science and Innovation) and the FLUχPEC project "Monitoring changes in water and carbon fluxes from remote and proximal sensing in a Mediterranean dehesa ecosystem" (http://www.lineas.cchs.csic.es/fluxpec) (CGL2012-34383, Ministry of Economy and Competitiveness).

REFERENCES

Abdou, W.A., Helmlinger, M.C., Conel, J.E., Bruegge, C.J., Pilorz, S.H., Martonchik, J.V., & Gaitley, B.J. (2001). Ground measurements of surface BRF and HDRF using PARABOLA III. *Journal of Geophysical Research: Atmospheres, 106*, 11967-11976

Ahamed, T., Tian, L., Jiang, Y., Zhao, B., Liu, H., & Ting, K.C. (2012). Tower remote-sensing system for monitoring energy crops; image acquisition and geometric corrections. *Biosystems Engineering, 112*, 93-107

Asner, G.P., Braswell, B.H., Schimel, D.S., & Wessman, C.A. (1998). Ecological Research Needs from Multiangle Remote Sensing Data. *Remote Sensing of Environment, 63*, 155-165

Asner, G.P., Wessman, C.A., & Privette, J.L. (1997). Unmixing the directional reflectances of AVHRR sub-pixel landcovers. *Geoscience and Remote Sensing, IEEE Transactions on, 35*, 868-878

Bacour, C., & Bréon, F.-M. (2005). Variability of biome reflectance directional signatures as seen by POLDER. *Remote Sensing of Environment, 98*, 80-95

Baldocchi, D.D. (2003). Assessing the eddy covariance technique for evaluating carbon dioxide exchange rates of ecosystems: past, present and future. *Global Change Biology, 9*, 479-492

Balzarolo, M., Anderson, K., Nichol, C., Rossini, M., Vescovo, L., Arriga, N., Wohlfahrt, G., Calvet, J.-C., Carrara, A., Cerasoli, S., Cogliati, S., Daumard, F., Eklundh, L., Elbers, J.A., Evrendilek, F., Handcock, R.N., Kaduk, J., Klumpp, K., Longdoz, B., Matteucci, G., Meroni, M., Montagnani, L., Ourcival, J.-M., Sánchez-Cañete, E.P., Pontailler, J.-Y., Juszczak, R., Scholes, B., & Martín, M.P. (2011). Ground-Based Optical Measurements at European Flux Sites: A Review of Methods, Instruments and Current Controversies. *Sensors, 11*, 7954-7981

Bendig, J., Yu, K., Aasen, H., Bolten, A., Bennertz, S., Broscheit, J., Gnyp, M.L., & Bareth, G. (2015). Combining UAV-based plant height from crop surface models, visible, and near infrared vegetation indices for biomass monitoring in barley. *International Journal of Applied Earth Observation and Geoinformation, 39*, 79-87

Boggs, G.S. (2010). Assessment of SPOT 5 and QuickBird remotely sensed imagery for mapping tree cover in savannas. *International Journal of Applied Earth Observation and Geoinformation, 12*, 217-224

Brach, E.J., Poirier, P., Desjardins, R.L., & Lord, D. (1983). Multispectral radiometer to measure crop canopy characteristics. *Review of Scientific Instruments, 54*, 493-500

Brown de Colstoun, E.C., & Walthall, C.L. (2006). Improving global scale land cover classifications with multi-directional POLDER data and a decision tree classifier. *Remote Sensing of Environment, 100*, 474-485

Bruegge, C.J., Helmlinger, M.C., Conel, J.E., Gaitley, B.J., & Abdou, W.A. (2000). PARABOLA III: A sphere-scanning radiometer for field determination of surface anisotropic reflectance functions. *Remote Sensing Reviews, 19*, 75-94

Burkart, A., Aasen, H., Alonso, L., Menz, G., Bareth, G., & Rascher, U. (2015). Angular Dependency of Hyperspectral Measurements over Wheat Characterized by a Novel UAV Based Goniometer. *Remote Sensing, 7*, 725

Burkart, A., Cogliati, S., Schickling, A., & Rascher, U. (2014). A Novel UAV-Based Ultra-Light Weight Spectrometer for Field Spectroscopy. *Sensors Journal, IEEE, 14*, 62-67

Byambakhuu, I., Sugita, M., & Matsushima, D. (2010). Spectral unmixing model to assess land cover fractions in Mongolian steppe regions. *Remote Sensing of Environment, 114*, 2361-2372

Casals, P., Gimeno, C., Carrara, A., Lopez-Sangil, L., & Sanz, M.J. (2009). Soil CO2 efflux and extractable organic carbon fractions under simulated precipitation events in a Mediterranean Dehesa. *Soil Biology and Biochemistry, 41*, 1915-1922

Cierniewski, J., Gdala, T., & Karnieli, A. (2004). A hemispherical–directional reflectance model as a tool for understanding image distinctions between cultivated and uncultivated bare surfaces. *Remote Sensing of Environment, 90*, 505-523

Colgan, M., Baldeck, C., Féret, J.-B., & Asner, G. (2012). Mapping Savanna Tree Species at Ecosystem Scales Using Support Vector Machine Classification and BRDF Correction on Airborne Hyperspectral and LiDAR Data. *Remote Sensing, 4*, 3462

Colomina, I., & Molina, P. (2014). Unmanned aerial systems for photogrammetry and remote sensing: A review. *ISPRS Journal of Photogrammetry and Remote Sensing, 92*, 79-97

Courbaud, B.t., de Coligny, F., & Cordonnier, T. (2003). Simulating radiation distribution in a heterogeneous Norway spruce forest on a slope. *Agricultural and Forest Meteorology, 116*, 1-18

Cui, S., Yang, S., Zhu, C., & Wen, N. (2014). Remote sensing of surface reflective properties: Role of regularization and a priori knowledge. *Optik - International Journal for Light and Electron Optics, 125*, 7106-7112

Chen, J.M., Liu, J., Leblanc, S.G., Lacaze, R., & Roujean, J.-L. (2003). Multi-angular optical remote sensing for assessing vegetation structure and carbon absorption. *Remote Sensing of Environment, 84*, 516-525

Chopping, M.J. (2000). Testing a LiSK BRDF Model with in Situ Bidirectional Reflectance Factor Measurements over Semiarid Grasslands. *Remote Sensing of Environment, 74*, 287-312

Chopping, M.J., Su, L.H., Rango, A., & Maxwell, C. (2004). Modelling the reflectance anisotropy of Chihuahuan Desert grass–shrub transition canopy–soil complexes. *International Journal of Remote Sensing, 25*, 2725-2745

Dangel, S., Verstraete, M.M., Schopfer, J., Kneubuhler, M., Schaepman, M., & Itten, K.I. (2005). Toward a direct comparison of field and laboratory goniometer measurements. *Geoscience and Remote Sensing, IEEE Transactions on, 43*, 2666-2675

de Abelleyra, D., & Verón, S.R. (2014). Comparison of different BRDF correction methods to generate daily normalized MODIS 250 m time series. *Remote Sensing of Environment, 140*, 46-59

de Wasseige, C., & Defourny, P. (2002). Retrieval of tropical forest structure characteristics from bi-directional reflectance of SPOT images. *Remote Sensing of Environment, 83*, 362-375

Detto, M., Montaldo, N., Albertson, J.D., Mancini, M., & Katul, G. (2006). Soil moisture and vegetation controls on evapotranspiration in a heterogeneous Mediterranean ecosystem on Sardinia, Italy. *Water Resources Research, 42*, W08419

Dickinson, R.E., Pinty, B., & Verstraete, M.M. (1990). Relating surface albedos in GCM to remotely sensed data. *Agricultural and Forest Meteorology, 52*, 109-131

Diner, D.J., Braswell, B.H., Davies, R., Gobron, N., Hu, J., Jin, Y., Kahn, R.A., Knyazikhin, Y., Loeb, N., Muller, J.-P., Nolin, A.W., Pinty, B., Schaaf, C.B., Seiz, G., & Stroeve, J. (2005). The value of multiangle measurements for retrieving structurally and radiatively consistent properties of clouds, aerosols, and surfaces. *Remote Sensing of Environment, 97*, 495-518

Duchemin, B.t., Berthelot, B., Dedieu, G., Leroy, M., & Maisongrande, P. (2002). Normalisation of directional effects in 10-day global syntheses derived from VEGETATION/SPOT:: II. Validation of an operational method on actual data sets. *Remote Sensing of Environment, 81*, 101-113

Duchemin, B.t., & Maisongrande, P. (2002). Normalisation of directional effects in 10-day global syntheses derived from VEGETATION/SPOT:: I. Investigation of concepts based on simulation. *Remote Sensing of Environment, 81*, 90-100

Dupigny-Giroux, L.-A.L. (2007). Using AirMISR data to explore moisture-driven land use–land cover variations at the Howland Forest, Maine — A case study. *Remote Sensing of Environment, 107*, 376-384

Durbha, S.S., King, R.L., & Younan, N.H. (2007). Support vector machines regression for retrieval of leaf area index from multiangle imaging spectroradiometer. *Remote Sensing of Environment, 107*, 348-361

Dwyer, J., & Schmidt, G. (2006). The MODIS Reprojection Tool. In J. Qu, W. Gao, M. Kafatos, R. Murphy, & V. Salomonson (Eds.), *Earth Science Satellite Remote Sensing* (pp. 162-177): Springer Berlin Heidelberg

Eklundh, L., Jin, H., Schubert, P., Guzinski, R., & Heliasz, M. (2011). An Optical Sensor Network for Vegetation Phenology Monitoring and Satellite Data Calibration. *Sensors, 11*, 7678-7709

Fassnacht, F., & Koch, B. (2012). Review of Forestry Oriented Multi-Angular Remote Sensing Techniques. *International Forestry Review, 14*, 285-298

Gamon, J.A., Coburn, C., Flanagan, L.B., Huemmrich, K.F., Kiddle, C., Sanchez-Azofeifa, G.A., Thayer, D.R., Vescovo, L., Gianelle, D., Sims, D.A., Rahman, A.F., & Pastorello, G.Z. (2010). SpecNet revisited: bridging flux and remote sensing communities. *Canadian Journal of Remote Sensing, 36*, S376-S390

Gamon, J.A., Cheng, Y., Claudio, H., MacKinney, L., & Sims, D.A. (2006a). A mobile tram system for systematic sampling of ecosystem optical properties. *Remote Sensing of Environment, 103*, 246-254

Gamon, J.A., Rahman, A.F., Dungan, J.L., Schildhauer, M., & Huemmrich, K.F. (2006b). Spectral Network (SpecNet)—What is it and why do we need it? *Remote Sensing of Environment, 103*, 227-235

Gao, F., Li, X., Strahler, A., & Schaaf, C. (2000). Evaluation of the Li transit kernel for BRDF modeling. *Remote Sensing Reviews, 19*, 205-224

Guanter, L., Alonso, L., & Moreno, J. (2005). First results from the PROBA/CHRIS hyperspectral/multiangular satellite system over land and water targets. *Geoscience and Remote Sensing Letters, IEEE, 2*, 250-254

Guerschman, J.P., Hill, M.J., Renzullo, L.J., Barrett, D.J., Marks, A.S., & Botha, E.J. (2009). Estimating fractional cover of photosynthetic vegetation, non-photosynthetic vegetation and bare soil in the Australian tropical savanna region upscaling the EO-1 Hyperion and MODIS sensors. *Remote Sensing of Environment, 113*, 928-945

Hakala, T., Suomalainen, J., & Peltoniemi, J.I. (2010). Acquisition of Bidirectional Reflectance Factor Dataset Using a Micro Unmanned Aerial Vehicle and a Consumer Camera. *Remote Sensing, 2*, 819

Hall, F.G., Hilker, T., & Coops, N.C. (2011). PHOTOSYNSAT, photosynthesis from space: Theoretical foundations of a satellite concept and validation from tower and spaceborne data. *Remote Sensing of Environment, 115*, 1918-1925

Hall, F.G., Hilker, T., Coops, N.C., Lyapustin, A., Huemmrich, K.F., Middleton, E., Margolis, H., Drolet, G., & Black, T.A. (2008). Multi-angle remote sensing of forest light use efficiency by observing PRI variation with canopy shadow fraction. *Remote Sensing of Environment, 112*, 3201-3211

Hansen, P. (2007). Regularization Tools version 4.0 for Matlab 7.3. *Numerical Algorithms, 46*, 189-194

Hansen, P.C. (1992). Analysis of Discrete Ill-Posed Problems by Means of the L-Curve. *SIAM Review, 34*, 561-580

Hasegawa, K., Matsuyama, H., Tsuzuki, H., & Sweda, T. (2010). Improving the estimation of leaf area index by using remotely sensed NDVI with BRDF signatures. *Remote Sensing of Environment, 114*, 514-519

Hautecœur, O., & Leroy, M.M. (1998). Surface bidirectional reflectance distribution function observed at global scale by POLDER/ADEOS. *Geophysical Research Letters, 25*, 4197-4200

Hilker, T., Coops, N.C., Coggins, S.B., Wulder, M.A., Brownc, M., Black, T.A., Nesic, Z., & Lessard, D. (2009a). Detection of foliage conditions and disturbance from multi-angular high spectral resolution remote sensing. *Remote Sensing of Environment, 113*, 421-434

Hilker, T., Coops, N.C., Hall, F.G., Black, T.A., Wulder, M.A., Nesic, Z., & Krishnan, P. (2008a). Separating physiologically and directionally induced changes in PRI using BRDF models. *Remote Sensing of Environment, 112*, 2777-2788

Hilker, T., Coops, N.C., Nesic, Z., Wulder, M.A., & Black, A.T. (2007). Instrumentation and approach for unattended year round tower based measurements of spectral reflectance. *Computers and Electronics in Agriculture, 56*, 72-84

Hilker, T., Coops, N.C., Schwalm, C.R., Jassal, R.S., Black, T.A., & Krishnan, P. (2008b). Effects of mutual shading of tree crowns on prediction of photosynthetic light-use efficiency in a coastal Douglas-fir forest. *Tree Physiology, 28*, 825-834

Hilker, T., Hall, F.G., Coops, N.C., Lyapustin, A., Wang, Y., Nesic, Z., Grant, N., Black, T.A., Wulder, M.A., Kljun, N., Hopkinson, C., & Chasmer, L. (2010a). Remote sensing of photosynthetic light-use efficiency across two forested biomes: Spatial scaling. *Remote Sensing of Environment, 114*, 2863-2874

Hilker, T., Hall, F.G., Tucker, C.J., Coops, N.C., Black, T.A., Nichol, C.J., Sellers, P.J., Barr, A., Hollinger, D.Y., & Munger, J.W. (2012). Data assimilation of photosynthetic light-use efficiency using multi-angular satellite data: II Model implementation and validation. *Remote Sensing of Environment, 121*, 287-300

Hilker, T., Lyapustin, A., Hall, F.G., Wang, Y., Coops, N.C., Drolet, G., & Black, T.A. (2009b). An assessment of photosynthetic light use efficiency from space: Modeling the atmospheric and directional impacts on PRI reflectance. *Remote Sensing of Environment, 113*, 2463-2475

Hilker, T., Nesic, Z., Coops, N.C., & Lessard, D. (2010b). A new, automated, multiangular radiometer instrument for tower-based observations of canopy reflectance (AMSPEC II). *Instrumentation Science & Technology, 38*, 319-340

Hill, M., Hanan, N., Hoffmann, W., Scholes, R., Prince, S., Ferwerda, J., Lucas, R., Baker, I., Arneth, A., & Higgins, S. (2011). Remote sensing and modeling of savannas: The state of the dis-union. In, *34th International Symposium on Remote Sensing of Environment - The GEOSS Era: Towards Operational Environmental Monitoring* (p. 6). Sydney, NSW ISPRS

Huber, S., Tagesson, T., & Fensholt, R. (2014). An automated field spectrometer system for studying VIS, NIR and SWIR anisotropy for semi-arid savanna. *Remote Sensing of Environment, 152*, 547-556

Julitta, T. (2015). Optical proximal sensing for vegetation monitoring. In, *Department of Earth and Environmental Sciences* (p. 136). Milano, Italy: University of Milano-Bicocca

Kasper, v.W., John A, S., William, N., & Luis, T. (2002). Data and model uncertainty estimation for linear inversion. *Geophysical Journal International, 149*, 625-632

Kimes, D.S., Newcomb, W.W., Nelson, R.F., & Schutt, J.B. (1986). Directional Reflectance Distributions of a Hardwood and Pine Forest Canopy. *Geoscience and Remote Sensing, IEEE Transactions on, GE-24*, 281-293

Kriebel, K.-T. (1996). On the limited validity of reciprocity in measured BRDFs. *Remote Sensing of Environment, 58*, 52-62

Kriebel, K.T. (1975). On the variability of the reflected radiation field due to differing distributions of the irradiation. *Remote Sensing of Environment, 4*, 257-264

Kriebel, K.T. (1978). Average variability of the radiation reflected by vegetated surfaces due to differing irradiations. *Remote Sensing of Environment, 7*, 81-83

Kuusinen, N., Tomppo, E., & Berninger, F. (2013). Linear unmixing of MODIS albedo composites to infer subpixel land cover type albedos. *International Journal of Applied Earth Observation and Geoinformation, 23*, 324-333

Lei, M., Manchun, L., Lihua, T., Yafei, W., & Liang, C. (2013). Using unmanned aerial vehicle for remote sensing application. In, *Geoinformatics (GEOINFORMATICS), 2013 21st International Conference on* (pp. 1-5)

Leuning, R., Hughes, D., Daniel, P., Coops, N.C., & Newnham, G. (2006). A multi-angle spectrometer for automatic measurement of plant canopy reflectance spectra. *Remote Sensing of Environment, 103*, 236-245

Liu, R., Chen, J.M., Liu, J., Deng, F., & Sun, R. (2007). Application of a new leaf area index algorithm to China's landmass using MODIS data for carbon cycle research. *Journal of Environmental Management, 85*, 649-658

Lucht, W. (1998). Expected retrieval accuracies of bidirectional reflectance and albedo from EOS-MODIS and MISR angular sampling. *Journal of Geophysical Research: Atmospheres, 103*, 8763-8778

Lucht, W., & Roujean, J.L. (2000). Considerations in the parametric modeling of BRDF and albedo from multiangular satellite sensor observations. *Remote Sensing Reviews, 18*, 343-379

Lucht, W., Schaaf, C.B., & Strahler, A.H. (2000). An algorithm for the retrieval of albedo from space using semiempirical BRDF models. *Geoscience and Remote Sensing, IEEE Transactions on, 38*, 977-998

Lyapustin, A.I., & Privette, J.L. (1999). A new method of retrieving surface bidirectional reflectance from ground measurements: Atmospheric sensitivity study. *Journal of Geophysical Research: Atmospheres, 104*, 6257-6268

MacArthur, A., MacLellan, C.J., & Malthus, T. (2012). The Fields of View and Directional Response Functions of Two Field Spectroradiometers. *Geoscience and Remote Sensing, IEEE Transactions on, 50*, 3892-3907

Marks, A., Fragiacomo, C., MacArthur, A., Zibordi, G., Fox, N., & King, M.D. (2015). Characterisation of the HDRF (as a proxy for BRDF) of snow surfaces at Dome C, Antarctica, for the inter-calibration and inter-comparison of satellite optical data. *Remote Sensing of Environment, 158*, 407-416

Martonchik, J.V. (1994). Retrieval of surface directional reflectance properties using ground level multiangle measurements. *Remote Sensing of Environment, 50*, 303-316

MEA (2005). *Millennium Ecosystem Assessment—Ecosystems and Human Well-Being: Desertification Synthesis*. Washington, DC: World Resources Institute

Meroni, M., Barducci, A., Cogliati, S., Castagnoli, F., Rossini, M., Busetto, L., Migliavacca, M., Cremonese, E., Galvagno, M., Colombo, R., & Di Cella, U.M.

(2011). The hyperspectral irradiometer, a new instrument for long-term and unattended field spectroscopy measurements. *Review of Scientific Instruments, 82*

Middleton, E., Corp, L.A., & Cook, B.D. (2013). FUSION: Canopy Tower System for Remote Sensing Observations of Terrestrial Ecosystems. In, *White Paper*

Nicodemus, F.E., Richmond, J.C., Hsia, J.J., Ginsberg, I.W., & Limperis, T. (1977). Geometrical Consideration and Nomenclature for Reflectance. In U.D.o.C. National Bureau of Standards (Ed.) (p. 52). Washington, DC

O'Brien, D.M., Mitchell, R.M., Edwards, M., & Elsum, C.C. (1998). Estimation of BRDF from AVHRR Short-Wave Channels: Tests over Semiarid Australian Sites. *Remote Sensing of Environment, 66*, 71-86

Pacheco-Labrador, J., Ferrero, A., & Martín, M.P. (2014). Characterizing integration time and gray-level-related nonlinearities in a NMOS sensor. *Applied Optics, 53*, 7778-7786

Pacheco-Labrador, J., & Martín, M. (2015). Characterization of a Field Spectroradiometer for Unattended Vegetation Monitoring. Key Sensor Models and Impacts on Reflectance. *Sensors, 15*, 4154-4175

Pacheco-Labrador, J., & Martin, M.P. (2014). Nonlinear Response in a Field Portable Spectroradiometer: Characterization and Effects on Output Reflectance. *Geoscience and Remote Sensing, IEEE Transactions on, 52*, 920-928

Peltoniemi, J., Hakala, T., Suomalainen, J., & Puttonen, E. (2009). Polarised bidirectional reflectance factor measurements from soil, stones, and snow. *Journal of Quantitative Spectroscopy and Radiative Transfer, 110*, 1940-1953

Peltoniemi, J.I., Kaasalainen, S., Näränen, J., Rautiainen, M., Stenberg, P., Smolander, H., Smolander, S., & Voipio, P. (2005). BRDF measurement of understory

vegetation in pine forests: dwarf shrubs, lichen, and moss. *Remote Sensing of Environment, 94*, 343-354

Pinker, R.T., & Laszlo, I. (1992). Modeling Surface Solar Irradiance for Satellite Applications on a Global Scale. *Journal of Applied Meteorology, 31*, 194-211

Pinty, B., Roveda, F., Verstraete, M.M., Gobron, N., Govaerts, Y., Martonchik, J.V., Diner, D.J., & Kahn, R.A. (2000). Surface albedo retrieval from Meteosat: 1. Theory. *Journal of Geophysical Research: Atmospheres, 105*, 18099-18112

Plaza, A., Bioucas-Dias, J.M., Simic, A., & Blackwell, W.J. (2012). Foreword to the Special Issue on Hyperspectral Image and Signal Processing. *Selected Topics in Applied Earth Observations and Remote Sensing, IEEE Journal of, 5*, 347-353

Pokrovsky, I., Pokrovsky, O., & Roujean, J.-L. (2003a). Development of an operational procedure to estimate surface albedo from the SEVIRI/MSG observing system by using POLDER BRDF measurements: I. Data quality control and accumulation of information corresponding to the IGBP land cover classes. *Remote Sensing of Environment, 87*, 198-214

Pokrovsky, I., Pokrovsky, O., & Roujean, J.-L. (2003b). Development of an operational procedure to estimate surface albedo from the SEVIRI/MSG observing system by using POLDER BRDF measurements: II. Comparison of several inversion techniques and uncertainty in albedo estimates. *Remote Sensing of Environment, 87*, 215-242

Pokrovsky, O., & Roujean, J.-L. (2003a). Land surface albedo retrieval via kernel-based BRDF modeling: I. Statistical inversion method and model comparison. *Remote Sensing of Environment, 84*, 100-119

Pokrovsky, O., & Roujean, J.-L. (2003b). Land surface albedo retrieval via kernel-based BRDF modeling: II. An optimal design scheme for the angular sampling. *Remote Sensing of Environment, 84*, 120-142

Proud, S.R., Qingling, Z., Schaaf, C., Fensholt, R., Rasmussen, M.O., Shisanya, C., Mutero, W., Mbow, C., Anyamba, A., Pak, E., & Sandholt, I. (2014). The Normalization of Surface Anisotropy Effects Present in SEVIRI Reflectances by Using the MODIS BRDF Method. *Geoscience and Remote Sensing, IEEE Transactions on, 52*, 6026-6039

Qi, J., Kerr, Y.H., Moran, M.S., Weltz, M., Huete, A.R., Sorooshian, S., & Bryant, R. (2000). Leaf Area Index Estimates Using Remotely Sensed Data and BRDF Models in a Semiarid Region. *Remote Sensing of Environment, 73*, 18-30

Reda, I., & Andreas, A. (2004). Solar position algorithm for solar radiation applications. *Solar Energy, 76*, 577-589

Román, M.O., Gatebe, C.K., Schaaf, C.B., Poudyal, R., Wang, Z., & King, M.D. (2011). Variability in surface BRDF at different spatial scales (30 m–500 m) over a mixed agricultural landscape as retrieved from airborne and satellite spectral measurements. *Remote Sensing of Environment, 115*, 2184-2203

Roosjen, P., Bartholomeus, H., Suomalainen, J., & Clevers, J. (2015). Investigating BRDF effects based on optical multi-angular laboratory and hyperspectral UAV measurements. In, *Fourier Transform Spectroscopy and Hyperspectral Imaging and Sounding of the Environment* (p. JM3A.15). Lake Arrowhead, California: Optical Society of America

Ross, J. (1981). *The radiation regime and architecture of plant stands*. The Hague: W. Junk

Roujean, J.-L., Leroy, M., & Deschamps, P.-Y. (1992). A Bidirectional Reflectance Model of the Earth's Surface for the Correction of Remote Sensing Data. *J. Geophys. Res., 97*, 20455-20468

Roy, D.P., Lewis, P.E., & Justice, C.O. (2002). Burned area mapping using multi-temporal moderate spatial resolution data—a bi-directional reflectance model-based expectation approach. *Remote Sensing of Environment, 83*, 263-286

Sakowska, K., Gianelle, D., Zaldei, A., MacArthur, A., Carotenuto, F., Miglietta, F., Zampedri, R., Cavagna, M., & Vescovo, L. (2015). WhiteRef: A New Tower-Based Hyperspectral System for Continuous Reflectance Measurements. *Sensors, 15*, 1088

Salamí, E., Barrado, C., & Pastor, E. (2014). UAV Flight Experiments Applied to the Remote Sensing of Vegetated Areas. *Remote Sensing, 6*, 11051

Sandmeier, S.R. (2000). Acquisition of Bidirectional Reflectance Factor Data with Field Goniometers. *Remote Sensing of Environment, 73*, 257-269

Scanlon, T.M., Albertson, J.D., Caylor, K.K., & Williams, C.A. (2002). Determining land surface fractional cover from NDVI and rainfall time series for a savanna ecosystem. *Remote Sensing of Environment, 82*, 376-388

Schaaf, C.B., Gao, F., Strahler, A.H., Lucht, W., Li, X., Tsang, T., Strugnell, N.C., Zhang, X., Jin, Y., Muller, J.-P., Lewis, P., Barnsley, M., Hobson, P., Disney, M., Roberts, G., Dunderdale, M., Doll, C., d'Entremont, R.P., Hu, B., Liang, S., Privette, J.L., & Roy, D. (2002). First operational BRDF, albedo nadir reflectance products from MODIS. *Remote Sensing of Environment, 83*, 135-148

Schaepman-Strub, G., Schaepman, M.E., Painter, T.H., Dangel, S., & Martonchik, J.V. (2006). Reflectance quantities in optical remote sensing—definitions and case studies. *Remote Sensing of Environment, 103*, 27-42

Schopfer, J., Dangel, S., Kneubühler, M., & Itten, K. (2008). The Improved Dual-view Field Goniometer System FIGOS. *Sensors, 8*, 5120

Sjöström, M., Ardö, J., Eklundh, L., El-Tahir, B.A., El-Khidir, H.A.M., Hellström, M., Pilesjö, P., & Seaquist, J. (2009). Evaluation of satellite based indices for gross primary production estimates in a sparse savanna in the Sudan. *Biogeosciences, 6*, 129-138

Snyder, W.C., & Zhengming, W. (1998). BRDF models to predict spectral reflectance and emissivity in the thermal infrared. *Geoscience and Remote Sensing, IEEE Transactions on, 36*, 214-225

Strub, G., Schaepman, M.E., Knyazikhin, Y., & Itten, K.I. (2003). Evaluation of spectrodirectional alfalfa canopy data acquired during DAISEX'99. *Geoscience and Remote Sensing, IEEE Transactions on, 41*, 1034-1042

Suomalainen, J., Hakala, T., Peltoniemi, J., & Puttonen, E. (2009a). Polarised Multiangular Reflectance Measurements Using the Finnish Geodetic Institute Field Goniospectrometer. *Sensors, 9*, 3891

Suomalainen, J., Hakala, T., Puttonen, E., & Peltoniemi, J. (2009b). Polarised bidirectional reflectance factor measurements from vegetated land surfaces. *Journal of Quantitative Spectroscopy and Radiative Transfer, 110*, 1044-1056

Thomas, S., Stefan, Z., & Ioannis, M. (2004). Field goniometer system for accompanying directional measurements. In, *Second CHRIS/Proba Workshop*. ESRIN, Frascati, Italy

Tikhonov, A.N., & Arsenin, V.Y. (1977). *Solutions of Ill-posed Problems*. New York: John Wiley and Sons

Van De Geer, S.A. (2005). "Least Squares Estimation". In B.S. Everitt, & D.C. Howell (Eds.), *Encyclopedia of Statistics in Behavioral Science* (pp. 1041–1045). Chichester: John Wiley & Sons, Ltd

Vermote, E.F., El Saleous, N., Justice, C.O., Kaufman, Y.J., Privette, J.L., Remer, L., Roger, J.C., & Tanré, D. (1997). Atmospheric correction of visible to middle-infrared EOS-MODIS data over land surfaces: Background, operational algorithm and validation. *Journal of Geophysical Research: Atmospheres, 102*, 17131-17141

von Bueren, S.K., Burkart, A., Hueni, A., Rascher, U., Tuohy, M.P., & Yule, I.J. (2015). Deploying four optical UAV-based sensors over grassland: challenges and limitations. *Biogeosciences, 12*, 163-175

Wang, G., Gertner, G., & Anderson, A.B. (2005). Sampling design and uncertainty based on spatial variability of spectral variables for mapping vegetation cover. *International Journal of Remote Sensing, 26*, 3255-3274

Wang, Y., Li, X., Nashed, Z., Zhao, F., Yang, H., Guan, Y., & Zhang, H. (2007). Regularized kernel-based BRDF model inversion method for ill-posed land surface parameter retrieval using smoothness constraint. *Remote Sensing of Environment, 111*, 36-50

Wang, Z., Schaaf, C.B., Lewis, P., Knyazikhin, Y., Schull, M.A., Strahler, A.H., Yao, T., Myneni, R.B., Chopping, M.J., & Blair, B.J. (2011). Retrieval of canopy height using moderate-resolution imaging spectroradiometer (MODIS) data. *Remote Sensing of Environment, 115*, 1595-1601

Wanner, W., Li, X., & Strahler, A.H. (1995). On the derivation of kernels for kernel-driven models of bidirectional reflectance. *J. Geophys. Res., 100*, 21077-21089

Wanner, W., Strahler, A.H., Hu, B., Lewis, P., Muller, J.P., Li, X., Schaaf, C.L.B., & Barnsley, M.J. (1997). Global retrieval of bidirectional reflectance and albedo over land from EOS MODIS and MISR data: Theory and algorithm. *Journal of Geophysical Research: Atmospheres, 102*, 17143-17161

Webster, R., Curran, P.J., & Munden, J.W. (1989). Spatial correlation in reflected radiation from the ground and its implications for sampling and mapping by ground-based radiometry. *Remote Sensing of Environment, 29*, 67-78

Weyermann, J., Damm, A., Kneubuhler, M., & Schaepman, M.E. (2014). Correction of Reflectance Anisotropy Effects of Vegetation on Airborne Spectroscopy Data and Derived Products. *Geoscience and Remote Sensing, IEEE Transactions on, 52*, 616-627

Xiaowen, L., & Strahler, A.H. (1985). Geometric-Optical Modeling of a Conifer Forest Canopy. *Geoscience and Remote Sensing, IEEE Transactions on, GE-23*, 705-721

Xiaowen, L., & Strahler, A.H. (1992). Geometric-optical bidirectional reflectance modeling of the discrete crown vegetation canopy: effect of crown shape and mutual shadowing. *Geoscience and Remote Sensing, IEEE Transactions on, 30*, 276-292

You, D., Wen, J., Xiao, Q., Liu, Q., Liu, Q., Tang, Y., Dou, B., & Peng, J. (2015). Development of a High Resolution BRDF/Albedo Product by Fusing Airborne CASI Reflectance with MODIS Daily Reflectance in the Oasis Area of the Heihe River Basin, China. *Remote Sensing, 7*, 6784

APPENDIX I. LIST OF SYMBOLS

Symbol	Magnitude
A	Predictors matrix of known observations
b	Observations vector
b/r	Relative crown shape
C	Predictors matrix of known observations in the regularized system
d	Observations vector in the regularized system
DRF_{λ}	Spectral Directional Response Function
G	Subscript that stands for "grass cover"
h	Integral of a kernel-driven function over the hemisphere
h/b	Relative crown height
j	Cover type
k	BRDF or HDRDF model parameter
k_{iso}	BRDF or HDRDF model isometric parameter
k_{geo}	BRDF or HDRDF model geometric parameter
$k_{\mathrm{geo}_{RC}}$	BRDF or HDRDF model geometric parameter of the $K'_{\mathrm{geo}_{\mathrm{RC}}}$ function
k_{vol}	BRDF or HDRDF model volumetric parameter
$k_{\mathrm{vol}_{RT}}$	BRDF or HDRDF model geometric parameter of the $K'_{\mathrm{vol}_{\mathrm{RT}}}$ function
K	Kernel-driven function that describes bidirectional scatter
K'_{geo}	Geometric-optical function that describes HDRDF
$K'_{\mathrm{geo}_{\mathrm{RC}}}$	Geometric-optical function that describes HDRDF based on the 3D ray casting model
K'_{vol}	Volumetric function that describes HDRDF
$K'_{\mathrm{vol}_{\mathrm{RT}}}$	Volumetric function that describes HDRDF based on the Ross Thick kernel-driven function
L	Identity matrix or derivative operator
n	Number of observations
m	Number cover types observed
p	p-value
q	Subscript that indicates the row or column number of a matrix
r^2	Coefficient of determination

sh	Subscript that stands for “shaded”
sl	Subscript that stands for “sunlit”
T	Subscript that stands for “tree cover”
T_{inv}	Student’s cumulative distribution value
ν	Degree of freedom
x	System solution
x_{β}	System regularized solution
x^*	Prior estimate of the system solution
Z	Set of predictors
α	Contribution to an observation
α_{sl}	Contribution of the sunlit fraction to an observation
α_{sh}	Contribution of the shadow fraction to an observation
β	Regularization error’s weight
γ	Confidence level
δ_{dif}	Diffuse-to-Global Radiation Ratio
$\delta_{\hat{\mathrm{x}}}$	Uncertainty half-band associated to the vector of coefficients
$\delta_{\hat{\mathrm{y}}}$	Propagated to produce the uncertainty half-band of the prediction
ε	Vector of random disturbances
θ_{s}	Zenith illumination angle
θ_{v}	Zenith view angle
λ	Subscript that denotes the spectral nature of a variable
ϕ	View-sun relative azimuth angle
σ^2	Error variance

APPENDIX II. LIST OF ACRONYMS AND ABBREVIATIONS

ALS**:** *Airborne Laser Scanning*

AMBRALS: *Algorithm for MODIS Bidirectional Reflectance Anisotropies of the Land Surface*

AMSPEC: *Automated Multiangular Spectro-radiometer for Estimation of Canopy reflectance*

AMSPEC-MED: AMSPEC system deployed in the Mediterranean tree-grass ecosystem in las Majadas del Tiétar site, Cáceres, Spain.

AVHRR: *Advanced Very High Resolution Radiometer*

BRDF: *Bidirectional Reflectance Distribution Function*

BRF: *Bidirectional Reflectance Factor*

CHRIS: *Compact High Resolution Imaging Spectrometer*

DN: *Digital Number*

DGM: *Digital Ground Model*

DSM: *Surface Model*

FIGOS: *Swiss Field-Goniometer System*

FOV: *Field of View*

GPS: *Global Positioning System*

HCRF: *Hemispherical-Conical Reflectance Factor*

HDRDF: *Hemispherical-Directional Reflectance Distribution Function*

HDRF: *Hemispherical-Directional Reflectance Factor*

LAI: *Leaf Area Index*

LED: *Light-Emitting Diode*

LiDAR: *Light Detection and Ranging*

MIRS: *Multi-Angle Imaging Spectra-Radiometer*

MODIS: *Moderate Resolution Imaging Spectroradiometer*

MSG: *Meteosat Second Generation*

NIR: *Near Infrared*

OLS: *Ordinary Least Squares*

PARABOLA: *Portable Apparatus for Rapid Acquisition of Bidirectional Observation of the Land and Atmosphere*

PNOA: *Spanish National Plan for Aerial Orthophotography*

POLDER: *Polarization and Directionality of Earth Reflectance*

PRI: *Photochemical Reflectance Index*

PTU: *Pan-Tilt Unit*

RMSE: *Root Mean Squared Error*

RRMSE: *Relative Root Mean Squared Error*

RPAS: *Remotely Piloted Aircraft Systems*

RTLSR BRDF: *Ross-Thick-Li-Sparse-Reciprocal BRDF model*

SWIR: *Short Wave Infrared*

TW: *Time Window*

5. CONCLUSIONS AND FUTURE RESEARCH

The first part of the present Thesis has focused on the characterization of a field dual channel spectrometer later installed in an automated multi-angular system outdoors. The second has been dedicated to the analysis of the directional responses observed by the system in a heterogeneous ecosystem.

The continuous and automated nature of the system has been common to both parts of the study. Automated systems acquire measurements under ranges of environmental variables likely much larger than hand-held systems. This means that the influence of these variables must be subtracted from the measurements prior to analyze the information.

5.1 INSTRUMENTAL CHARACTERIZATION

The Unispec DC is a spectrometer largely used in the study of vegetation and remote sensing; among the first instruments to be automatized. However, a detailed characterization of this instrument had not been previously reported. This study has identified and characterized different instrumental artifacts that can compromise data quality.

Special attention has been put on the characterization of non-linearities since these jeopardize the study of variables that, as the spectral measurement, are also dependent on the incoming or the reflected radiation fluxes. These could be vegetation physiology, quantification of energy fluxes or BRDF analysis. Gray-level-related non-linearity can be controlled by integration time optimization procedures, though characterization and correction would still be recommendable, or even necessary for

some applications. The integration-time-related nonlinearity has been to our knowledge, reported here for first time in a field spectroradiometer. Though it is likely to have little effect in outdoor measurements, where radiation fluxes are high; it can dramatically affect laboratory measurements and the parametrization of other sensor models, where radiation sources are usually less powerful.

Instrumental dependences on temperature have been also analyzed. This was critical for a system that lacks of shutter for recording the dark current signal; and that in addition was installed in a system that cannot include temperature stabilization, due to power supply limitations. Both features would be desirable for automated systems and should be provided whenever is possible.

The directional response of the cosine receptor was also modeled in order to correct the effects of the different illumination heights and the diffuse component of irradiance. Also this type of characterization would be especially relevant in automated systems.

Instrumental artifacts are specific of each sensor type, and unique for each instrument. Though some of them can be prevented via system design, this might not be always possible and sensor models should be developed and parametrized. Especially in the case of automated systems, especial efforts should be done to guarantee data quality and comparability. It must be also considered that the significance of biases and uncertainties and the corresponding impacts would also depend on the requirements of each application.

Further efforts are needed to develop procedures for the characterization of outdoors automated spectral systems. Especial attention must be paid to the maintenance and update of sensor models. These tasks can be costly and difficult in the

case of automated systems as they could require dismounting the part or the whole system to perform laboratory measurements. Different solutions could be explored to guarantee regular update of sensor models of sensors installed in automated systems. In example, the use of modular systems could facilitate the disassembling and rearrangement after maintenance and characterization. A second option could be the development of characterization benchmarks that could be operated outdoors.

5.2 HDRDF MODELING AND UNMIX

In the second part of this study, we have proposed an innovative methodology for the analysis of the directional responses. To our knowledge, this is the first automated multi-angular tower-based system that unmixes the directional responses of the different covers simultaneously observed within the FOV of the sensor. The separation of directional functions is based on the 3D modeling of the ecosystem and the characterization of the optics used. The ecosystem model was derived from non-synchronized ALS data, assuming low temporal variability. The accuracy with which scene and optics are modeled determines the quality of the unmixing. New methods should be tested to model observed scene covers and shadow fractions efficiently. In example, multi-angular RGB images and structure from motion techniques could be suitable in ecosystems where structure varied also across time. Terrestrial LiDAR could provide detailed topography of the observed scene if the system range is sufficient, and also provide information about canopy transmittance. These methods would allow also estimate shadow fraction to derive ΔPRI-based LUE.

The approach proposed also accounts for the effect of diffuse radiation on the directional responses of vegetation, modeling the HDRDF instead of the BRDF.

However, further efforts are needed to improve the measurements of the diffuse component of irradiance in these systems, both, in the spectral and the directional domains. Radiative transfer, bi-conical or shadow band sensors or hemispherical cameras among other approaches could be tested. Also, new data processing approaches should be explored in order to optimize variances and distributions in datasets used for model inversion.

The strong directional effects found in this work and others, makes highly recommendable for automated hyperspectral systems to adopt a multi-angular approach. This would allow not only the characterization of directional effects for correction and comparison with remote observations and sensors; but also chances for a better constrained inversion of radiative transfer models for the retrieval of biophysical parameters of vegetation. AMSPEC-MED HDRDF derived data have not been fully exploited yet. Future analyses would include the use of this information for the retrieval of biophysical variables or biospheric fluxes.